

The International Workshop
on Computational Nanotechnology

IWCN 2021

May 24-June 6, 2021

Online Conference

BOOK OF ABSTRACTS

International Workshop on Computational Nanotechnology

<http://iwcn2021.org/>

KAIST

IWCN 2021

Sponsors

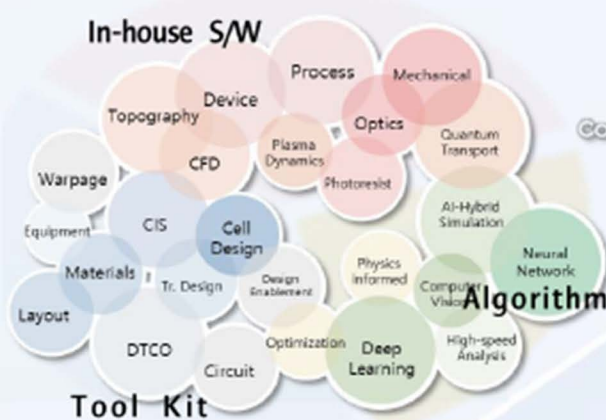
We gratefully acknowledge the support of our sponsors:



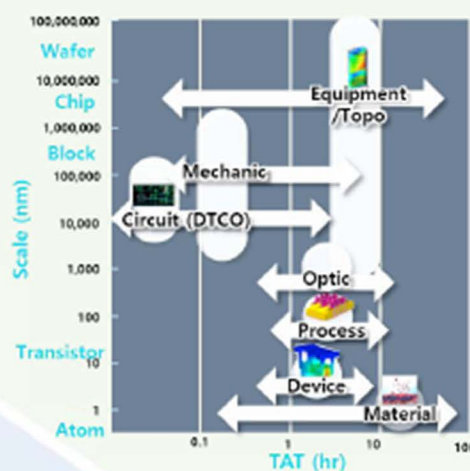
DIT Center CSE Team

DATA & INFORMATION TECHNOLOGY CENTER
COMPUTATIONAL SCIENCE & ENGINEERING TEAM

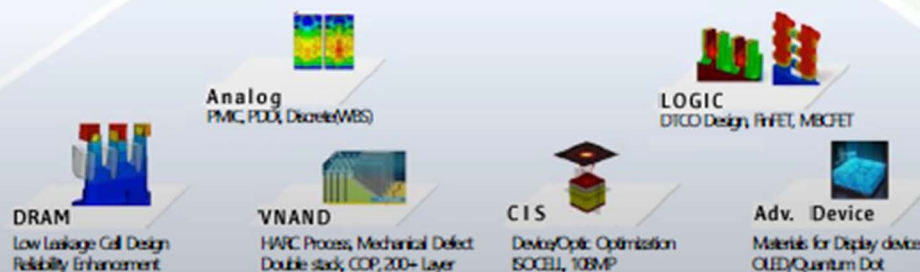
CSE S/W Tool



Modeling & Simulation



Product Solution



SW Development

Technology Design Automation Tool
Physics based TCAD Simulator



AI Algorithm

Machine/Deep Learning Model



Data Analysis

Data Mining, Big Data Analysis
Forecasting & Optimization



Device Simulation

Transistor-level Electrical Properties



Process Simulation

Semiconductor Process Modeling



Material Simulation

Atomic-level modeling and new material design



Mechanical Simulation

Structural Stability and Machine Defect Analysis



Circuit Simulation

Compact Modeling and Pathfinding PDK



Optic Simulation

CIS & Instrumentation Facility Optical Analysis

Welcome

Welcome to the International Workshop on Computational Nanotechnology 2021

IWCN is a forum for research on the development and application of advanced simulations of nanostructures, nanomaterials, and nanodevices.

IWCN 2021 is the 21st in the series of International Workshops, until 2015 titled "Computational Electronics" and changed to "Computational Nanotechnology" in 2017. The new name, IWCN, reflects the longstanding aim of the Workshop to generate interdisciplinary research and collaboration in solid-state materials and device simulation, and the increasingly dominant presence of nanoscale structures and devices in high performance electronics and photonics. The full history of workshops is provided at the IWCN portal website <http://iwcn.info>.

Topics include electronic structure calculations; simulations of electronic, optical and mechanical properties of nanostructures; simulations of electronic, thermal, spin and molecular transport processes; multiscale and multiphysics simulations; computational design and evaluation of engineered nanomaterials and nanostructures; simulation of nanodevice processing and performance.

IWCN 2021 is held as a virtual workshop from May 24 to June 6 due to the global pandemic. A satellite workshop, The International Wigner Workshop 2021, is also held online one week prior to IWCN.

The Organizing Committee

Mincheol Shin, KAIST, Korea (General Chair)

Sung-Min Hong, GIST, Korea (Program Committee Chair)

Jiwon Chang, Yonsei University, Korea

Hoon Ryu, KISTI, Korea

Yong-Hoon Kim, KAIST, Korea

Advisory Committee

Marc Bescond, University of Tokyo, Japan
György Csaba, Pázmány Péter Catholic University, Hungary
Aldo Di Carlo, University of Rome "Tor Vergata", Italy
Philippe Dollfus, University Paris-Sud, France
David Ferry, Arizona State University, USA
Stephen Goodnick, Arizona State University, USA
Karol Kalna, Swansea University, UK
Robert Kelsall, University of Leeds, UK
Gerhard Klimeck, Purdue University, USA
Irena Knezevic, University of Wisconsin, USA
Hans Kosina, Technical University Vienna, Austria
Tillmann Kubis, Purdue University, USA
Paolo Lugli, Free University of Bozen-Bolzano, Italy
Massimo Macucci, University of Pisa, Italy
Nobuya Mori, Osaka University, Japan
Xavier Oriols, Universidad Autonoma de Barcelona, Spain
Wolfgang Porod, University of Notre Dame, USA
Nobuyuki Sano, Tsukuba University, Japan
Siegfried Selberherr, Technical University Vienna, Austria
Mincheol Shin, KAIST, Korea
William Vandenberghe, University of Texas at Dallas, USA
Dragica Vasileska, Arizona State University, USA
Josef Weinbub, Technical University Vienna, Austria

Program Committee

Sung-Min Hong (Chair), GIST, Korea
Doosik Kim, SK Hynix, Korea
Uihui Kwon, Samsung, Korea
Yiming Li, NCTU, Taiwan
Nobuya Mori, Osaka University, Japan
Hideki Minary, Sony, Japan
Rajib Rahman, University of New South Wales, Australia
Gianluca Fiori, University of Pisa, Italy
Elena Gnani, University of Bologna, Italy
Neophytos Neophytou, University of Warwick, UK
Marco Pala, CNRS, France
Vihar Georgiev, University of Glasgow, UK
Mathieu Luisier, ETH, Swiss
Christoph Jungemann, RWTH, Germany
Woosung Choi, Samsung USA, USA
M. P. Anantram, University of Washington, USA
Youngki Yoon, University of Waterloo, Canada
Zlatan Aksamija, University of Massachusetts, USA
Jing Guo, University of Florida, USA

Workshop Program

Session 1: First Principles Calculations and Materials Simulations

(Invited) Machine learning potentials enabling realistic-size simulation and accelerated material discovery

Seungwu Han (*Department of Materials Science and Engineering, Seoul National University, South Korea*)

1

Numerical calculation of the transverse modes in 1T' MoS₂ nanoribbons

Hans Kosina¹, Heribert Seiler¹, and Viktor Sverdlov² (*¹Institute for Microelectronics, TU Wien, Austria, ²Christian Doppler Laboratory for Nonvolatile Magnetoresistive Memory and Logic at the Institute for Microelectronics, TU Wien, Austria*)

9:10-9:25

2

Pair-production in vacuum and plasmas using the Wigner formalism

Haidar Al-Naseri, Jens Zamanian, and Gert Brodin (*Dept. of Physics, Umeå University, Sweden*)

9:25-9:40

4

Density functional theory modeling of chemical reactions at interfaces

Namita Narendra¹, Jinying Wang², James Charles¹, and Tillmann Kubis^{1,2,3,4} (*¹School of Electrical and Computer Engineering, Purdue University, USA, ²Network for Computational Nanotechnology, Purdue University, USA, ³Purdue Center for Predictive Materials and Devices, USA, ⁴Purdue Institute of Inflammation, Immunology and Infectious Disease, USA*)

10:40-10:55

6

Electronic states in 4H-SiC MOS inversion layers considering crystal structure using empirical pseudopotential method

Sachika Nagamizo, Hajime Tanaka, and Nobuya Mori (*Graduate School of Engineering, Osaka University, Japan*)

8

First-principles study of gate field effect in vertical van der Waals heterostructures

Juho Lee, Tae Hyung Kim, Ryong Gyu Lee, and Yong-Hoon Kim (*School of Electrical Engineering, Korea Advanced Institute of Science and Technology, South Korea*)

10

Multiscale investigation of the transport properties in partially overlapped van der Waal structure of 2D materials

Emmanuele Cannavò¹, Damiano Marian¹, Enrique G. Marin², Giuseppe Iannaccone¹, and Gianluca Fiori¹ (*¹Dipartimento di Ingegneria dell'Informazione, Università di Pisa, Italy, ²Dpto. Electrónica, Fac. Ciencias, Universidad de Granada, Spain*)

12

Simulation web platform for electro-chemical oxygen reduction reaction

Seungchul Kim¹, Chan-Woo Lee², Byeong-Joo Lee³, Donghyuk Seol³, Doyeon Kim¹, Assel Kembay¹, Kayong Yun¹, Semi Jang^{1,4}, and Jungho Lee⁴ (*¹Computational Science Research Center, Korea Institute of Science and Technology, South Korea, ²Platform Technology Laboratory, Korea Institute of Energy Research, South Korea, ³Department of Materials Science and Engineering, Pohang University of Science and Technology, South Korea, ⁴Virtual Lab Inc., South Korea*)

14

- First-principles calculation of the non-equilibrium quasi-Fermi level in WSe₂ p-n junctions**
Tae Hyung Kim, Juho Lee, Jun Seong Lee, and Yong-Hoon Kim (*School of Electrical Engineering, Korea Advanced Institute of Science and Technology, South Korea*) 16
- Anomalous thermoelectric transport in biased bilayer WSe₂**
Vassilios Vargiamidis¹, Panagiotis Vasilopoulos², and Neophytos Neophytou¹ (*¹School of Engineering, University of Warwick, United Kingdom, ²Department of Physics, Concordia University, Canada*) 18
- Accurate band-gap database for semiconducting inorganic materials: beyond the level of PBE**
Sangtae Kim¹, Miso Lee¹, Changho Hong¹, Youngchae Yoon¹, Hyungmin An¹, Dongheon Lee¹, Wonseok Jeong¹, Dongsun Yoo¹, Purun-hanul Kim¹, Youngho Kang², Yong Youn¹, and Seungwu Han¹ (*¹Department of Materials Science and Engineering, Seoul National University, South Korea, ²Department of Materials Science and Engineering, Incheon National University, South Korea*) 20
- THz optical properties of graphene quantum dot with transition metal adatom – time dependent DFT study**
Do Hyeon Kim and Byoung Don Kong (*Department of Electrical Engineering, Pohang University of Science and Technology, South Korea*) 22
- Session 2: Quantum Transport in Ultimately Scaled Devices**
- (Invited) Ultrafast electron dynamics in a silicon quantum-dot single-electron pump**
Akira Fujiwara¹, Gento Yamahata¹, Nathan Johnson¹, Sungguen Ryu², Heung-Sun Sim², and Masaya Kataoka³ (*¹NTT Basic Research Laboratories, NTT Corporations, Japan, ²Korea Advanced Institute of Science and Technology, South Korea, ³National Physical Laboratory, United Kingdom*) 24
- Interfacial trap effects in InAs gate-all-around nanowire tunnel field-effect transistors: first-principles-based approach**
Hyeongu Lee, Yucheol Cho, Seonghyeok Jeon, and Mincheol Shin (*School of Electrical Engineering, Korea Advanced Institute of Science and Technology, South Korea*) 25
- Equivalent model for tunneling simulation of direct-gap semiconductor nanowires**
Jo Okada, Futo Hashimoto, and Nobuya Mori (*Graduate School of Engineering, Osaka University, Japan*) 27
- DFT-NEGF study of biaxial strain effects on Co₂FeAl-based magnetic tunnel junctions**
Seongcheol Noh and Mincheol Shin (*School of Electrical Engineering, Korea Advanced Institute of Science and Technology, South Korea*) 29
- Simulation of AC responses using non-equilibrium Green's function at finite frequencies**
Phil-Hun Ahn and Sung-Min Hong (*School of Electrical Engineering and Computer Science, Gwangju Institute of Science and Technology, South Korea*) 31
- Assessing quantum thermalization in small isolated quantum systems through local-in-position weak values of the momentum**
Carlos F. Destefani¹, Guillermo Albareda², and Xavier Oriols¹ (*¹Universitat Autònoma de Barcelona, Spain, ²Max Planck Institute for the Structure and Dynamics of Matter, Germany*) 33

- Highly efficient thermionic cooling semiconductor devices based on tilted-barrier heterostructures**
 Marc Bescond^{1,2} and Kazuhiko Hirakawa^{1,2} (¹LIMMS-CNRS, Japan, ²Institute of Industrial Science and INQIE, University of Tokyo, Japan) 35
- Effects of thin dipole layer in silicon tunnel field effect transistors**
 Yeongjun Lim, Junbeom Seo, and Mincheol Shin (*School of Electrical Engineering, Korea Advanced Institute of Science and Technology, South Korea*) 37
- Quantum transport framework for highly conductive δ -layer systems**
 Juan P. Mendez, Denis Mamaluy, Xujiao Gao, and Shashank Misra (*Sandia National Laboratories, USA*) 39
- Quantum transport simulation on 2D ferroelectric tunnel junctions**
 Eunyeong Yang and Jiwon Chang (*Department of Electrical Engineering, Ulsan National Institute of Science and Technology, South Korea*) 41
- Session 3: Simulations of Emerging Devices**
- (invited) Computational research of CMOS channel material benchmarking for future technology nodes: missions, learnings, and remaining challenges**
 Raseong Kim, Uygur E. Avci, and Ian A. Young (*Components Research, Intel Corporation, USA*) 43
- (Invited) Advanced modeling of emerging nonvolatile magnetoresistive devices**
 J. Ender¹, S. Fiorentini¹, R. Orio², S. Selberherr², W. Goes³, and V. Sverdlov¹ (¹Christian Doppler Laboratory for Nonvolatile Magnetoresistive Memory and Logic at the ²Institute for Microelectronics, TU Wien, Austria, ³Silvaco Europe, United Kingdom) 45
- Multiscale modeling of hole avalanche multiplication and excess noise in amorphous selenium semiconductors**
 Atreyo Mukherjee¹, Richard Akis², Dragica Vasileska³, and A. H. Goldan² (¹Department of Electrical Engineering, Stony Brook University, USA, ²Department of Radiology, School of Medicine, Stony Brook University, USA, ³School of Electrical, Computer and Energy Engineering, Arizona State University, USA) 10:55-11:10 47
- Asymmetry of current-induced heating in magnetic tunnel junctions**
 Tomáš Hádámek¹, Siegfried Selberherr², Wolfgang Goes³, and Viktor Sverdlov¹ (¹Christian Doppler Laboratory for Nonvolatile Magnetoresistive Memory and Logic at the ²Institute for Microelectronics, TU Wien, Austria, ³Silvaco Europe, United Kingdom) 49
- Spin drift-diffusion approach for the computation of torques in multi-layered structures**
 S. Fiorentini¹, J. Ender¹, R. Orio², S. Selberherr², W. Goes³, and V. Sverdlov¹ (¹Christian Doppler Laboratory for Nonvolatile Magnetoresistive Memory and Logic at the ²Institute for Microelectronics, TU Wien, Austria, ³Silvaco Europe, United Kingdom) 51
- Improved sampling algorithms for Monte Carlo device simulation**
 Markus Kamp¹, Hans Kosina², and Michael Walt¹ (¹CDL for Single-Defect Spectroscopy at the Institute for Microelectronics, TU Wien, Austria, ²Institute for Microelectronics, TU Wien, Austria) 53

- Scattering implementation in the quantum transport BITLLES simulator**
Matteo Villani and Xavier Oriols (*Universitat Autònoma de Barcelona, Spain*) 55
- How to preserve the Kramers-Kronig relation in inelastic atomistic quantum transport calculations**
Daniel Lemus¹, James Charles¹, and Tillmann Kubis^{1,2,3,4} (*¹School of Electrical and Computer Engineering, Purdue University, USA, ²Network for Computational Nanotechnology, Purdue University, USA, ³Purdue Center for Predictive Materials and Devices, USA, ⁴Purdue Institute of Inflammation, Immunology and Infectious Disease, USA*) 57
- Efficient machine-learning-based optimization of 3-nm node nanosheet FETs**
Bokyeom Kim and Mincheol Shin (*School of Electrical Engineering, Korea Advanced Institute of Science and Technology, South Korea*) 59
- Deep learning-supported gate-structure design for a high performance graphene FET**
Gyeong Min Seo and Byoung Don Kong (*Department of Electrical Engineering, Pohang University of Science and Technology, South Korea*) 61
- Simulation of ballistic spin-MOSFET devices with ferromagnetic channels**
Patrizio Graziosi^{1,2} and Neophytos Neophytou² (*¹CNR—ISMN, Italy, ²School of Engineering, University of Warwick, United Kingdom*) 63
- Modeling dark current in vertically stacked amorphous selenium based photodetectors**
Le Ho¹, Atreyo Mukherjee¹, Dragica Vasileska², Richard Akis³, and Amir H. Goldan³
(*¹Department of Electrical Engineering, Stony Brook University, USA, ²School of Electrical, Computer and Energy Engineering, Arizona State University, USA, ³Department of Radiology, School of Medicine, Stony Brook University, USA*) 65
- Effective Monte Carlo simulator of hole transport in SiGe alloys**
Caroline Soares¹, Alan C. J. Rossetto², Dragica Vasileska³, and Gilson I. Wirth¹
(*¹Programa de Pós-Graduação em Microeletrônica, Universidade Federal do Rio Grande do Sul, Brazil, ²Centro de Desenvolvimento Tecnológico, Universidade Federal de Pelotas, Brazil, ³School of Electrical, Computer and Engineering, Arizona State University, USA*) 67
- Two-dimensional diffusion process simulation of Si-implanted Ga₂O₃**
In Ki Kim and Sung-Min Hong (*School of Electrical Engineering and Computer Science, Gwangju Institute of Science and Technology, South Korea*) 69
- Temperature dependent electrical characteristics and single charge trap induced by random telegraph noise of bulk FinFETs**
Sekhar Reddy Kola and Yiming Li (*Parallel and Scientific Computing Laboratory, Electrical Engineering and Computer Science International Graduate Program, Department of Electrical and Computer Engineering, National Yang Ming Chiao Tung University, Taiwan*) 71
- Session 4: Photonics, Optoelectronics, and Thermal Transport**
- (Invited) Thermoelectric properties of complex band and nanostructured materials**
Neophytos Neophytou¹, Patrizio Graziosi², Zhen Li¹, and Vassilios Vargiamidis¹ (*¹School of Engineering, University of Warwick, United Kingdom, ²CNR—ISMN, Italy*) 73

- (Invited) Multiscale modeling and simulation of advanced photovoltaic devices**
Yongjie Zou¹, Reza Vatan Meidanshahi¹, Raghuraj Hathwar¹, and Stephen Goodnick¹ (¹*School of Electrical Computer and Energy Engineering, Arizona State University, USA*) 75
- Monte Carlo study of single photon avalanche diodes: quenching statistics**
Thibault Cazimajou¹, Marco Pala¹, Jérôme Saint-Martin¹, Denis Rideau², and Philippe Dollfus¹ (¹*Université Paris-Saclay, CNRS, C2N, France*, ²*STMicroelectronics, France*) 9:40-9:55 77
- Study of the modal contributions to the heat flux to characterize the phonon transport regime in Si/Ge heterojunctions**
N. D. Le¹, B. Davier^{1,2}, P. Dollfus¹, and J. Saint-Martin¹ (¹*Université Paris-Saclay, CNRS, Centre de Nanosciences et de Nanotechnologies, France*, ²*Department of Mechanical Engineering, University of Tokyo, Japan*) 79
- Elastic-wave scattering from an object above a rough surface: A numerical time-domain technique**
Laleh Avazpour, Michelle L. King, Sina Soleimanikahnoj, and Irena Knezevic (*Department of Electrical and Computer Engineering, University of Wisconsin-Madison, USA*) 81
- 2D plasmon-polariton excitation in plasmonic THz detector with 2D diffraction grating structure**
Yuma Sasaki, Taiichi Otsuji, and Akira Satou (*Research Institute of Electrical Communication, Tohoku University, Japan*) 83
- A density-matrix model for photon-assisted electron transport in quantum cascade lasers**
S. Soleimanikahnoj, M. L. King, and I. Knezevic (*Department of Electrical and Computer Engineering, University of Wisconsin-Madison, USA*) 85
- FDTD algorithm for fields and potentials with convolutional perfectly matched layer absorbing boundary conditions**
Michelle L. King, Laleh Avazpour, Samuel W. Belling, Stefan Schmidt, and Irena Knezevic (*Department of Electrical and Computer Engineering, University of Wisconsin-Madison, USA*) 87
- Simulation of graphene photodetectors incorporating the photo-gating effect**
Shingo Aida, Matsuto Ogawa, and Satofumi Souma (*Department of Electrical and Electronic Engineering, Kobe University, Japan*) 89
- Second-order Hall effect in insulators: the effect of interband Berry curvature dipole**
Mahmut Sait Okyay, Beomseop Kim, and Noejung Park (*Department of Physics, Ulsan National Institute of Science and Technology, South Korea*) 91
- Time-dependent density functional theory calculations for spin-phonon-polarization dynamics and band topology**
Mahmut Sait Okyay, Beomseop Kim, and Noejung Park (*Department of Physics, Ulsan National Institute of Science and Technology, South Korea*) 92

Session 5: Methodology and Numerical Techniques

A Godunov-type stabilization scheme for solving the stationary and transient Boltzmann transport equation

Paul Luckner, Hendrik Leenders, Tobias Linn, Maziar Noei, and Christoph Jungemann (*Chair of Electromagnetic Theory, RWTH Aachen University, Germany*)

9:55-10:10

93

Dynamic modelling of quantum transport within MGFETs

Lukas Schulz, Mathias Pech, and Dirk Schulz (*Chair for High Frequency Techniques, TU Dortmund, Germany*)

10:10-10:25

95

Parallel solver study for solving the Boltzmann transport equation using spherical harmonics expansions on supercomputers

Felipe Senra Ribeiro, Karl Rupp, and Tibor Grasser (*Institute for Microelectronics, TU Wien, Austria*)

97

Ab initio quantum transport simulation of lateral heterostructures based on 2D materials: assessment of the coupling Hamiltonians

Adel M'foukh and Marco Pala (*Université Paris-Saclay, CNRS, Centre de Nanosciences et de Nanotechnologies, France*)

99

Feature scale modeling of fluorocarbon plasma etching for via structures including faceting phenomena

Frâncio Rodrigues¹, Luiz Felipe Aguinisky¹, Alexander Toiff¹, Andreas Hössinger², and Josef Weinbub¹ (*¹Christian Doppler Laboratory for High Performance TCAD, Institute for Microelectronics, TU Wien, Austria, ²Silvaco Europe Ltd., United Kingdom*)

101

Modeling GaN nanowire and nanofin FETs electrostatics using fast 2D/3D Schrödinger-Poisson solver

Viswanathan Naveen Kumar¹, Pranay Kumar Reddy Baikadi¹, Dragica Vasileska¹, Michael Povolotskyi^{1,2} (*¹School of ECEE, Arizona State University, USA, ²Vantage Point Consulting Inc., USA*)

103

A practical Peierls phase recipe for periodic atomistic systems under magnetic fields

Alessandro Cresti (*Univ. Grenoble Alpes, Univ. Savoie Mont Blanc, CNRS, Grenoble INP, IMEP-LAHC, France*)

105

Recursive open boundary and interfaces method for material property predictions

James Charles¹, Sabre Kais^{2,3}, and Tillmann Kubis^{1,4,5,6} (*¹School of Electrical and Computer Engineering, Purdue University, USA, ²Department of Physics and Astronomy, Purdue University, USA, ³Department of Chemistry, Purdue University, USA, ⁴Network for Computational Nanotechnology, Purdue University, USA, ⁵Purdue Center for Predictive Materials and Devices, USA, ⁶Purdue Institute of Inflammation, Immunology and Infectious Disease, USA*)

107

Exciton diffusion properties in carbon nanotube films

Yichen Li, S. W. Belling, and I. Knezevic (*Department of Electrical and Computer Engineering, University of Wisconsin–Madison, USA*)

109

Constructing machine-learning potentials derived from disordered structures for crystal structure prediction

Changho Hong¹, Jeong Min Choi¹, Wonseok Jeong¹, Sungwoo Kang¹, Suyeon Ju¹, Kyeongpung Lee¹, Jisu Jung¹, Yong Youn², and Seungwu Han¹ (¹*Department of Materials Science and Engineering and Research Institute of Advanced Materials, Seoul National University, South Korea*, ²*Center for Green Research on Energy and Environmental Materials and International Center for Materials Nanoarchitectonics, National Institute for Materials Science, Japan*)

111

Numerical solution of Poisson and Landau-Khalatnikov equations for negative capacitance devices with PZT and HZO ferroelectric films

Yu-Chin Tsai^{1-2,5-6} and Yiming Li¹⁻⁸ (¹*Parallel and Scientific Computing Laboratory*, ²*Institute of Biomedical Engineering*, ³*Institute of Communications Engineering*, ⁴*Department of Electrical and Computer Engineering*, ⁵*Parallel and Scientific Computing Laboratory*, ⁶*Institute of Biomedical Engineering*, ⁷*Institute of Communications Engineering*, ⁸*Department of Electrical and Computer Engineering, National Yang Ming Chiao Tung University, Taiwan*)

113

Analysis and simulation of basic memristor properties

Bernardo Tellini¹, Mauro Bologna², Kristopher J. Chandia², and Massimo Macucci³ (¹*Dipartimento di Ingegneria dell'Energia, dei Sistemi, del Territorio e delle Costruzioni, University of Pisa, Italy*, ²*Departamento de Ingeniería Eléctrica – Electrónica, Universidad de Tarapacá, Chile*, ³*Dipartimento di Ingegneria dell'Informazione, University of Pisa, Italy*)

115

Session 6: Novel Devices and Future Computing

(Invited) Hybrid modeling of TCAD and AI for semiconductor design

Changwook Jeong, Sanghoon Myung, Jinwoo Kim, Hyunjae Jang, Byungseon Choi, Hyowon Moon, Jisu Ryu, Jae Myung Choe, and Dae Sin Kim (*Data & Information Technology Center, Samsung Electronics, South Korea*)

117

(Invited) Quantum information and quantum foundations with spins in silicon

Andrea Morello (*Centre for Quantum Computation and Communication Technology, School of Electrical Engineering and Telecommunications, UNSW Sydney, Australia*)

119

(Invited) Analogue computing with resistive memory devices

Daniele Ielmini (*Politecnico di Milano, Italy*)

120

Mechanism of resistance switching in hexagonal boron nitride

Fabian Ducry, Jan Aeschlimann, and Mathieu Luisier (*Integrated Systems Laboratory, ETH Zurich, Switzerland*)

10:25-10:40

121

Extraction of contact resistance from Green's function simulations of 2D material nanoribbon devices

Mirko Poljak and Mislav Matić (*Computational Nanoelectronics Group, Faculty of Electrical Engineering and Computing, University of Zagreb, Croatia*)

123

Machine learning models for diffused copper doping profiles in CdTe solar cells

Ghaith Salman¹, Stephen Goodnick², Abdul R. Shaik², and Dragica Vasileska² (¹*Computing, Informatics, and Decision Systems Engineering, Arizona State University, USA*, ²*School of Electrical, Computer and Energy Engineering, Arizona State University, USA*)

125

Understanding sensitivity of entangled qubit logic operations in electrode-driven semiconductor quantum dot platforms

Hoon Ryu (*Division of National Supercomputing, Korea Institute of Science and Technology Information, South Korea*)

127

Inverse-designed spin dynamics for neuromorphic computation

Adam Papp¹, Gyorgy Csaba¹, and Wolfgang Porod² (*¹Faculty for Information Technology, Pázmány Péter Catholic University, Hungary, ²Department of Electrical Engineering, University of Notre Dame, USA*)

129

Analytical models of ferroelectric field effect transistor with two-dimensional channel material

Jeonghyeon Kim and Jiwon Chang (*Department of Electrical Engineering, Ulsan National Institute of Science and Technology, South Korea*)

131

Metadynamics sampling in atomic environment space for collecting training data for machine learning potentials

Dongsun Yoo^{1,2}, Jisu Jung¹, Wonseok Jeong¹, and Seungwu Han¹ (*¹Department of Materials Science and Engineering and Research Institute of Advanced Materials, Seoul National University, South Korea, ²Samsung Display Co., Ltd., South Korea*)

133

Machine learning potentials enabling realistic-size simulation and accelerated material discovery

Seungwu Han

*Department of Materials Science and Engineering, Seoul National University,
Seoul 08826, South Korea
hansw@snu.ac.kr*

Recently, machine-learning (ML) approaches to developing interatomic potentials are attracting considerable attention because it is poised to overcome the major shortcoming inherent to the classical potential and density functional theory (DFT), i.e., difficulty in potential development and huge computational cost, respectively. In particular, the high-dimensional neural network potential (NNP) suggested by Behler and Parrinello is attracting wide interests with applications demonstrated over various materials. In this presentation, we first introduce our in-house code for training and executing NNP called SIMPLE-NN (SNU Interatomic Machine-learning Potential package-version Neural Network) [1] and discuss its unique feature such as GDF weighting [2] which significantly improves stability of ML potentials during MD simulations. We further discuss on the fundamental aspect of ML potentials that enables the transferability of the potential.[3] We show that the ML potential is nothing but a manifestation of O(N) method of DFT, which is realized in terms of atomic energies.

As application examples, we present our recent results on phase change behavior of chalcogenides [4] and silicidation process [5] in semiconductor fabrication. Furthermore, we will show that ML potentials can be used as highly accurate surrogate models in exploring large space of crystal structures [6]. This enables finding the stable crystal structure for complicated multicomponent systems. [7]

[1] K. Lee et al, *Comp. Phys. Comm.*, **242**, 95 (2019).

[2] W. Jeong et al, *J. Phys. Chem. C*, **122**, 22790 (2018).

[3] D. Yoo et al, *Phys. Rev. Mater.*, **78**, 093802 (2019).

[4] D. Lee et al, *Comp. Mater. Sci.*, **181**, 109725 (2020).

[5] W. Jeong et al, *J. Phys. Chem. Lett.*, **11**, 6090 (2020).

[6] C. Hong et al, *Phys. Rev. B*, **102**, 224104 (2020)

[7] S. Kang et al, in preparation.

Numerical Calculation of the Transverse Modes in 1T' MoS₂ Nanoribbons

Hans Kosina¹, Heribert Seiler¹, and Viktor Sverdlov²

¹*Institute for Microelectronics, TU Wien, Austria*
hans.kosina@tuwien.ac.at

²*Christian Doppler Laboratory for Nonvolatile Magnetoresistive Memory and Logic*
at the Institute for Microelectronics, TU Wien, Austria

Recently it has been found that MoS₂ in the 1T' phase is a topological insulator [1]. Ab-initio calculations predict an inverted band structure. Adopting the parabolic band approximation for the band extrema and taking spin-orbit interaction into account yields the following effective Hamiltonian [2]

$$\mathbf{H}(k_x, k_y) = \begin{pmatrix} \delta - c_1 k_x^2 - c_2 k_y^2 & c_6 k_y - \alpha E_z + i c_5 k_x \\ c_6 k_y - \alpha E_z - i c_5 k_x & -\delta + c_3 k_x^2 + c_4 k_y^2 \end{pmatrix} \quad (1)$$

with the coefficients

$$c_1 = \frac{\hbar^2}{2m_x^p}, \quad c_2 = \frac{\hbar^2}{2m_y^p}, \quad c_3 = \frac{\hbar^2}{2m_x^d}, \quad c_4 = \frac{\hbar^2}{2m_y^d}, \quad c_5 = \hbar v_1, \quad c_6 = \hbar v_2.$$

Here, the x -coordinate represents the longitudinal direction, the y -coordinate the transverse direction, and the z -coordinate the direction perpendicular to the nanoribbon.

The characteristic polynomial $p(k_x, k_y, E) = \text{Det}(E\mathbf{I} - \mathbf{H})$ is of fourth degree in k_y . For given energy E and longitudinal momentum k_x there exist four roots designated as k_y^j . We adopt a mode space approach with wavefunctions $\psi(x, y) = \exp(ik_x x) \varphi(y)$ where $\varphi(y)$ is the transverse mode.

$$\varphi(y) = \sum_{j=1}^4 A_j \begin{pmatrix} a \\ b \end{pmatrix} \exp(ik_y^j y) \quad (2)$$

The spinor $(a, b)^T$ is an eigenvector of (1). Setting the wave function to zero at both edges of the nanoribbon yields a homogeneous equation system for the coefficients A_j . The resulting matrix $\mathbf{M} = (\mathbf{m}_1, \mathbf{m}_2, \mathbf{m}_3, \mathbf{m}_4)$ is composed of the column vectors \mathbf{m}_j defined as

$$\mathbf{m}_j = (a, b, a \exp(ik_y^j d), b \exp(ik_y^j d))^T, \quad j = 1, 2, 3, 4. \quad (3)$$

For the simultaneous solution of the characteristic equation, $p(k_x, k_y, E) = 0$, and the quantization condition, $\text{Det}(\mathbf{M}) = 0$, we propose a modified Newton scheme. We choose the unknown vector as $\mathbf{x} = (k_y^1, k_y^2, k_y^3, k_y^4, E)^T$ and treat k_x as an input parameter. Since the k_y^j satisfy Vieta's formulae, we use the latter as the defining equations. Adding the quantization condition, $\text{Det}(\mathbf{M}) = 0$, gives a nonlinear equation system of the form $\mathbf{F}(\mathbf{x}) = \mathbf{0}$. The update vector is multiplied by a damping factor $\alpha < 1$ so as to keep the updates of the energy and of the wavenumbers below predefined limits. In the course of the Newton

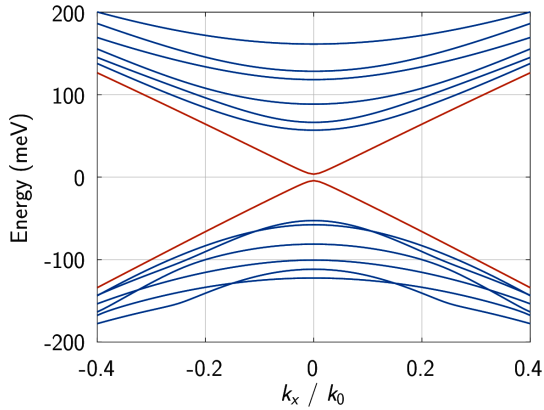


Figure 1: Subbands in a nanoribbon of the width $d = 40/k_0$ at $E_z = 0$. The almost linear dispersion corresponds to topologically protected edge states.

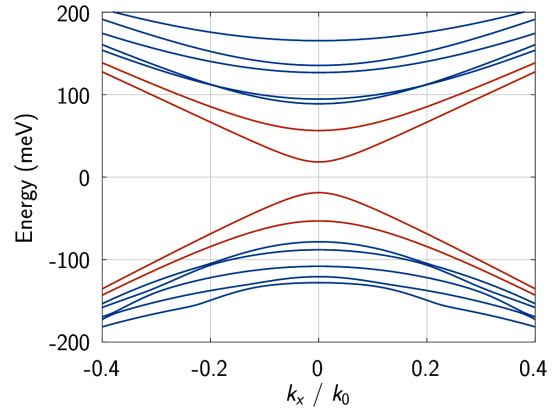


Figure 2: Subband energies at $\alpha E_z = v_2$. Red lines describe subbands with two real and two complex k_y , while blue subbands have four real k_y at small k_x .

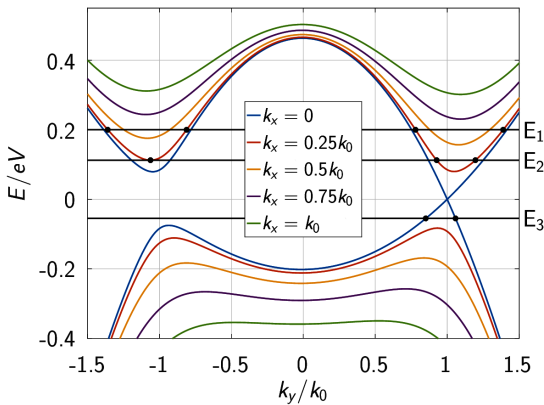


Figure 3: Contour lines of the bulk dispersion relation of 1T' MoS₂. At a vertical field of $\alpha E_z = v_2$ the band gap closes in the point $(k_x, k_y) = (0, k_0)$.

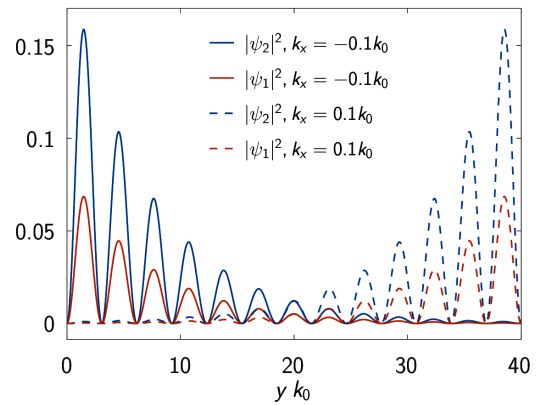


Figure 4: Wave functions squared of the topological edge states at $k_x = \pm 0.1k_0$ and $E_z = 0$. The related energy is 48.9 meV, see Fig. 1.

iteration, E can only assume real values, whereas the k_y^j are complex variables. The Newton scheme has been used to calculate the subbands shown in Fig. 1 and 2. In an extremum of a contour line ($E = E_2$ and $k_x = 0.25k_0$ in Fig. 3) a doubly degenerate solution k_y exists. Also in this case the system $\mathbf{MA} = \mathbf{0}$ has a nontrivial solution \mathbf{A} . However, with this coefficient vector the wavefunction (2) is identically zero. These spurious solutions which have to be disregarded have led to an incorrect interpretation of the subband structure in [3]. Fig. 4 shows that edge states with opposite signs of k_x are localized at opposite edges.

- [1] X. Qian, J. Liu, L. Fu, and J. Li, "Quantum spin Hall effect in two-dimensional transition metal dichalcogenides," *Science*, vol. 346, no. 6215, pp. 1344–1347, 2014.
- [2] V. Sverdlov, A.-M. El-Sayed, H. Kosina, and S. Selberherr, "Conductance in a Nanoribbon of Topologically Insulating MoS₂ in the 1T' Phase," *IEEE Transactions on Electron Devices*, vol. 67, no. 11, pp. 4687–4690, 2020.
- [3] B. Das, D. Sen, and S. Mahapatra, "Tuneable quantum spin Hall states in confined 1T' transition metal dichalcogenides," *Scientific Reports*, vol. 10, 66770, 2020.

Pair-production in vacuum and plasmas using the Wigner formalism

Haidar Al-Naseri¹, Jens Zamanian¹ and Gert Brodin¹

¹ *Dept of Physics, Umeå University, SE 901 87 Umeå, Sweden*

Email corresponding author: haidar.al-naseri@umu.se

For ultra-strong electromagnetic fields, much new phenomena, such as e.g. relativistic Landau quantization and pair-production enters the picture. This can be studied making a gauge-invariant Wigner transform of the Dirac equation, such that the coupled strong field dynamics of electrons and positrons is described in phase space. The 16 scalar equations resulting from this, first derived by Ref. [1], are usually referred to as the Dirac-Heisenberg-Wigner (DHW) equations. The coupling of the electron and positron degrees of freedom makes the interpretation of the theory slightly non-trivial. However, the system has a number of conservation laws (energy, momentum, angular momentum, etc.), which help guiding the intuition. The DHW-equations have been used for studying pair-production in given electric fields through the Schwinger mechanism (see e.g. Refs. [2,3]), which we briefly review. Some newly studied aspects related to the momentum perpendicular to the electric field, which has been omitted in previous works, are also discussed [4]. Adding a plasma into the picture, it turns out that pair-production can be possible even in linearized theory, although a high frequency is required [5]. To understand this properly, a renormalization must be made, in order to handle the ultra-violet divergences

[1] I. Bialynicki-Birula, P Gornicki and J Rafelski, Phys. Rev. D **44**, 1825 (1991).

[2] F. Hebenstreit et al. Phys. Rev. Lett, **107**, 180403 (2011).

[3] Xin-li Sheng, *et al.*, Phys. Rev. D, **99**, 056004 (2019).

[4] H. Al-Naseri, J. Zamanian and G. Brodin, In preparation.

[5]] G. Brodin H. Al-Naseri and J. Zamanian, In preparation.

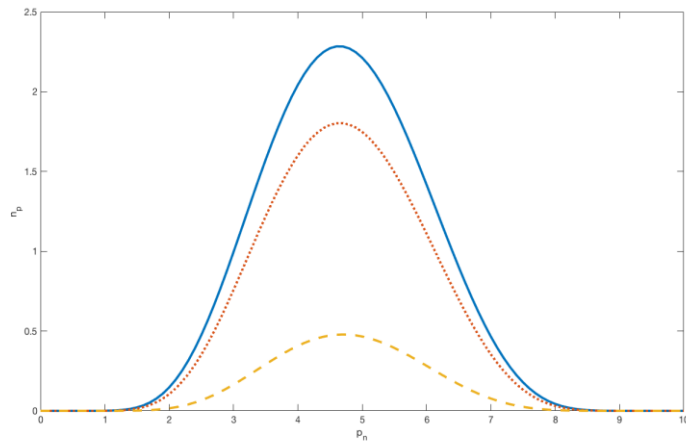


Fig.1 The number of generated electron-positron pairs as a function of normalized parallel momentum, for different values of the normalized perpendicular momentum.

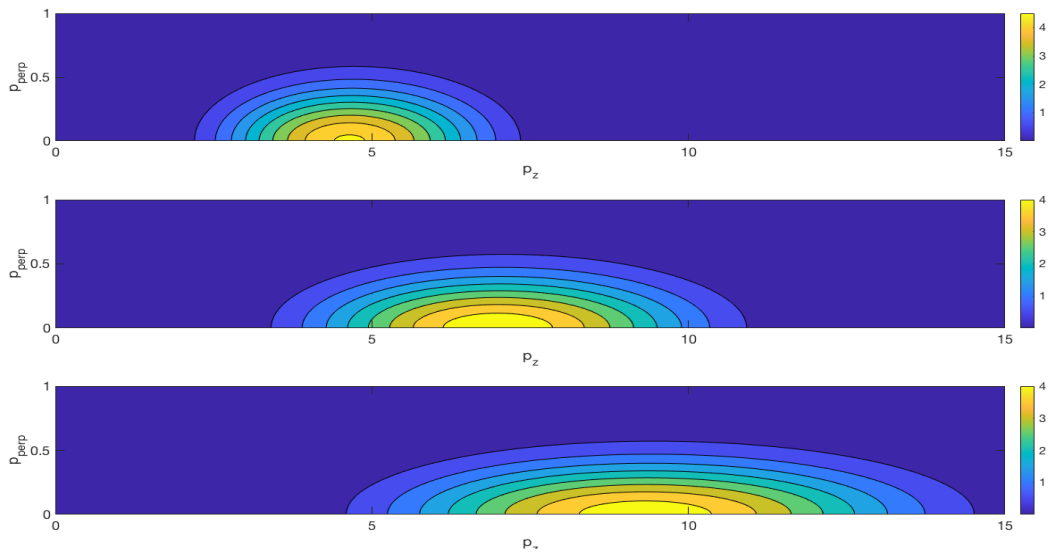


Fig.2 Contour curves in momentum space for the generated electron-positron pairs for different magnitudes of the electric field.

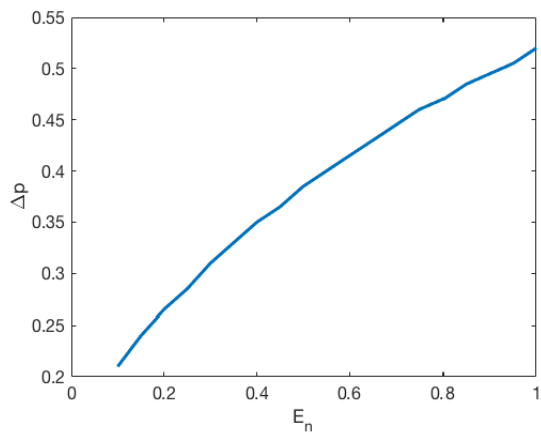


Fig.3 The spread in perpendicular momentum as a function of the normalized electric field. .

Density functional theory modeling of chemical reactions at interfaces

Namita Narendra¹, Jinying Wang², James Charles¹, Tillmann Kubis^{1,2,3,4}

¹ *School of Electrical and Computer Engineering, Purdue University, W. Lafayette, IN, USA*

² *Network for Computational Nanotechnology, Purdue University, W. Lafayette, IN, USA*

³ *Purdue Center for Predictive Materials and Devices, W. Lafayette, IN, USA*

⁴ *Purdue Institute of Inflammation, Immunology and Infectious Disease, W. Lafayette, IN, USA*

nnarendr@purdue.edu

Density functional theory (DFT) models are among the most transferable models for electronic, molecular and mechanical properties of solids, liquids and gases; however their numerical load is typically preventing solving systems with more than several 100 atoms. This limit is particularly problematic when solving molecules at interfaces or in liquid solvents with very irregular solvent molecule distributions. Modeling these systems requires a large number of solvent molecules to ensure the results are unaffected by the simulation domain boundaries.

In this work, we introduce a DFT-based method to predict energies of solute molecules in bulk solution and in various distances to solvent/air interfaces [1]. The solute and all solvent molecules (~1400 atoms) are explicitly considered, and their electrons solved self-consistently in density functional tight binding. The statistical nature of the solvent molecule distribution and their orientations is included with 100 solvent samples for each solute configuration.

Rotations of the solute molecule at the solvent surface are found to critically change their reaction energy barriers. Changes in the molecular energies of protonated reactant and transition state for hydrazone reaction at the solvent/air interfaces are used to predict reaction acceleration factors at solvent/air interfaces. The predicted acceleration factors of up to 4 orders of magnitude at solvent surfaces compared to the bulk solvent are in agreement with recent experimental observations of reactions in solvent microdroplets [2].

The presented method can be applied on liquids, crystalline and irregular materials, as well as all their interfaces. Our method shows DFT-based calculations of molecules and their explicit environments are not only feasible, but required for reliable predictions of interfaces.

[1] Narendra, N et al. *J. Pys. Chem. A* **124**, 24 (2020)

[2] Yan, X et al, *Angew. Chem. Int. Ed.* **55**, 42 (2016)

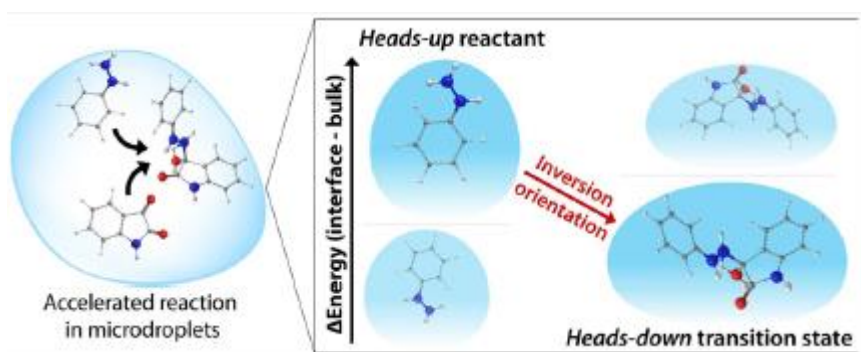


Fig. 1: Atomistic simulation of molecules at methanol/air interface reveals the pathway for reaction acceleration in microdroplets. The pathway through which an unsolvated/partially-solvated charged reactant (heads-up) transforms into a fully-solvated charged transition state (heads-down) shows reaction acceleration factor consistent with experiments.

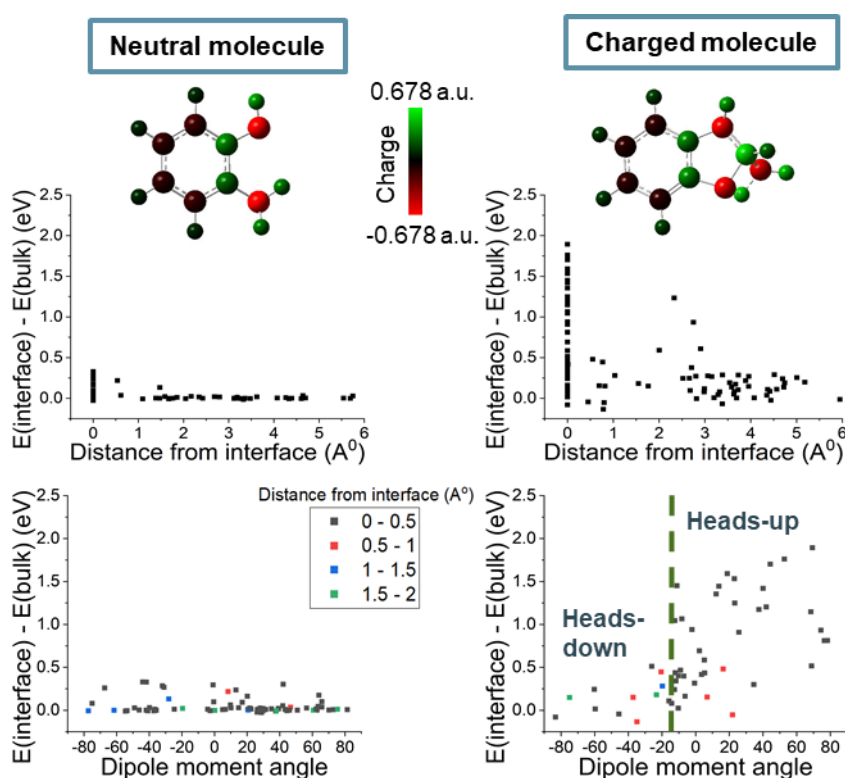


Fig. 2: DFTB calculation elucidates difference in behavior of neutral vs charged molecule at methanol/air interface. The neutral molecule does not have a large energy difference at interface compared to bulk and does not show any dipole dependence. The charged molecule exhibits a large energy change at interface of up to 1.9 eV and is very sensitive to dipole orientation at interface.

Electronic States in 4H-SiC MOS Inversion Layers Considering Crystal Structure Using Empirical Pseudopotential Method

Sachika Nagamizo, Hajime Tanaka, and Nobuya Mori

Graduate School of Engineering, Osaka University,

2-1 Yamada-oka, Suita, Osaka 565-0871, Japan

e-mail: {nagamizo, tanaka, mori}@si.eei.eng.osaka-u.ac.jp

4H-SiC MOSFETs have been attracting attention as a power switching device realizing high breakdown voltage and low on-resistance. A recent *ab initio* simulation revealed that the electronic states at the conduction band minimum (CBM) of SiC consist of the floating electron states [1], which distribute not near atomic sites, but in internal channel space. This feature is ignored in the effective-mass approximation. In this study, to analyze the electronic states in 4H-SiC MOS inversion layers taking account of this feature, we described the crystal structure of 4H-SiC including the internal channel space using the empirical pseudopotential method, and we calculated the electronic states in the triangular potential well.

We first obtained the empirical pseudopotential of bulk 4H-SiC. The pseudopotential of bulk 4H-SiC is described by the pseudopotentials of Si and C atoms arranged according to the crystal structure of 4H-SiC. Then, by arranging these pseudopotentials of each atom in a slab structure, we described the pseudopotential of a 4H-SiC slab. In the empirical pseudopotential method, the plane wave expansion is usually employed. In this study, however, we adopted real-space discretization for the thickness direction, while the plane wave expansion is used for the in-plane directions. To model the confinement of electrons at the MOS interface, we applied triangular potential determined by a uniform electric field to the 4H-SiC slab described above.

The empirical pseudopotential of bulk 4H-SiC and the calculated probability density distribution of the electronic states at the CBM are shown in Fig. 1. The feature of the floating electron states [1] is confirmed. Fig. 2 shows the model of the 4H-SiC slab adopted in this study. In the positive and negative directions of z -axis, there are surfaces terminated with C and Si atoms, respectively, with the latter set to $z = 0$. Fig. 3 shows the pseudopotential of 4H-SiC slab described using the above method. We applied a uniform electric field to the 4H-SiC slab to make the Si-terminated surface be the bottom of the potential. Fig. 4 shows the probability density distribution of the state at the CBM with a 0.8 MV/cm electric field. The feature of the floating electron states appeared also in this case, while the state is confined near the Si-terminated surface. Fig. 5 shows the dependence of effective-mass on applied electric field. As the electric field increases, $m_{M\Gamma}$ increases, and m_{MK} decreases. These trends can be explained by the nonparabolicity of the band structure of bulk 4H-SiC. The results suggest that our methodology can describe the 4H-SiC MOS inversion layers taking account of the floating electron states and the band structure beyond the effective-mass approximation.

[1] Y.-I. Matsushita *et al.*, *PRL* **108**, 246404 (2012). [2] Y.-I. Matsushita *et al.*, *JPSJ* **86**, 054702 (2017).

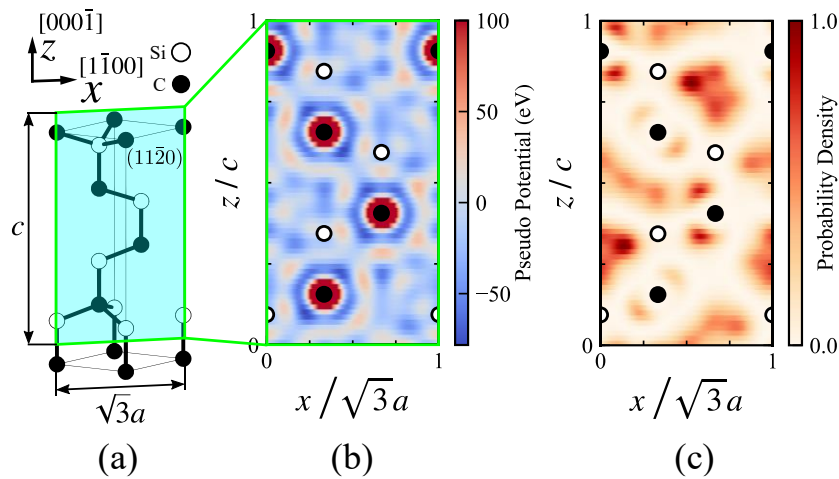


Fig. 1: (a) The primitive unit cell of 4H-SiC. c is the length of a unit cell in the [000 $\bar{1}$] direction. a is the distance between adjacent Si (or C) atoms. We set $c = 1.008$ nm and $a = 0.3081$ nm in this study. The blue plane is the (11 $\bar{2}$ 0) plane that is parallel to [000 $\bar{1}$] and [1 $\bar{1}$ 00] directions. On this plane, we defined x and z axes along the [000 $\bar{1}$] and [1 $\bar{1}$ 00] directions, respectively. (b) The pseudopotential distribution of bulk 4H-SiC on the (11 $\bar{2}$ 0) plane. (c) The probability density distribution of the state at the conduction band minimum of bulk 4H-SiC calculated with the empirical pseudopotential method.

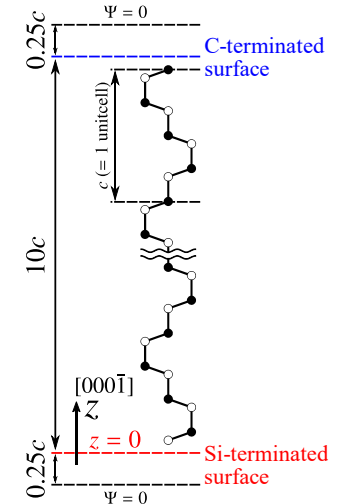


Fig. 2: The structure and dimensions of the 4H-SiC slab. The thickness direction is along the [000 $\bar{1}$] direction. The structure includes a 10 c -thick 4H-SiC slab and 0.25 c -thick vacuum regions terminated by the boundary conditions with the wavefunction Ψ set to zero.

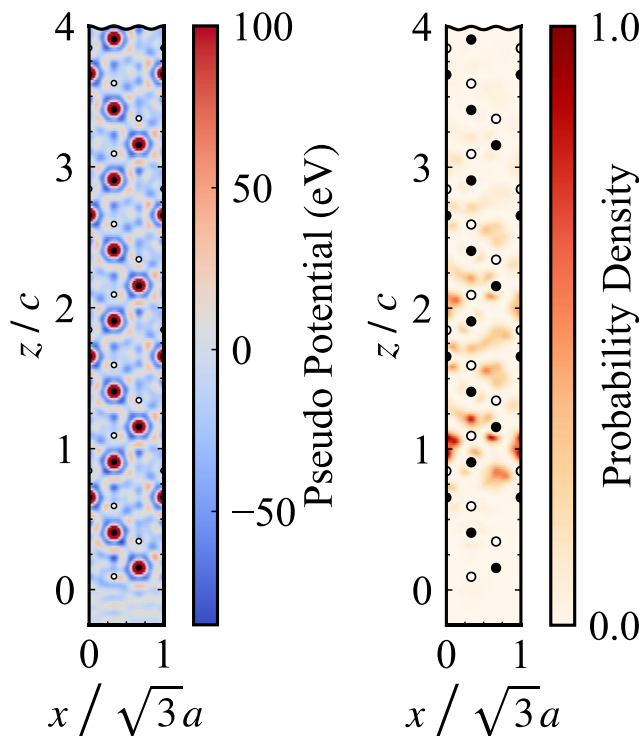


Fig. 3 (left): The pseudopotential distribution of the 4H-SiC slab on the (11 $\bar{2}$ 0) plane. Only the area near the Si-terminated surface is shown. The pseudopotential of atoms extends into the vacuum region.

Fig. 4 (right): The probability density distribution of the state at the conduction band minimum of the 4H-SiC slab with an electric field of 0.8 MV/cm.

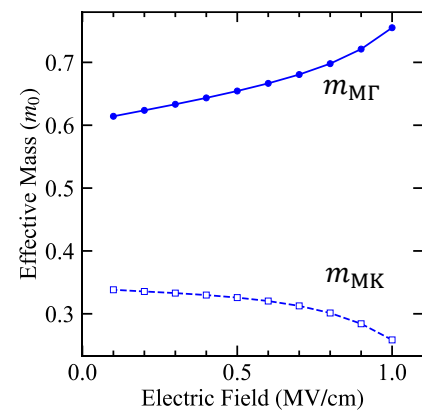


Fig. 5: The dependence of effective-masses at the conduction band minimum of the 4H-SiC slab on the applied electric field. $m_{M\Gamma}$ and m_{MK} are the effective masses along the M Γ and MK directions, respectively. As the electric field increases, $m_{M\Gamma}$ increases, and m_{MK} decreases. These trends are consistent with the change in effective mass with increasing wavenumber in the z direction in the E - k dispersion of bulk 4H-SiC.

First-principles study of gate field effect in vertical van der Waals heterostructures

Juho Lee, Tae Hyung Kim, Ryong Gyu Lee and Yong-Hoon Kim*

School of Electrical Engineering, Korea Advanced Institute of Science and Technology, 291 Daehak-ro, Yuseong-gu, Daejeon 34141, Korea
y.h.kim@kaist.ac.kr

Recent developments in the technology of vertically stacked two-dimensional (2D) van der Waals (vdW) heterostructures have already come up with promising tunneling-based field-effect devices (FED) architectures. Despite the need for a better understanding of quantum tunneling across the vdW heterojunctions for the development of advanced FEDs, most theoretical works currently resort to semi-classical approaches, eliminating the possibility of interpreting and predicting effects that involve atomistic details in an *ab initio* manner. In this presentation, we newly establish the first-principles method of FEDs within the recently developed multi-space constrained-search density functional theory (MS-DFT) formalism (Fig. 1)[1] and report the non-equilibrium electronic structures and quantum transport properties of graphene-based vdW FEDs. Providing the comparable transport properties with the previous experimental report [2], we determine the validity of the vdW FED simulations within MS-DFT. In particular, focusing on the gate field effect in the graphene-based metal-insulator-semiconductor (MIS) tunnel junctions (Fig. 2), we provide not only the mechanism of tunnel diode characteristics in the MIS junction but also design guidelines for the development of advanced graphene-based vdW FEDs.

[1] H.S. Kim and Y.-H. Kim, arXiv:1808.03608[cond-mat.mes-hall] (2018); J. Lee et al, Adv. Sci., **7**, 2001038 (2020); J. Lee et al, Proc. Natl. Adv. Sci. U.S.A., **117**, 10142 (2020)

[2] L. Britnell et al, Nat. Commun. **4**, 1794 (2013)

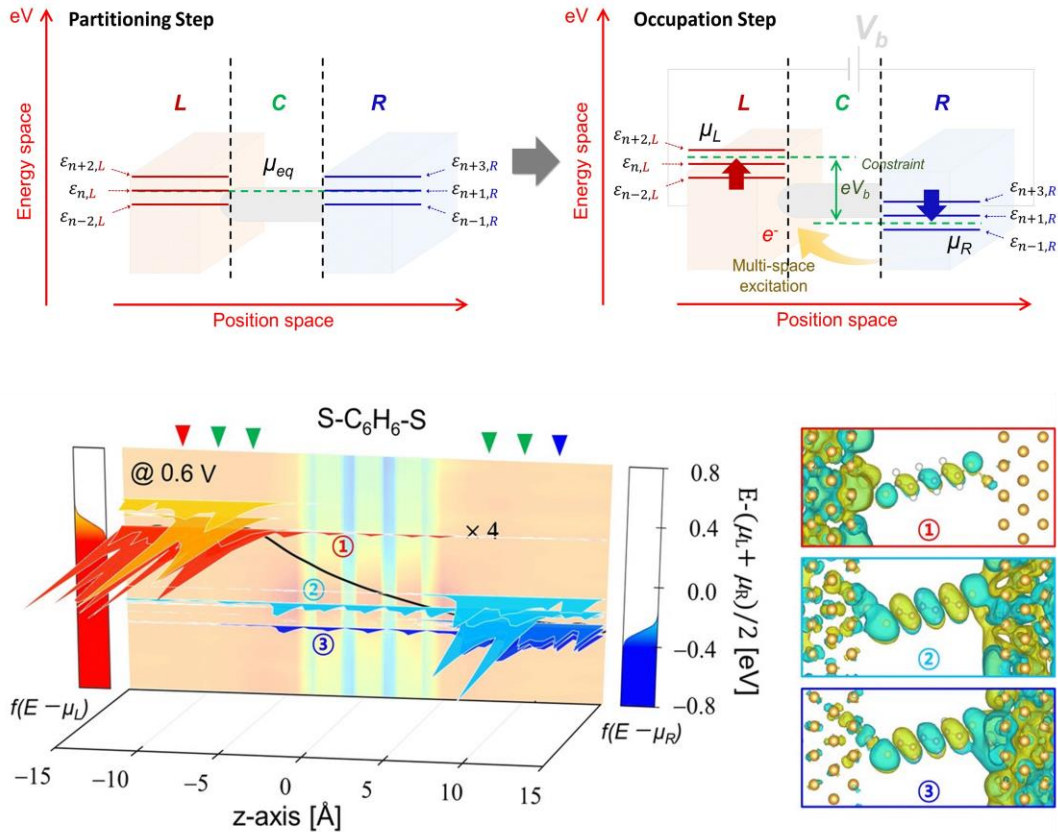


Fig. 1. (top) The newly developed multi-space constrained-search density functional theory (MS-DFT) for the simulation of nanodevice at finite bias voltages. Copyright 2020 Wiley-VCH. (bottom) The quasi-Fermi level splitting within a single molecular junction calculated with MS-DFT (bottom). Copyright 2020 National Academy of Sciences.

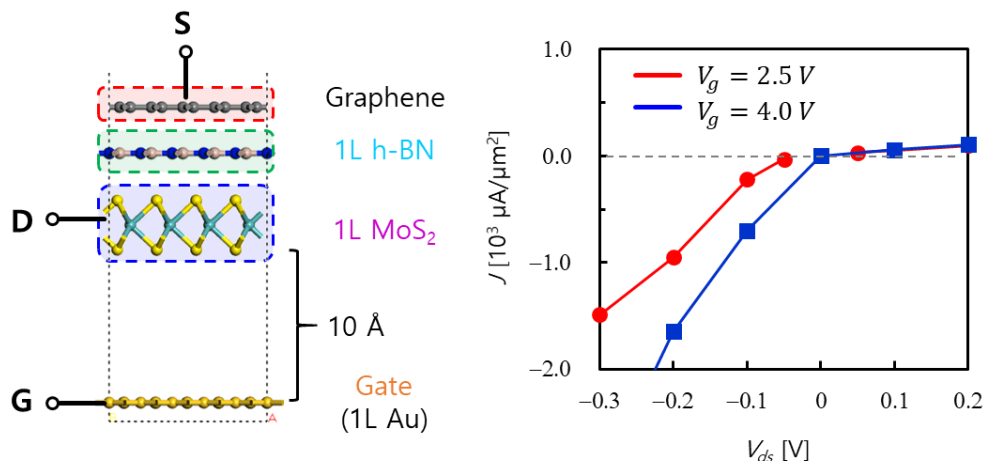


Fig. 2. (left) Atomic structure of graphene/hBN/MoS₂ vertical heterojunctions with finite gate electrode. Here, Au monolayer was used for the atomic gate electrode. (right) The gate-field dependent current density – drain bias ($J - V_{SD}$) curves of the graphene/hBN/MoS₂ vertical junction at $V_g = 2.5$ V (red solid line) and 4.0 V (blue solid line).

Multiscale investigation of the transport properties in partially overlapped van der Waal structure of 2D materials

Emmanuele Cannavò¹, Damiano Marian¹, Enrique G. Marin², Giuseppe Iannaccone¹, and Gianluca Fiori¹

¹ *Dipartimento di Ingegneria dell'Informazione, Università di Pisa, 56122, Pisa, Italy*

² *Dpto. Electrónica, Fac. Ciencias, Universidad de Granada, 18071, Granada, Spain*
emmanuele.cannavo@phd.unipi.it

Understanding transport across the vertical stacking of two-dimensional (2D) materials, i.e. in van der Waals homo- and heterostructures, is of primary interest both from a fundamental and from an application-oriented point of view [1]. We present a multiscale method able to compute transport in partially overlapped structures of 2D flakes in a precise and scalable way. Starting from an *ab-initio* DFT [2] calculation of a bilayer (Fig. 1a), we extract a tight-binding-like Hamiltonian expressed in terms of Maximally Localized Wannier Functions [3]. By properly performing the wannierization, it is possible to obtain a bilayer tight-binding Hamiltonian, composed by the specific blocks corresponding to the single layer as in Fig. 1b, in a similar procedure to Refs. [4], which is further exploited to compute transport using the *in-house* software NanoTCAD_VIDES [5], through non-equilibrium Green's function formalism (Fig. 1d). We apply this approach to two different homostructures of MoS₂ and WSe₂, and one heterostructure of MoS₂-WSe₂, considering two different stacking (AA' and AB) (Fig. 2) and several overlaps (from 12 nm up to 100nm). We first exemplify our procedure comparing the bands extracted from the bilayer Hamiltonians of MoS₂ and WSe₂ with the ones obtained from an isolated monolayer (Figs. 3 and 5), evidencing that both the homo- and the heterostructure bilayer Hamiltonians contain the information of the individual layers. Homostructures transmission coefficient are reported in Fig. 4: large differences between the two stacking are observed, while no difference is noticed as the overlapping length is varied (Fig. 4). For the MoS₂-WSe₂ heterostructure, we do not observe any significant variation on the stacking and the overlapping length (Fig. 6), while the null transmission region is widened by the particular alignment of the two materials. The present scheme can be used to study transport in van der Waals devices as well as to understand and investigate transport in highly heterogeneous structures, as the case for 2D inkjet-printed devices [6].

[1] A. K. Geim et al., *Nature*, **499**, 419 (2013).

[2] P. Giannozzi et al., *J. Phys.: Cond Matt.*, **21**, 395502 (2009).

[3] A. A. Mostofi et al., *Comput. Phys. Commun.*, **185**, 2309 (2014).

[4] A. Szabo et al., *IEEE Electr. Dev. Lett.*, **36**, 514 (2015); A. Szabo et al., *Nano Lett.*, **19**, 3641 (2019).

[5] NanoTCAD_VIDES available at: <http://vides.nanotcad.com/vides/>

[6] M. Perruchini et al., submitted (2020).

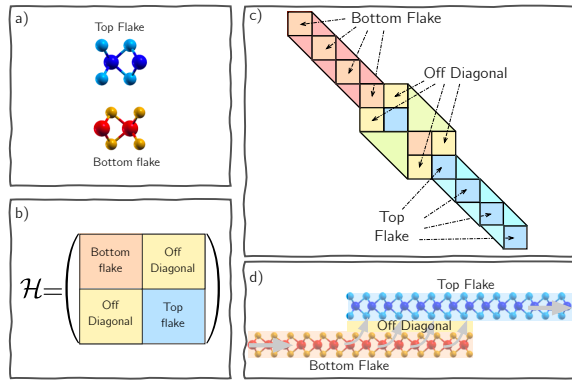


Fig.1: a) Typical simulated structure by ab-initio DFT calculations. b) Schematic depiction of the Wannier Hamiltonian with different blocks indicating, bottom flake (upper left), top flake (bottom right) and the off diagonal elements connecting the two flakes (bottom left and upper right). c) Extended Hamiltonian with different regions of monolayers and overlapping regions (the triangular regions indicate the connections between adjacent cells). d) Schematic depiction of the structure through which transport is computed.

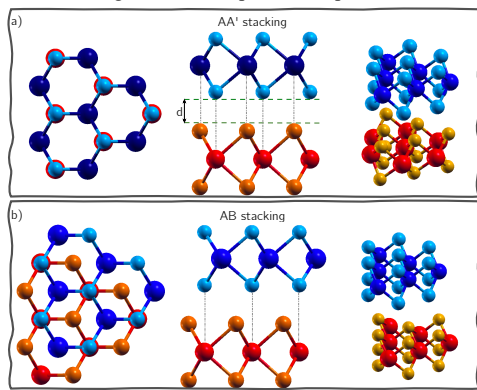


Fig.2: Different TMDs stacking considered a) AA' and b) AB.

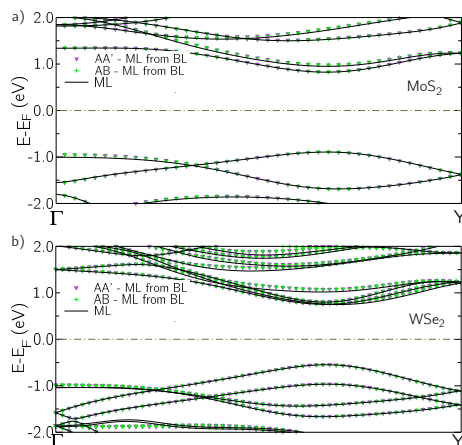


Fig.3: Comparison between monolayer bands (solid line) and extracted bands from bilayer Hamiltonian for a) MoS₂ and b) WSe₂ for the different stacking considered.

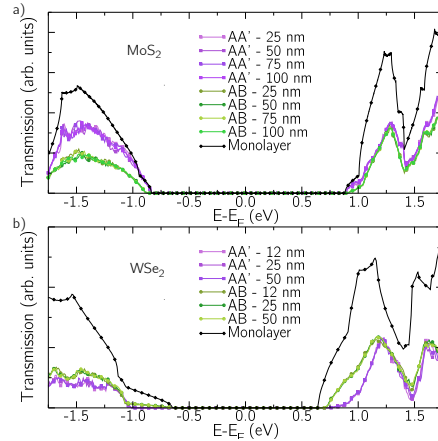


Fig.4: Transmission coefficient for a) MoS₂ and b) WSe₂ for the two different stacking considered and for overlapping length ranging from 12 nm till 100 nm. For comparison the monolayer transmission is reported for both materials.

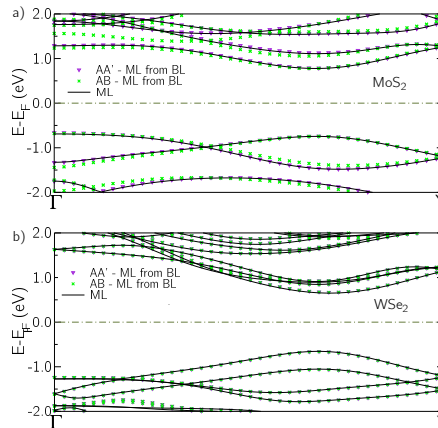


Fig.5: Comparison between monolayer bands (solid line) and extracted bands from the heterostructure bilayer Hamiltonian for a) MoS₂ and b) WSe₂ for the different stacking considered.

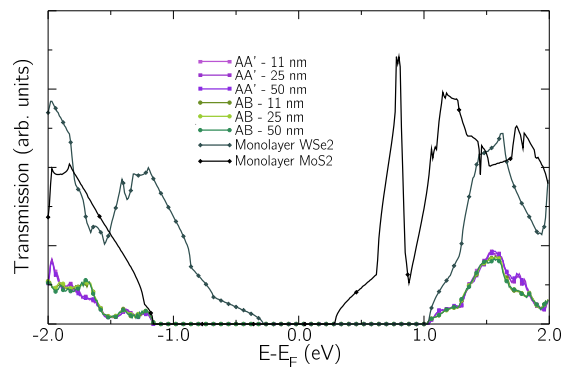


Fig.6: Transmission coefficient for the MoS₂-WSe₂ heterostructure for different overlapping lengths for the two stackings considered. Monolayer of isolated MoS₂ and WSe₂ are reported for reference.

Simulation web platform for electro-chemical oxygen reduction reaction

Seungchul Kim¹, Chan-Woo Lee², Byeong-Joo Lee³, Donghyuk Seol³, Doyeon Kim¹, Assel Kembay¹, Kayong Yun¹, Semi Jang^{1,4}, Jungho Lee⁴

¹ *Computational Science Research Center, Korea Institute of Science and Technology*

² *Platform Technology Laboratory, Korea Institute of Energy Research*

³ *Department of Materials Science and Engineering, Pohang University of Science and Technology*

⁴ *Virtual Lab Inc.*

sckim@kist.re.kr (e-mail address of the corresponding author)

Computer simulations of materials in atomic and electronic scale are widely used during the last few decades, yet, it is not easily applicable to majority of researchers. This difficulty is not only because of simulation theories to be learned but also because of preparing computer facilities necessary for the simulation and many other research skills to be familiar with. The simulation web platform we have developed recently is a good research equipment that solves this difficulties and allows researchers to focus not on the techniques to do researches but on their research target. In this presentation, we are going to demonstrate simulation platform for oxygen reduction reaction (ORR) in electro-chemical cell. The platform, named at qCat, has functions to build atomic structure of catalysts, analyzing electronic structures, calculating adsorption energies of chemicals and drawing reaction diagrams (Fig. 1). The qCat also provides simulation tools to find thermally stable atomic configurations of alloy particles (Fig. 2), and to test chemical stability by performing desolution simulations. Density functional theory (DFT), molecular dynamics (MD), and Monte Carlo (MC) software are used behind the qCat along with postprocessing programs. Most of simulation parameters were preset and not shown to users so that they do not need to care about simulation techniques in detail. Using this qCat, even researchers who does not have an experience in simulations can do simulations for ORR by themselves, after just one or two days of practice.

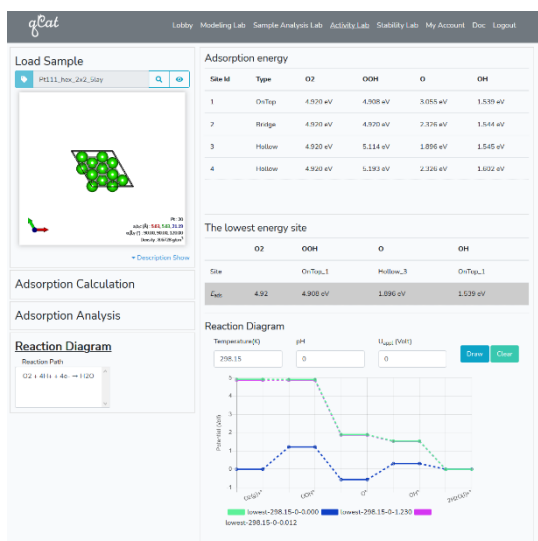


Fig.1: Activity test and reaction diagram of ORR in qCat. DFT calculations is used.

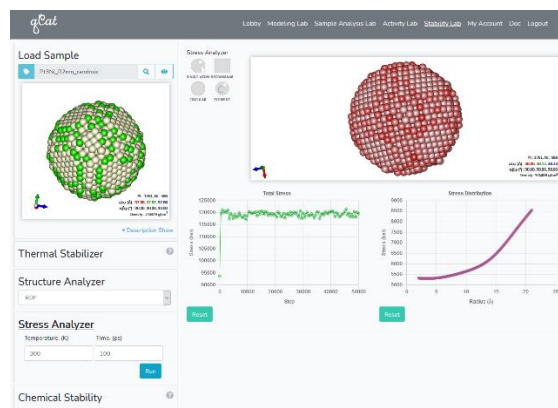


Fig.2: Thermally stable atomic configuration of Pt3Ni nanoparticle and stress distribution calculated in the qCat. MC and MD simulations were performed with 2NNMEAM potential.

First-principles calculation of the non-equilibrium quasi-Fermi level in WSe₂ *p-n* junctions

Tae Hyung Kim, Juho Lee, Jun Seong Lee, and Yong-Hoon Kim*

School of Electrical Engineering, Korea Advanced Institute of Science and Technology, 291 Daehak-ro, Yuseong-gu, Daejeon 34141, Korea
y.h.kim@kaist.ac.kr

While the two-dimensional (2D) *p-n* junctions have been extensively studied for electronic and optoelectronic devices, the semiclassical approaches without considering atomistic details are still insufficient to describe its electronic structures, such as long depletion width and band edge profiles. To overcome such limitations, we combine the multi-space constrained-search density functional theory (MS-DFT) formalism [1] together with the simulated doping method [2] for describing the doped *p-n* junction under finite-bias conditions. Then, by calculating the lateral WSe₂ *p-n* junctions, we find that the depletion width calculated within the first-principles approach is several times longer than that of the analytic expressions, which affects the current-voltage characteristics in the 2D *p-n* junctions. Thanks to the MS-DFT that uniquely allows plotting quasi-Fermi levels (QFLs) profiles within the first-principles calculation [1], we also extract the QFLs profiles from the lateral WSe₂ *p-n* junctions under finite-bias conditions and show that the QFLs profiles gradually expand into the depletion region with increasing forward bias voltage. Finally, based on the QFLs profiles and electronic structures, we study the recombination-generation processes of charge carriers inside the depletion layer, including quantum effects. Our findings highlight the importance of the first-principles approaches for 2D *p-n* junction devices in terms of the design of next-generation 2D *p-n* junction devices.

[1] J. Lee, H. S. Kim, and Y.-H. Kim, *Adv. Sci.* **7**, 2001038 (2020); J. Lee, H. Yeo, Y.-H. Kim, *Proc. Natl. Acad. Sci. U.S.A.* **19**, 10142-10148 (2020).

[2] O. Sinai and L. Kronik, *Phys. Rev. B* **87**, 235305 (2013).

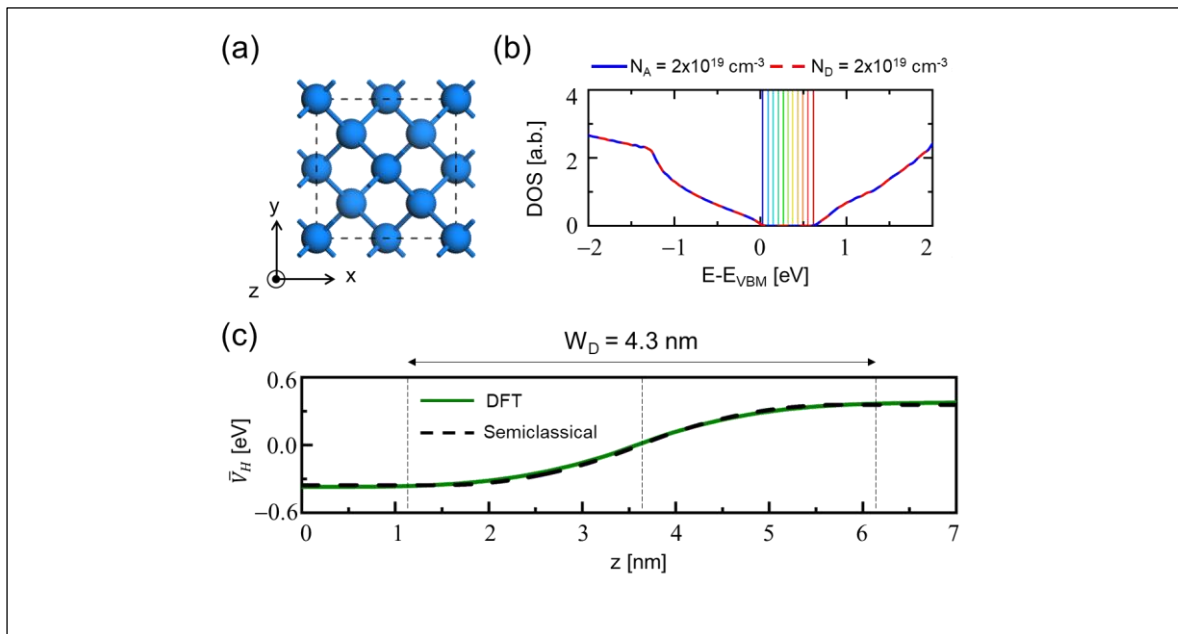


Fig.1: (a) Unit cell structure for bulk silicon crystal. (b) Density of states for p -doped (blue solid line) and n -doped (red dashed line) bulk silicon, in which doping concentration varies from $N_A = 2 \times 10^{19} \text{ cm}^{-3}$ to $N_D = 2 \times 10^{19} \text{ cm}^{-3}$. (c) The comparison of electrostatic potentials for bulk silicon p - n junction within DFT and semiclassical approaches, where the doping concentrations are $N_A = 10^{20} \text{ cm}^{-3}$ and $N_D = 10^{20} \text{ cm}^{-3}$ for p - and n -doped region, respectively.

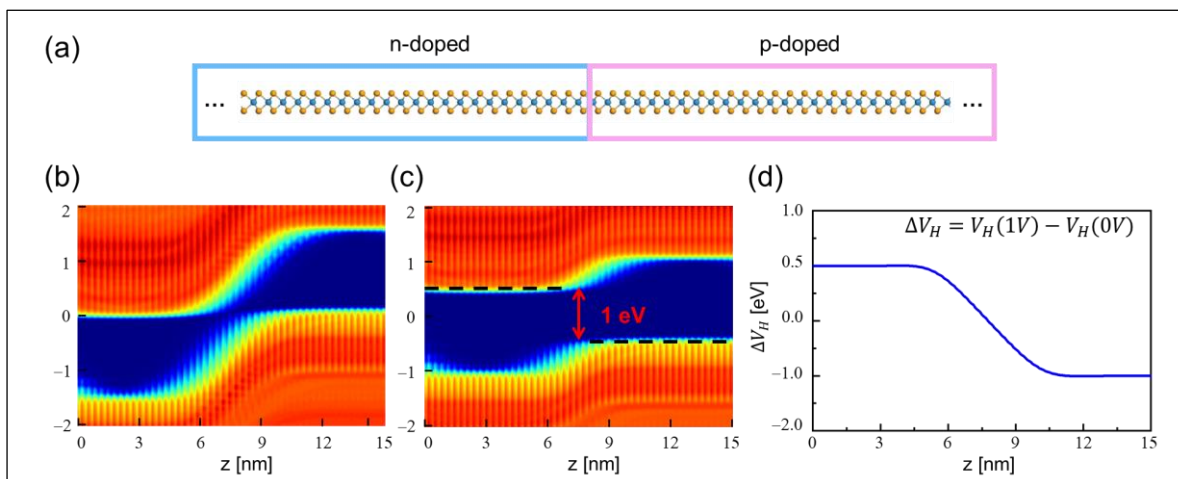


Fig.2: (a) Two-dimensional WSe_2 p - n junction structure. Spatially-resolved density of states for monolayer WSe_2 p - n junction at (b) 0 V and (c) 1 V forward bias voltage, where the doping concentrations are $N_A = 10^{13} \text{ cm}^{-2}$ and $N_D = 10^{13} \text{ cm}^{-2}$ for p - and n -doped region, respectively. (d) Electrostatic potential differences calculated from $\Delta V_H = V_H(1V) - V_H(0V)$ for monolayer WSe_2 p - n junction.

Anomalous Thermoelectric Transport in biased bilayer WSe₂

Vassilios Vargiamidis¹, Panagiotis Vasilopoulos², and Neophytos Neophytou¹

¹ School of Engineering, University of Warwick, Coventry, CV4 7AL, United Kingdom

² Department of Physics, Concordia University, 7141 Sherbrooke Ouest, Montreal, Quebec
H4B 1R6, Canada

V.Vargiamidis@warwick.ac.uk

Two-dimensional (2D) materials with hexagonal structure and transition metal dichalcogenides (TMDs) are furnished with inequivalent valleys at the K and K' points of the Brillouin zone, which are local extrema of the electronic band structure [1]. In these materials an electron not only has spin, but also a valley degree of freedom, which acts as a pseudospin. Promising possibilities for spintronic and valleytronic devices for logic and memory with ultra-low power dissipation have been proposed. However, research in understanding phenomena such as valley- and spin-Hall effects for the K and $K' = -K$ Dirac valleys is still at the fundamental level [1]. The realization of these effects is based on the control of properties that differ between the two valleys [2] in particular the Berry curvature (Ω) upon breaking of space-inversion (P) symmetry. The Berry curvature gives rise to the valley-Hall effect in which electrons at the two valleys drift to opposite edges of the material in the presence of an in-plane electric field due to the equal but opposite Berry curvatures at the two valleys (see Fig. 1). A nonzero Ω in TMDs also leads to various anomalous transport phenomena. In this work, we investigate the berry curvature and one of these effects, the anomalous Nernst effect (ANE) [3] in bilayer WSe₂ with broken P symmetry via gating.

In Fig. 2 we show the energy dispersion $E_{\lambda s_z}^{\mu}$ of bilayer WSe₂ for the K valley versus k/k_c where $k_c = \pi/a$ and $a = 3.32\text{\AA}$ is the lattice constant, $\lambda = c(v)$ for the conduction (valence) band, $\mu = +1(-1)$ is the layer pseudospin for the top (bottom) layer, and s_z is the spin. For finite electrostatic energy V , the spin degeneracy of the subbands is lifted. In bilayer TMDs, for $V = 0$ the origin of finite $\Omega(\mathbf{k})$ is the SOC as shown in Fig. 3. In Fig. 4 notice that for $V \approx 7.5\text{meV}$, which is the SOC for electrons, $\Omega_{c,\downarrow}^b = \Omega_{c,\downarrow}^t$. Also, $\Omega_{v,\downarrow}^b = \Omega_{v,\downarrow}^t$ at $V \approx 112.5\text{meV}$, which is the SOC for holes. The ANC is shown in Fig. 5 for increasing values of V . For $V = 0$, P is preserved and $\alpha_{xy}^v = 0$. However, a $V > 0$, leads to finite α_{xy}^v , whose magnitude and sign is proportional the $\Omega(\mathbf{k})$ of the respective bands, and can be controlled by V . In a similar manner, in Fig. 6 the spin-Nernst effect is also controlled by V .

[1] D. Xiao et al., Phys. Rev. Lett. **108**, 196802 (2012); [2] D. Xiao et al., Phys. Rev. Lett. **99**, 236809 (2007); [3] V. Vargiamidis et al., Phys. Rev. B **102**, 235426 (2020).

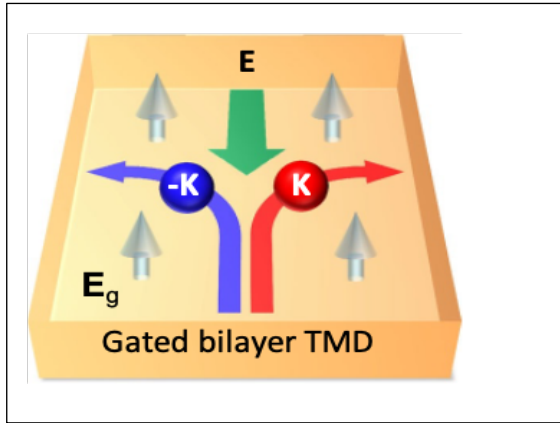


Fig.1: Valley Hall effect in bilayer transition metal dichalcogenide (TMD) in the presence of in-plane and out of plane electric fields E , and E_g , respectively (E_g , shown by the out-of-plane white arrows).

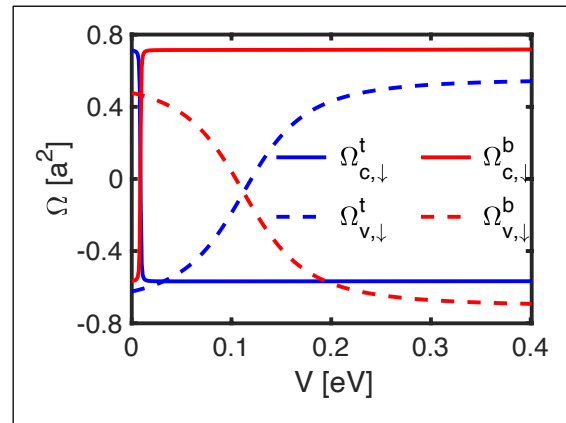


Fig.4: Berry curvature of spin-down bands versus V for $k/k_c \approx 0$. The polarity of $\Omega(\mathbf{k})$ changes when $V=7.5\text{meV}$ or 112.5meV , i.e., at the values of spin-orbit coupling for electrons and holes.

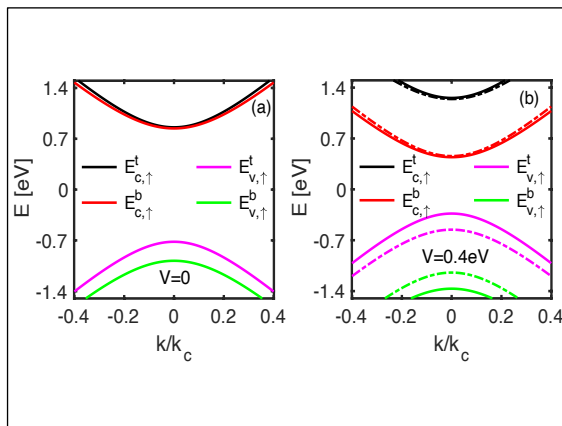


Fig.2: Energy dispersion near the \mathbf{K} valley for bilayer WSe_2 in the absence (left panel) and presence (right panel) of a perpendicular electric field corresponding to a potential energy $V = 0.4\text{eV}$. The solid curves are for spin-up bands and the dash-dotted ones for spin-down.

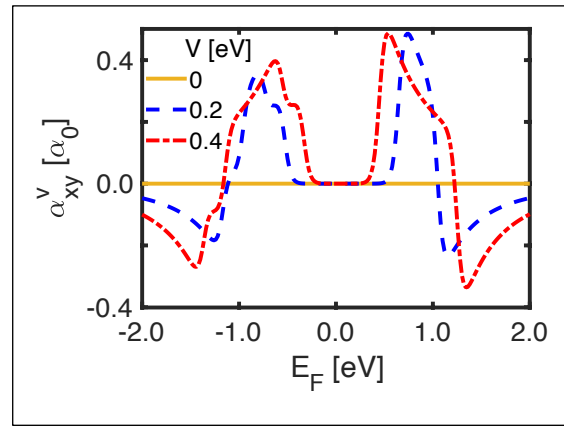


Fig.5: Anomalous Nernst coefficient (ANC) α_{xy}^v for the \mathbf{K} valley versus E_F for increasing values of electrostatic potential V , in units $\alpha_0 = ek_B/4\pi^2\hbar$. The temperature is $T=300\text{K}$.

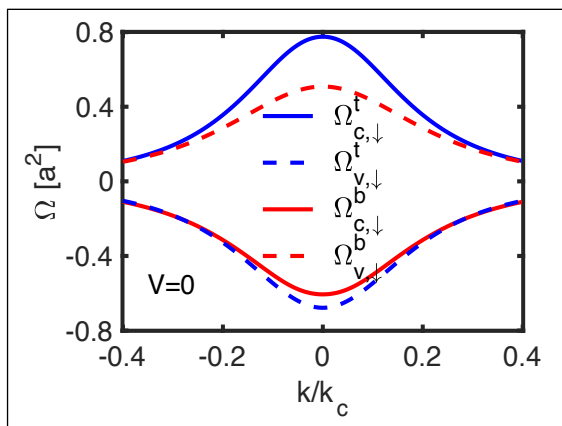


Fig.3: Berry curvature $\Omega(\mathbf{k})$ of spin-down bands versus k/k_c near the \mathbf{K} valley for zero electrostatic potential ($V=0$). Distributions of $\Omega(\mathbf{k})$ have opposite signs in the $\mathbf{K}'=-\mathbf{K}$ valley.

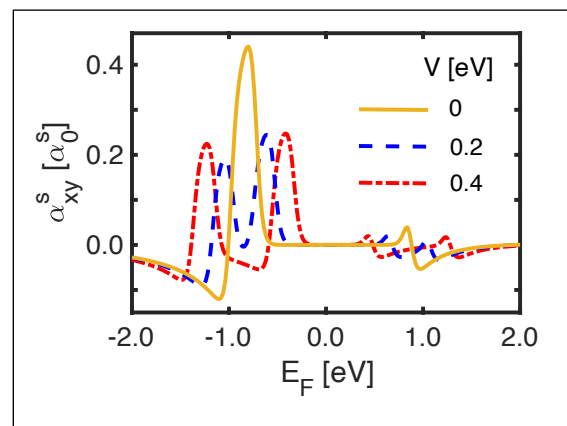


Fig.6: Spin Nernst coefficient (SNC) α_{xy}^s for the \mathbf{K} valley versus E_F for increasing values of electrostatic potential V , in units $\alpha_0^s = \alpha_0(\hbar/2e)$. The temperature is $T=300\text{K}$.

Accurate band-gap database for semiconducting inorganic materials: beyond the level of PBE

Sangtae Kim¹, Miso Lee¹, Changho Hong¹, Youngchae Yoon¹, Hyungmin An¹, Dongheon Lee¹, Wonseok Jeong¹, Dongsun Yoo¹, Purun-hanul Kim¹, Youngho Kang², Yong Youn¹, and Seungwu Han^{1,*}

¹ *Department of Materials Science and Engineering, Seoul National University, Seoul 08826, Korea.*

² *Department of Materials Science and Engineering, Incheon National University, Incheon 22012, Korea.*

hansw@snu.com (e-mail address of the corresponding author)

Semiconducting inorganic materials with band gaps ranging between 0 and 5 eV constitute major components in electronic, optoelectronic and photovoltaic devices. In particular, semiconductors are used in various fields because of the unique characteristics of materials. For instance, in photovoltaic devices, materials with a direct E_g of ~ 1.3 eV, corresponding to the Shockley-Queisser limit, are favored as photo-absorbers that maximize the solar-cell efficiency. In power electronics, semiconductors with $E_g \geq 3$ eV are employed to sustain high electric fields. Currently, there are several inorganic material databases providing band gaps based on the Generalized Gradient Approximation (GGA) functional, including Materials Project [1], the Automatic Flow of Materials Discovery Library (AFLOWLIB) [2], the Open Quantum Materials Database (OQMD) [3], and the Joint Automated Repository for Various Integrated Simulations (JARVIS) (the JARVIS provides E_g based on meta-GGA, which significantly improves the accuracy) [4]. However, they suffer from computational limitations such as band-gap underestimation and metastable magnetism. In this study, we present a computational database of band gaps for 10,481 materials compiled by applying a hybrid functional and considering the stable magnetic ordering [5]. For benchmark materials, the root-mean-square error in reference to experimental data is 0.36 eV, significantly smaller than 0.75-1.05 eV in the existing databases. Furthermore, we classify many small-gap materials that are misclassified as metals in other databases. By providing accurate band gaps, the present database will be useful in screening materials in diverse applications.

- [1] Jain, A. et al., APL Mater., **1**, 011002 (2013).
[2] Curtarolo, S. et al., Comput. Mater. Sci., **58**, 227 (2012).
[3] Saal, J. E. et al., JOM, **65**, 1501 (2013).
[4] Choudhary, K. et al., Sci. Data., **5**, 180082 (2018).
[5] Youn, Y. et al., Comput. Phys. Commun., **256**, 107450 (2020).

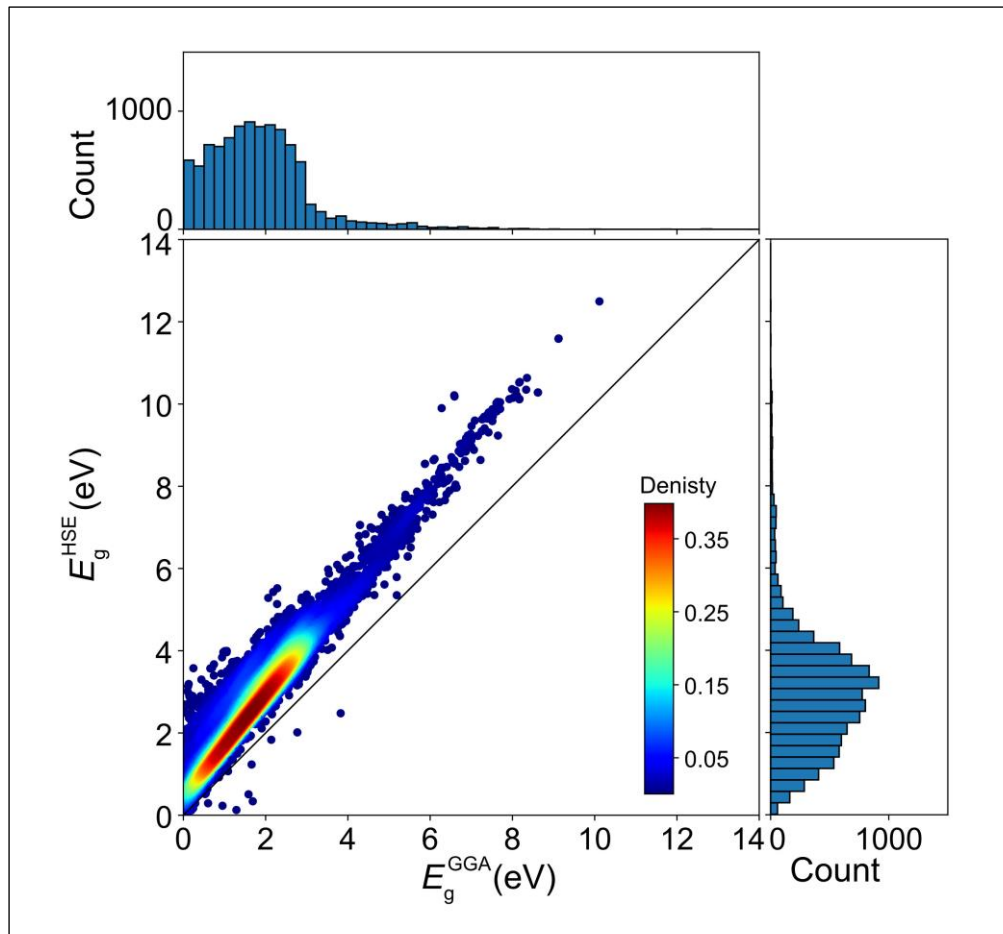


Fig.1: Distribution of E_g^{GGA} and E_g^{HSE} . Top and right are occurrence histograms of E_g^{GGA} and E_g^{HSE} , respectively

THz Optical Properties of Graphene Quantum Dot with Transition Metal Adatom - Time Dependent DFT Study

Do Hyeon Kim¹ and Byoung Don Kong¹

¹ *Department of Electrical Engineering, Pohang University of Science and Technology (POSTECH), Pohang 37673*

bdkong@postech.ac.kr

Mono-layer graphene quantum dots with an attached transition metal adatom were considered for the next generation optical devices [1]. Due to their intriguing tunabilities due depending on their size and the type of adatoms, the graphene quantum dot(GQD) can have wide range of photo luminescence spectra. Their emission frequencies which cover from mid to far infrared, and the device utilizing them can provide a fundamental solution in this spectral region. However, understanding the electron transition behavior between the excitation states from first principles, which is essential to understand the optical responses of the GQD, is a challenging topic since density functional theory is basically aimed to find the ground state solutions. In order to describe energy gap between excited states, the time dependant density functional theory(TD-DFT) has been developed and widely adopted.

In this study, we present a systematically approach to obtain the transition rates between excited state from the TD-DFT study. By carefully investigating to the transition metal graphene quantum dot system in THz region, we examine the applicability of the developed approach to the general optical response problems. We considered three size of GQDs(GQD-4, GQD-12 and GQD-16) and five heavy transition metals (Cr, Mo, W, Pd and Pt). As illustrated in Fig. 1, all of the adhesion metal were optimized with the most stable position (hollow or bridge depending on the elements), at first. As the next step, frontier orbital states including HOMO and LUMO that were mixed into SOC excited states [3],[4] were obtained. Then, Fermi's Golden rule was applied to calculate the transition dipole matrix in order to obtain the life time of triplet sub-levels. The results indicate that structures named GQD-12 are predicted to absorb dominant THz spectra due to the relatively small energy gap between frontier orbitals (Fig. 2). In Fig. 3, absorption peak analysis clearly shows that heavier transition metals interact more strongly. Zero-field spiltting(ZFS) originated from these heavy atoms is considered to lift the degeneracy among triplet-sublevels [5]. Therefore, GQD-12 with both Pt and W have largest peak spectrum.

ACKNOWLEDGEMENT: This work was supported in parts by the BK21 Plus program and the Samsung Research Funding and Incubation Center of Samsung Electronics, Korea (SFRC-IT1802-01).

- [1] X. Hai et al., *J. Mater. Chem. B*, **vol. 6**, no. 20, pp. 3219–3234 (2018)
- [2] P. Adrien Maurice Driac, *Proc. R. Soc. A*, **vol. 114**, no. 767, pp. 243–265 (1927)
- [3] B. De Souza et al., *J. Chem. Theory Comput.*, **vol. 15**, no. 3, pp. 1896–1904 (2019)
- [4] F. Neese et al., *Wiley Interdiscip. Rev. Comput. Mol. Sci.*, **vol. 8**, no. 1, pp. 4–9 (2018)
- [5] K. Mori et al., *Phys. Chem. Chem. Phys.*, **vol. 16**, no. 28, pp. 14523–14530 (2014)

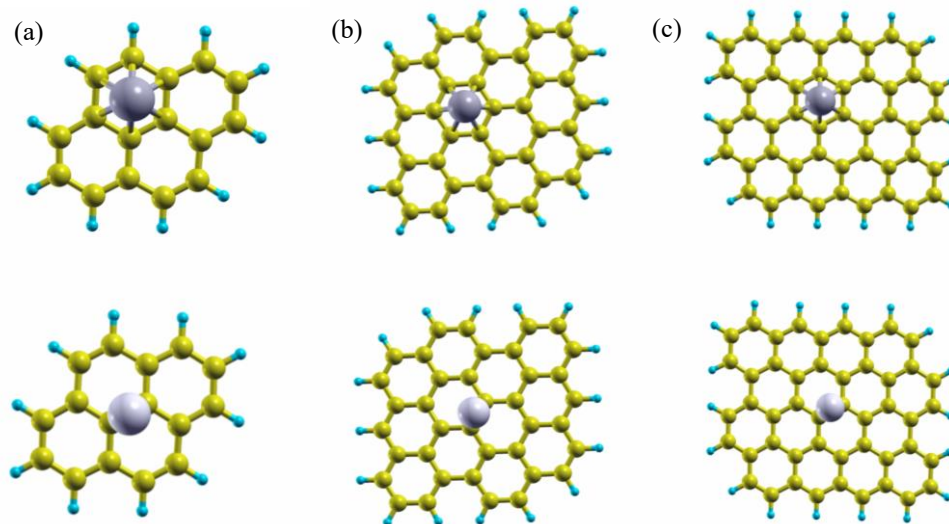


Fig. 1: Hollow and bridge transition metal absorption site for various GQDs: (a) GQD-4, (b) GQD-12, and (c) GQD-16. All of graphene quantum dots are terminated by hydrogen.

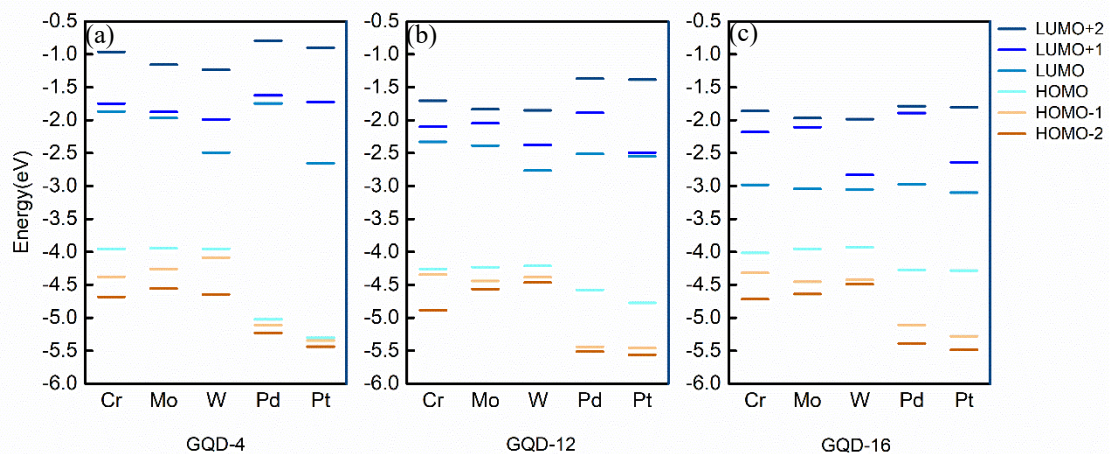


Fig. 2: Frontier molecular orbital analysis for (a) GQD-4, (b) GQD-12 and (c) GQD-16 with five different transition metal. Note that x-axis has no scale but indicate type of metal.

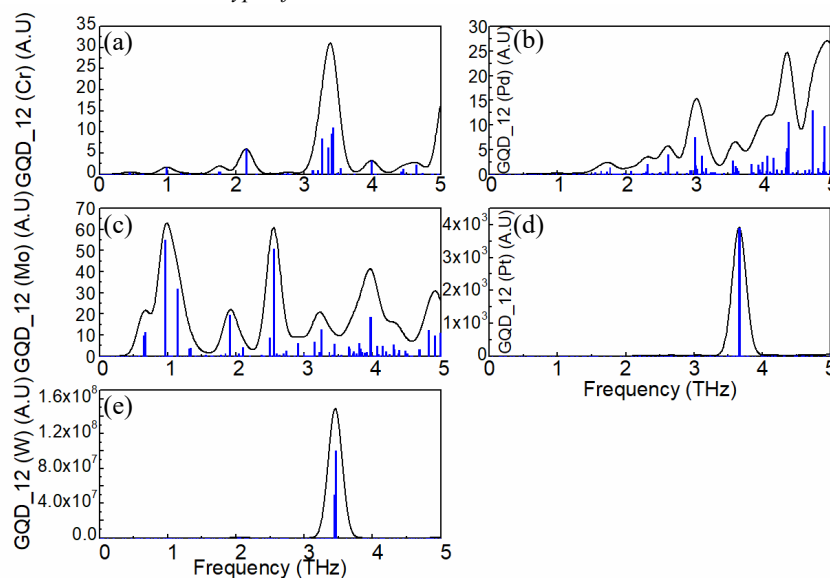


Fig. 3: Optical absorption spectra analysis on (a) Cr-GQD-12, (b) Pd-GQD-12, (c) Mo-GQD-12, (d) Pt-GQD-12 and (e) W-GQD-12 obtained from Fermi's Golden Rule transition rate calculation. The results of five different transition metal are corrected for comparison.

Ultrafast Electron Dynamics in a Silicon Quantum-Dot Single-Electron Pump

Akira Fujiwara¹, Gento Yamahata¹, Nathan Johnson¹,
Sungguen Ryu², Heung-Sun Sim², and Masaya Kataoka³

¹ *NTT Basic Research Laboratories, NTT Corporations*

² *Korea Advanced Institute of Science and Technology (KAIST)*

³ *National Physical Laboratory (NPL)*

akira.fujiwara.kd@hco.ntt.co.jp

A tunable-barrier single-electron pump [1] is a promising device for metrological current standards [2] and coherent single-electron sources for electron quantum optics [3] due to its capabilities of high-frequency (>GHz) operation and tunable electron emission energy; a single electron is captured into a dynamically gate-defined quantum dot (QD) via the entrance barrier and then ejected via the exit barrier. While it generates a DC current proportional to the pump frequency, the current can significantly reflect capture/ejection processes into/from the QD, which occur in a shorter time scale within a small fraction of the whole pump cycle. This provides us opportunities to perform ultrafast (on the orders of picoseconds) sampling of spatial and energy distributions of the single electron inside a dynamic QD, or electron dynamics in a QD such as quantum charge oscillation, energy excitation and relaxation.

In this talk we will introduce our recent work on fast electron dynamics in a silicon QD single-electron pump. We have demonstrated the detection of picoseconds coherent oscillation of a single electron in a QD by utilizing the electron ejection via a resonant trap level in the exit barrier [4]. We have also investigated temperature [5] and frequency [6] dependence of the electron capture process. We have found that electron dynamics such as thermal and nonadiabatic excitation, energy relaxation by electron-phonon scattering, and heat flow could play significant roles in the electron capture under high-frequency operation. These findings would be important for deeper understanding of ultrafast electron dynamics in a QD to realize precise control of charge and quantum states of single electrons for future metrology and quantum technology.

[1] B. Kaestner and V. Kashcheyevs, *Rep. Prog. Phys.* **78**, 103901 (2015).

[2] S. Giblin et al., *Metrologia* **56**, 044004 (2019).

[3] C. Bäuerle et al., *Rep. Prog. Phys.* **81**, 056503 (2018).

[4] G. Yamahata et al., *Nat. Nanotechnol.* **14**, 1019 (2019).

[5] N. Johnson et al., *Appl. Phys. Lett.* **115**, 162103 (2019).

[6] N. Johnson et al., in preparation.

Interfacial Trap Effects in InAs Gate-all-around Nanowire Tunnel Field-Effect Transistors: First-Principles-Based Approach

Hyeongu Lee¹, Yucheol Cho¹, Seonghyeok Jeon¹, and Mincheol Shin*¹

¹ School of Electrical Engineering, Korea Advanced Institute of Science and Technology,
Daejeon 34141, Republic of Korea
mshin@kaist.ac.kr

III-V materials have been actively adopted for the channel material to improve on-current of tunnel field-effect transistors (TFETs). But, one of the issues in practical III-V channel TFETs is the possible presence of interfacial traps between III-V channel and dielectric oxide [1]. A recent first-principles study reported that the dangling bond and anti-site traps can induce the bandgap states which critically affect the TFET performance [2]. However, the effects of these traps using full quantum transport simulation has not yet been investigated. To correctly understand the trap effects and provide practical guidelines for better TFET performance, it is essential to rigorously capture the impact of trapped charges and trap-assisted tunneling (TAT). In this work, we investigated the effects of the traps, Arsenic dangling bond (As_{DB}) and Arsenic anti-site (As_{In}) traps, in InAs gate-all-around nanowire TFETs, using the trap Hamiltonian obtained from the first-principles calculations. The transport properties were treated by nonequilibrium Green's function including the phonon scattering with self-consistent Born approximation. We have focused on the effects of the gate length (L_G) and the trap position (x_T).

The schematic of the simulated device are shown in Fig. 1. Local density of state and current spectrums are shown in Fig. 2, where the As_{DB} trap is located above the valence band edge and the As_{In} trap is at the midgap. Fig. 3 shows the transfer characteristics for $L_G = 7, 10, 14,$ and 17 nm. The traps mainly affect the subthreshold properties, and the impact becomes more significant as L_G decreases. The average SS (SS_{avg}) and I_{ON}/I_{OFF} are depicted in Fig. 4 which reveals that the As_{In} trap is the most detrimental trap for deep L_G scaling. Fig. 5 shows that the degradation by the As_{In} trap is caused by the trap charges (hole) which effectively block the gate electric field so that the TAT leakage current continues to take place. The effect of x_T is shown in Fig. 6 which shows that even a single trap can have significant effects on the reliability and the traps located near source-side are more responsible than the traps near drain-side.

Acknowledgments

This work was supported by Samsung Research funding and the Incubation Center of Samsung Electronics under project number SRFC-TA1703-10

[1] M. R. Tripathy et al, IEEE Trans. Electron Devices, **67**, 1285 (2020)

[2] G. Greene-Diniz et al, J. Appl. Phys., **121**, 075703 (2017)

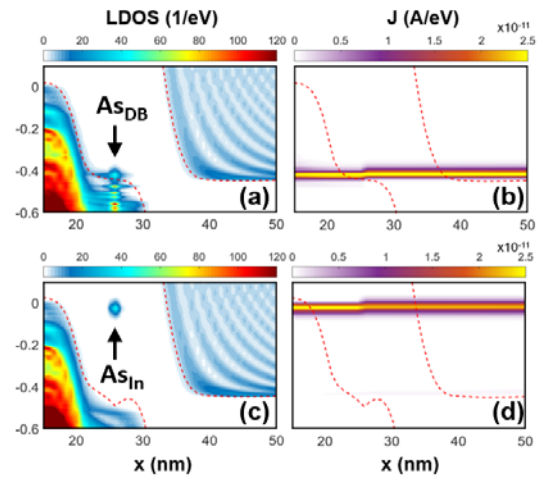
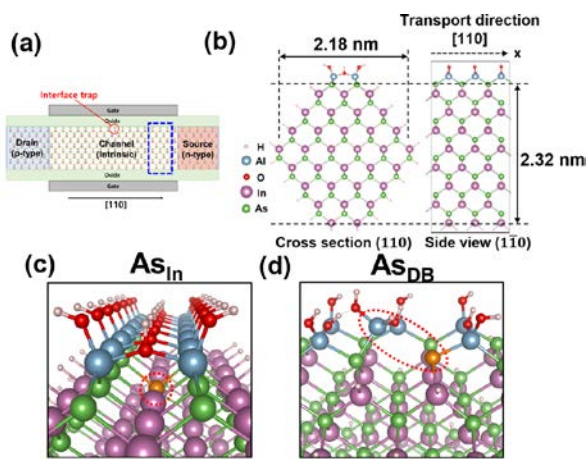


Fig. 1. (a) Schematic of InAs TFET with [110] transport direction. The dashed box indicates the defect-free supercell for density functional theory calculation. Relaxed atomistic structures of (b) the defect-free supercell and the supercell with (c) As_{In} trap and (d) As_{DB} trap. The traps are indicated by red circle.

Fig. 2. Local density of states (LDOS) and current spectrum (J) for $L_G = 10$ nm. LDOS of (a) As_{DB} trap and (c) As_{In} trap. J of (b) As_{DB} trap and (d) As_{In} trap. The drain Fermi level is set to zero.

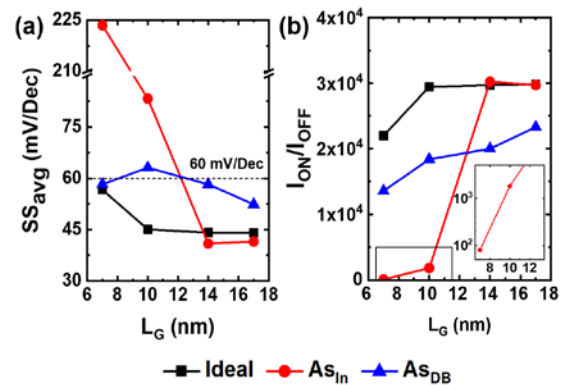
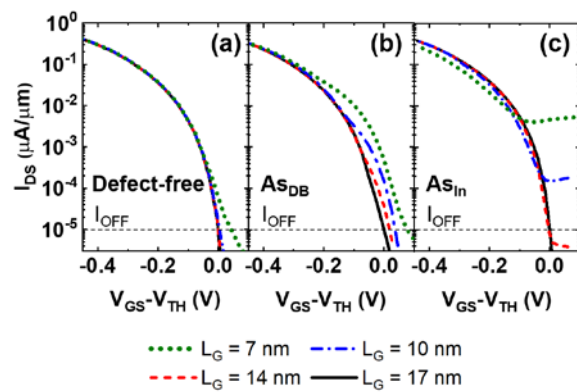


Fig. 3. Transfer characteristics of InAs TFETs (a) without the trap, (b) with As_{DB} trap, and (c) with As_{In} trap. The gate voltage is shifted by the threshold voltage of the device with $L_G = 17$ nm.

Fig. 4. (a) SS_{avg} and (b) I_{ON}/I_{OFF} as functions of L_G . SS_{avg} is calculated over the three orders of magnitude of the drain current from $I_{OFF} = 10^{-5}$ A/m.

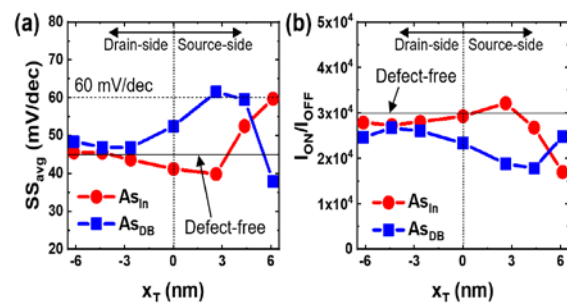
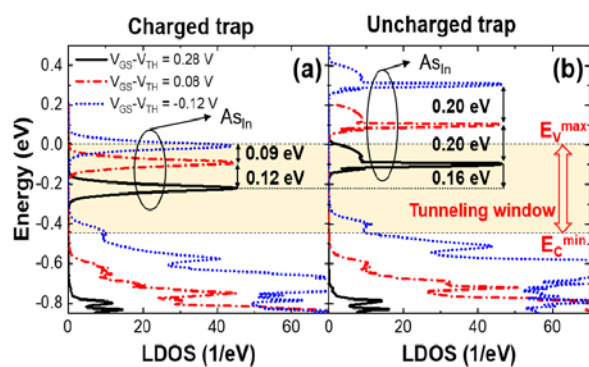


Fig. 5. LDOS of the transport unit cell where the trap is located: (a) with the trap being charged and (b) without the trap being charged. E_C^{min} and E_V^{max} are the conduction band minima and valence band maxima throughout the device, respectively. The tunneling window is shaded.

Fig. 6. (a) SS_{avg} and (b) I_{ON}/I_{OFF} as a function of x_T . The gate length is 17 nm. The dashed lines indicate the performance of TFETs without trap. x_T is measured from the center of the channel.

Equivalent Model for Tunneling Simulation of Direct-Gap Semiconductor Nanowires

Jo Okada, Futo Hashimoto, and Nobuya Mori

*Graduate School of Engineering, Osaka University,
2-1 Yamada-oka, Suita, Osaka 565-0871, Japan
e-mail: {okada, hashimoto, mori}@si.eei.eng.osaka-u.ac.jp*

It is important to develop a method to reduce the order of Hamiltonian describing the electronic state of a device to improve the speed of quantum transport simulation [1]. We have developed a method that uses adaptive moment estimation with automatic differentiation to construct a small equivalent Hamiltonian which reproduces the real band structure within a transport energy window of a target system [2]. In this study, we extend the method and construct an equivalent model that reproduces not only the real band structure but also the complex band structure of a direct-gap semiconductor nanowire for quantum transport simulation of tunneling transistors. The performance of the equivalent model was evaluated by calculating the band-to-band tunneling probability of direct-gap semiconductor nanowires.

We have considered a III-V semiconductor nanowire whose schematic diagram is given in Fig. 1(a). In the equivalent model, the system is represented by a pseudo-one-dimensional chain, as schematically shown in Fig. 1(b) [2]. The parameter matrices D and S of the equivalent model were determined using the adaptive moment estimation with automatic differentiation [3] to reproduce the real and complex band structure of the target system (see Fig. 2). Figure 3(a) shows the band structure of a GaAs nanowire with a square cross section of 1.41 nm per side, calculated with the $sp^3d^5s^*$ tight-binding approximation model (TBM) whose Hamiltonian size is 600×600 . The band structure of the equivalent model (EM), which was constructed to reproduce the TBM band structure, is shown in Fig. 3(b). The size of EM is 48×48 . We see that EM correctly reproduces the real band structure (right panel, $E-k$ diagram) and complex band structure (left panel, $E-\kappa$ diagram, the values of k are also plotted in color) within the transport window.

We have calculated the band-to-band tunneling probability with the non-equilibrium Green's function method. We have applied Eckart-type potential shown in the inset of Fig. 4(b). Figure 4(a) shows the energy dependence of transmission function $T(E)$, and 4(b) the tunnel distance dependence of the tunnel probability. The results of an InAs nanowire are also plotted in the figures. In both cases, we see that EM correctly reproduces the TBM results.

[1] G. Mil'nikov, N. Mori, and Y. Kamakura, *Physical Review B* **85**, 035317 (2012). [2] J. Okada, F. Hashimoto, and N. Mori, *Japanese Journal of Applied Physics*, **60** SBBH08 (2021). [3] TensorFlow, <https://github.com/tensorflow/tensorflow>

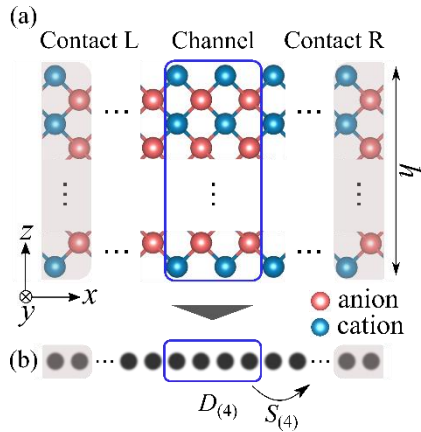


Fig. 1: Schematic diagram of a (100) wurtzite semiconductor nanowire. (a) Tight-binding approximation model (TBM) and (b) equivalent model (EM) representation.

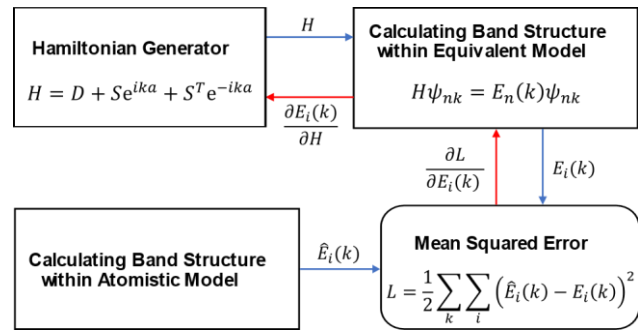


Fig. 2: Processes to reproduce the target band structure through minimization of the loss function L . Red arrows represent the automatic differentiation.

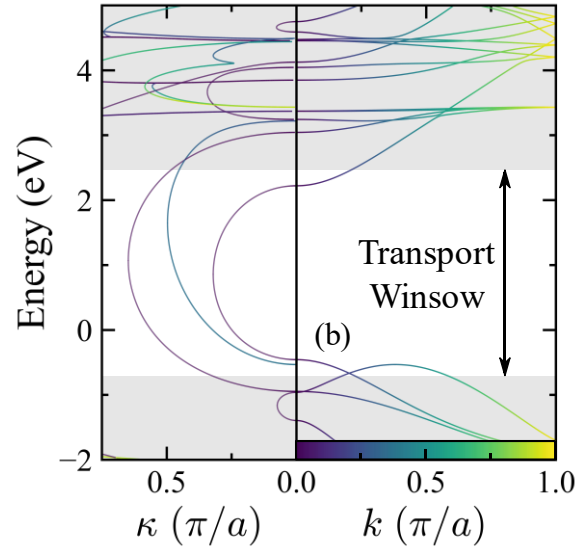
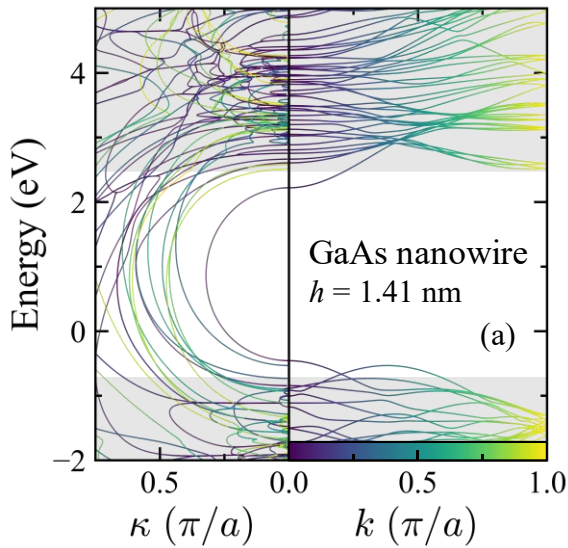


Fig. 3: (a) Band structure of a 1.41 nm \times 1.41 nm GaAs nanowire calculated with TBM whose Hamiltonian size is 600 \times 600. (b) Band structure calculated with EM whose Hamiltonian size is 48 \times 48.

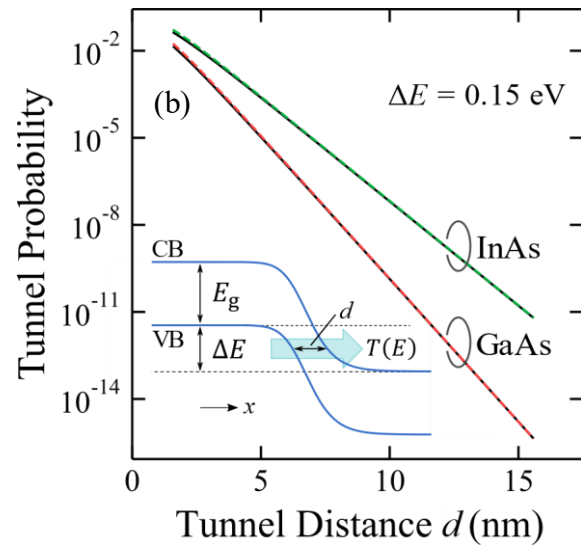
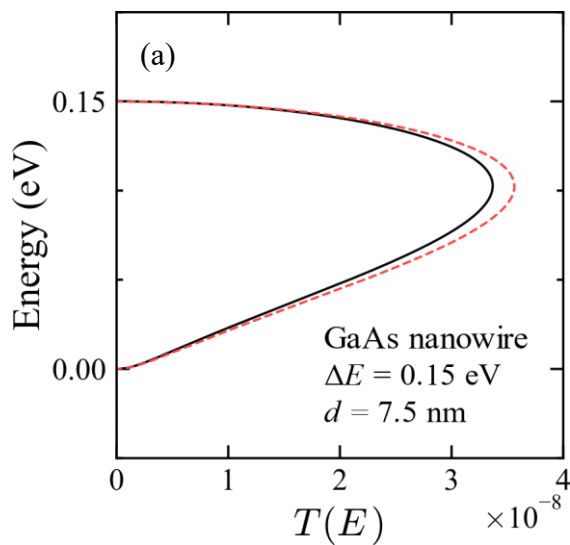


Fig. 4: (a) The energy dependence of transmission function calculated with TBM (solid line) and with EM (dashed line). (b) The tunnel distance dependence of tunnel probability calculated with TBM (solid line) and with EM (dashed line). Inset shows the potential profile.

DFT-NEGF study of biaxial strain effects on Co₂FeAl-based magnetic tunnel junctions

Seongcheol Noh, Mincheol Shin

School of Electrical Engineering, Korea Advanced Institute of Science and Technology

(KAIST), Daejeon 34141, Republic of Korea

mshin@kaist.ac.kr

Spin-transfer torque-based magnetoresistive random access memory (STT-MRAM) is the most promising candidate for energy-efficient future memory. Due to its fast switching speed and nonvolatile nature, there have been numerous attempts to replace DRAM as well as L3 cache memory. Still, STT-MRAM based on perpendicular-type magnetic tunnel junction (pMTJ) encounters the issues with respect to high current density and low thermal stability for a write operation and responsible data retention, respectively. Heusler alloy has been suggested as an alternative for resolving these problems by significantly decreasing Gilbert damping constant while preserving approximately 100% spin polarization. In particular, L_{21} ordered Co₂FeAl (CFA)-based MTJ exhibits not only outstanding half-metallicity [1], but perpendicular magnetocrystalline anisotropy (PMA) characteristic arising from Fe-O or Co-O orbital hybridization at the interface [2].

In this research, we investigate the biaxial strain effects of CFA-based MTJ by manually adjusting in-plane bulk lattice constants (a) from -4% to +4% (from 5.57 Å to 6.03 Å), while the atoms are relaxed in the transverse direction. The CFA-MTJ structure is comprised of MgO as a tunnel barrier and two CFA layers as semi-infinite magnetic leads (Fig. 1). The geometric optimization and transport calculations were carried out with SIESTA and SMEAGOL package to perform DFT-NEGF simulations. Figs. 2 and 3 show the calculated transport characteristics in a low bias voltage range in the parallel and antiparallel configurations, respectively, demonstrating dissimilar I-V behaviors under the compressive and tensile strain. Different behaviors of I-V can be explained by analyzing transmission peaks in the vicinity of the Fermi energy. As illustrated in Figs. 4, 5 and 6, biaxial strain and bias voltage effectively translocate the transmission peaks, which in turn results in the different tendencies of tunneling magnetoresistance (TMR) upon the compressive and tensile strain (Fig. 7).

Acknowledgement: We gratefully thank Prof. Stefano Sanvito at Trinity College Dublin for providing SMEAGOL package with helpful advice. This work was supported by the MOTIE (10080725) and KSRC support program for the development of the future semiconductor device.

[1] I. Galanakis et al., Phys. Rev. B 66, 174429 (2002).

[2] J. Okabayashi et al., Appl. Phys. Lett. **103**, 102402 (2013).

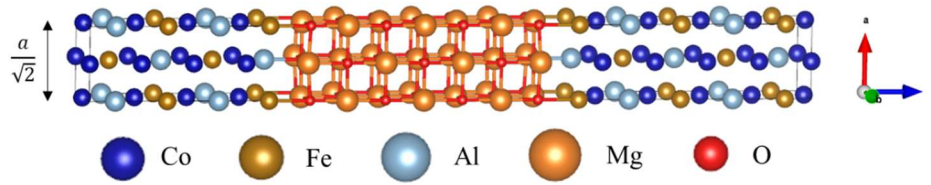


Fig. 1: Schematic crystal structure of Co_2FeAl (8ML)- MgO (9ML)- Co_2FeAl (8ML) magnetic tunnel junction structure.

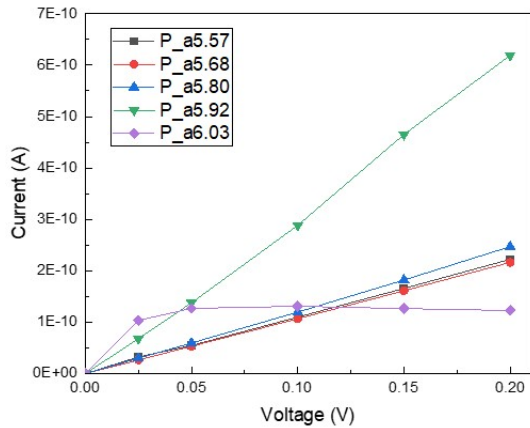


Fig. 2: I - V characteristics of parallel (P) configuration. Each symbol indicates the in-plane unit cell lattice constant (a) of Co_2FeAl from 5.57 \AA to 6.03 \AA .

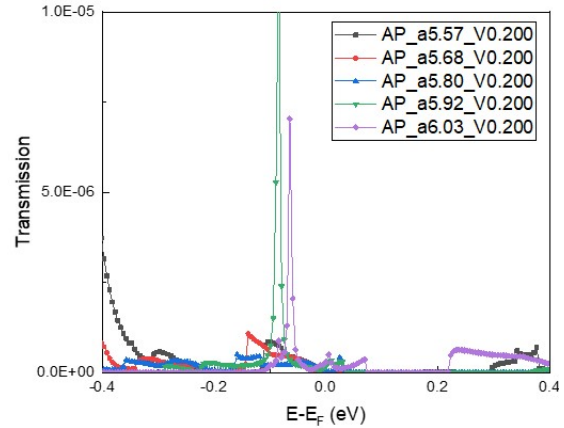


Fig. 5: Strain-induced transmission peak translocation for AP configuration under $0.2V$.

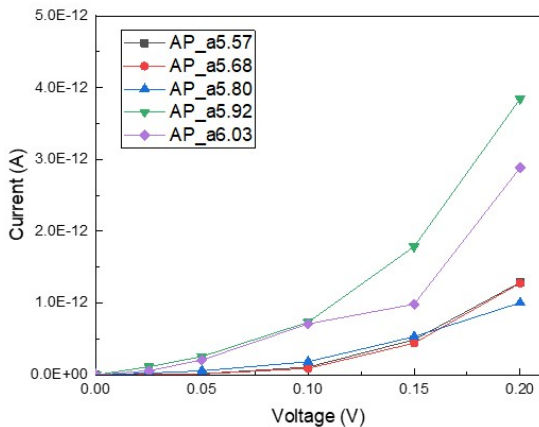


Fig. 3: I - V characteristics of antiparallel (AP) configuration for various in-plane unit cell lattice constants.

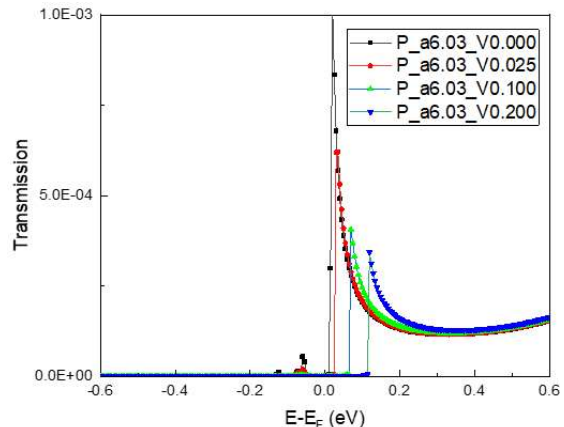


Fig. 6: Voltage-induced transmission peak translocation for P configuration under tensile strain ($a = 6.03 \text{ \AA}$).

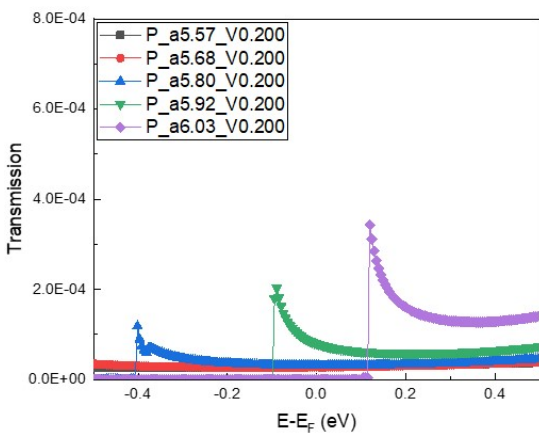


Fig. 4: Strain-induced transmission peak translocation for P configuration under $0.2V$.

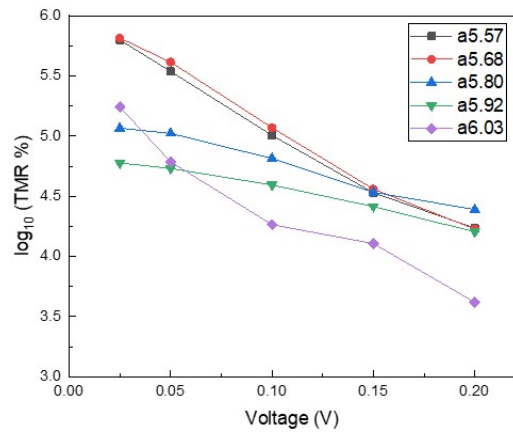


Fig. 7: Tunneling magnetoresistance (TMR) ratio is saturated under compressive strain ($a = 5.57 \text{ \AA}$ and 5.68 \AA), whereas degraded under tensile strain ($a = 5.92 \text{ \AA}$ and 6.03 \AA).

Simulation of AC Responses Using Non-Equilibrium Green's Function at Finite Frequencies

Phil-Hun Ahn and Sung-Min Hong

School of Electrical Engineering and Computer Science,

Gwangju Institute of Science and Technology, Korea

smhong@gist.ac.kr

The theory of AC quantum transport has been well established during the last decades. However, there are only a few papers where the AC quantum transport theory is applied to electronic devices [1-3]. Therefore, it is timely to investigate the AC characteristics of a three-dimensional nanosheet MOSFET with the AC NEGF method.

A nanosheet MOSFET with a rounded corner is used for the simulation as shown in Fig. 1. The corner radius is assumed to be 2.5 nm. The silicon channel is undoped and the gate length is 10 nm. The source and drain regions are doped with a donor concentration of 10^{20} cm^{-3} . The channel direction is [100] and (001) surface is considered. The wavefunction vanishes completely at the silicon-oxide interface. Contacts are considered as semi-infinite leads and the workfunction of the gate contact is 4.3eV. Ballistic transport and effective mass approach are also assumed to simplify the simulation.

In this work, the AC NEGF simulation using the decoupled mode-space approach [4] is tried. To consider the effect of Coulomb interaction, the AC NEGF and Poisson equations are solved self-consistently. The DC and AC NEGF simulation capability has been implemented into our in-house simulator, G-Device. DC NEGF results are shown in Fig.2.

Some of the key equations in the AC NEGF simulation are introduced in Tab. 1 [1-2]. Firstly, the simulation under the zero-frequency limit ($\omega \rightarrow 0$) is implemented. The results are shown in Figs. 3 and 4. The results of transconductance and output resistance from the AC NEGF simulation are consistent with DC NEGF results. The AC electron density under a gate excitation agrees well with the DC results by a finite difference. The AC electron density results at finite frequencies with different bias conditions are shown in Fig. 5. As the frequency increases, the electron density along the channel fluctuates.

Acknowledgement: This work was supported by the National Research Foundation of Korea grant funded by the Korea government (NRF-2019R1A2C1086656 and NRF-2020M3H4A3081800) and the GIST Research Institute grant funded by the GIST in 2021.

[1] Y. Wei and J. Wang, Phys. Rev. B., **79**, 195315 (2009)

[2] M. P. Anantram and S. Datta, Phys. Rev. B., **51**, 7632 (1995)

[3] T. M. Philip and M. J. Gilbert, Journal of Computational Electronics, **17**, 934-948 (2018)

[4] R. Venugopal et al. Journal of Applied Physics, **92**, 3730 (2002)

$$G_{AC}^r(E) = G_{DC}^r(E + \hbar\omega)[V_{AC}(\omega) + \Sigma_{AC}^r(E + \hbar\omega, E)]G_{DC}^r(E), \quad G_{AC}^a(E) = G_{DC}^a(E + \hbar\omega)[V_{AC}(\omega) + \Sigma_{AC}^a(E + \hbar\omega, E)]G_{DC}^a(E) \quad (1)$$

$$\Sigma_{AC}^y(E + \hbar\omega, E) = \frac{qv_{ac}}{\hbar\omega} [\Sigma_{DC}^y(E + \hbar\omega) - \Sigma_{DC}^y(E)] \quad (y = r, a, <) \quad (2)$$

$$G_{AC}^<(E) = G_{DC}^r(E + \hbar\omega)\Sigma_{AC}^<(E + \hbar\omega, E)G_{DC}^r(E)^\dagger + G_{AC}^r(E)\Sigma_{DC}^<(E)G_{DC}^r(E)^\dagger + G_{DC}^r(E + \hbar\omega)\Sigma_{DC}^<(E + \hbar\omega)G_{AC}^a(E) \quad (3)$$

Table.1 AC NEGF equations.

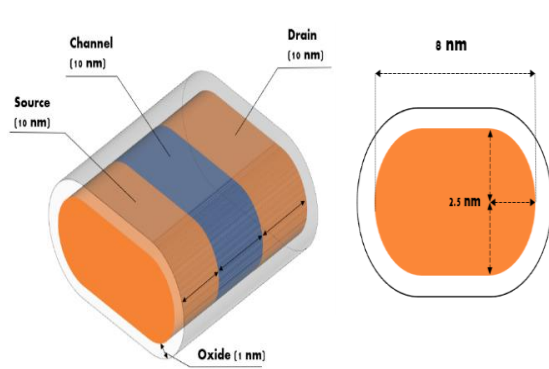


Fig.1: Nanosheet MOSFET used in this work. The right subfigure shows the cross-section along the channel.

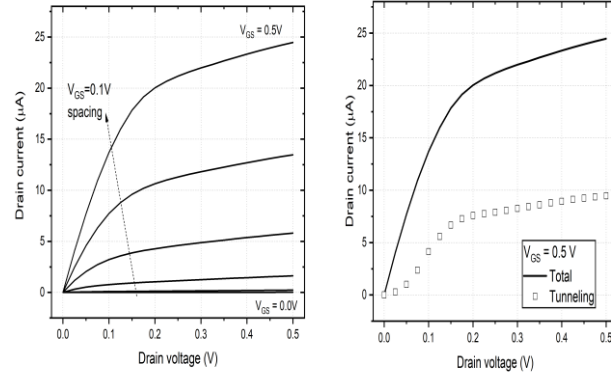


Fig.2: I-V curves of the DC NEGF. The tunneling current curve when gate voltage is 0.5V is shown in the right subfigure.

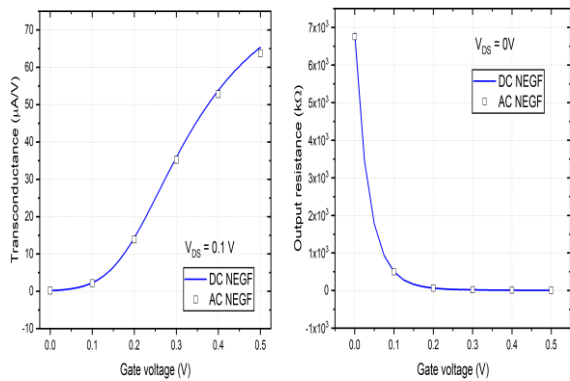


Fig.3: Transconductance and output resistance curves. Blue solid lines are calculated from the DC NEGF with a small excitation. Symbols are from the AC NEGF results under the zero-frequency limit.

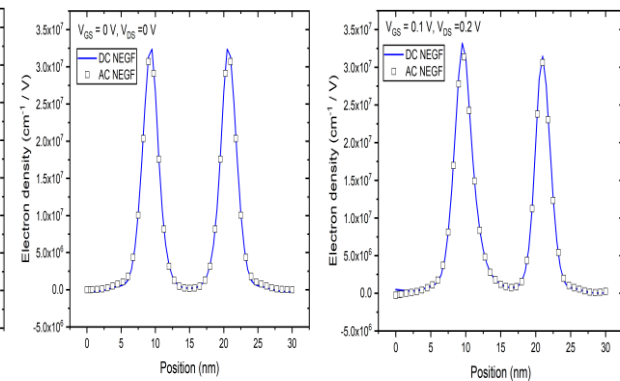


Fig.4: AC electron density according to a gate excitation under the zero-frequency limit. The left subfigure shows the AC electron density at equilibrium. The right one shows a non-equilibrium condition: $V_{GS} = 0.1V, V_{DS} = 0.2V$.

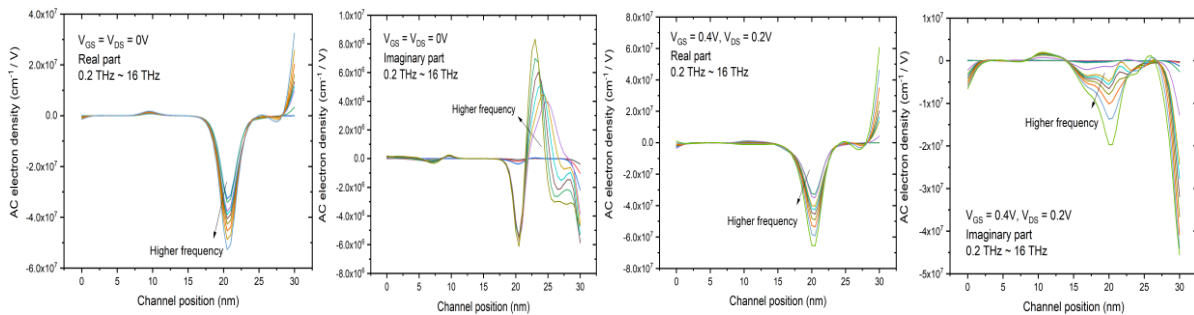


Fig.5: AC electron density according to a drain excitation at a non-zero frequency (0.2 THz ~ 16 THz). Real and imaginary parts are represented separately. Two subfigures on the left show results at equilibrium. Other subfigures on the right show results for a non-equilibrium condition.

Assessing quantum thermalization in small isolated quantum systems through local-in-position weak values of the momentum

Carlos F. Destefani¹, Guillermo Albareda², and Xavier Oriols¹

¹ *Universitat Autònoma de Barcelona, Barcelona, Spain*

² *Max Planck Institute for the Structure and Dynamics of Matter, Hamburg, Germany*
Carlos.Destefani@uab.cat

The study of thermal equilibrium in isolated quantum systems is nowadays among the most intriguing and fundamental problems in statistical mechanics [1]. In the literature, the understanding of thermalization usually differentiates between two types of systems: large isolated systems, where equilibration is reached only by their macroscopic properties, and small isolated systems, where their microscopic properties themselves reach equilibrium values [2]. The later type of thermalization has been experimentally demonstrated for a system with as few as 6 degrees of freedom [3].

The question of how information of a small and isolated quantum system can be extracted without perturbing it appears as a challenging technological and even fundamental (due to contextuality) problem. In this respect, there is large theoretical and experimental interests on weak values because they provide information on quantum systems beyond what is obtained from conventional expectation values. Weak value thus arises as the only tool that can provide dynamical information of a closed system with few degrees of freedom without perturbing it (with zero back-action).

In this work we show that local-in-position weak values of the momentum are an advantageous tool to study quantum thermalization in isolated quantum systems with few degrees of freedom. Such local-in-position weak values have already been experimentally measured in the laboratory and their prediction, from the theoretical viewpoint, just require a Bohmian (hydrodynamic) formulation of the dynamics of the isolated quantum system [4,5].

As an example, here, we consider the quantum dynamics of a coherent state in a one-dimensional harmonic oscillator under the presence of different amplitudes and correlation lengths of a random Gaussian disorder potential [6]. Fig. 1 shows a typical situation: harmonic potential plus a small amplitude disordered potential (left panel), initial and final wavefunctions within the classical turning points (right panel). By solving the time-dependent Schrodinger equation we first discuss a particular criterion for assessing the disorder-assisted equilibration, which is based on the analysis of the kinetic and potential energies alongside the conservation of the total energy (Fig. 2, top panel). The Bohmian (hydrodynamic) formulation of the problem provides information on the local-in-position weak values of the momentum (Bohmian velocities), showing that equilibration in this simple example corresponds to final quantum trajectories localized at certain real-space configurations (vanishing Bohmian velocities) as if they were associated to a stationary state (Fig. 2, bottom panel).

The great merit of the novel proposed way of understanding thermalization in terms of local-in-position weak values (Bohmian velocities) is that such dynamic information is available experimentally [7], ensuring no contamination (zero back-action) from the measuring apparatus [5].

[1] C. Gogolin and J. Eisert, *Rep. Prog. Phys.* **79**, 056001 (2016).

[2] G. Albareda, A. Riera, M. González, J. M. Bofill, I. P. R. Moreira, R. Valero, and I. Tavernelli, *Phys. Chem. Chem. Phys.* **22**, 22332 (2020).

[3] A. M. Kaufman, et al., *Science* **353**, Issue 6301, 794 (2016).

[4] H. M. Wiseman, *New J. Phys.* **9**, 165 (2007).

[5] F. L. Traversa, G. Albareda, M. Di Ventura, and X. Oriols, *Phys. Rev. A* **87**, 052124 (2013)

[6] Y.-W. Hsueh, C.-H. Hsueh, and W.-C. Wu, *Entropy* **22**, 855 (2020).

[7] D. Marian, N. Zanghì, and X. Oriols, *Phys. Rev. Lett.* **116**, 110404 (2016).

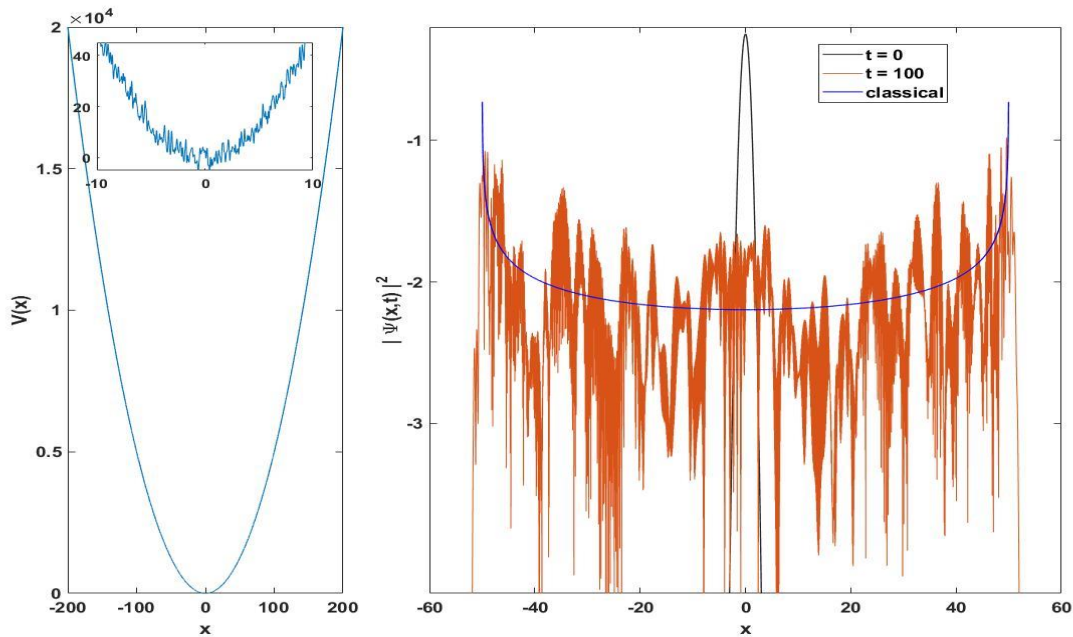


Fig. 1. *Left Panel:* Harmonic potential data: x -grid $[-64\pi, 64\pi]$, k -grid: $[-96, 96]$, $N=12288$ points, resolutions $dx=0.0327$ and $dk=0.0156$; inset: zoom showing the random disorder with amplitude $V_D=50$ and correlation length $\sigma_D=0.01$. *Right Panel* (logarithmic scale in vertical axis): Gaussian initial wavefunction (black) at $t=0$, with initial velocity $v=50$; final wavefunction (red) at time $t=100$, with time step $dt=0.0001$; classical distribution (blue) $1/\pi \sqrt{v^2 - x^2}$, with turning points at $x=\pm 50$. Atomic units are implicit.

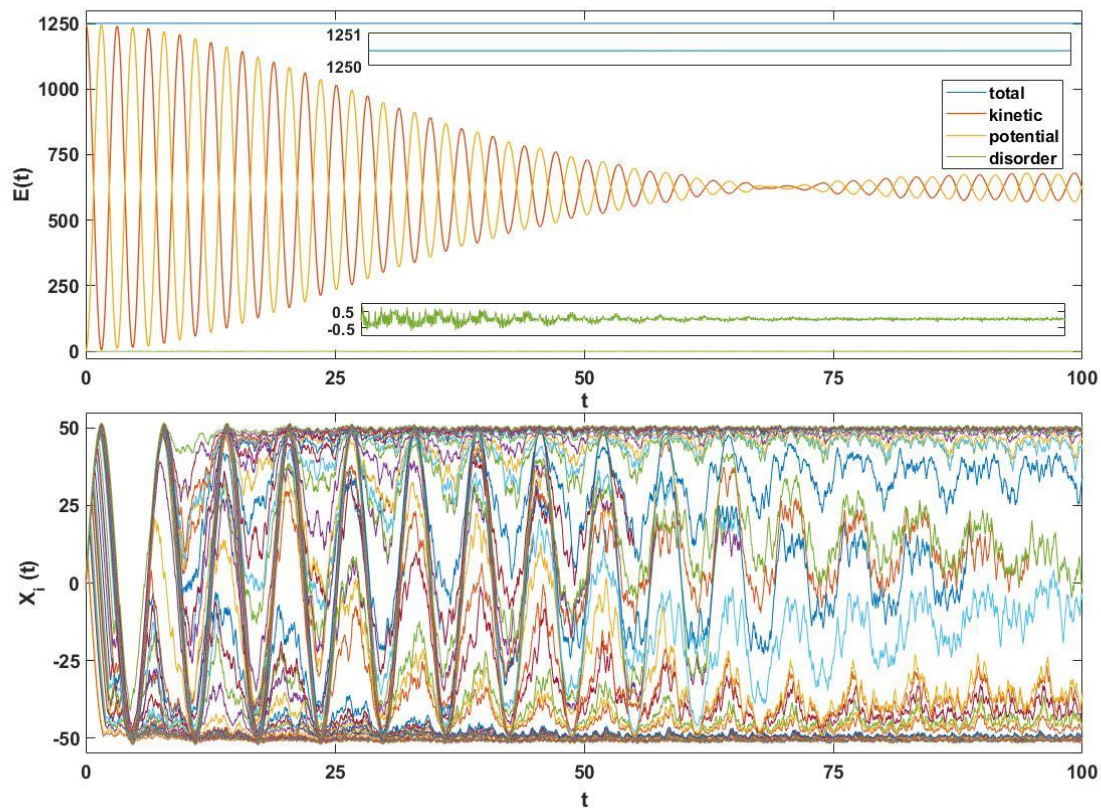


Fig. 2: *Top Panel:* Time evolution of energies $E(t)$: total (blue), kinetic (red), harmonic plus disorder potentials (yellow), only disorder (green); insets: zooms showing total (upper) and disorder (lower) energies. *Bottom Panel:* Bohmian trajectories $X_i(t)$, $i=1 \dots 100$. Atomic units are implicit.

Highly Efficient Thermionic Cooling Semiconductor Devices based on Tilted-Barrier Heterostructures

Marc Bescond^{1,2*}, Kazuhiko Hirakawa^{1,2}

¹ LIMMS-CNRS, UMI 2820, Tokyo, Japan

² Institute of Industrial Science and INQIE, University of Tokyo, Tokyo, Japan

*bescond@iis.u-tokyo.ac.jp

The understanding and control of cooling properties at the nanoscale represent major scientific and industrial issues. In that context, thermoelectricity appears to be a relevant solution as a "green" approach. Moreover, at the nanoscale, transport properties allow to develop highly efficient thermoelectric devices operating in a non-equilibrium regime: this is the field of thermionic cooling. We recently demonstrated both experimentally and theoretically [1] that an asymmetric AlGaAs/GaAs double barrier thermionic cooling heterostructure (Fig. 1) can act on the electronic and phononic bath's refrigeration. In this structure, "cold" electrons are injected from the emitter into the GaAs quantum well (QW) *via* a resonant tunneling effect through the thin potential emitter barrier. "Hot" electrons are then removed from the QW through a thermionic process above the thick AlGaAs alloy collector barrier, extracting the activation energy W from the lattice *via* phonon absorption. As a result, the QW cools and the collector heats.

In this work, we assess the cooling performances of this structure, using an "in-house" non-equilibrium Green's Function formalism, in which the electrical and thermal transport equations are self-consistently solved [2]. We first report an extensive study of the impact of W by varying the QW thickness (L_{QW}) on the electrical and cooling properties (Fig. 2). We demonstrate that the best cooling characteristics are obtained for W close to the polar optical phonon energy of the material, $\hbar\omega_{LO}$ (≈ 35 meV in GaAs) (Fig.3). This is the key parameter. Although promising, the performances are found to degrade at high bias due to the tunneling of electrons across the collector barrier (Fig. 4-a) and Fig. 5). We therefore propose an original structure with a tilted potential in the collector barrier that is able to reduce this parasitic tunnel escape of electrons in the QW (Fig. 4-b)). Simulations indicate that such a structure leads to an improvement of the coefficient of performance over the entire applied bias range by at least 60 %, while maintaining a similar cooling power (Fig. 6) [3]. Therefore, we believe that the present low-energy-injection/high-energy-extraction structure coupled with a tilted potential barrier may lead to the conception of thermionic cooling nanodevices of crucial technological interest.

[1] A. Yangui, M. Bescond, T. Yan, N. Nagai, and K. Hirakawa, *Nature Commun.* **10**, 4504 (2019).

[2] M. Bescond, D. Logoteta, F. Michelini, N. Cavassilas, T. Yan, A. Yangui, M. Lannoo, K. Hirakawa, *J. Phys.: Condens. Matter* **30**, 064005 (2018).

[3] M. Bescond and K. Hirakawa, *Phys. Rev. Appl.* **14**, 064022 (2020).

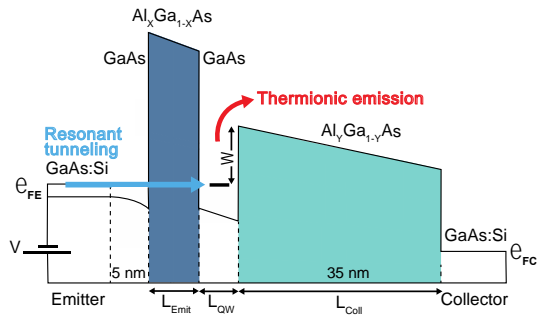


Fig. 1: Considered asymmetric double-barrier heterostructure. For all the considered devices, doping in the emitter and the collector is 10^{18} cm^{-3} . Here L_{QW} denotes the quantum well thickness and W denotes the activation energy. $L_{Emit} = 2 \text{ nm}$ and $L_{Coll} = 35 \text{ nm}$, with $X = 0.4$ and $Y = 0.15$, their respective aluminum concentrations.

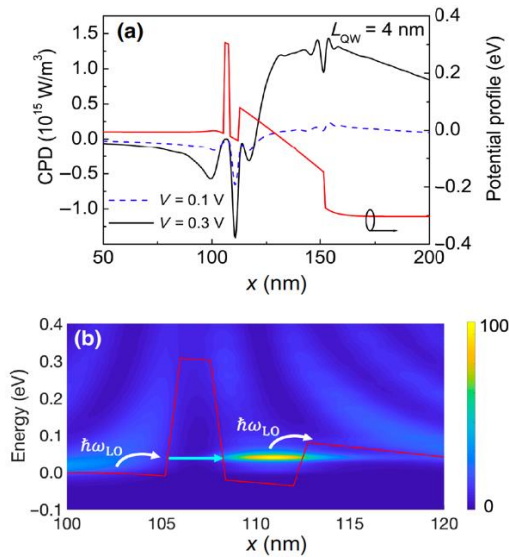


Fig. 3: (a) Cooling power density (CPD) for $V = 0.1 \text{ V}$ (dashed line) and $V = 0.3 \text{ V}$ (solid line); (b) LDOS in the QW region at $V = 0.3 \text{ V}$. In both panels, the solid red line represents the energy potential profile. Here $L_{QW} = 4 \text{ nm}$.

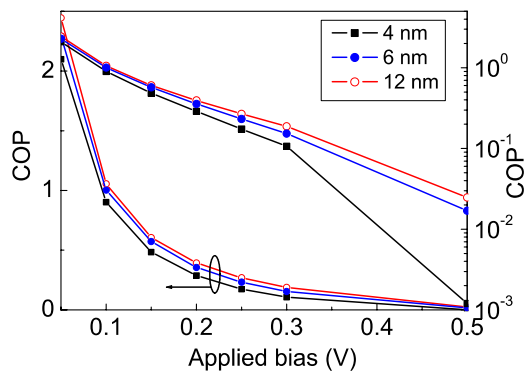


Fig. 5: Coefficient of performance (COP) for three L_{QW} : 4 nm (filled squares), 6 nm (filled circles), and 12 nm (open circles). The COP is degraded at high bias, in particular, due to tunneling effect across the collector barrier.

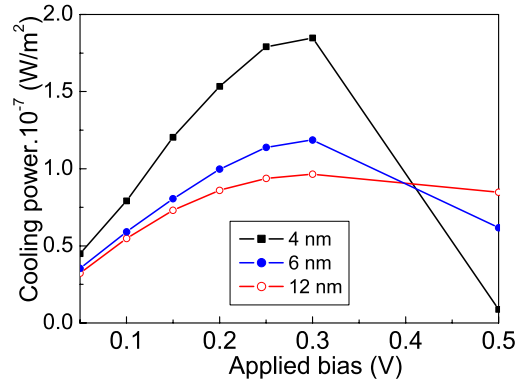


Fig. 2: Cooling power for three L_{QW} : 4 nm (filled squares), 6 nm (filled circles), and 12 nm (open circles). The best cooling is reached for $L_{QW} = 4 \text{ nm}$.

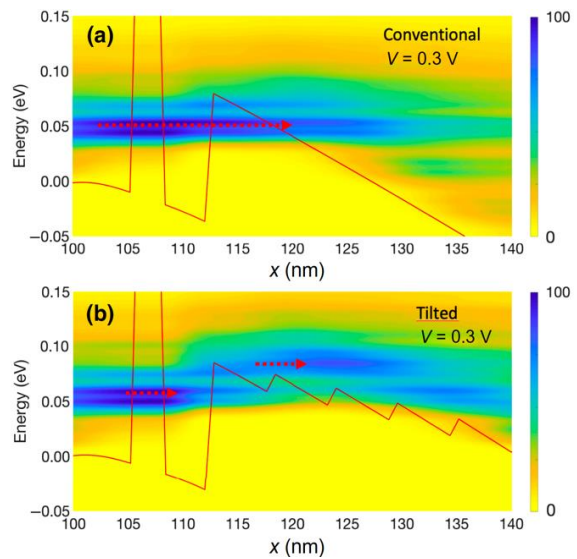


Fig. 4: Current spectra for (a) the conventional structure with $Y = 0.15$ and (b) the tilted structure with Y varying from 0.15 to 0.3 in steps of 5 nm. The red arrows indicate the electron flux through and above the collector barrier. Here $L_{QW} = 4 \text{ nm}$ and the applied bias is $V = 0.3 \text{ V}$.

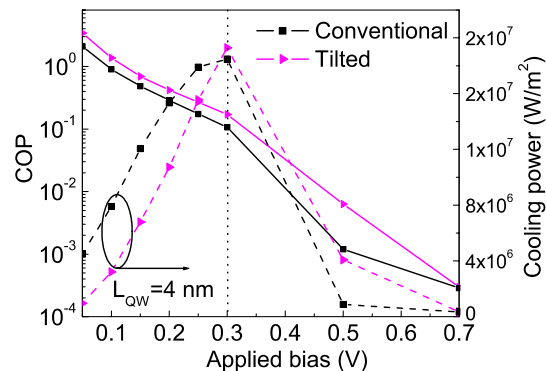


Fig. 6: Comparison of COP and cooling power of the conventional and tilted devices. The tilted device clearly provides enhanced performances at high bias, where the thermionic cooling structures are the most relevant.

Effects of Thin Dipole Layer in Silicon Tunnel Field Effect Transistors

Yeongjun Lim, Junbeom Seo, and Mincheol Shin

*School of Electrical Engineering, Korea Advanced Institute of Science and Technology
(KAIST), Daejeon 34141, Republic of Korea*

mshin@kaist.ac.kr

Tunnel FETs (TFETs) are a promising device for low-power integrated circuits owing to its low operation voltage and steep sub-threshold swing. However, Si TFETs have limitations in terms of on-state current (I_{on}) and on-off ratio due to large band gap and heavy tunneling effective mass [1]. One of the approaches to overcome these shortcomings is to devise TFETs with broken/staggered band gap by forming heterostructures. The band offset of heterojunction III-V materials which have polar interface can be controllable by inserting group-IV ultra-thin layer [2]. Similarly, band alignments can be engineered by inserting a dipole layer in an otherwise homogeneous structure. In this study, we have constructed silicon ultra-thin body (UTB) double-gate (DG) TFETs in the (110)/[001] orientation with III-V ultra-thin layers inserted to create band offset between source and channel region. The density functional theory (DFT) is employed and full quantum transport simulations are performed.

The DFT Hamiltonians are extracted by SIESTA code and all the atomic structures are fully relaxed. The size of the Hamiltonians is reduced by reduced basis transform method for efficient transport simulation [3]. To calculate the current, non-equilibrium Green's function and Poisson's equation are self-consistently solved.

The insertion of the III-V layer in the silicon channel forms dipoles and the electric field induced by dipoles shift the electrostatic potential, resulting in a staggered gap (Fig.3). As a consequence, the band-to-band tunneling distance can be effectively reduced, so I_{on} can be increased by a few orders of magnitude compared to Si homojunction TFET without dipole layer (Fig. 4, 5). Furthermore, we expect that silicon's large band gap will effectively suppress the ambipolar behavior, which is an issue in TFETs.

Acknowledgement : This work was supported by the Basic Science Research Program through the National Research Foundation of Korea (NRF) funded by the Ministry of Science and ICT under Grant 2017R1A2B2005679.

[1] A.C. Seabaugh and Q. Zhang, Proc. IEEE., **98**, 2095-2110 (2010)

[2] A. Franciosi and C.G Van de Walle, Surf. Sci. Rep., **25**, 1-140 (1996)

[3] M. Shin et al, J. Appl. Phys., **119**, 154505 (2016)

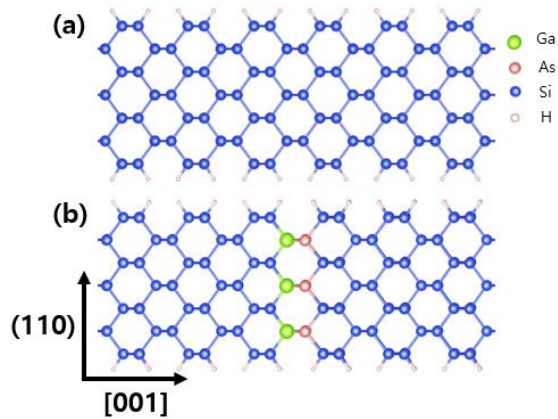


Fig.1: Atomic structures of (a) Si homojunction and (b) insertion of III-V (GaAs) dipole layer.

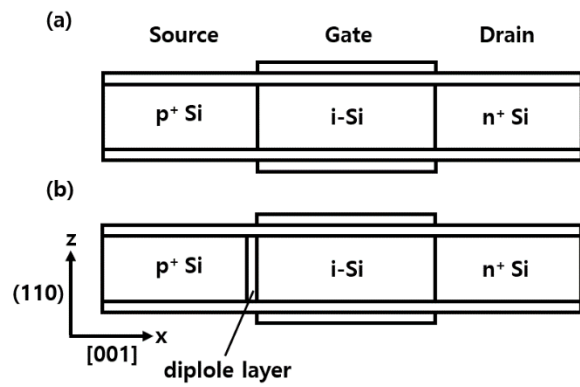


Fig.2: Schematics of DG (a) Si homojunction TFET and (b) insertion of dipole layer.

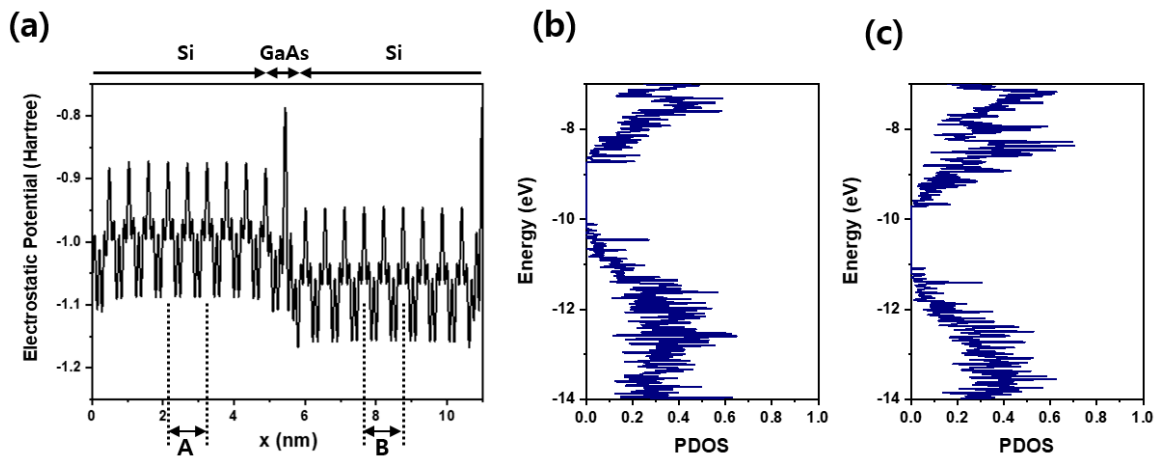


Fig.3: (a) Electrostatic potential and PDOS of (b) left side (region A of (a)) and (c) right side (region B of (a)) of the dipole layer. The UTB has a body thickness of 2nm.

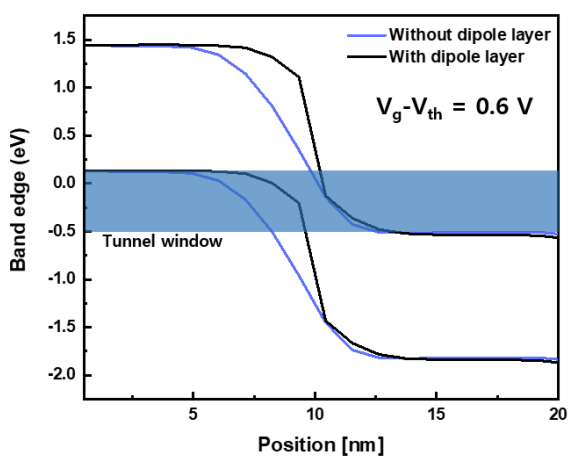


Fig.4: Band diagrams at on-state ($V_g - V_{th} = 0.6 V$) of TFETs with and without GaAs dipole layer. $V_d = 0.5 V$. $V_{th} = V_g @ I_{ds} = 10^{-5} \mu A/\mu m$.

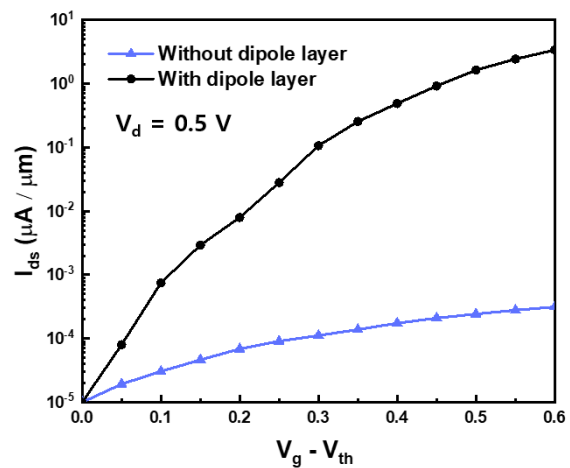


Fig.5: Transfer IV characteristics of TFETs with and without GaAs dipole layer.

Quantum Transport Framework for Highly Conductive δ -layer Systems

Juan P. Mendez¹, Denis Mamaluy¹, Xujiao Gao¹ and Shashank Misra¹

¹*Sandia National Laboratories*

jpmende@sandia.gov

The need for alternative beyond-Moore computing systems has raised a particular interest in δ -layer systems, which consist of a very highly doped monolayer of dopants in an intrinsic semiconductor. These systems have shown promising applications due to their high current density. Several approaches have been used to investigate such systems. However, these approaches are mainly based on periodic boundary conditions along the propagation direction, i.e. the in-plane direction. Therefore, they are mainly limited to investigate equilibrium properties, and additional approximations are required to extract the conductive properties.

In this work, we propose a new open-system quantum transport (QT) framework, based on the Non-Equilibrium Green Function (NEGF) and the effective mass theory, which allow us a direct way to investigate the conductive properties of δ -layer systems. Our QT framework requires a repeated solution of the effective mass Schrödinger equation and the non-linear Poisson equation [1-4] (Fig. 1). For an efficient implementation of the NEGF formalism, we utilized the Contact Block Reduction (CBR) method [1,2]; and, for the charge self-consistent solution of the non-linear Poisson equation, we employed a combination of the predictor-corrector approach and Anderson mixing scheme [3,4].

We have applied this QT framework to study the conductive band structure and the corresponding conductive properties for Si:P δ -layer wires (Fig. 2). Our simulations reveal new physics insights. Firstly, our LDOS analysis predicts a peculiar quantized structure of the conductive sub-bands (Fig. 3), as well as it shows that the free electrons are spatially separated in layers with different average kinetic energies (Fig. 3). Secondly, the number of existing conductive sub-bands is determined by the thickness and sheet doping density of the δ -layer. Finally, as a result of this quantized sub-band structure, we predict: 1) a non-linear dependence of the electron cloud confinement on the δ -layer doping profile (Fig. 4); 2) an increase of the sheet resistivity for sharper δ -layer doping profiles (Fig. 5).

[1] D. Mamaluy et al., J. Appl. Phys. **93**, 4628 (2003).

[2] D. Mamaluy et al., Phys. Rev. B. **71**, 245321 (2005).

[3] H. R. Khan et al., IEEE T. Electron Dev. **54**, 245321 (2007).

[4] X. Gao et al., J. Appl. Phys. **115**, 13707 (2014).

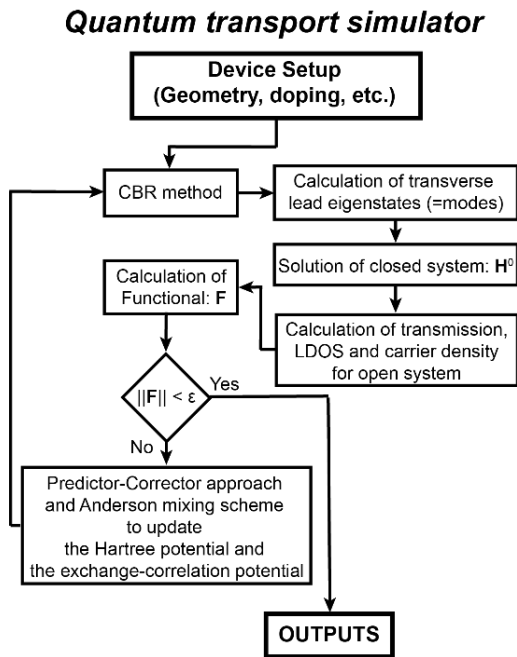


Fig. 1: A simplified flow chart of the self-consistent Quantum Transport method to solve the effective mass Schrödinger equation and the non-linear Poisson equation. ϵ is the non-linear Poisson residuum tolerance.

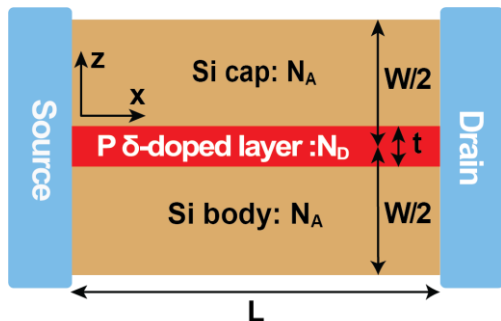


Fig. 2: Schematic model of the Si:P δ -layer system. It is composed of a Si body, a very high P-doped layer, and a Si cap. The conductor channel is in contact with two semi-infinite leads, the source, and drain, respectively.

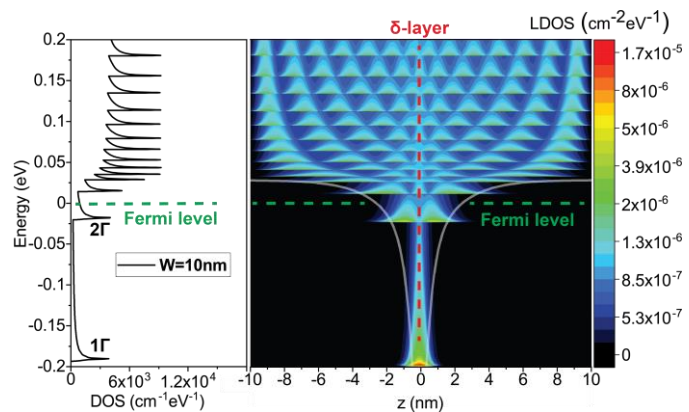


Fig. 3: Right panel: LDOS(z,E) of a Si: P δ -layer wire ($W=20\text{nm}$ and an acceptor density of 10^{17} cm^{-3}). Left panel: corresponding total DOS of the system.

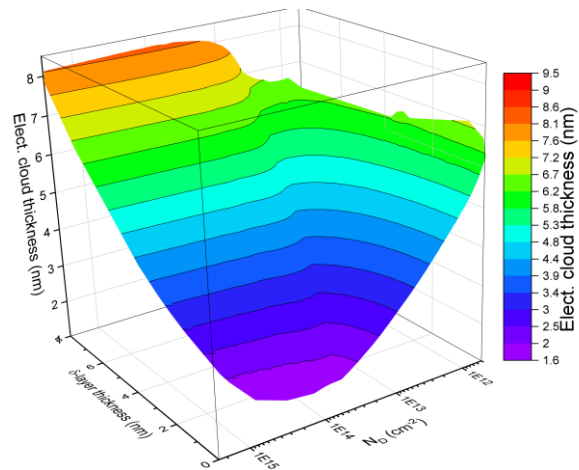


Fig. 4: Effective electron cloud thickness around the δ -layer plane as a function of the δ -layer thickness and the sheet doping density N_D .

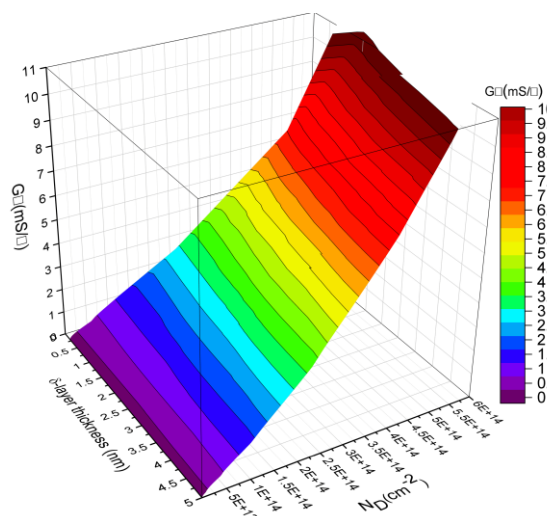


Fig. 5: Sheet electrical conductance for Si: P δ -layer wire in function of the δ -layer thickness and doping density.

Quantum Transport Simulation on 2D Ferroelectric Tunnel Junctions

Eunyeong Yang¹, Jiwon Chang^{*}

¹ *Department of Electrical Engineering, Ulsan National Institute of Science and Technology (UNIST), Republic of Korea*
jiwon.chang@unist.ac.kr

Ferroelectric material has been recognized as an excellent candidate for the low-power non-volatile memories (NVM) due to its spontaneous polarization in the absence of an external bias. One of the NVM based on ferroelectric is ferroelectric tunnel junctions (FTJs) composed of insulating ferroelectric material sandwiched by metal plates. FTJs operate as resistive switching devices by modulating the tunneling potential barrier height. In this work, we consider a simple asymmetric structure of metal-ferroelectric-metal (MFM) FTJs with two different ferroelectric materials, Hf_{0.5}Zr_{0.5}O₂ (HZO) and CuInP₂S₆ (CIPS), respectively. To investigate the performance of FTJs theoretically, we first explore complex band structures of HZO and CIPS with density functional theory (DFT) using Atomistic ToolKit (ATK) simulation^[1]. Then, for the efficient device simulation using quantum transport, two bands $k \cdot p$ model^[2] is established by fitting with DFT results as shown in Fig.1, 2. To calculate the transmission in FTJs, we develop the numerical quantum transport simulator based on Usuki's method^[3] using a recursive scattering matrix. The potential profiles of MFM FTJs are self-consistently computed, as in Fig.3, 4, considering the Thomas-Fermi screening, P-V model for the ferroelectric polarization, and Poisson's equation. Calculating the transmission for a given potential profile, we can calculate the characteristics of FTJs operation. The barrier height modulation by polarization switching in ferroelectric leads to the different ON/OFF conductance and TER ratio. We investigate the dependency of TER ratio on the ferroelectric thickness and polarization and benchmark FTJs based on HZO and CIPS, as shown in Fig.5 and 6.

Acknowledgments This research was supported by the Basic Science Research Program through the National Research Foundation of Korea (NRF) funded by the Ministry of Science, ICT & Future Planning (2020R1F1A1069417).

References

- [1] M. Zhao et al., *Nanoscale*. **12**, 12522 (2020).
- [2] Z. Dong et al., *J. Appl. Phys.* **123**, 094501 (2018).
- [3] R. Akis et al., Springer, NY. 359 (2011).

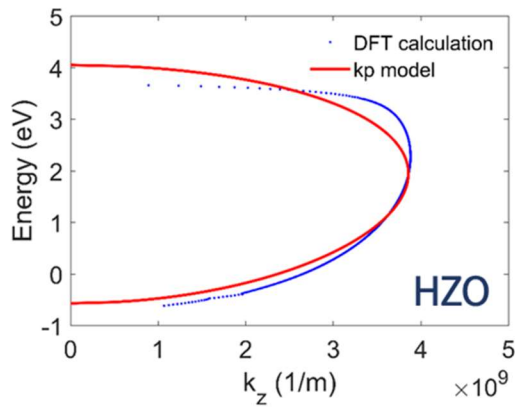


Fig.1: Fitting complex band structure of HZO

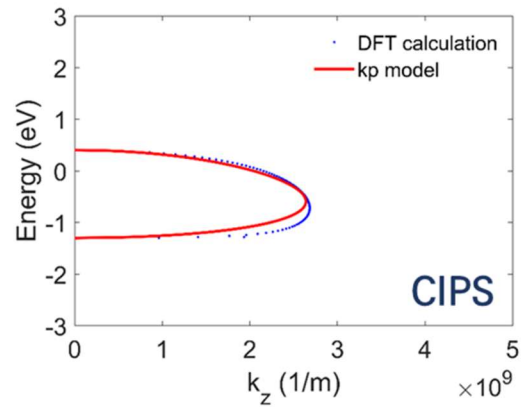


Fig.2: Fitting complex band structure of CIPS

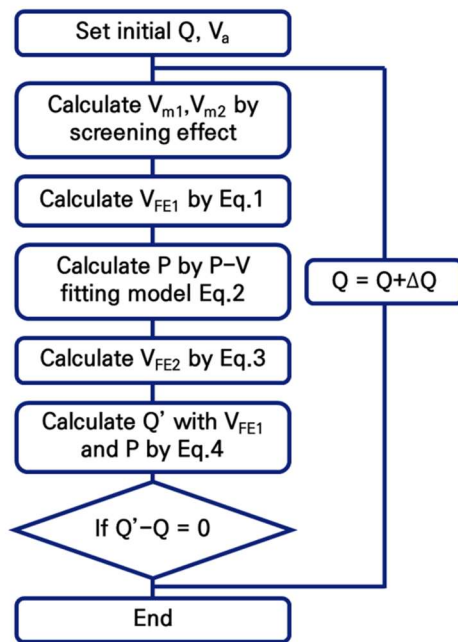


Fig.3: Self-consistent potential calculation workflow for MFM

- Thomas-Fermi screening

$$V_{m1} = -\frac{Q \cdot r_{m1}}{\epsilon} e^{-\frac{x}{r_{m1}}} \quad V_{m2} = \frac{Q \cdot r_{m2}}{\epsilon} e^{-\frac{x}{r_{m2}}}$$
- Bias on FE by screening effect

$$V_{FE1} = V_{m1} - V_{m2} + V_a \quad (\text{Eq.1})$$
- P-V fitting model

$$P(V) = P_s \tanh[w(V \pm V_c)]$$

$$W = \frac{1}{2V_c} \ln \frac{P_s + P_r}{P_s - P_r} \quad (\text{Eq.2})$$
- Poisson's equation

$$V_{FE2} = -\frac{(P-Q)t_{FE}}{\epsilon_0 \cdot \epsilon_{FE}} \quad (\text{Eq.3})$$
- Surface charge on metal-FE surface

$$Q = P + \frac{V_{FE1} \epsilon_0 \cdot \epsilon_{FE}}{t_{FE}} \quad (\text{Eq.4})$$

Fig.4: Underlying physical equations for FTJs

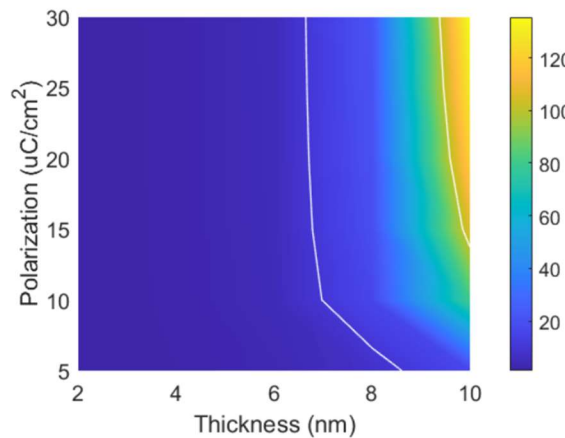


Fig.5: TER contour plot of HZO FTJ in log scale

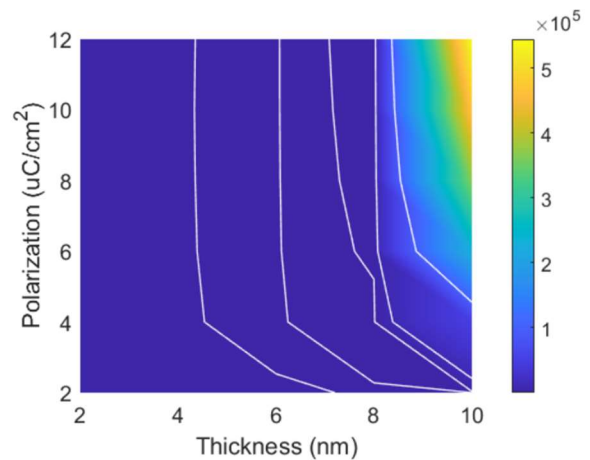


Fig.6: TER contour plot of CIPS FTJ in log scale

Computational Research of CMOS Channel Material Benchmarking for Future Technology Nodes: Missions, Learnings, and Remaining Challenges

Raseong Kim, Uygur E. Avci, and Ian A. Young

Components Research, Intel Corporation, Hillsboro, OR 97124 USA

raseong.kim@intel.com

In this abstract, we review our journey of doing CMOS channel material benchmarking for future technology nodes. Through the comprehensive computational research for past several years [1-7], we have successfully projected the performance of various novel material CMOS based on rigorous physics models, and we have also obtained new physical insights and learnings on the key design considerations for extremely scaled n- and pMOS transistors. There are, however, still research gaps and challenges remaining to complete the whole picture and provide an ultimate theoretical guidance on the material choice for future CMOS, as will be discussed at the end of this abstract.

For the model device, we considered double-gate (DG) or gate-all-around (GAA) nanowire (NW) MOSFETs with the gate length (L_G) of 13 nm for various n- and pMOS materials (Fig. 1). We first showed that it is essential to optimize the device design depending on each material. As shown in Fig. 2, it is critical to optimize the source/drain (S/D) design such as the tip doping density (N_{tip}) to balance the source exhaustion [8] vs. tunneling leakage for materials with small effective mass (m^*) and bandgap, such as III-V's and Ge [1, 9]. For materials with multiple valleys (Γ , L , and X), it is also important to optimize the crystal orientation [10, 11]. In Fig. 3, we show that quantum confinements in Ge NW nMOS with [110] transport may result in optimum density-of-states (DOS) and injection velocity, providing good ballistic performance topping Si or III-V nMOS [3].

Another important issue is the carrier transport model. To simulate the upper limit of current drivability, ballistic transport model has been widely used in many benchmarking studies [12, 13]. Even for extremely scaled devices ($L_G \lesssim 15$ nm), however, carrier scattering effects may be still significant [14]. While it is also critical to consider quantum transport effects such as tunneling in extremely scaled devices, it is very expensive numerically to incorporate scattering effects within a quantum transport simulation framework. In this study, to capture both effects of quantum transport and carrier scattering, we take a hybrid approach [6], by calculating the so-called "ballistic ratio" (BR) [15] from full-band Monte Carlo (MC) simulations [16, 17] and applying them as correction factors to the ballistic current-voltage (I - V) from atomistic quantum transport simulation [18-20] (Fig. 4).

While many benchmarking studies focus on the I - V characteristics of intrinsic devices, parasitic components such as S/D resistance (R_{SD}) may critically impact the actual performance. We have included realistic values of R_{SD} in most of our benchmarking studies, and we also showed that R_{SD} may also significantly depend on the S/D contact geometry due to the carrier scattering and momentum distribution effects [5], especially for light m^* materials such as III-V nMOS (Fig. 5). We also note that in addition to I - V 's, capacitance-voltage (C - V) and circuit performance metrics such as the effective drive current (I_{eff}) [21], switching energy (CV^2), and switching delay (CV/I) including relevant parasitics (such as R_{SD} and parasitic capacitance (C_{par})) and loading effects (gate or wire capacitance loading) are as important to correctly compare various CMOS combinations (homogeneous or heterogeneous) [4, 6] as shown in Fig. 6. We also note that for some channel materials such as Ge, we may have different S/D designs (e.g. N_{tip} 's) that provide optimum performance for the given operation target (high performance or low power).

Finally, while most of previous studies have been done at room temperature (T), we showed that the higher operating T 's for circuits and systems [22] may have significant implications regarding CMOS benchmarking, especially for novel channel materials (Fig. 7) [7]. Due to different T -dependences of thermionic vs. tunneling leakages, for example, performance metrics such as the maximum supply voltage ($V_{DD,max}$) may increase at high T , providing improved I_{eff} in a wider range of V_{DD} while still satisfying Si-like leakage power conditions [7, 23].

While we have achieved significant benchmarking results for novel CMOS channel materials, there are still research gaps to be filled. First, while we introduced a hybrid approach [6] by combining results from two different simulation tools (quantum ballistic (fundamental) + MC (correction factors)) to capture both effects of quantum transport and carrier scattering, the research community may develop a more unified way (e.g. a new, numerically efficient approach to incorporate scattering into the quantum simulation framework) to accurately include those effects within a single, self-consistent simulation tool. Also, while we did consider some circuit aspects in our benchmarking (I_{eff} , CV^2 , CV/I , operating T 's), more in-depth simulations for the process and circuits may be done to analyze the material impact on the layout, fabrication, and system-level performance ("system-technology co-optimization"). This may be particularly important because novel CMOS channel materials may not only promise performance boost for individual transistors but also give integration challenges to the existing Si-based technology.

[1] R. Kim et al., IEEE J. Electron Devices Soc. **3**, 37 (2015).
 [2] R. Kim et al., IEEE Trans. Electron Devices **62**, 713 (2015).
 [3] R. Kim et al., IEEE Electron Device Lett. **36**, 751 (2015).
 [4] R. Kim et al., in IEDM Tech. Dig., 34.1.1, Dec. 2015.
 [5] R. Kim et al., IEEE Trans. Electron Devices **66**, 1189 (2019).
 [6] R. Kim et al., IEEE J. Electron Devices Soc. **8**, 505 (2020).
 [7] R. Kim et al., IEEE Electron Device Lett. **41**, 1332 (2020).
 [8] P. M. Solomon et al., in IEDM Tech. Dig., 95-98, Dec. 2001.

[9] Z. Jiang et al., IEEE Trans. Electron Devices **64**, 945 (2017).
 [10] M. Rodwell et al., in Proc. Device Res. Conf., 149, Jun. 2010.
 [11] R. Kim et al., IEEE Electron Device Lett. **32**, 746 (2011).
 [12] N. Takiguchi et al., IEEE Trans. Electron Devices **59**, 206 (2012).
 [13] S. H. Park et al., IEEE Trans. Electron Devices **59**, 2107 (2012).
 [14] M. Luisier et al., in IEDM Tech. Dig., 251-254, Dec. 2011.
 [15] M. Lundstrom, IEEE Electron Device Lett. **18**, 361 (1997).
 [16] M. Stettler et al., in IEDM Tech. Dig., 39.1.1, Dec. 2019.

[17] Synopsys Inc., *Sentaurus Device Monte Carlo User Guide*, 2019.
 [18] T. B. Boykin et al., *Phys. Rev. B* **66**, 125207 (2002).
 [19] T. B. Boykin et al., *Phys. Rev. B* **69**, 115201 (2004).
 [20] M. Luisier et al., in *Proc. 8th IEEE Conf. NANO*, 354, Aug. 2008.
 [21] M. H. Na et al., in *IEDM Tech. Dig.*, 121, Dec. 2002.
 [22] J.-L. Tsai et al., *Proc. IEEE* **94**, 1502 (2006).
 [23] A. Agrawal et al., in *IEDM Tech. Dig.*, 2.2.1, Dec. 2020.

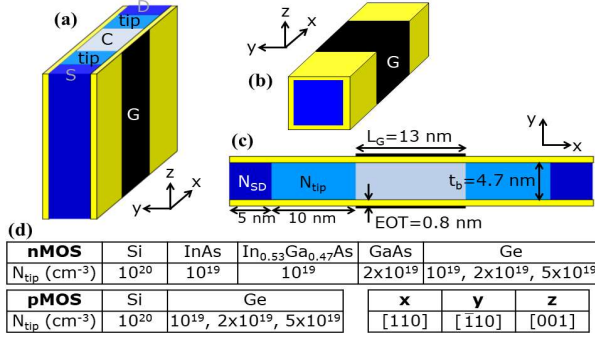


Fig. 1: Structures and parameters of $L_G=13$ nm model device (EOT: equivalent oxide thickness, t_b : body thickness, N_{SD} : S/D doping). (a) DG and (b) GAA NW MOSFETs. (c) Cross-sectional view. (d) n- and pMOS channel materials (with optimized N_{tip} 's) and crystal orientations (x, y, z).

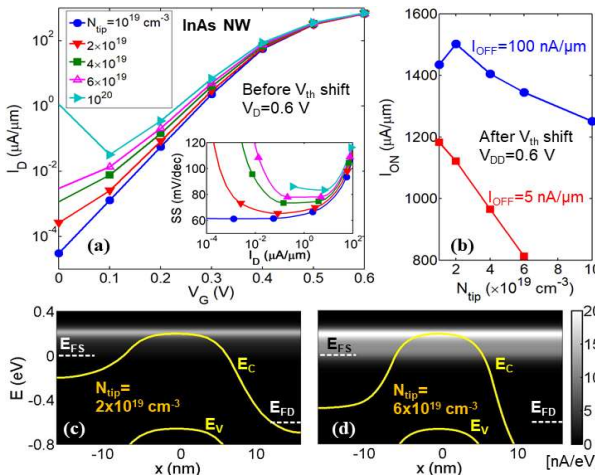


Fig. 2: Simulation results for (a) ballistic I_D vs. V_G (no R_{SD}) for various N_{tip} 's for InAs NW nMOS. (Inset) SS vs. I_D . (b) I_{ON} vs. N_{tip} for two I_{OFF} targets (V_{th} : threshold voltage, V_{DD} : supply voltage). (c)-(d) OFF-state (at $V_G=0.2$ V in (a)) energy-resolved current and band profiles for low and high N_{tip} 's (E_C/E_V : conduction/valence band, E_{FS}/E_{FD} : source/drain Fermi level).

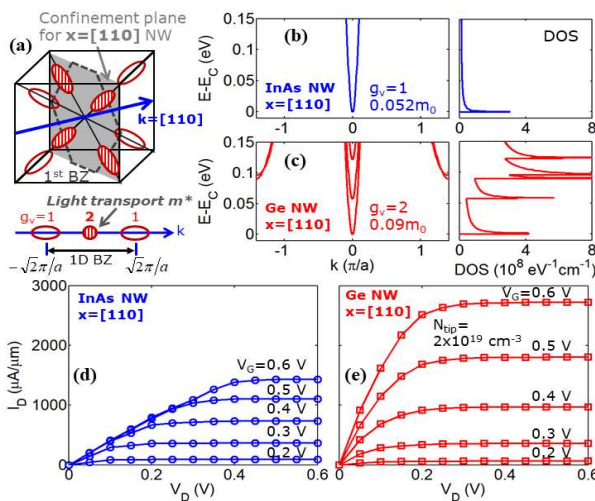


Fig. 3: (a) 2D confinement of L -valleys of Ge for $x=[110]$ (g_v : valley degeneracy). 1D E-k and DOS of (b) InAs and (c) Ge NWs (g_v and m^* of the lowest band also shown, m_0 : free electron mass). Simulation results for ballistic I_D vs. V_D ($I_{OFF}=100$ nA/ μ m, $V_{DD}=0.6$ V, no R_{SD}) for (d) InAs and (e) Ge NW nMOS with $x=[110]$.

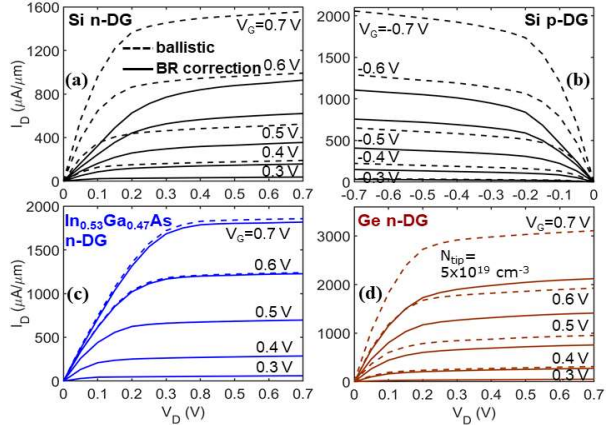


Fig. 4: Simulation results for I_D vs. V_D (dashed lines: quantum ballistic, solid lines: with BR correction, $I_{OFF}=5$ nA/ μ m, $V_{DD}=0.7$ V, no R_{SD}) for DG (a) Si nMOS, (b) Si pMOS, (c) In_{0.53}Ga_{0.47}As nMOS, and (d) Ge nMOS.

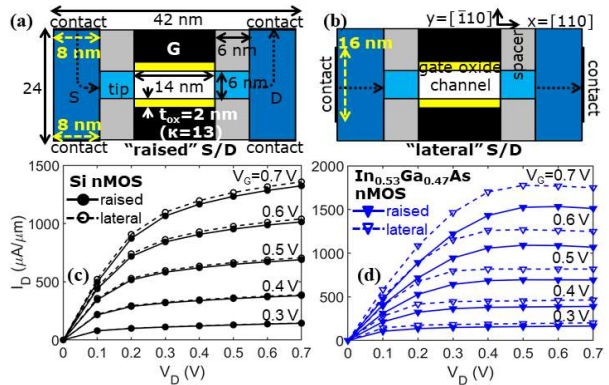


Fig. 5: Schematics of DG FETs with (a) "raised" and (b) "lateral" S/D contacts. MC simulation results for I_D vs. V_D ($I_{OFF}=100$ nA/ μ m, $V_{DD}=0.7$ V, contact resistivity= 2×10^{-9} Ω -cm²) for (c) Si and (d) In_{0.53}Ga_{0.47}As nMOS.

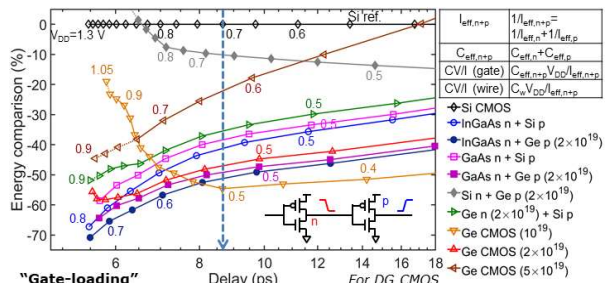


Fig. 6: Relative comparison of CV^2 vs. CV/I (gate capacitance loading) for various CMOS combinations against Si CMOS. $R_{SD}=200$ Ω - μ m, $C_{par}=0.6$ fF/ μ m, and carrier scattering effects are all included. Formulations to calculate circuit metrics are also shown. Values in () are N_{tip} in cm⁻³ for Ge.

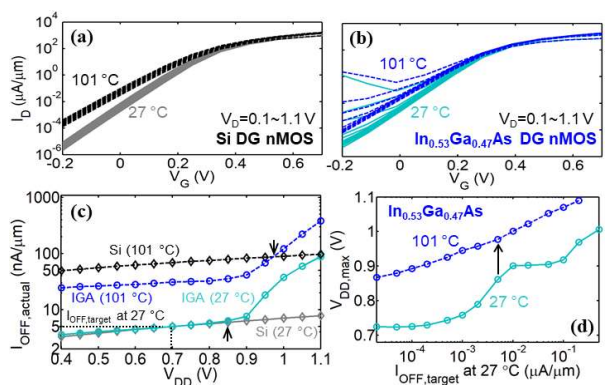


Fig. 7: Simulation results for (a)-(b) I_D vs. V_G , (c) $I_{OFF,actual}$ (I_D at $V_G=0$ V, $V_D=V_{DD}$) vs. V_{DD} , and (d) $V_{DD,max}$ vs. $I_{OFF,target}$ (I_{OFF} target at 27 $^\circ$ C and $V_{DD}=0.7$ V) at 27 $^\circ$ C vs. 101 $^\circ$ C for Si and In_{0.53}Ga_{0.47}As (IGA) DG nMOS.

Advanced Modeling of Emerging Nonvolatile Magnetoresistive Devices

J. Ender¹, S. Fiorentini¹, R. Orio², S. Selberherr², W. Goes³, and V. Sverdlov¹

¹ *Christian Doppler Laboratory for Nonvolatile Magnetoresistive Memory and Logic at the*

² *Institute for Microelectronics, TU Wien, Gusshausstraße 27–29, A-1040 Wien, Austria*

³ *Silvaco Europe, Cambridge, United Kingdom*

sverdlov@iue.tuwien.ac.at

As scaling of CMOS transistors shows signs of saturation, considerable research is focusing on exploring new computing paradigms for energy efficient scalable devices based on novel physical principles. Emerging nonvolatile magnetoresistive memories are CMOS-compatible and electrically addressable. They possess a simple structure and require only a few additional masks for fabrication while offering high endurance and a speed superior to that of flash memory. Fast operation of magnetoresistive memories makes them suitable for SRAM applications [1], while their broad temperature operation range is attractive for flash replacement in, e.g., automotive applications [2]. Nonvolatile magnetoresistive devices integrated with CMOS can not only efficiently store, but also help to process the information, opening perspectives for conceptually new low power and high-performance computing paradigms. As spin-transfer torque (STT) magnetoresistive random access memory (MRAM) is entering mass production, TCAD tools and performance optimization tools facilitating the design for specific applications are urgently needed.

We pursue a fully three-dimensional finite element method (FEM) based modeling and simulation approach (Fig.1) incorporating all essential physical phenomena responsible for proper MRAM operation, sufficient stability, and reliability. To solve the Landau-Lifshitz-Gilbert equation describing the magnetization dynamics in an MRAM cell, the effective field and current-induced torques must be computed. To efficiently compute the contribution of the demagnetizing field, a hybrid approach with the FEM coupled to the boundary element method (hybrid FEM-BEM) [3] is employed in order to restrict the computational effort to the magnetic domain (Fig.2). By modeling the tunnel barrier of a magnetic tunnel junction (MTJ) as a poor conductor with a magnetization-dependent conductivity, we extend the spin transport approach (Fig.3) commonly applied in metallic valves to compute the spin accumulation in an MTJ (Fig.4). By adjusting the diffusion coefficient in the barrier, a free parameter of the model, the spin accumulation continuity is preserved allowing to evaluate the torques (Fig.5). A unique framework to evaluate torques and magnetization dynamics in spin valves and MTJs allows to efficiently describe the behavior of emerging STT-MRAM.

[1] S.H. Han et al., Proc. IEDM, 215 (2020).

[2] V.B. Naik et al., Proc. IEDM, 219 (2020); Y.-C. Shih et al., Proc. IEDM, 223 (2020).

[3] D.R. Fredkin et al., IEEE T-Magnetics, **26**, 415 (1990); J. Ender et al., Proc. SISPAD, 213 (2020).

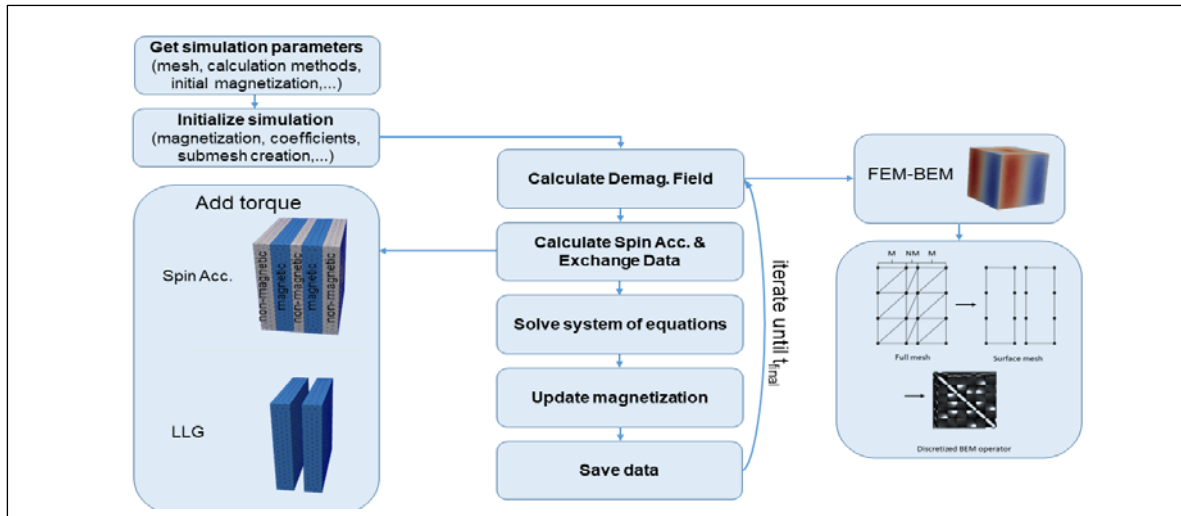


Fig.1: Structure of FEM-based simulator of magnetization dynamics.

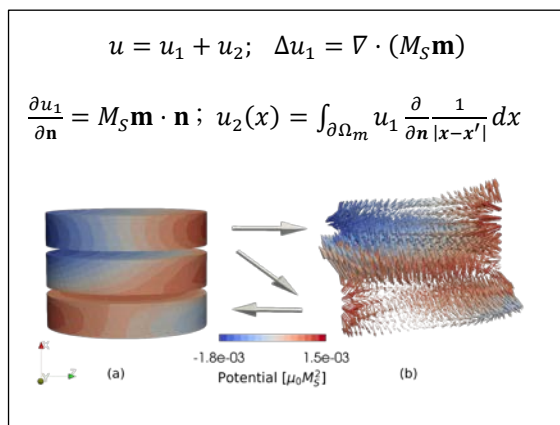


Fig.2: Magnetic potential (left) and demagnetization field (right) in a three-layer structure with noncolinear magnetizations (middle).

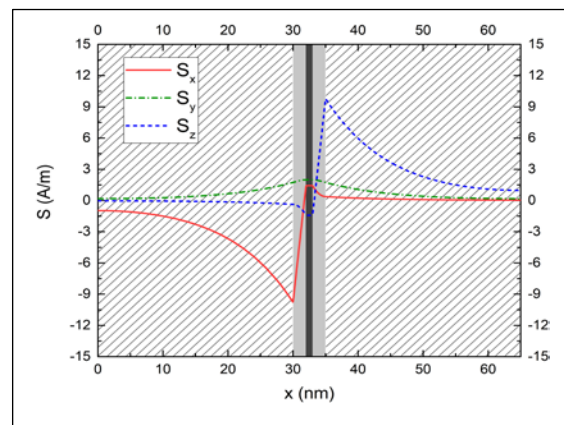


Fig.4: Spin accumulation S in an MTJ (gray) with a barrier (black) connected to normal contacts (shaded) created by the current.

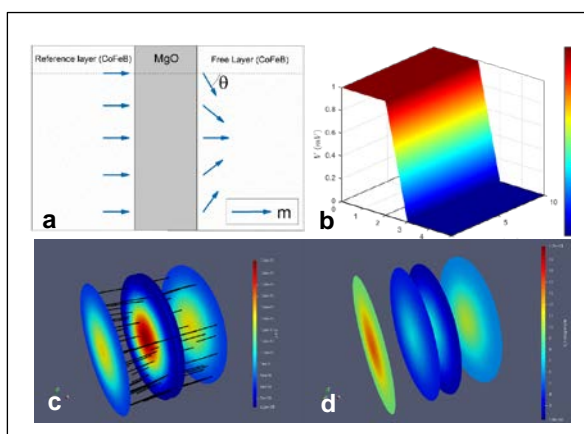


Fig.3: An MTJ with nonuniform relative magnetization; b. Potential drop across an MTJ; c. Current density distribution; d. Spin accumulation created by the current.

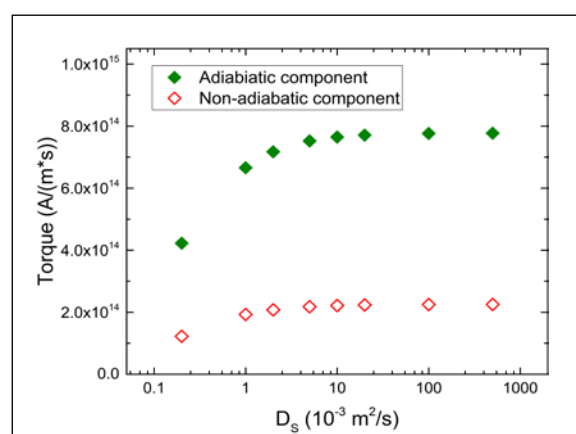


Fig.5: Torque dependence on the diffusion coefficient in the barrier modeled as a poor conductor with the resistivity depending on the relative magnetization orientation across the barrier.

Multiscale Modeling of Hole Avalanche Multiplication and Excess Noise in Amorphous Selenium Semiconductors

Atreyo Mukherjee¹, Richard Akis², Dragica Vasileska³, and A.H. Goldan²

¹ *Department of Electrical Engineering, Stony Brook University, NY, USA*

² *Department of Radiology, School of Medicine, Stony Brook University, NY, USA*

³ *School of Electrical, Computer and Energy Engineering, Arizona State University, AZ, USA*
amirhossein.goldan@stonybrookmedicine.edu

Amorphous selenium (*a*-Se) is a large-area imaging detector material with avalanche gain for low-light and low-dose radiation detection applications.[1] A stark similarity in short range order exists between allotropic forms of selenium, which when augmented with a shift to non-activated extended states transport at high electric fields, allows us to describe the general details of the extended-state hole-phonon interaction in the amorphous phase by modeling band-transport lattice theory of its crystalline counterpart trigonal selenium (*t*-Se). [2] An in-house bulk Monte Carlo algorithm is employed to solve the semiclassical Boltzmann transport equation (MC-BTE). The extended state hole-phonon interaction and the lack of long-range order in *a*-Se is modeled as individual scattering processes, namely acoustic, polar, and non-polar optical phonons, hole-dipole scattering, and impact ionization gain which is modeled using a Keldysh fit. The energy and phonon band structure (**ref. Fig. 1**), along with the valence band density of states (VB-DOS), for *t*-Se, was calculated using density functional theory (DFT) and a non-parabolic approximation to the VB-DOS was used in the simulation (**ref. Fig. 2**). For the first time, we have formulated the interaction of holes in extended states with dipole type defects (the so-called valence alternation pair) present in the chalcogenide family using a non-parabolic VB-DOS approximation. To validate, we compare our drift (**ref. Fig. 3**) and time-of-flight mobility (**ref. Fig. 4**), impact ionization gain (**ref. Fig. 5**), and ensemble energy with experimental findings.[3][4][5][6] This multi-scale approach of combining DFT and MC-BTE is next used in calculating the excess noise factor (ENF) (**ref. Fig. 6**) and spatial resolution in avalanche *a*-Se layers.

[1] Andy LaBella et al., ACS Photon., **6**, 1338-1344, (2019)

[2] Atreyo Mukherjee et al., J. Appl. Phys., **124**, 235102, (2018)

[3] J Mort, Phys. Rev. Lett., **18**, 540, (1967)

[4] Robert Fairman et al., "Semiconducting Chalcogenide Glass I", Academic Press, 2004.

[5] K. Tuji et al., Optoelectron. Devices Technol., **9**, 367-378, (1994).

[6] A. Reznik et al., J. Appl. Phys., **102**, 053711, (2007)

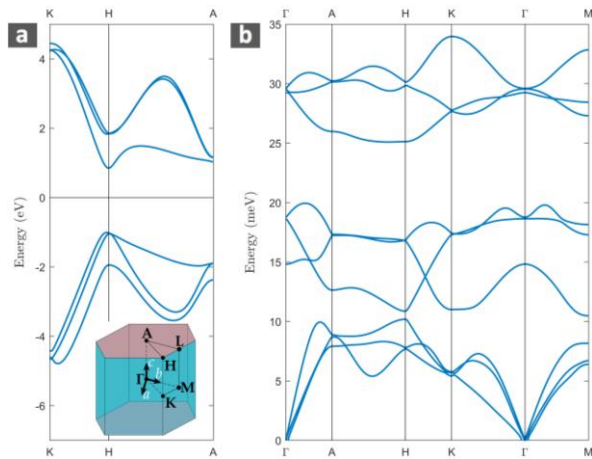


Fig.1: a) DFT calculated electronic band structure for *t*-Se showing a direct bandgap of 1.9 eV at the H point and (b) phonon dispersion. The Brillouin zone for *t*-Se is shown as an inset to Fig. 1.

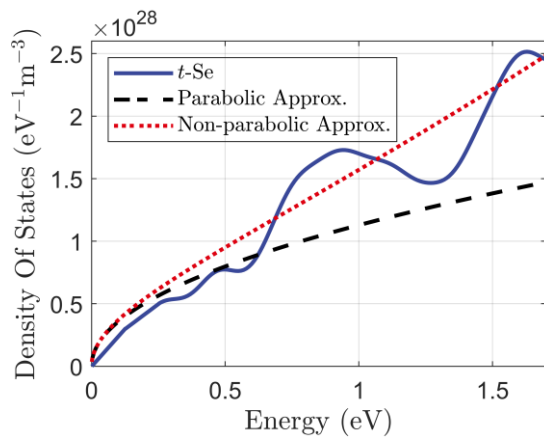


Fig.2: DFT calculations of the VB-DOS are shown by the solid blue line. The dotted red line represents the non-parabolic band approximation ($\alpha = 0.15$) to the VB-DOS. The dashed line represents the parabolic approximation.

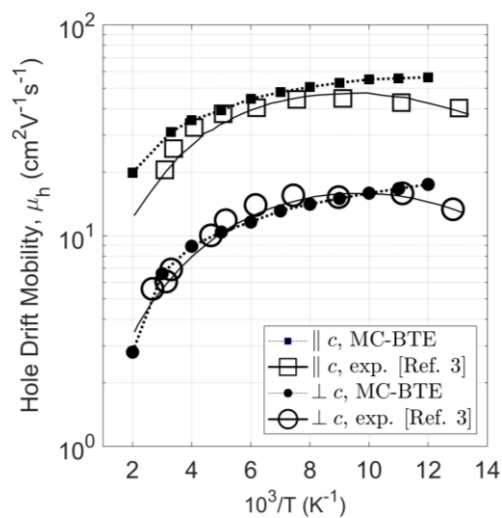


Fig.3: MC-BTE calculated low-field drift mobility values comparison with experiment in the perpendicular and parallel directions to the *c*-axis in *t*-Se, respectively. [3]

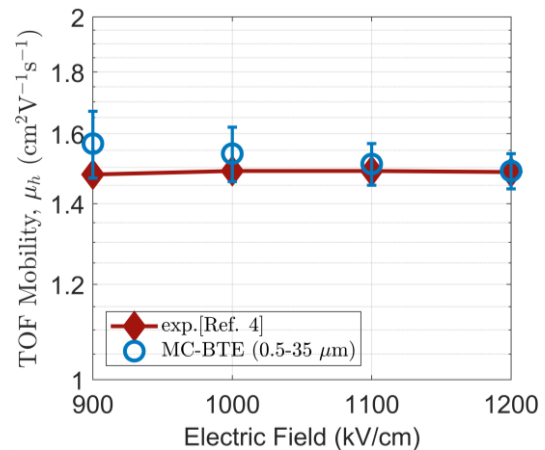


Fig.4: TOF non-parabolic MC-BTE calculated mobility (hollow markers) compared with experimental measured saturated and electric field-independent mobility (solid markers) in *a*-Se. [4]

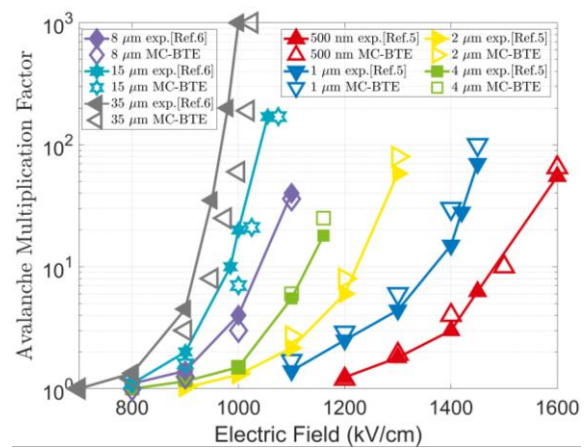


Fig.5: Impact Ionization gain calculated using non-parabolic MC-BTE and compared with experimentally measured gain for 0.5-35 μm thick *a*-Se films. [5][6]

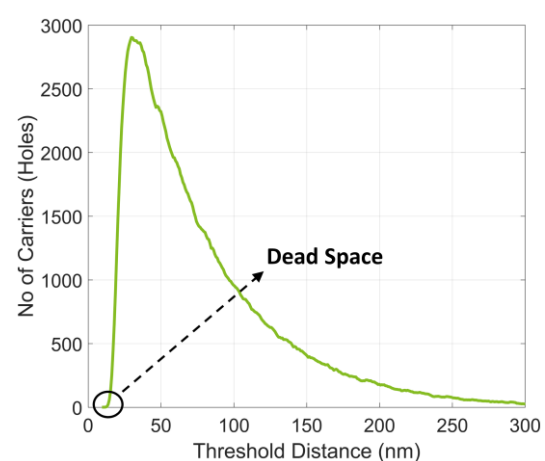


Fig.6: Threshold distance distribution showing the presence of a "dead-space" (defined as the minimum distance of travel in the direction of electric field before a carrier undergoes impact ionization avalanche) in 500 nm *a*-Se layers, resulting in a calculated ENF of ~ 1.4 .

Asymmetry of Current-Induced Heating in Magnetic Tunnel Junctions

Tomáš Hádámek¹, Siegfried Selberherr², Wolfgang Goes³, and Viktor Sverdlov¹

¹ Christian Doppler Laboratory for Nonvolatile Magnetoresistive Memory and Logic at the

² Institute for Microelectronics, TU Wien, Gußhausstraße 27–29, A-1040 Wien, Austria

³ Silvaco Europe, Cambridge, United Kingdom

hadamek@iue.tuwien.ac.at

Magnetoresistive random access memories (MRAM) are promising for automotive applications due to their broad temperature range of operation [1]. Additional heat is generated during the writing process due to the current running through a magnetic tunnel junction (MTJ). The increase in temperature facilitates the free layer switching but also lowers the cell thermal stability. Therefore, for long retention, the temperature must relax fast after the writing process is finished. To account for temperature in TCAD optimization of MRAM is therefore urgently needed.

We consider a CoFeB/MgO/CoFeB MTJ connected to normal metal (NM) electrodes (Fig.1). The current density $j(\mathbf{r})$ at a position \mathbf{r} in the metal contact and the ferromagnetic layers produces a power density $q(\mathbf{r}) = j^2(\mathbf{r})\rho$ [2], where ρ is the resistivity of the material. The power generated by hot electrons tunneling through the barrier in positive x direction can be written as

$$Q(\mathbf{r}) = (1 \pm \alpha(\Delta U)) \frac{j\Delta U}{2\lambda} \exp\left(-\frac{|x-x_{F/P}|}{\lambda}\right). \quad (1)$$

Here j and ΔU are the current density and the potential drop across the barrier at a point (y, z) and $x_{F/P}$ is the x position of the interface between the barrier and the free/pinned layer. The upper/lower sign corresponds to the heat generation in the free/pinned layer. The signs are inverted for the reverse current direction. The energy of a tunneling electron is relaxed down to the Fermi energy in the receiving electrode within a distance $\lambda=1\text{nm}$. The tunneling electron leaves an empty spot in the energy distribution within the emitting electrode, which is occupied by an electron relaxing from the Fermi-energy. Since electrons with a higher energy tunnel easier through the barrier, more heat is generated in the receiving electrode. This asymmetry is described by $\alpha(\Delta U)$ in (1). Because the asymmetry appears only at a finite voltage, $\alpha(\Delta U) = \alpha_1\Delta U$ is a linear function of ΔU in the first approximation [3].

The temperature increase simulated with the parameters from Table 1 after the current pulse is turned on is shown in Fig.2. The increase saturates after 200ps. Fig.3 shows the temperature relaxation after the pulse is turned off. Again, the temperature of the environment is reached after 200ps. Fig.4 shows the temperature behaviour for a 0.4ns current pulse with consequent cooling, for several voltages. The curves for different voltages divided by the total voltage square are shown in Fig.5. Fig.5 demonstrates that the maximum saturation temperature T_{SAT} increases faster than the pulse power by ΔT_{SAT} which scales linearly with voltage (Fig.5, Inset) due to the linear dependence of α on ΔU .

[1] V.B. Naik et al., Proc. IEDM, 219 (2020); Y.-C. Shith et al., Proc. IEDM, 223 (2020).

[2] I.L.Prejbeanu, Phys.: Cond.Matt. **19**, 165218, 2007.

[3] A.F. Hebard, Phys.Rev.B. **14**, 1751 (1976); I. Bat'ko et al., Eur. Phys. J Appl.Phys. **31**, 191(2005).

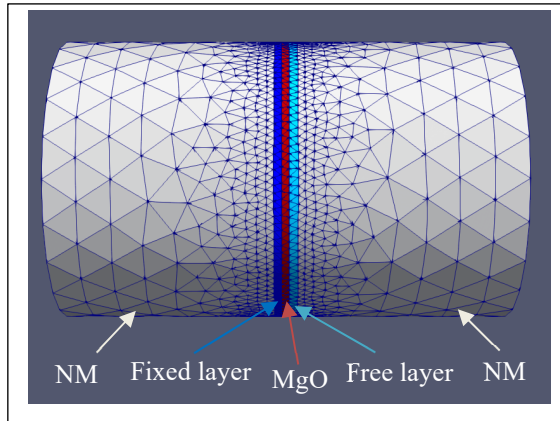


Fig.1: Simulated cylindrical structure of 40nm diameter. The MTJ consisting of a fixed CoFeB layer (1nm), MgO layer (1nm) and CoFeB free layer (1.2nm) is connected to metal contacts (NM) (30nm). Both ends are kept at a constant temperature.

	MgO	FeCoB	NM
Density [kgm^{-3}]	340	7200	8000
c_v [$\text{J K}^{-1}\text{kg}^{-1}$]	796	500	500
κ [$\text{W K}^{-1}\text{m}^{-1}$]	0.38	43	43
ρ_e [Ωm]	-	2×10^{-5}	2×10^{-5}

Table 1: Parameters used in simulation: Density, thermal capacitance c_v , thermal conductivity κ and electric resistivity ρ_e .

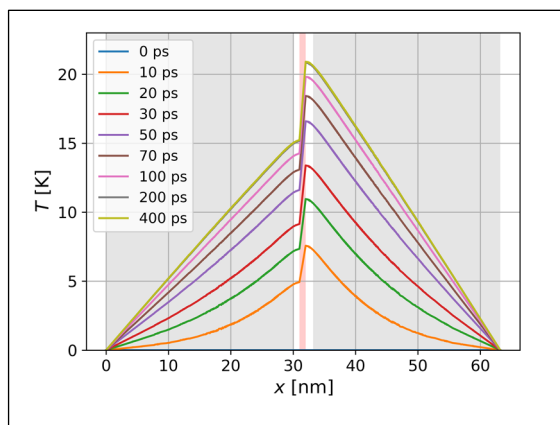


Fig.2: Temperature increase in the structure due to a current from right to left. The asymmetry in hot-electron heating causes an asymmetry in the temperature profile. The temperature saturates after 200ps. The voltage across the structure is 1V.

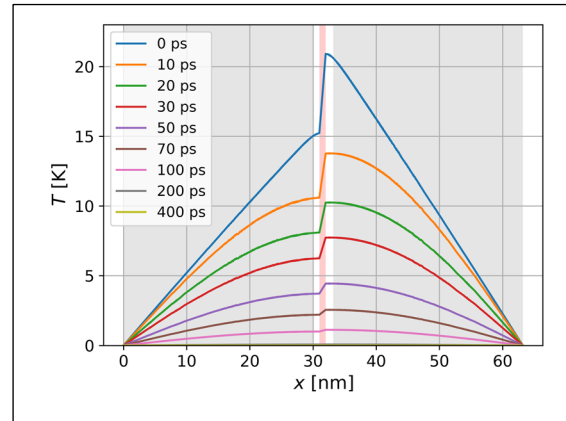


Fig.3: Fig.4: Temperature decrease of the structure after the voltage driven current pulse is switched off. The temperature relaxes after 200ps.

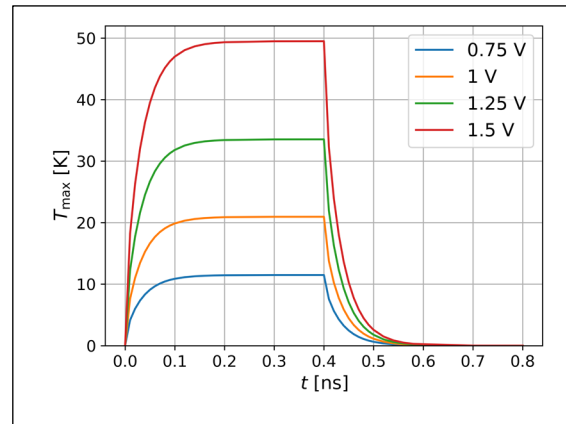


Fig.4: Maximum temperature T_{max} for different voltages U across the structure. Saturation of T_{max} is observed at 200ps. At 400ps the voltage is turned off and cooling is observed.

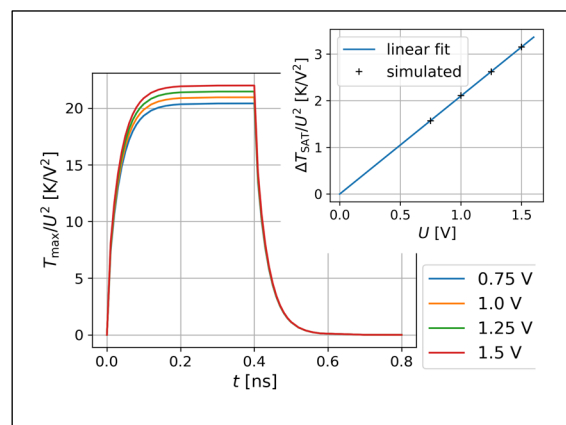


Fig.5: Heating-cooling cycle for different voltages from Fig.4 normalized to U^2 . Inset: ΔT_{SAT} as a function to the voltage U .

Spin Drift-Diffusion Approach for the Computation of Torques in Multi-Layered Structures

S. Fiorentini¹, J. Ender¹, R. Orio², S. Selberherr², W. Goes³, and V. Sverdlov¹

¹ *Christian Doppler Laboratory for Nonvolatile Magnetoresistive Memory and Logic at the*

² *Institute for Microelectronics, TU Wien, Gußhausstraße 27–29, A-1040 Wien, Austria*

³ *Silvaco Europe, Cambridge, United Kingdom*

fiorentini@iue.tuwien.ac.at

Nonvolatile magnetoresistive memories are an emerging solution for the typically increasing standby power consumption and leakages of shrunk CMOS devices. They possess high endurance and operation speed and have already been shown to be suitable for both SRAM and flash memory applications [1][2]. The design of novel devices for specific applications is nowadays supported by simulation tools.

We implemented a finite-element solver for computing the torques acting in magnetoresistive devices via the spin and charge drift-diffusion approach using the open source library MFEM [3]. The solver was tested against known analytical solutions [4] in order to confirm the accuracy of the results. The comparison for the spin accumulation is shown in Fig.1, while the torques are reported in Fig.2. Both show perfect agreement with the theoretical predictions. The angular dependence of the torque in a spin valve structure, with non-magnetic leads (NM) and a non-magnetic spacer layer between the magnetic free (FL) and reference (RL) layers, follows perfectly the shape predicted in a ballistic scenario in [5]. By using a long spin-flip length, the extracted value of the spin polarization parameter P coincides with the parameter $\beta_\sigma = 0.9$ entering the drift-diffusion equations (Fig.3). In systems with a lower spin-flip length, the extracted P reduces to a value of around 0.5, and the drift-diffusion approach allows to introduce dependences on other system parameters: The dependence on the diffusion coefficient in the NM layers is reported in Fig.4. Another advantage of the drift-diffusion approach is the straightforward possibility to compute the torques acting in all the ferromagnetic layers in realistic structures. In [6], the failure of writing of the cell at a high current density was linked to the destabilization of the RL. We investigated how the picture of the torques acting on the RL is modified in the presence of a pinned layer (PL) antiferromagnetically coupled to the RL. We show that, while writing the FL from parallel (P) to anti-parallel (AP) FL-RL configuration, the additional PL torque, initially stabilizing the RL along the $+x$ axis (Fig.5), also helps to reduce the torque destabilizing the RL at the end of switching (Fig.6). These findings suggest that the presence of the PL can help to prevent unwanted switching of the RL, but does not solve the issue completely. The computation of the torques acting in multi-layered structures and the understanding of their dependence on system parameters enables the efficient simulation of emerging magnetoresistive devices.

- [1] S.H. Han et al., Proc. IEDM, 215 (2020). [4] S. Zhang et al., Phys. Rev. Lett. 88, 236601 (2002).
 [2] V.B. Naik et al., Proc. IEDM, 219 (2020). [5] J.C. Slonczewski, J. Mag. Mat. 159, L1 (1996).
 [3] <https://mfem.org/> [6] C. Abert et al., Phys. Rev. App. 9, 054010 (2018).

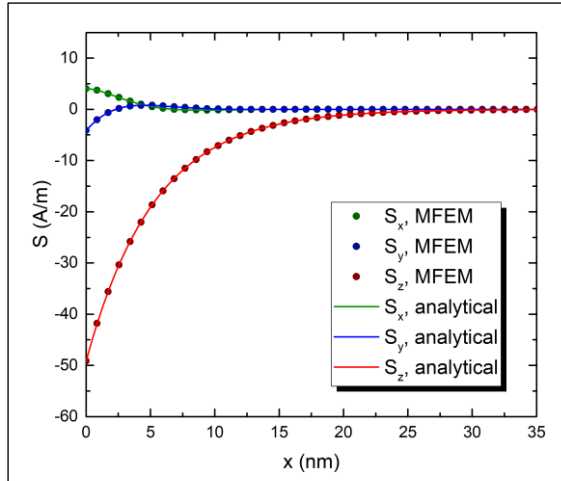


Fig.1: Comparison between the spin accumulation computed analytically (solid lines) and using our Finite Element solver (dots). The analytical solution is properly reproduced.

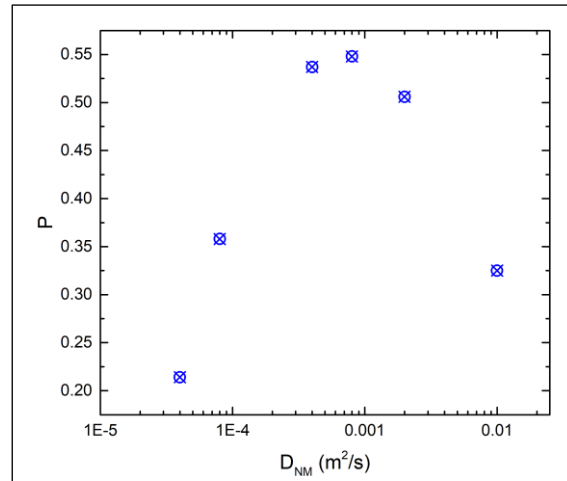


Fig.4: Dependence of the polarization parameter P , extracted from fitting the angular dependence of the torque, on the diffusion coefficient in the non-magnetic layers.

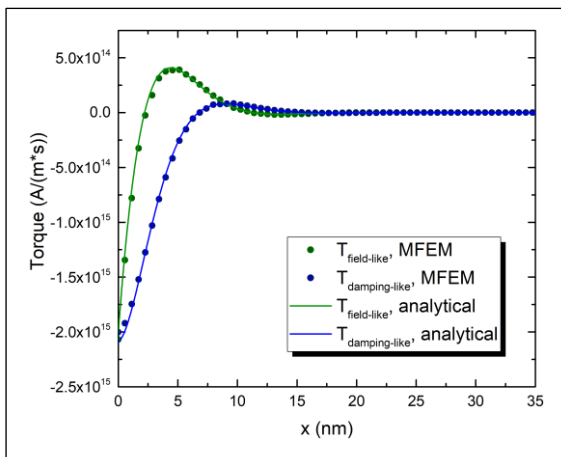


Fig.2: The torque computed using the numerical solution (dots) is in very good agreement with the theoretical one (solid lines).

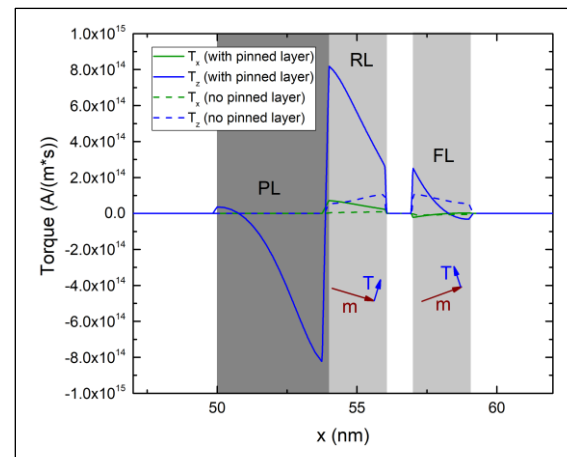


Fig.5: Damping-like torque in a multi-layered structure with quasi-parallel magnetization vectors in the FL and the RL. The solid lines are computed including PL, while the dashed lines do not include PL.

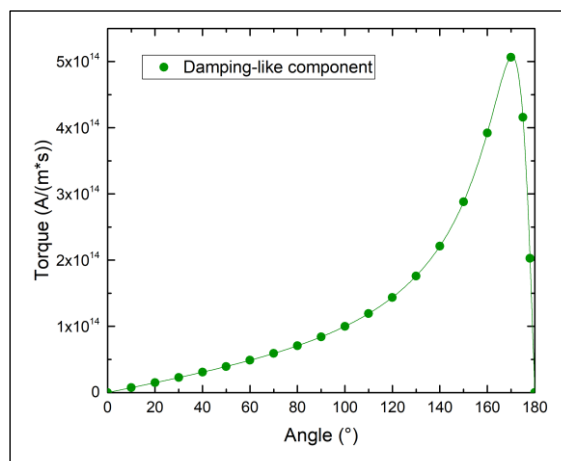


Fig.3: Angular dependence of the torque for a spin-flip length of 100 nm. The line represents a fit of the data with the equation reported in [5].

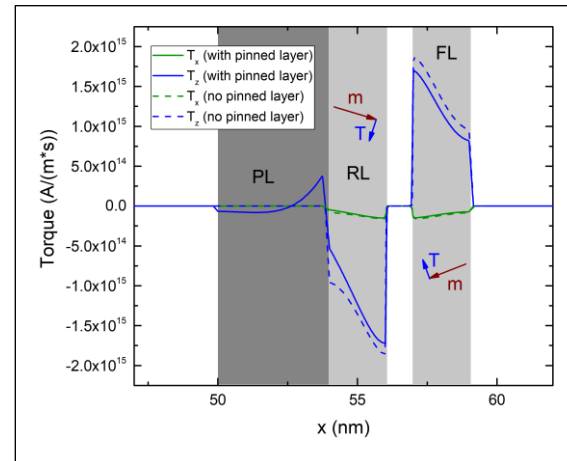


Fig.6: Damping-like torque in a multi-layered structure with quasi-antiparallel magnetization vectors in the FL and the RL. The solid lines are computed including PL, while the dashed lines do not include PL.

Improved Sampling Algorithms for Monte Carlo Device Simulation

Markus Kampl¹, Hans Kosina², and Michael Waltl¹

¹ CDL for Single-Defect Spectroscopy at the Institute for Microelectronics, TU Wien, Austria

² Institute for Microelectronics, TU Wien, Austria

kampl@iue.tuwien.ac.at

Monte Carlo (MC) is a widely used method to statistically estimate integrals and the solution of integral equations. In semiconductor physics, the method is often used to estimate the solution of the Boltzmann transport equation (BTE) [1] [2].

In stationary simulations, statistical averages can be obtained by the so-called before-scattering method. This method, however, becomes ineffective when applied to small devices where the mean-free-path is larger than the average size of the mesh cells. We present a new method which is better suited for small devices and which can even be applied in the quasi-ballistic transport regime.

Estimation of Non-Equilibrium Averages

Before scattering method - Trajectories are sampled before a scattering event takes place. The sample values are weighted with the reciprocal of total scattering rate $\Gamma(\vec{k})$ [1][4][5]. When the simulation domain is decomposed into Voronoi volumes V_j , averages of local attributes can be built for every discretization volume V_j separately [6][7].

Boundary method - Particle states are sampled whenever a particle crosses an interface between two Voronoi volumes. The sample values have to be weighted with the reciprocal of the velocity component perpendicular to the interface $|v_{\perp}(\vec{k})|$ [3]. The benefit of this method is that the number of sampling points now depends on the surface of a Voronoi box, and not on the volume. With mesh refinement the surface of a cell scales more favorably than the volume.

Combination of methods - The samples obtained by the before-scattering method and from the boundary method can be combined. This combination of samples gives a smaller statistical error than the ones of each method individually.

Generation of an Equilibrium Distribution

In a MC simulation, particles are injected at a contact from an equilibrium distribution. Especially in the backward MC method, one can employ different variants of a weighted equilibrium distribution. Here, two methods for generating such distributions in a full-band simulation are shown. To obtain an equilibrium distribution, the electric field is set to zero.

Box Method - A single-particle MC simulation is performed for a uniform semiconductor with a finite length in one dimension, the so-called box. Perfectly reflecting boundary conditions are assumed. Every time the carrier hits a boundary and gets reflected, its state is added to the sample. The distribution of the generated sample represents a velocity weighted Maxwellian distribution [3] $f_v(\vec{k}) = |v_{\perp}(\vec{k})| f(\vec{k})$ where $|v_{\perp}(\vec{k})|$ is the velocity component perpendicular to the boundary.

Bulk Method - A single-particle MC simulation is performed for a uniform semiconductor with no boundaries. In this case the trajectory is sampled before a scattering event occurs (*before scattering method*). The distribution of the generated sample is a Maxwellian weighted with the total scattering rate, $f_{\Gamma}(\vec{k}) = \Gamma(\vec{k}) f(\vec{k})$ [4][5].

Constant Time Step Method - Sampling the equilibrium trajectory with a constant time step yields the equilibrium distribution $f(\vec{k})$ directly.

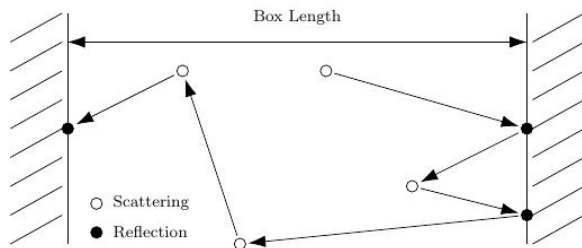


Fig. 1: Generating an equilibrium sample using the box method.

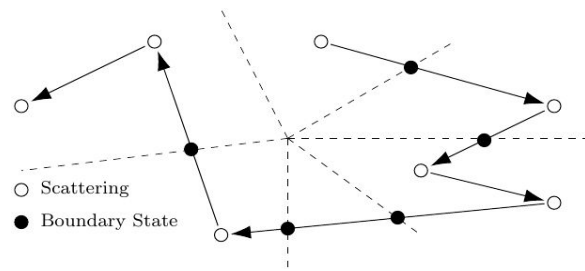


Fig. 2: Boundary and before-scattering method sampling in a device. The dashed lines are the boundaries between the Voronoi volumes.

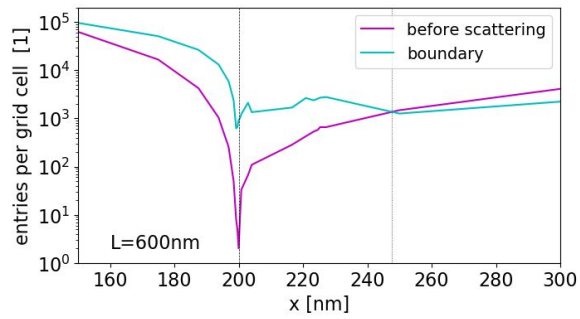
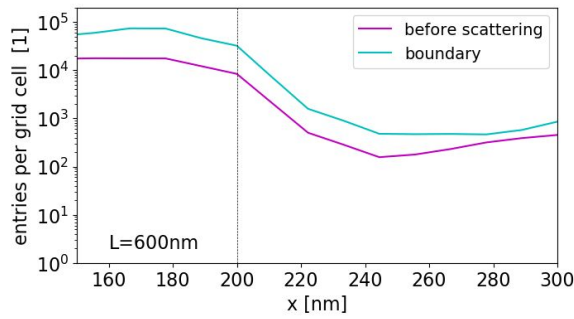


Fig. 3: Comparison of two different averaging methods in an silicon **600nm** $n^+n^-n^+$ diode with constant (a) and variable (b) grid size. Both images show the region around the n^+n^- junction at $200nm$.

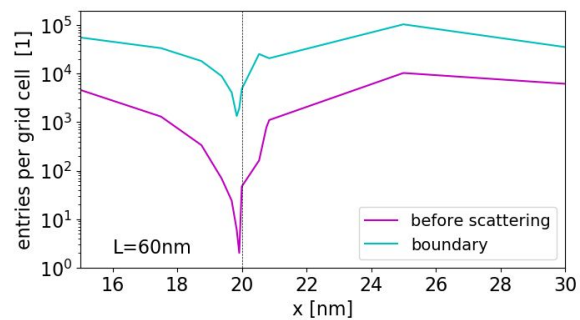
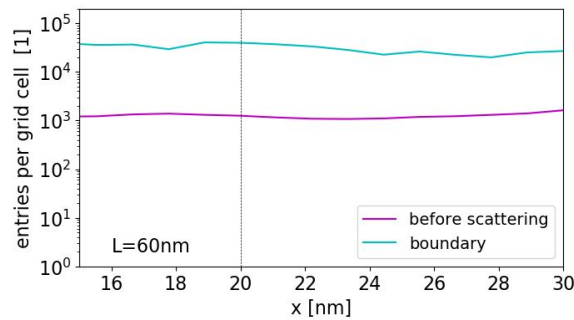


Fig. 4: Comparison of two different averaging methods in an silicon **60nm** $n^+n^-n^+$ diode with constant (a) and variable (b) grid size. Both images show the region around the n^+n^- junction at $20nm$. The box method yield a considerably higher number of sampling points and thus higher accuracy.

Acknowledgement: Financial support by the Austrian Federal Ministry for Digital and Economic Affairs, the National Foundation for Research, Technology and Development and the Christian Doppler Research Association is gratefully acknowledged.

[1] C. Jungemann et al., Springer, 2003
 [2] C. Jacoboni et al., Springer, 1989.
 [3] M. Lundstrom, Cambridge University Press, 2000.
 [4] C. Jacoboni et al., Rev. Mod. Phys.55, 1983.
 [5] H. Kosina, PhD thesis. Technische Universität Wien, 1992.
 [6] E. Sangiorgi et al., IEEE Transactions on Computer-Aided Design of Integrated Circuits and Systems, 1988.
 [7] M. Kampl, PhD thesis. Technische Universität Wien, 2019.

Scattering implementation in the quantum transport BITLLES simulator

Matteo Villani¹, Xavier Oriols¹

¹ *Universitat Autònoma de Barcelona, Bellaterra, Barcelona, Spain*

xavier.oriols@uab.es

Among the different implementations of scattering in the literature that allow to effectively account for the perturbation induced by the non-simulated degrees of freedom on the simulated ones, the direct implementation of the Fermi golden rule, developed to study transitions between an initially-prepared and a finally-measured pure state (see Fig. 1(a)), is the most simple and intuitive. However, describing pure state transitions inside the active region of a nanoelectronic device bears two important difficulties. First, open quantum systems cannot be represented in terms of pure states, except for Markovian processes. Second, in the transition from one pure state to another, some type of decoherent phenomena have to be added to break the unitary evolution of the system (See Fig 1(b)).

In this conference, we show that Bohmian conditional wave functions (CWFs) [1] allow a simple and rigorous way of implementing the Fermi golden rule transitions between pre- and post-selected pure states in open quantum systems both under Markovian or non-Markovian conditions [3] solving the two mentioned problems, as indicated in Fig.1(d). We discuss the practical application of the method for light-matter interaction, with emission/absorption of photons in double barrier structure of a Resonant Tunneling Device (RTD). As a practical discussion, we study Model A where the final CWF is post-selected by increasing/decreasing the initial energy of the pre-selected CWF (satisfying overall energy conservation), and Model B where such transition is done with the mean momentum increased/decreased. Such Model B is only valid for flat potential conditions where energy and momentum operators commute. For arbitrary potentials, as the double barrier considered here where energy and momentum do not commute, Model B leads to unphysical scattering processes without energy conservation (see fig. 2(b)). These unphysical features are clearly seen in the oscillatory behavior of the CWF in Fig. 3(c) when photon absorption is considered. On the contrary, Model A perfectly captures the physics of the absorption (and spontaneous emission not plotted) as seen in Fig. 3(b), which becomes relevant phenomena for high frequency (THz) quantum transport [5].

This scattering process between pre- and post-selected CWF, within Model A, provides the last ingredient for the BITLLES simulator [4] to become a general purpose, versatile and intuitive quantum transport simulator ready for the electronic industry.

[1] X. Oriols and J. Mompart, Jenny Stanford Publishing: Singapore, (2019)

[2] D. Pandey et al., *Entropy*, **21**, 12, 1148 (2019)

[3] M. Villani et al., *IEEE EDL*, **42**, 2, 224-227, (2021)

[4] The BITLLES simulator. Available online: <http://europe.uab.es/bitlles>.

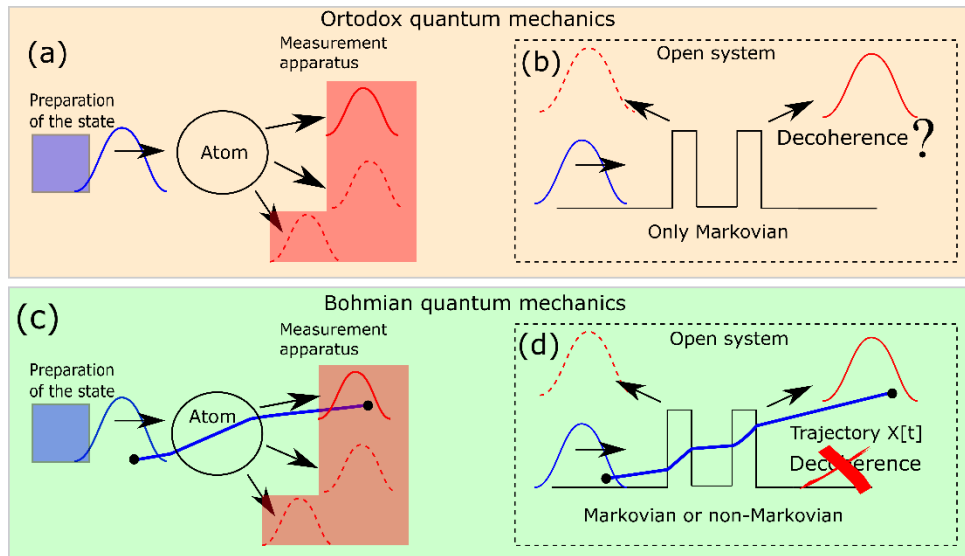


Figure 1: Schematic representation of the Fermi Golden rule from orthodox quantum mechanics in (a) and (b), and from Bohmian quantum theory in (c) and (d). The preparation and measurements of pure states in closed system, (a) and (c), is unproblematic, while in open system is problematic in (b) with pure states, but not in (d) with conditional wave functions.

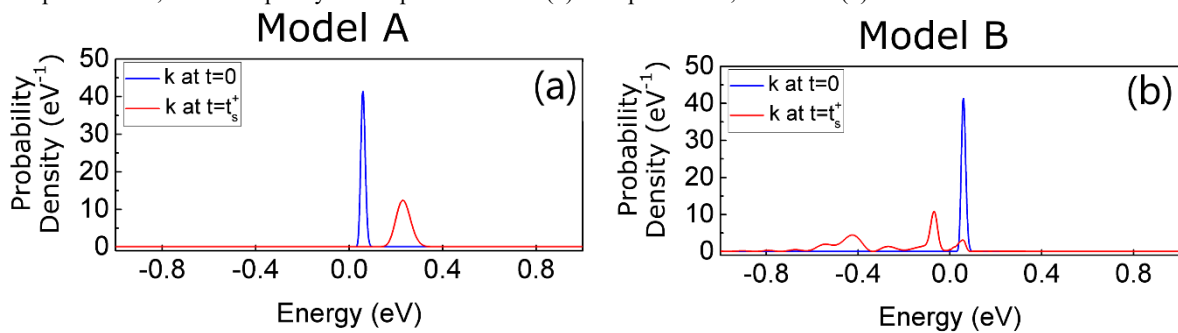


Figure 2: Evolution of the probability density of the CWF components due to photon absorption with Model A in (a) and Model B in (b). Blue lines denote the probability distribution before the scattering, while red lines after it.

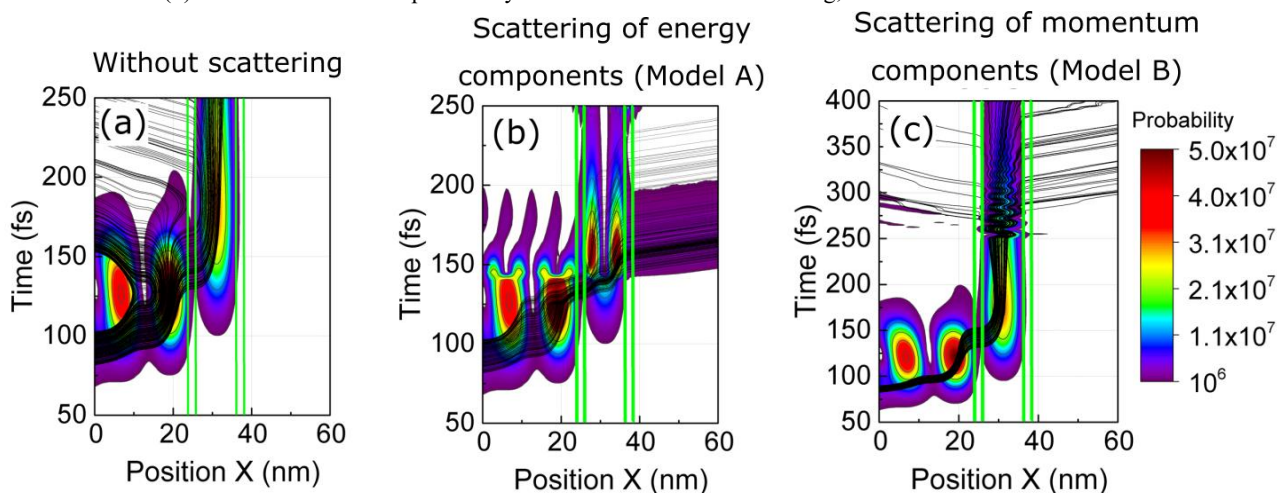


Figure 3: Evolution of the CWF and the Bohmian trajectories $X[t]$ in space and time. (a) without photon absorption, (b) with photon absorption using model A, (c) with photon absorption using model B. In (b) the CWF transition from the first to the second resonant level of the quantum well is clearly seen (Model A), while in (c), unphysical oscillations appear (Model B).

How to preserve the Kramers-Kronig relation in inelastic atomistic quantum transport calculations

Daniel Lemus¹, James Charles¹, Tillmann Kubis^{1,2,3,4}

¹*School of Electrical and Computer Engineering, Purdue University, W. Lafayette, IN, USA*

²*Network for Computational Nanotechnology, Purdue University, W. Lafayette, IN, USA*

³*Purdue Center for Predictive Materials and Devices, W. Lafayette, IN, USA*

⁴*Purdue Institute of Inflammation, Immunology and Infectious Disease, W. Lafayette, IN, USA*

dlemus@purdue.edu

The nonequilibrium Green's function method (NEGF) is often used to predict quantum transport in atomically resolved nanodevices. This yields a high numerical load when inelastic scattering is included. Atomistic NEGF had been regularly applied on nanodevices, such as nanotransistors. However, incoherent scattering is still subject to significant approximation. A very common approximation to scattering is to neglect the real part of the retarded scattering self-energies, which fundamentally violates the causality relation. Neglecting that real part is known to alter electronic energies, which in turn impacts transistor I-V characteristics [1,2]. In this work, [3] the atomistic mode space approach of Mil'nikov et al. [4] is extended by including the exact calculation of the real part of retarded scattering self-energies in the reduced basis representation using the Kramers–Kronig relation. The real part of the retarded scattering self-energy, $\Sigma(\mathbf{r}, \mathbf{r}', E)_{i,j,real}^R = \mathcal{H}(\Sigma(\mathbf{r}, \mathbf{r}', E)_{i,j,imag}^R)$, is solved with a Hilbert transform of each matrix element i, j of the imaginary part of Σ for all energies E . Performing this calculation in a typical atomistic basis such as tight binding is prohibitively numerically expensive [2]. However, the mode space basis reduction reduces the numerical load to under 1% of the operations in the original basis which effectively enables scattered atomistic NEGF on nanodevices without losing the predictive power of NEGF. All atomistic quantum transport simulations in this work utilize NEMO5 and Victory Atomistic and include deformation potential scattering on acoustic and optical phonons, as well as Fröhlich scattering on polar optical phonons. The non-local nature of polar optical phonon scattering is included using a cross-section-dependent compensation factor [5]. The impact of the real part of the retarded scattering self-energies is exemplified on atomically resolved InAs nanowire tunneling field effect transistors. Depending on the device physics, the real part of retarded self-energies alters the transistor performance, increasing the OFF and decreasing the ON current.

[1] J. Charles et al., *J. Comput. Electron.*, **15** (2016).

[2] A. Esposito, et al. *J. Comput. Electron.*, **8**, (2009).

[3] D. A. Lemus et al., *J. Comput. Electron.*, **19**, (2020).

[4] G. Mil'nikov, et al., *Phys. Rev. B*, **85**, 035317, (2012).

[5] P. Sarangapani, et al., *Phys. Rev. Appl.*, **12**, 044045, (2019).

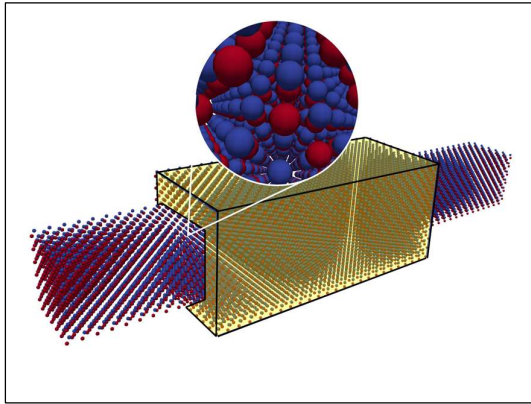


Fig.1: $3.64 \text{ nm} \times 3.64 \text{ nm} \times 30.29 \text{ nm}$ InAs TFET device with a 1 nm gate oxide layer surrounding the center of the device (in yellow), used in all calculations in this work.

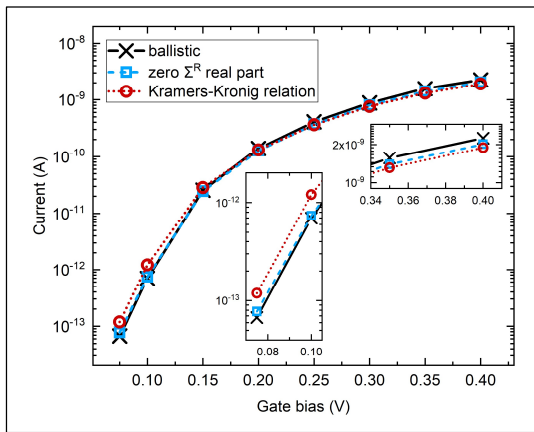


Fig.2: I - V characteristics for a $2.42 \text{ nm} \times 2.42 \text{ nm} \times 30.29 \text{ nm}$ InAs TFET device solved in NEGF including incoherent scattering on polar optical phonons, acoustic phonons and optical deformation potential phonons. Scattering, even without a real part of Σ^R , increases the off-current densities and lowers on-current densities. When the real part of the retarded self-energy Σ^R is included, the Kramers-Kronig relations are obeyed and scattering shows an even larger impact. The insets zoom into the first two and the last two points of the curves.

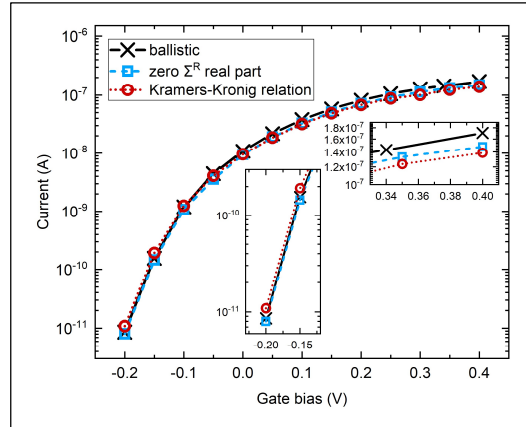


Fig.3: I - V characteristics of a $3.64 \text{ nm} \times 3.64 \text{ nm} \times 30.29 \text{ nm}$ InAs TFET device, comparing the same ballistic and scattering configurations of Fig. 2. Scattering has a greater effect on the ON state for this device geometry, in particular when the real part of the retarded self-energy Σ^R is included.

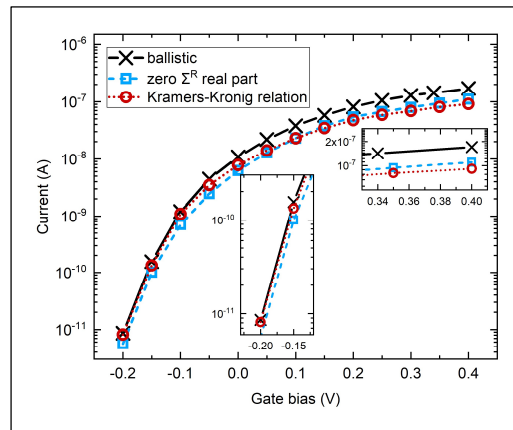


Fig.4: Similar to Fig. 3, the I - V characteristics of $3.64 \text{ nm} \times 3.64 \text{ nm} \times 30.29 \text{ nm}$ InAs TFET device, but with the scattering strength multiplied by 10. The inclusion of the real part of the retarded self-energy Σ^R in cases with higher scattering strength is shown to have a significant effect on device performance and must therefore be included.

Efficient Machine-learning-based Optimization of 3-nm Node Nanosheet FETs

Bokyeom Kim¹, and Mincheol Shin¹

¹ *School of Electrical Engineering, Korea Advanced Institute of Science and Technology, Daejeon, 34141, South Korea*
mshin@kaist.ac.kr

Advanced nanoscale metal-oxide-semiconductor field-effect transistors (MOSFETs) exhibit short-channel effects (SCE), quantum mechanical effects (QME), and self-heating effects (SHE), which means that design of them requires complex modeling and analysis. Recently, several works have employed machine-learning (ML) techniques and data-intensive neural networks (NN) to model the complex relationships and optimize devices [1]. The Bayesian optimization (BO) has been adopted to realize ML-based data-efficient optimization of MOSFET device, as it requires only a small number of training data in finding the global optimum. However, the previous works used a preset number of iterations (ex. 100 iterations) for the stopping condition [2], which deteriorates efficiency and reliability of BO. Therefore, an effective stopping condition (ESC) which enhances efficiency and reliability of BO needs to be explored. In this work, we constructed a ML-based MOSFET optimization framework (Fig. 1) and investigated ESC by using 2,800 single-gate n-type MOSFETs simulation data (Fig. 2). The data consist of subthreshold swing (SS) and ON-state current with 5-dimensional device specifications. We utilized the maximum expected improvement (EI_{\max}) scheme to explore the ESC [3] and stopped BO when EI_{\max} are less than 1% of unit value. Our ESC greatly increases the efficiency of BO since it reduces training data up to 87.6% compared to the previous works (Figs. 3(a)-(c)). Our scheme is reliable since the global optimum can be reached before stopping (Figs. 3(d)-(f)). As an application of our ESC scheme to a practical problem, we have optimized a 3-nm node nanosheet (NS) FET in a 5D design space considering QME, SCE, and SHE using a 3D TCAD simulator (Fig. 4). RC delay, SS, and ON-state maximum temperature were minimized by multi-objective optimization which required small number of training data (<100). Our ML-based optimized 3-nm NSFET exhibits superior performance (22% faster) than human-based optimized one [4] (Fig. 5).

Acknowledgement: The EDA tool was supported by the IC Design Education Center (IDEC), Korea.

[1] MH. Oh et al., IEEE Electron Device Lett. 41, 1548-1551 (2020)

[2] W. Lyu et al. PMLR, vol. 80, pp. 3306-3314 (2018)

[3] V. Nguyen et al. PMLR, vol.77 pp. 279-294 (2017)

[4] H. Kim et al. IEEE Trans. Electron. Devices. 67, 1537-1541 (2020)

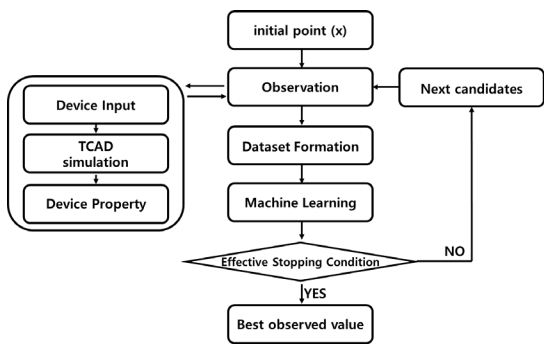


Fig. 1. ML-based MOSFET optimization framework

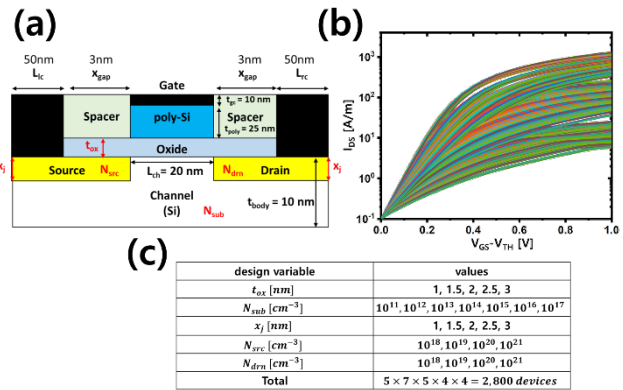


Fig. 2. (a) Device schematics, (b) I-V characteristics, and (c) 5D design space for 2800 single-gate n-type MOSFETs

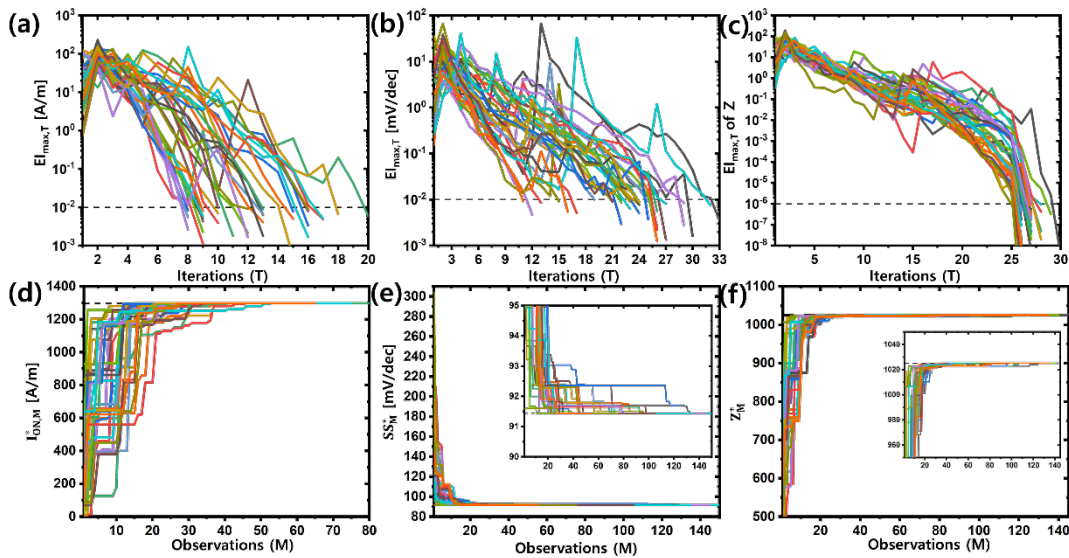


Fig. 3. Efficiency and robustness of ESC scheme. $E_{I_{max,T}}$ at T iteration for the cases of (a) ON-state current (I_{ON}), (b) SS, and (c) multi-objective function Z are drawn. 12.4, 23.1, and 27.4 iterations were required for optimization on average. The best value at M observation for (d) I_{ON} , (e) SS, and (f) Z are depicted. 34 different sampling seeds were used and every simulation converged to the global optimum.

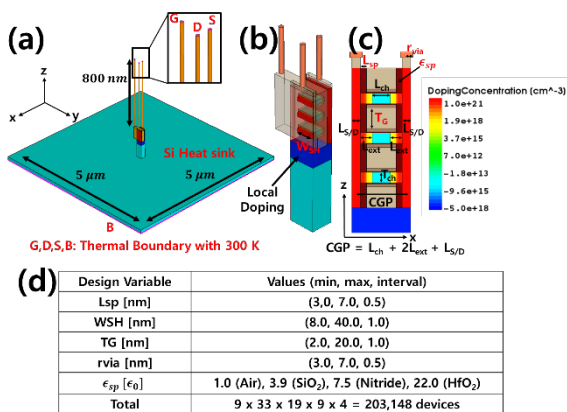


Fig. 4. (a) 3D NSFET structure with the thermal boundaries, (b) enlarged device region, (c) x-z plane view at $y = 0$, (d) 5D design space

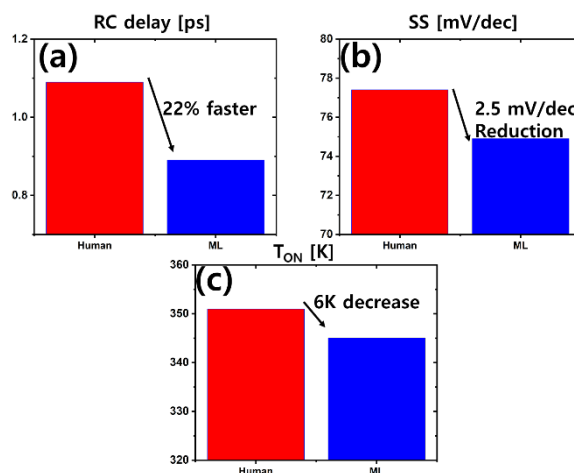


Fig. 5. A comparison between human-based [4] and ML-based optimization. The ML-based optimized device exhibits 22% faster speed, 2.5 mV/dec smaller SS, and 6K lower ON-state temperature than human-based optimized device.

Deep Learning-Supported Gate-Structure Design for a High Performance Graphene FET

Gyeong Min Seo, and Byoung Don Kong

Department of Electrical Engineering, Pohang University of Science and Technology

(POSTECH), Pohang 37673, Republic of Korea

seogm@postech.ac.kr

Graphene field effect transistors (GFETs) are a promising candidate for high-speed radiofrequency (RF) devices due to its high carrier mobilities. However, due to graphene's zero bandgap, the drain current saturation in GFETs that requires a depletion region is not formed. To induce the drain current saturation without opening the bandgap, graphene pseudo optics at p-n junctions, a concept of utilizing the inherent massless Dirac fermion property, was proposed [1]. In this approach, a trapezoidal gate (Fig.1a), designed to reflect the ballistic electrons and suppress Klein tunneling, plays the role of the energy bandgap and a depletion region. Fig.1b represents the saturated drain current of GFET with the trapezoidal gate.

Conventional inverse design method is an iterative optimization. For a defined gate structure of GFET, Id-Vd curve can be calculated by substituting transmission coefficient obtained from graphene finite-difference-time-domain simulation [2] into Landauer equation. The calculated Id-Vd curve is compared to the desired Id-Vd curve, and a little structure change can be applied. This iterative method is time consuming and requires exhaustive numerical simulation for every iteration. In contrast to the iterative optimization approach, deep learning (DL) and deep neural network (DNN) approach is not only able to predict the graphene pseudo-optic response of a specific gate structure of GFET, but is also able to handle the inverse design, providing an optimized gate structure for a targeted graphene pseudo-optic response.

Here, by utilizing the power of deep learning (DL), we report the possibility of discovering a novel design of the gate that maximizes cutoff frequency of GFET. Fig.2 illustrates a tandem architecture [3] for inverse design. A DNN was trained to discover the relation between the gate structure and the graphene pseudo-optics, and to design an optimized gate structure for an improved RF performance. Fig.3 represents a gate structure designed by the DNN and the saturated Id-Vd curve by the DNN-supported gate structure. To conclude, our study suggests that the RF performance of GFETs can be improved by a DNN-supported inverse design. Furthermore, the DNN-supported inverse design can be extended to a different design goal such as maximizing the on/off ratio for a logic device.

[1] Tan, Y et al., *Sci. Rep.* **7**, 9714 (2017)

[2] M.S. Jang et al., *Appl. Phys. Lett.* **97**, 043504 (2010)

[3] D. Liu et al., *ACS photonics.* **5**, 1365 (2018)

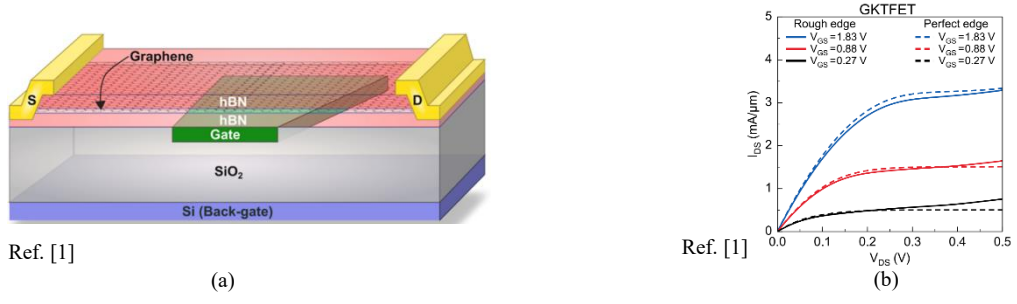


Fig. 1: (a) A trapezoidal gate designed to reflect the ballistic electrons and suppress Klein tunneling. (b) The saturated drain current of GFET with the trapezoidal gate.

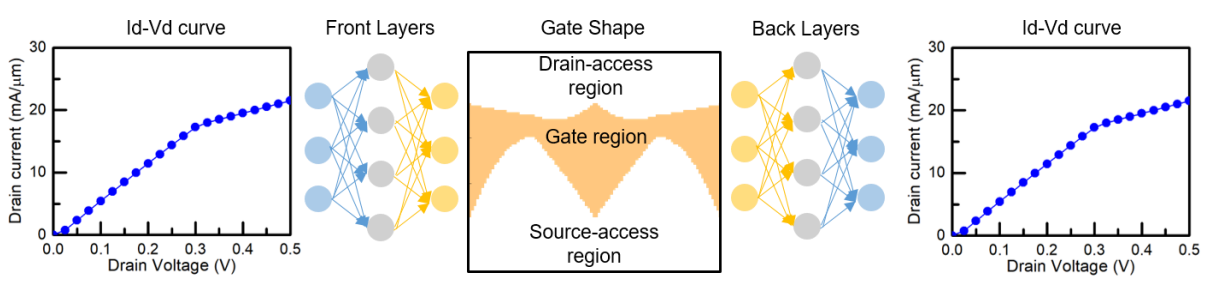


Fig. 2: A tandem architecture for inverse design of gate structure of GFET. Back layers were trained at first, and then front layers would be trained with fixed weights of back layers. After training, DNN of front layers designed an optimized gate structure corresponding to the desired Id-Vd curve.

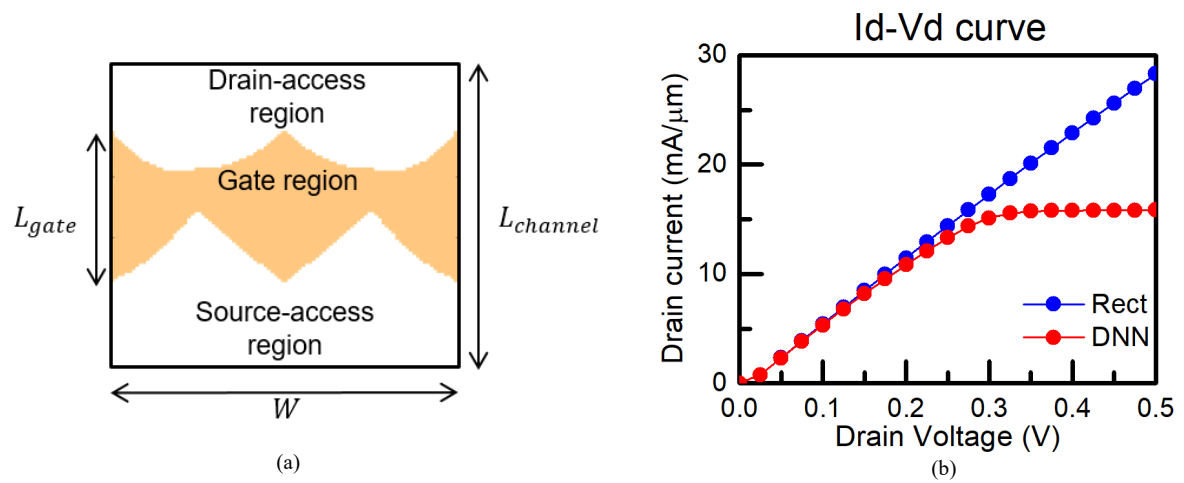


Fig. 3: (a) A DNN-designed gate structure. (b) Id-Vd curve of conventional (rectangular gate) GFET (blue line) and GFET with DNN-designed gate structure (red line).

Parameters:

$V_{top} = 0.1V, V_{bottom} = 50V$, top dielectric: $HfO_2(5nm)$, bottom dielectric: $SiO_2(90nm)$, $L_{channel} = 1\mu m, L_{gate} = 0.5\mu m, W = 1\mu m$

Simulation of ballistic spin-MOSFET devices with ferromagnetic channels

Patrizio Graziosi^{1,2*}, Neophytos Neophytou²

¹ *CNR—ISMN, v. Gobetti 101, 40129, Bologna, Italy*

² *School of Engineering, University of Warwick, Coventry CV4 7AL, United Kingdom*

**Patrizio.Graziosi@gmail.com*

Newly emerged materials from the family of Heusler alloys and complex oxides exhibit finite bandgaps and ferromagnetic behavior with Curie temperatures much higher than room temperature. In this work, using the semiclassical top-of-the-barrier FET model [1], and a spin dependent contact resistance model derived from [2] (Fig. 2), we explore the operation of a spin-MOSFET that utilizes such ferromagnetic semiconductors as channel materials, in addition to ferromagnetic source/drain contacts (Fig. 1) [3]. Such a device could retain the spin polarization of injected electrons, the loss of which limits the operation of traditional spin transistors with non-ferromagnetic channels, such as Si-spin MOSFETs [4].

We examine the operation of four material systems that are currently considered as some of the most prominent known ferromagnetic semiconductors, three Heusler-type alloys (Mn_2CoAl , CrVZrAl , CoVZrAl) and one from the oxide family (NiFe_2O_4) [5]. Importantly, a ferromagnetic semiconductor Heusler alloy has been recently verified [6]. We describe the band structures by using data from DFT calculations, but also consider the effect of 2D confinement in the bands. We investigate under which conditions high spin polarization and significant $I_{\text{ON}}/I_{\text{OFF}}$ ratio, two essential requirements for the spin-MOSFET operation, are both achieved. We show that these particular Heusler channels, in their bulk form, do not have adequate bandgap to provide high $I_{\text{ON}}/I_{\text{OFF}}$ ratios, and have small magneto-conductance compared to state-of-the-art devices (Fig. 3). However, with confinement into ultra-narrow sizes down to a few nanometers, and by engineering their spin dependent contact resistances, the proposed geometry can reach 10^3 $I_{\text{ON}}/I_{\text{OFF}}$ ratio and MR of tens of percentage units (Fig. 3-6). Thus, they could prove promising channel materials for the realization of spin-MOSFET transistor devices that offer combined logic and memory functionalities [3, 4]. Although the main compounds of interest in this paper are Mn_2CoAl , CrVZrAl , CoVZrAl , and NiFe_2O_4 alone, we expect that the insight we provide is relevant to other classes of such materials as well.

[1] A. Rahman et al., IEEE Trans. Electron Devices 50, 1853 (2003). [2] T. Valet and A. Fert, Phys. Rev. B 48, 7099 (1993). [3] T. Marukame et al., International Electron Devices Meeting (IEDM) 2009, pp. 1–4. [4] M. Ishikawa et al., J. Magn. Soc. Jpn. 44, 56 (2020). [5] P. Graziosi and N. Neophytou, J. Appl. Phys. 123, 084503 (2018). [6] G. M. Stephen et al., J. Appl. Phys. 125, 123903 (2019).

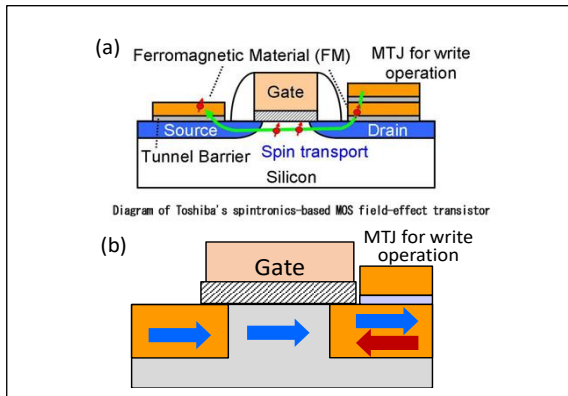


Fig. 1: Device schematic of (a) the traditional spin MOSFET concept presented in [3], and the proposed geometry where the channel is composed of a ferromagnetic semiconductor to retain the spin polarization (SP). The arrows indicate the magnetization direction. The drain magnetization can be switched (blue to red and reversely).

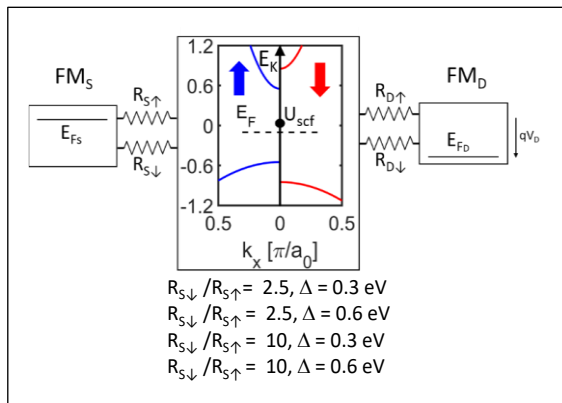


Fig. 2: The spin-MOSFET model with spin dependent series resistances introduced for the majority and minority spin carriers at the source/drain contacts. The studied values for the ratio of the majority and minority spin resistances are indicated, with the $R_{\uparrow} = 10^5 \Omega$. The device is symmetric so that the resistances at source and drain have the same values.

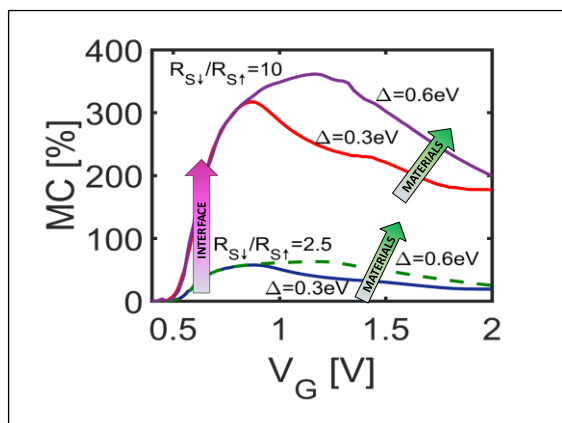


Fig. 3: The magnetoconductance (MC) percentage as a function of V_G for $V_D = 0.75 V$ for some parameter combinations as indicated, which shows separately the effect of the spin sub-bands separation Δ and $R_{\uparrow}/R_{\downarrow}$ on the MC. The arrows indicate the directions of improvement by engineering the material for Δ or the interfaces for the contact resistances.

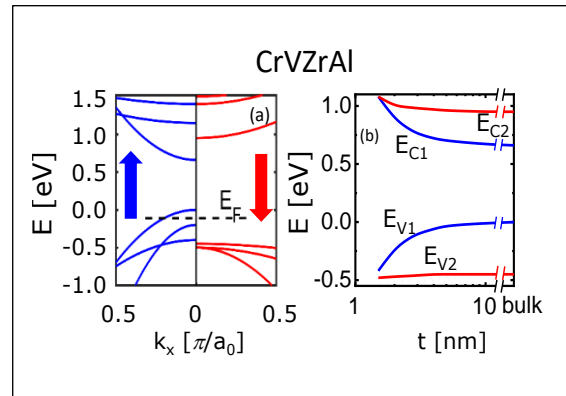


Fig. 4: Quantum confinement on the band structure in the Heusler alloy CrVZrAl (a) and shift of the band edges with confinement (b) using parabolic approximation (solid lines) or numerical bands, courtesy of M. Tas, (dashed lines). $E_{C1,2}$, $E_{V1,2}$ are the majority and minority conduction and valence bands edges, respectively.

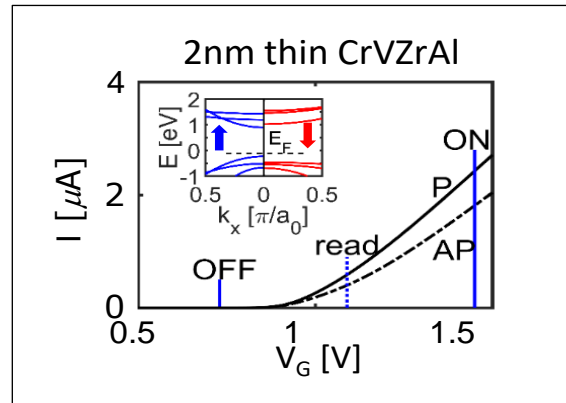


Fig. 5: I_D-V_G for a 2 nm narrow CrVZrAl Heusler alloy channel with parallel (P) and anti-parallel (AP) configurations, solid and dashed-dotted lines, respectively. The vertical solid blue lines show V_G^{OFF} and V_G^{ON} for which a $\sim 10^3 I_{ON}/I_{OFF}$ ratio is achieved at a bias window $V_G = V_D = 0.75 V$ for both magnetic configurations. The vertical dotted blue line represents the “read” gate bias V_G^{read} for memory operation.

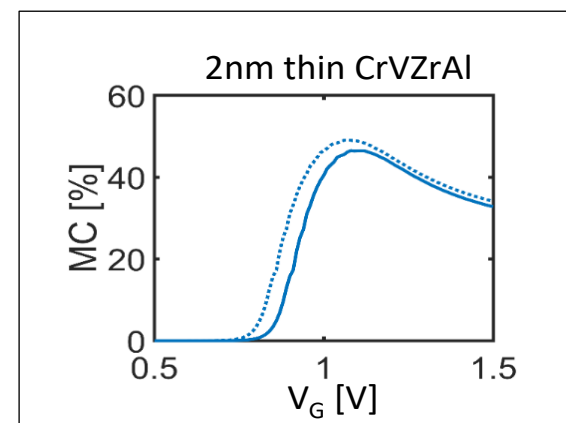


Fig. 6: MC versus V_G for the case reported in Fig. 5. The dotted line represents the MC when considering non-parabolicity effects, which increase the MC while the I_D-V_G is only slightly affected.

Modeling Dark Current in Vertically Stacked Amorphous Selenium Based Photodetectors

Le Ho¹, Atreyo Mukherjee¹, Dragica Vasileska²,

Richard Akis³, and Amir H. Goldan³

¹ Department of Electrical Engineering, Stony Brook University, NY, US

² School of Electrical, Computer and Energy Engineering, Arizona State University, AZ, US

³ Department of Radiology, School of Medicine, Stony Brook University, NY, US

le.ho@stonybrook.edu

Understanding of the transport characteristics and physical principles of blocking layers, including ways to control electrical hot spots, and thereby the breakdown voltage, is key to improving the performance of avalanche amorphous selenium (*a*-Se) devices. As a first step, technology for computer-aided design (TCAD) simulations are employed to identify relevant current carrying mechanisms in *a*-Se based detectors, which use a mixture of parameters obtained from experimental data, and in-house bulk Monte Carlo (MC) simulation. Based on the similarity in terms of hopping transport via localized states between disordered organic solids (molecularly doped polymers) and chalcogenide glasses (*a*-Se and As₂Se₃), [1] the bulk defect density of states (DDOS) distribution, and organic models such as the Poole-Frenkel mobility model (PFMOB) and the Langevin recombination, were used. The PFMOB is fitted with the measured field-dependent mobilities (**ref. Fig.1**). [2] We performed a calibration of the *a*-Se DDOS distribution (**ref. Fig.2**) by fitting the dark current density (J_D) in a Au/*a*-Se/Au structure with the measured values at low fields from Johanson, [3] and at high fields from Pfister (**ref Fig.3**). [4] At avalanche fields, when holes in *a*-Se undergo impact ionization, our simulations use Selberherr's impact ionization model with parameters obtained from the in-house MC simulations (**ref Fig.4**). [5] The simulated intrinsic *a*-Se layer (*i*-layer) is then used as a foundation for vertically stacked *a*-Se based photodiodes, with an *n*-like hole blocking layer (HBL) and a *p*-like electron blocking layer (EBL). Next, a structure with solution-processed quantum dot CeO₂ HBL and As₂Se₃ EBL is simulated. To validate, we compare our simulation result with the measured J_D in the *p-i-n* structure (**ref. Fig.5**). [6]

[1] G. Pfister et al., Adv. Phys., **27**, 747-798 (1978).

[2] G. Juska et al., Phys. Stat. Sol. (a), **59**, 389 (1980).

[3] R. E. Johanson et al., J. Non-Cryst. Solids, **227**, 1359-1362 (1998).

[4] G. Pfister et al., Phys. Rev. B, **6**, 3012 (1972).

[5] A. Mukherjee et al., J. Appl. Phys., **124**, 235102 (2018).

[6] H. Kannan et al., ACS Photon., **7**, 1367-1374 (2020).

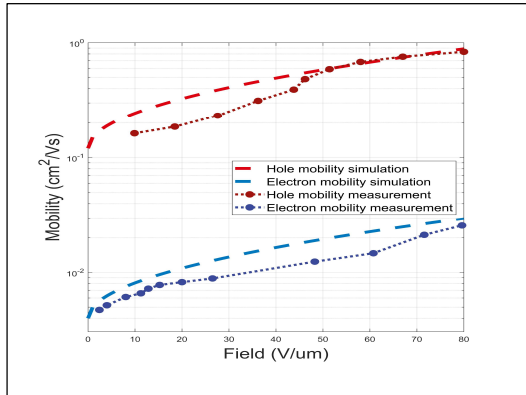


Fig.1: Mobility in a-Se using PFMOB compared with measured field dependent mobility from Juska et al. [1].

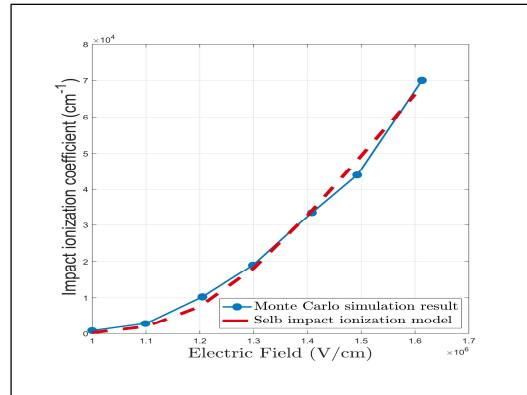


Fig.4: Field dependent impact ionization coefficients calculated from Selberr's impact ionization model, and from Monte-Carlo simulation.[5]

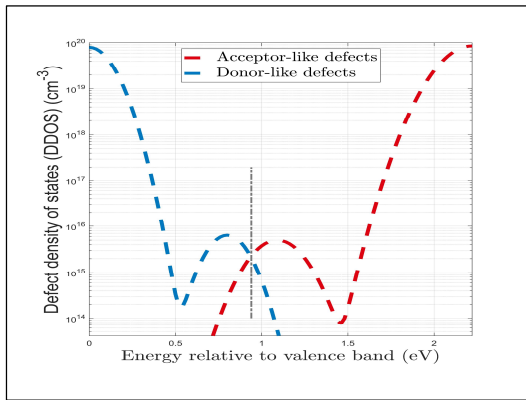


Fig.2: The donor and acceptor defect density of states distribution in the a-Se forbidden band gap.

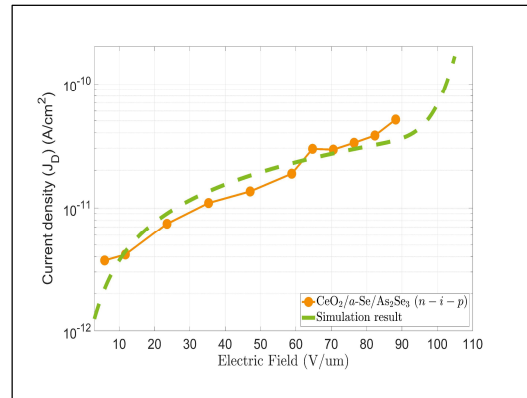


Fig.5: Dark current density as a function of electric field in p-i-n a-Se based avalanche structure with CeO₂ HBL and As₂Se₃ EBL from the simulation as compared to that from Kannan et al.[6].

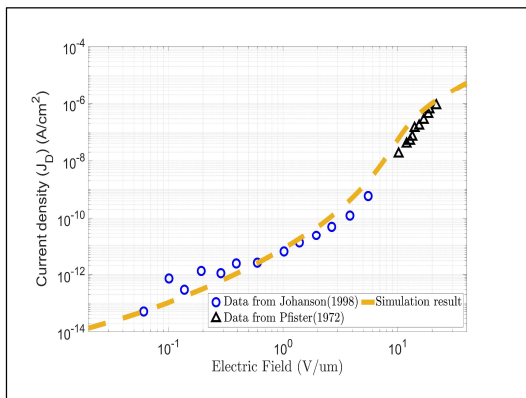


Fig.3: Dark current density as a function of electric field in Au/a-Se/Au structure. The circles are measurements at low fields from Johanson et al. [3] while triangles are measurements at high fields from Pfister et al. [4].

Effective Monte Carlo Simulator of Hole Transport in SiGe alloys

Caroline S. Soares¹, Alan C. J. Rossetto², Dragica Vasileska³, and Gilson I. Wirth¹

¹ *Programa de Pós-Graduação em Microeletrônica, Universidade Federal do Rio Grande do Sul, Porto Alegre, Brazil.*

² *Centro de Desenvolvimento Tecnológico, Universidade Federal de Pelotas, Pelotas, Brazil.*

³ *School of Electrical, Computer and Engineering, Arizona State University, Tempe, USA.*

santos.soares@ufrgs.br

It has been found that, with respect to the Negative Bias Temperature Instability (NBTI) effect, p-type silicon-germanium transistors have greater reliability than conventional p-type silicon devices [1]. It has also been shown that holes have higher mobility in SiGe alloys compared to pure silicon [2]. Because of that, it is expected that silicon-germanium alloys will replace pure silicon in the active channel region of the transistor. In this work, an Ensemble Monte Carlo (EMC) transport simulator is presented for simulation of hole transport in SiGe alloys.

In our theoretical model, to simulate the dynamics of holes in the SiGe alloys, the scattering mechanisms due to lattice vibrations [3] and alloy disorder [4], and an effective mass description are used. The nonparabolicity and the warping effect of the heavy-hole and light-hole bands were considered in their dispersion relation [5], while the split-off band was described as parabolic and spherical. The parameters of the dispersion relation were extracted by fitting the expression to the band structure calculated by the Empirical Pseudopotential Method.

The mobility of holes for a range of SiGe alloys was calculated at 300K at low electric field. The simulation mobility results agree well with the experimental data and with a more computationally expensive theoretical model [7] (Fig. 1). The profile of the mobility curve vs. Ge content suggests that the effect of each scattering mechanism on the mobility depends on the Ge content. The high occupancy of the heavy-hole band in high Ge content alloys (Fig. 2) suggests that for high Ge content the interband scattering is reduced. For high Ge content, the intraband alloy disorder scattering rate in the heavy-hole band is lower than for low Ge content (Fig. 3). For holes in the heavy-hole band with energy higher than the thermal energy at 300K, the phonon intraband scattering rates decreases as the Ge content increase (Fig. 4).

[1] J. Franco, et al. *Microelectronic Engineering*, 88, 7, 1388–1391 (2011).

[2] S. Kasap and P. Capper. Springer, (2006)

[3] C. Jacoboni and P. Lugli, Springer. (1989).

[4] C. Hamaguchi. New York: Springer (2001).

[5] Rodríguez-bolívar, F. M. Gómez-campos and J. Carceller. *Semiconductor Science and Technology*, 20, 1, 16-22, (2004)

[6] G. Busch and O. Vogt. *Helvetica Physica Acta*. 33. 437-458 (1960)

[7] M. V. Fischetti and S. E. Laux, *Journal of Applied Physics*, 80, 4, 2234-2252. (1996).

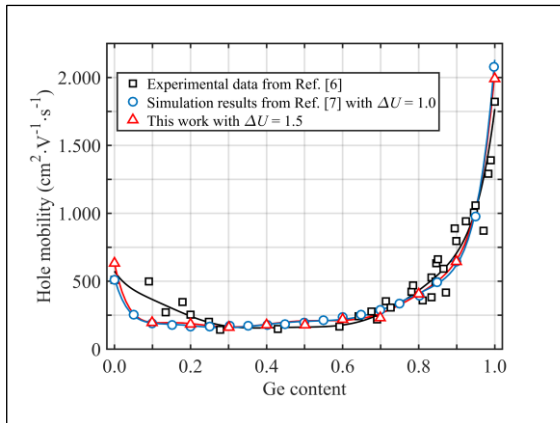


Fig.1: Comparison of the hole mobility in $Si_{1-x}Ge_x$ alloys versus germanium content. The alloy scattering potential used in the in-house simulator is equal to 1.5. The interpolated lines are a guide to the eye.

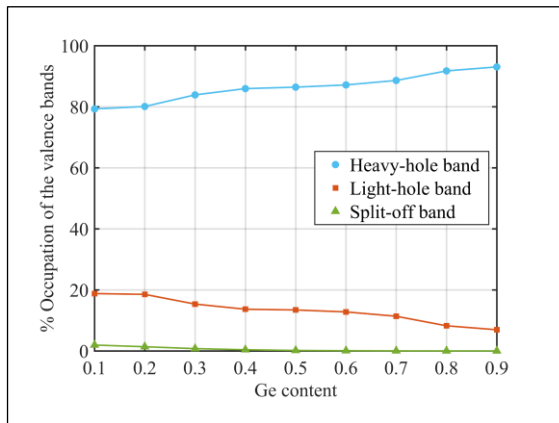


Fig.2: Occupation of heavy-hole band, light-hole band and split-off band versus Ge content. The lines are guide to the eye. This suggests that the interband scattering is reduced as the Ge content increases.

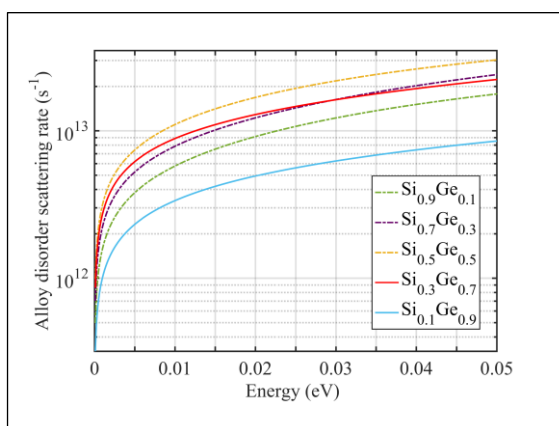


Fig.3: Alloy disorder scattering rate of $Si_{0.9}Ge_{0.1}$, $Si_{0.7}Ge_{0.3}$, $Si_{0.5}Ge_{0.5}$, $Si_{0.3}Ge_{0.7}$ and $Si_{0.1}Ge_{0.9}$. The alloy disorder scattering rates reaches its maximum value for $Si_{0.5}Ge_{0.5}$ and then decreases to reach its minimum value for $Si_{0.1}Ge_{0.9}$.

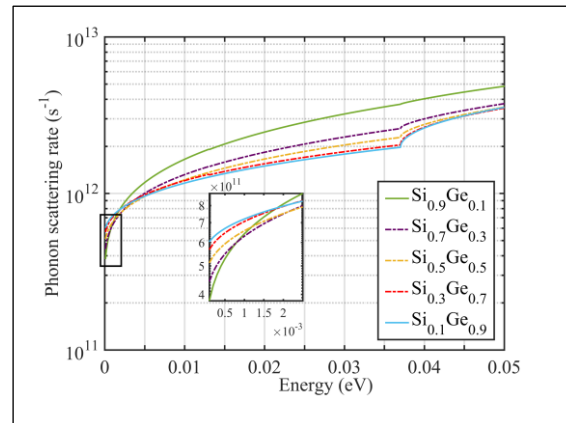


Fig.4: Phonon scattering rate of $Si_{0.9}Ge_{0.1}$, $Si_{0.7}Ge_{0.3}$, $Si_{0.5}Ge_{0.5}$, $Si_{0.3}Ge_{0.7}$ and $Si_{0.1}Ge_{0.9}$. The extremely low energy is depicted in zoom where the total scattering rate increases with the Ge content. For values of energy higher than the thermal energy at 300K, the total phonon scattering rates become smaller as the Ge content increases.

Two-Dimensional Diffusion Process Simulation of Si-Implanted Ga₂O₃

In Ki Kim, and Sung-Min Hong

School of Electrical Engineering and Computer Science, Gwangju Institute of Science and Technology (GIST), Gwangju, Cheomdangwagi-ro-123, South Korea
smhong@gist.ac.kr

Gallium oxide (Ga₂O₃) is a promising material for power electronics devices and UV detectors owing to its wide bandgap (~ 4.9 eV) [1]. The free electron concentration of Ga₂O₃ can be controlled in bulk growth process such as Molecular Beam Epitaxy or mist-Chemical Vapor Deposition process [2]. However, the ion implantation and the thermal annealing are required to form ohmic contacts of source and drain regions with selective and high concentration doping [3]. A simulation model of the dopant diffusion in Ga₂O₃ is required to predict the dopant distribution after the annealing process. In this work, we report two-dimensional simulation of Si dopant diffusion as a function of time at 1100 °C annealing temperature in O₂ and N₂ ambient. A diffusion model reported in [4] is adopted in the simulation and implantation profiles of dopant and damage are calculated from Stopping and Range of Ions in Matter (SRIM) simulation. The simulation is conducted in a 500 nm × 2000 nm Ga₂O₃ region. Figure 1 (a) and (b) show the profile of implanted Si into Ga₂O₃. The implantation profile along the vertical direction is calculated for $3.24 \times 10^{13} \text{ cm}^{-2}/30\text{keV}$, $5.72 \times 10^{13} \text{ cm}^{-2}/60\text{keV}$, and $8.1 \times 10^{13} \text{ cm}^{-2}/90\text{keV}$ with the SRIM simulation. The implantation window is open from -700 nm to 700 nm in the lateral position. Subsequently, the diffusion simulation is carried out during 60 s at 1100 °C temperature in either O₂ or N₂ ambient. In Figs. 2 and 3, the dopant profile is shown at three representative time instances, 20 s, 40 s, and 60 s. In the O₂ ambient simulation, the peak concentration of Si decreases to below $4.7 \times 10^{18} \text{ cm}^{-3}$ from $1.85 \times 10^{19} \text{ cm}^{-3}$, as shown in Fig. 2. Otherwise, almost no redistribution of Si is occurred in the N₂ ambient as shown in Fig. 3. In conclusion, the dopant diffusion of Si-implanted Ga₂O₃ has been simulated. Since the generated vacancy type is different according to the ambient, the Si redistribution is significantly affected by the ambient.

Acknowledgement: This work was supported by the National Research Foundation of Korea grant funded by the Korea government (NRF-2019R1A2C1086656 and NRF-2020M3H4A3081800) and the GIST Research Institute grant funded by the GIST in 2021.

- [1] S. J. Pearton et al., *Appl. Phys. Rev.*, **5**, 011301 (2018).
- [2] M. J. Tadjer et al., *ECS J. Solid State Sci. Technol.*, **8**, Q3133 (2019).
- [3] M. H. Wong et al., *IEEE Elect. Dev. Lett.*, **40**, 3 (2019).
- [4] R. Sharma et al., *AIP Adv.*, **9**, 085111 (2019).

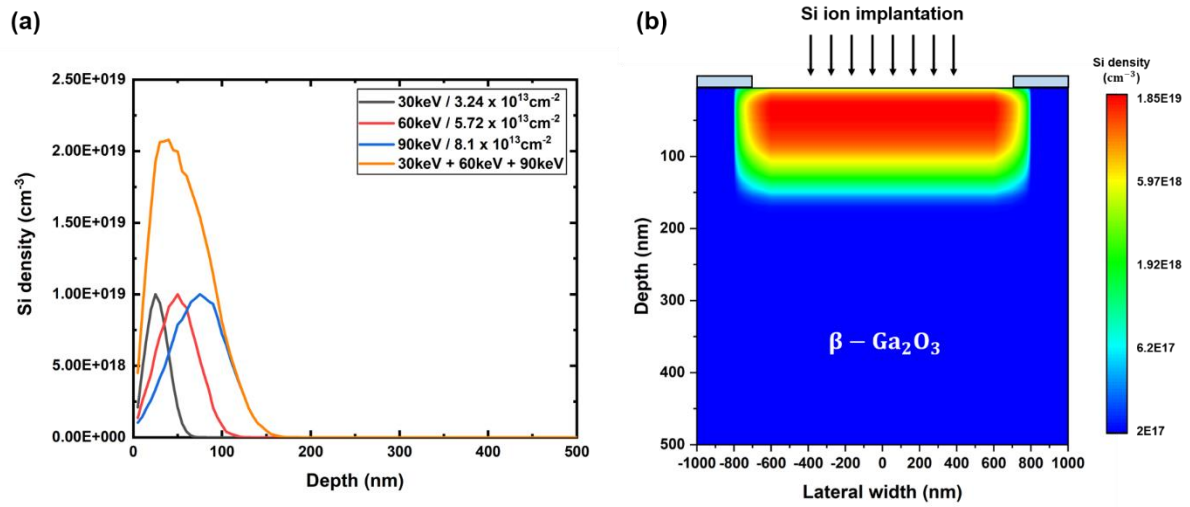


Fig.1: Implantation profile of Si. (a) Implanted Si profile as a function of depth calculated from the SRIM simulation. (b) Two-dimensional implantation profile of Si. The implantation window is open from -700 nm to 700 nm in the lateral position.

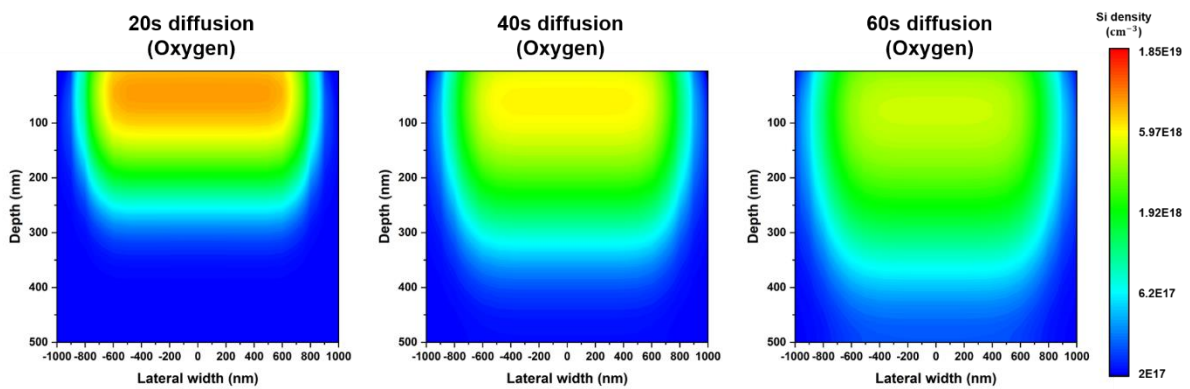


Fig.2: Simulated two-dimensional Si profile after annealing at 1100 °C temperature (20 s, 40 s, and 60 s) in the O₂ ambient.

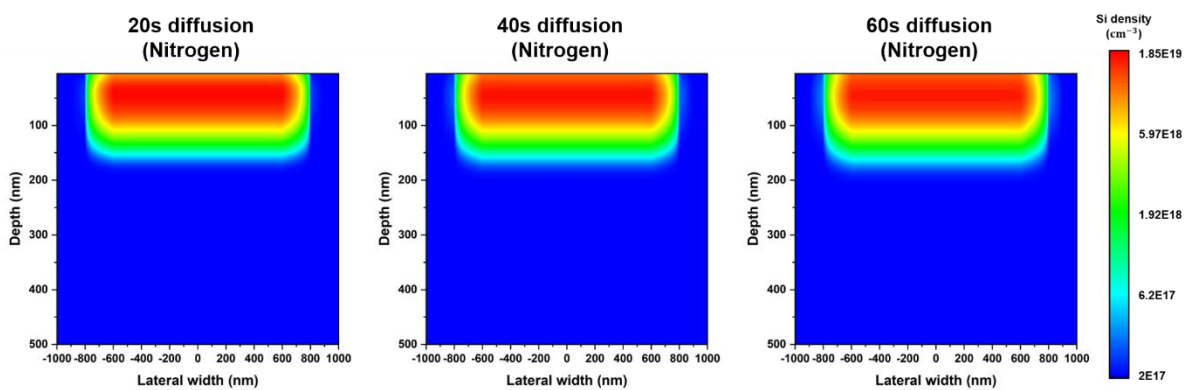


Fig.3: Simulated two-dimensional Si profile after annealing at 1100 °C temperature (20 s, 40 s, 60 s) in the N₂ ambient.

Temperature Dependent Electrical Characteristics and Single Charge Trap Induced by Random Telegraph Noise of Bulk FinFETs

Sekhar Reddy Kola and Yiming Li*

Parallel and Scientific Computing Laboratory, Electrical Engineering and Computer Science International Graduate Program, Department of Electrical and Computer Engineering, National Yang Ming Chiao Tung University, Ta-Hsueh Rd. 1001, Hsinchu 300, Taiwan.

Parallel and Scientific Computing Laboratory, Electrical Engineering and Computer Science International Graduate Program, Department of Electrical and Computer Engineering, National Chiao Tung University, Ta-Hsueh Rd. 1001, Hsinchu 300, Taiwan.

* yml@faculty.nctu.edu.tw

We for the first time study temperature dependent random telegraph noise (RTN) of bulk fin-type field effect transistors (FinFETs) induced by acceptor-type single-charge trap for sub-7-nm technologies. The significant reductions of off-state current of the explored bulk FinFETs under the reduced temperature and its enhanced device performance in terms of I_{on}/I_{off} ratio. For bulk FinFETs, the trap position at middle of the channel with different temperature, the RTN magnitude ($(\Delta I_D/I_D) \times 100\%$) is estimated. The impact of RTN is significant under the cryogenic (low) temperature.

Bulk FinFET has been the dominant technology on the VLSI technology for emerging electronic applications. It has the wonderful electrostatic control, effective immunity of short channel effects and CMOS comparable manufacturability [1]. The prediction of ITRS 2.0 roadmap [2], the FinFETs will continuous scaling trend of CMOS transistors to sub-5-nm technology nodes and beyond. As lowering the ambient temperature, the device performance improves in terms of I_{on}/I_{off} ratio and steeper subthreshold swing [3]. In this work, we computationally study the device transfer characteristic (I_D-V_G) with different temperatures. RTN influenced by acceptor-type single charge trap (SCT) presenting at middle of the channel between the silicon channel and gate dielectric is calculated with respect to different temperatures for bulk FinFETs by using the experimentally validated 3-D device simulation [4]. The magnitude of RTN induced by 3-D SCT having both length and width of 2-nm and 0.5-nm height locating middle of the channel [5-6]. At the high temperature due to low carrier mobility, the reduction of RTN is caused. By extracting SCE parameters, we discuss characteristic variability induced by SCT. We observe that the magnitude of RTN is high at low temperature.

Figure 1 illustrates the simulated 3-D structure for the nominal bulk FinFET with specified regions. The simulated device physical parameters with regions are listed in Table I. The device having 16-nm gate length with gate stack of Ti/HfO₂/SiO₂ and silicon. This simulation is examined by solving 3-D quantum-mechanically corrected density gradient model along with drift diffusion model, which is valid, by nonequilibrium green function [4]. We express the simulation results of the temperature varying from high to low, the transfer characteristics can be boosted, especially in terms of off-state current reduction as shown in Fig. 2. It is evident by observing the conduction band profile along the channel from source (S) to drain (D), as depicted in Fig. 3. The low temperature has a high off-state conduction barrier which leads to lower leakage at off-state and boost the device performance. The high-temperature device possesses the lower barrier, compared with the low-temperature one. To explore the most severe impact of the SCT on RTN, we further consider the density of interface trap of $10^{12} \text{ cm}^{-2} \text{ eV}^{-1}$. Figure 4 illustrates the calculated magnitude of the RTN in the presence of SCT (by calculating the deviation $\Delta I_D/I_D \times 100\%$.) due to trapping/de-trapping, where the SCT is positioned in the middle of the channel with different temperatures. The magnitude of RTN decreases with increasing V_G due to the low charge carriers. Finally, the RTN magnitude is large at low temperature because the increased carrier mobility causes to enhance the charge capture and emission rate of SCT [5]. From the RTN magnitudes comparison with respect to different temperature, the decreased temperature causes to an increased RTN magnitude. It is noticed from the off-state conduction band profile in the channel under the presence of SCT, the barrier height is enhanced with the reduced temperature; thus, it causes to high SCT fluctuation, as shown in Fig. 5.

In summary, we have investigated the SCT induced RTN for devices under different temperatures. Low-temperature operation can reduce the leakage and boost the device characteristics, but the magnitude of RTN becomes significant (about 40%) for devices operated at low temperature.

Acknowledgement

This work was supported in part by Ministry of Science and Technology (MOST) of Taiwan under Grant MOST-109-2221-E-009-033 and Grant MOST-109-2634-F-009-030, and in part by the "Center for mm Wave Smart Radar Technologies" under the Featured Areas Research Center Program within the framework of the Higher Education Sprout Project by Ministry of Education in Taiwan.

References

- [1] D. Nagy., et al., IEEE ACCESS, pp. 53196-53202, 2020.
- [2] IRDS, pp. 1-7, 2016.
- [3] K -H Kao., et al., IEEE EDL, PP. 1296-1299, 2020.
- [4] Y. Li et al., IEDM, pp. 887-890, 2015.
- [5] S. R. Kola., et al., J. Compute. Electron. pp. 253-262, 2020.
- [6] S.-C. Hsu and Y. Li, Nanoscale Res. Lett., vol. 9, 2014, 633, 2014.

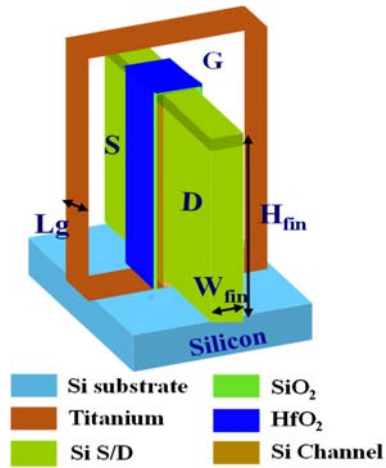


Fig. 1: A 3-D schematic structure of the explored 16-nm-wide (corresponding to sub-5-nm technological node) bulk FinFET with titanium gate metal and HfO₂/SiO₂ and silicon as gate stack and the regions are specified in appropriate color.

Tab. 1: List of the N-type nominal bulk FinFET device parameters, the regions and their specified values used in this simulation. Notice that the values presented here were calibrated with experimentally measured data for the best of simulation accuracy.

Device parameter	Value
Channel length (nm)	16
Channel doping (cm ⁻³)	5 × 10 ¹⁷
S/D extension (nm)	5
S/D length	12
Fin height (nm)	32
Fin width (nm)	8
Aspect ratio (Fin height / Fin width)	4
Work function (eV)	4.52
EOT (nm) (T _{siO2} +T _{hfo2} × e _{siO2} /e _{hfo2})	0.963
S/D doping (cm ⁻³)	1 × 10 ²⁰
S/D extension doping (cm ⁻³)	4.8 × 10 ¹⁸

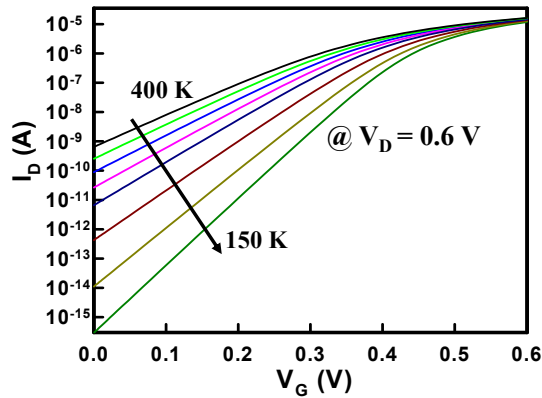


Fig. 2: The transfer characteristics (I_D - V_G) of the simulated bulk FinFET devices with respect to different temperature from high (400 K) to Low (150 K) at $V_D = 0.6$ V.

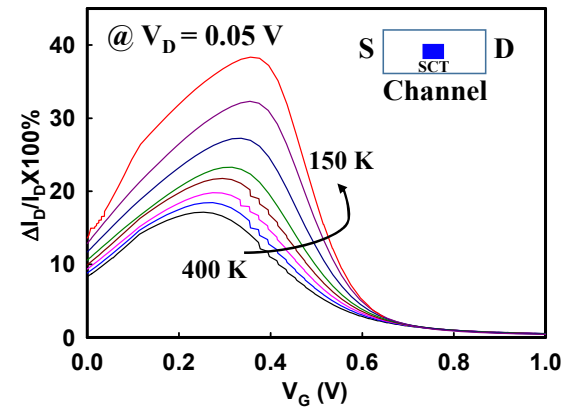


Fig. 4 The calculated magnitude of the random telegraph noise in the presence of the acceptor-type single charge trap at the middle of channel with varied temperature for the device at $V_D = 0.05$ V.

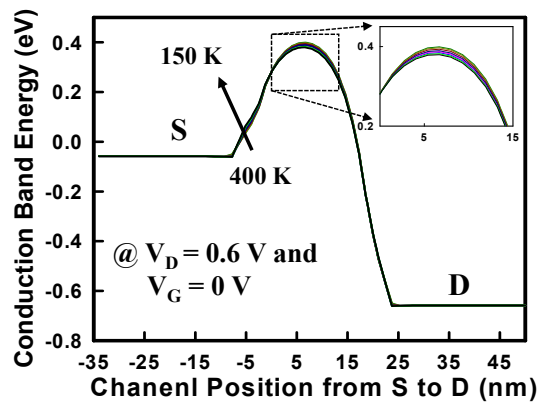


Fig. 3: Plot of the conduction band profile along the channel direction from source to drain with varied temperature from 400 K to 150 K under the off-state condition ($V_D = 0.6$ V and $V_G = 0$ V). The inset shows the zoom-in plot at the dotted area.

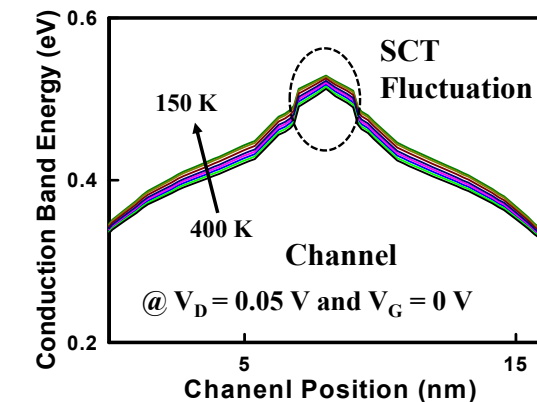


Fig. 5: The off-state ($V_D = 0.05$ V and $V_G = 0$ V) conduction band profile of the channel under the presence of SCT locating at the middle of channel with varied temperature, the inset circle represent the SCT induced fluctuation in the conduction band energy profiles.

Thermoelectric properties of complex band and nanostructured materials

Neophytos Neophytou¹, Patrizio Graziosi², Zhen Li¹, Vassilios Vargiamidis¹

¹ *School of Engineering, University of Warwick*

² *CNR—ISMN, v. Gobetti 101, 40129, Bologna, Italy*

n.neophytou@warwick.ac.uk

Thermoelectric (TE) materials convert heat from temperature gradients into useful electrical power. Over the last two decades, an enormous progress has been achieved, owing to the synthesis of complex bandstructure materials and their alloys (Fig. 1), and nanostructured materials (Fig. 2) [1]. The figure of merit, $ZT = \sigma S^2 T / \kappa$ where σS^2 is the power factor (PF) and κ the thermal conductivity, quantifies the efficiency. It has increased by 2-fold, to values above $ZT > 2$ across materials and operating conditions, with a maximum of $ZT = 2.6$.

In this work, we describe a computational framework to compute the electronic and thermoelectric transport in materials with multi-band electronic structures of an arbitrary shape (Fig. 3) by coupling density function theory (DFT) bandstructures to the Boltzmann Transport Equation (BTE). We explain the computational complexities and the approximations made. We then show how ‘real-space’ methods, such as the non-equilibrium Green’s function (Fig. 4) and the Monte Carlo methods (Fig. 5) can be used to design nanostructured materials with very high TE PFs. We elaborate on the computational framework needed to advance the field of TEs.

Here, we present four related studies. First: due to the complexity of the electronic structure, it is customary to use a constant value for the relaxation times within the BTE. We show that the full energy and momentum dependence of the relaxation times is essential in capturing the correct transport features [2]. Second: in order to identify high performance materials within the myriad of possibilities, we present the development of a set of descriptors that can be used in materials screening studies [3]. A combination of the number of valleys, dielectric constant, conductivity effective mass, deformation potential, and bandgap, forms a useful descriptor. Third: we present a study in which we show a possible route to achieve over an order of magnitude increase in the TE power factor, by utilizing narrow gap materials and bipolar transport, a regime which is usually avoided [4]. Four: We demonstrate a practical nanostructuring design which can also allow for 10-fold improvement in the PF [6, 7].

[1] D. Beretta et al., *Materials Science and Engineering: R: Reports*, **138**, 210–255, (2019). [2] P. Graziosi, *Journal of Applied Physics* **126**, 155701 (2019). [3] P. Graziosi, *ACS Appl. Energy Mater.*, **3**, 6, 5913–5926, (2020). [4] P. Graziosi, *Journal of Physical Chemistry C*, **124**, 34, 18462–18473, (2020). [6] N Neophytou et al., *European Physical Journal B*, **93**, 213, (2020). [7] N. Neophytou et al., *MaterialsToday Physics*, **11**, 100159, (2019).

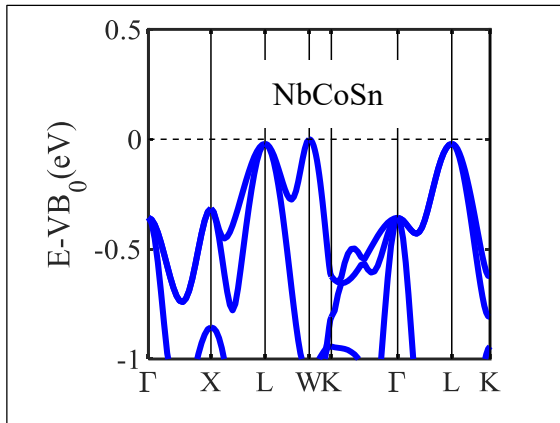


Fig.1: A typical example of a multi-band TE material, in this case the half-Heusler NbCoSn. Multiple pockets are available for electronic transport.

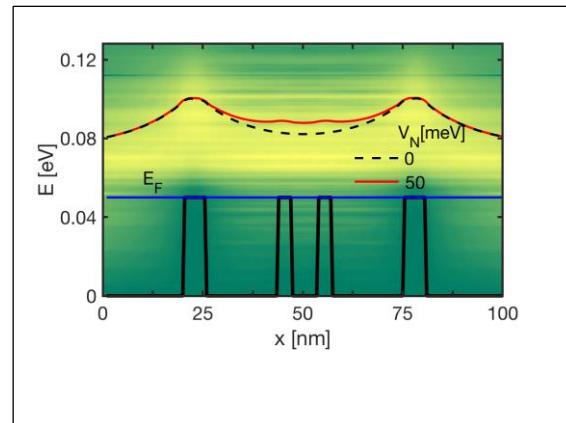


Fig.4: A typical NEGF simulation for the energy of the current flow in nanostructures, a quantity that determines the Seebeck coefficient. Phonon scattering (acoustic and optical) is included.

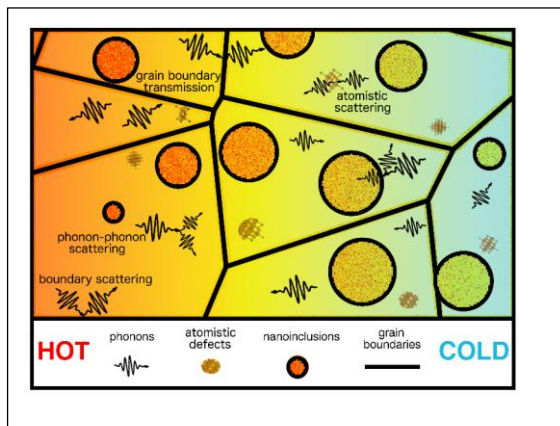


Fig.2: A typical nanostructured geometry, where grain boundaries appear at the macro-scale, nanoinclusions at the meso-scale, and atomic defects at the atomic scale. Phonons scatter effectively off these structures and the thermal conductivity is reduced. From [6].

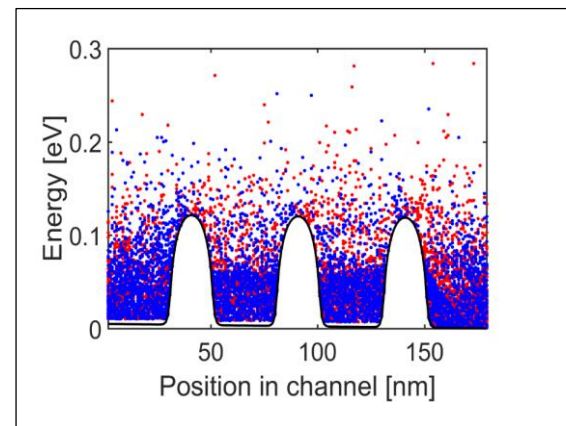


Fig.5: A snapshot from a Monte Carlo simulation in a material with alternative barriers and wells, an idealized schematic of a typical nanostructured TE material.

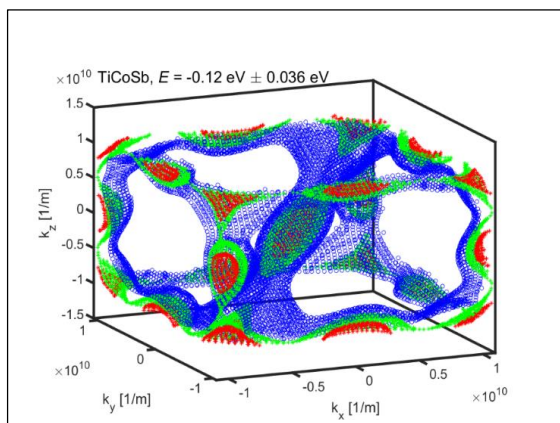


Fig.3: A typical energy surface in the 3D k -space of the valence band of TiCoSb. Points on the energy surface of different bands (blue, red, green) indicate the initial and final scattering states in the BTE.

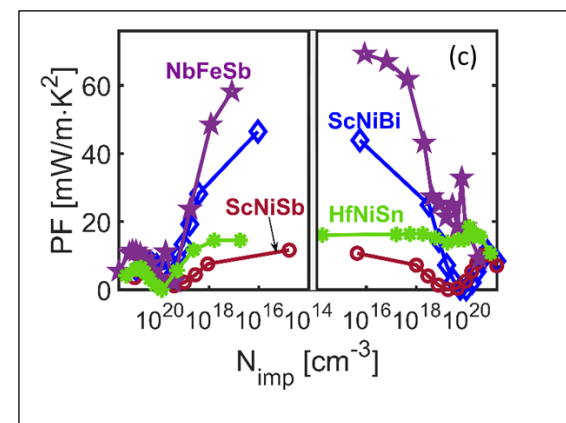


Fig.6: Low bandgap and highly anisotropic materials with regards to the properties of the conduction and valence bands can provide extremely high PRs. Adopted from [4].

Multiscale Modeling and Simulation of Advanced Photovoltaic Devices

Yongjie Zou¹, Reza Vatan Meidanshahi¹, Raghuraj Hathwar¹, and Stephen Goodnick¹

¹ *School of Electrical Computer and Energy Engineering, Arizona State University, Tempe, Arizona 85287 USA*
goodnick@asu.edu

The introduction of new materials, device concepts and nanotechnology-based solutions to achieve high efficiency and low cost in photovoltaic (PV) devices requires modeling and simulation well beyond the current state of the art. New materials and heterojunction interfaces require atomistic approaches to understand their electronic and optical properties. Current commercial photovoltaic device simulators based on classical drift and diffusion models are limited in terms of describing nonequilibrium physics in critical regions of conventional devices and in far from equilibrium carrier dynamics in advanced concept devices (e.g. multi-exciton and hot carrier solar cells). At the same time, the characteristic time scales to describe the physics of solar cells span many orders of magnitude, ranging from femtoseconds for carrier dynamics to milliseconds for characteristic lifetimes. Length scales vary similarly from nanometers at interfaces to centimeters for the solar cell apertures. Therefore, accurate modeling of the microscopic physics in critical regions of the device have to be coupled with less accurate, but more macroscopic models, over long time periods and large simulation domain sizes.

In this presentation, we discuss multiscale approaches used by our group in the modeling and simulation of several PV technologies, combining first principles modeling and transport simulation with commercial simulation tools. We first discuss crystalline Si/amorphous Si heterojunction devices, which have the highest reported efficiencies (>26%) for any Si technology [1], and the role of transport through the amorphous Si layers (Figures 1 and 2). We then discuss III-V on Si multi-junction solar cells for taking Si technology beyond its current single gap thermodynamic limits, and modeling of the heteropolar GaP/Si interface, and dilute nitrides for lattice matching and their optical and transport properties, and finally the impact on the expected two junction efficiency (Figures 3 and 4). The talk then concludes with a discussion of atomistic modeling of ultrafast carrier dynamics in nanowire arrays for application in multi-exciton generation and hot carrier solar cells [2] (Figures 5 and 6).

[1] K. Yoshikawa *et al.*, Nat. Energy, **4**,17032 (2017)

[2] R. Hathwar *et al.*, Topical Review in Journal of Physics D: Applied Physics **52**, 093001 (2019).

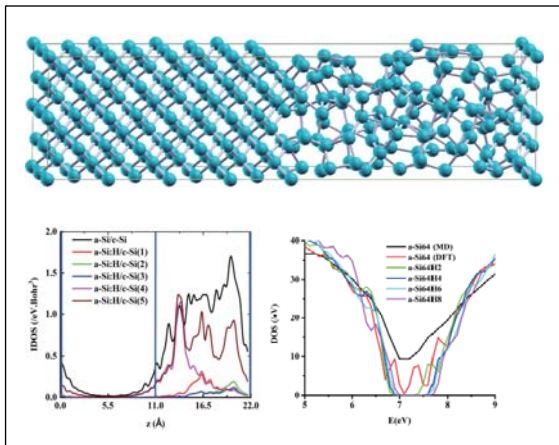


Fig.1: Simulated amorphous Si/crystalline Si interface using LAMMPS and the corresponding bandgap states as a function of position and energy from Quantum Espresso.

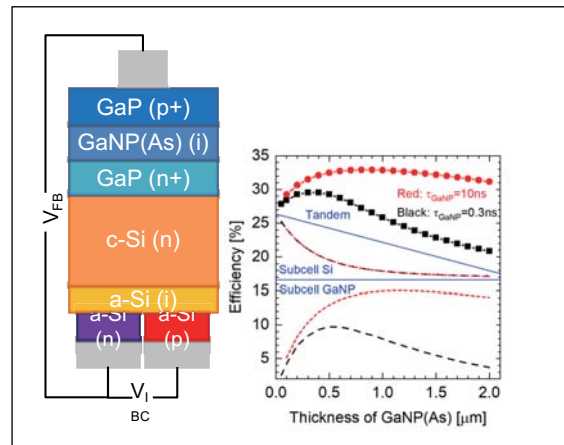


Fig.4: GaNP/GaP/Si three terminal tandem cell structure and the simulated maximum efficiency versus dilute nitride absorber thickness.

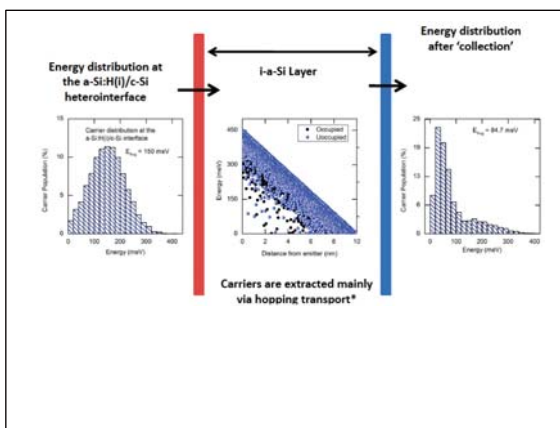


Fig.2: Coupled ensemble Monte Carlo and kinetic Monte Carlo simulation of transport through the a-Si layer in a Si HIT cell.

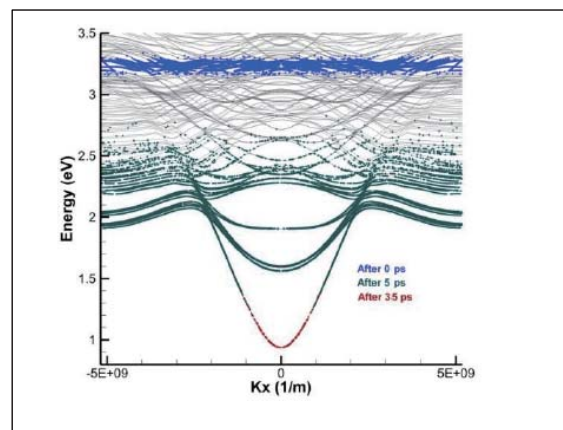


Fig.5: Simulated carrier distribution within the multi-subband nanowire structure for different times after initial excitation at high energy.

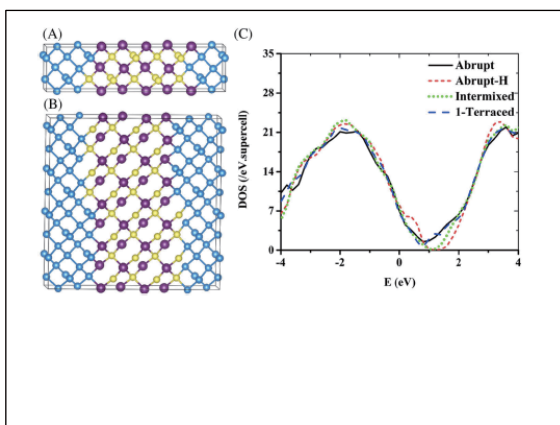


Fig.3: Simulated GaP/Si supercell, with different intermixing, and the simulated density of states in the gap.

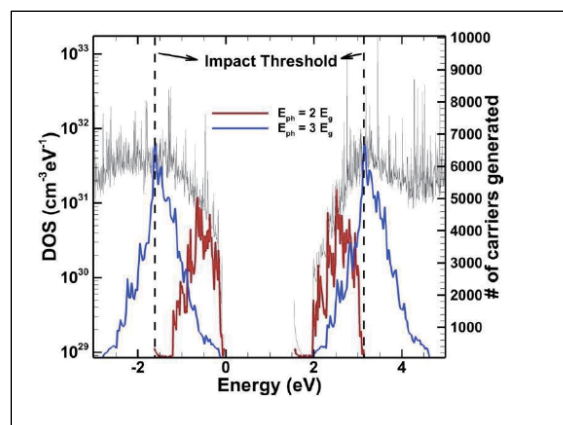


Fig.6: Photoexcited carrier distributions for two different photon energies superimposed on the density of states in a 2 nm nanowire structure.

Monte Carlo study of Single Photon Avalanche Diodes: quenching statistics

Thibault Cazimajou¹, Marco Pala¹, Jérôme Saint-Martin¹, Denis Rideau², Philippe Dollfus¹

¹ *Université Paris-Saclay, CNRS, C2N, F-91120 Palaiseau, France*

² *STMicronics, F-38920 Crolles, France*

thibault.cazimajou@universite-paris-saclay.fr

Single Photon Avalanche Diode (SPAD) is a reverse biased p-n or p-i-n junction, with an applied voltage V_a higher than the breakdown voltage V_B . Under such conditions, an electron-hole (e-h) pair generated by photon absorption (photo-generation) can be heated by the electric field, triggering impact ionization and generation of new e-h pairs. This avalanche phenomenon induces a strong increase of the diode current that is set to detect photon absorption. To detect another photon, The SPAD must be reset thanks to a quenching circuit, e.g. an RC circuit, able to stop the avalanche process and remove all excess e-h pairs. Astonishingly, the avalanche phenomenon in SPAD which is by nature a particle and stochastic effect has been rarely studied using particle Monte Carlo (MC) Simulation[1,2]. In particular the quenching process has never been considered using such tools as far as we know

In this work, a self-consistent 3D Monte Carlo algorithm is used to simulate SPAD in series with a passive quenching RC circuit, as shown in Fig.1. With this strategy, all stochastic features of quenching properties can be explored in details, including quench probability and last ionization time.

Once the device was set to steady state for a given V_{bias} , a free e-h pair was generated at a selected position X_{GEN} at $t = 0$, simulating a photon absorption. In Fig. 2 are plotted the time evolution of the number of impact ionization events, the current and the voltage across the SPAD connected to a quenching circuit. The results are shown for four different random choices of wave vectors of the initial e-h pair. Blue and pink curves correspond to a successful quench, whereas red and green curves are typical examples of non-successful quench. Fig. 3 shows the time to avalanche T_A and the breakdown probability as a function of R_Q while Fig. 4 shows the quenching probability and the extinction time T_{EXT} that is defined as the time between T_A and the last ionization event when the SPAD quenches. Remarkably, this probability changes from 0% for $R_Q = 300 \text{ k}\Omega$ to 100% for $R_Q = 1.3 \text{ M}\Omega$. This agrees with the idea that the quenching resistance must be high enough to obtain a successful quench [3]. This self-consistent MC approach turns out to be a powerful tool to investigate all statistical aspects of SPAD operation.

[1] R. J. Marshall et al., J. Appl. Phys., vol. 104, 013114 (2008).

[2] D. Dolgos et al., J. Appl. Phys., vol. 110, 084507 (2011)

[3] V. Savuskan et al., IEEE Sensors J., vol. 13 (6), 2322-2328 (2013)

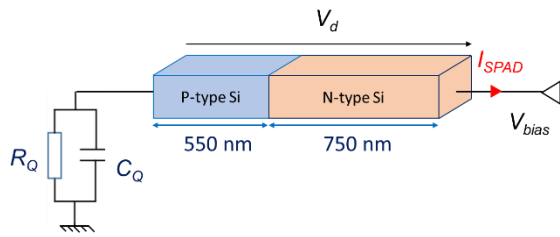


Fig.1: Sketch of simulated device in series with the external passive quench circuit (R_Q, C_Q).

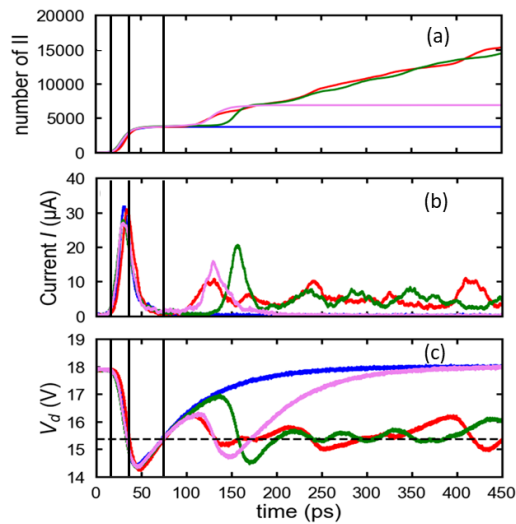


Fig.2: (a) Time evolution of the cumulated number of impact ionization events (II) for four different random choices of wave vectors of the initial $e-h$ pair generated at $t = 0$ with a quenching circuit ($R_Q = 500 \text{ k}\Omega$, $V_{bias} = 18 \text{ V}$, $X_{GEN} = 500 \text{ nm}$). (b) Corresponding time evolution of terminal current. (c) Corresponding time evolution of the SPAD voltage V_d

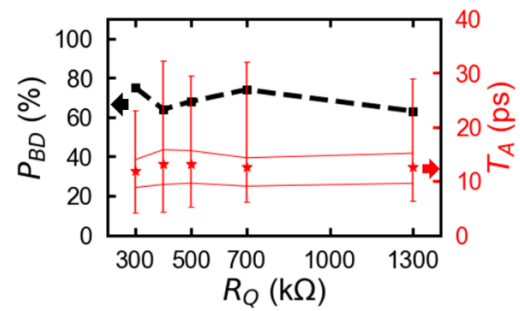


Fig.3: Avalanche time T_A (red stars) and breakdown probability (black squares) versus quenching resistance R_Q . Red stars are mean values of T_A , while vertical bars indicate minimum and maximum values. Half of the values are in the closed area.

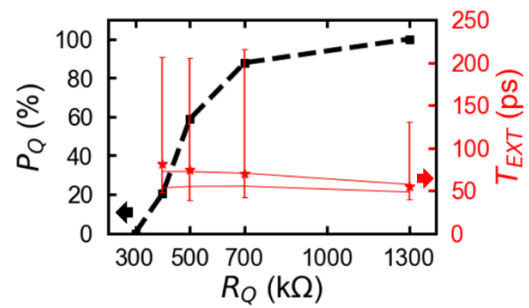


Fig.4: Extinction time (red stars) and quenching probability (black squares) versus R_Q . Red stars are mean values, vertical bars indicate minimum and maximum values. Half of the values are in the closed area.

Study of the modal contributions to the heat flux to characterize the phonon transport regime in Si/Ge heterojunctions

N. D. Le¹, B. Davier^{1,2}, P. Dollfus¹, J. Saint-Martin¹

¹ *Université Paris-Saclay, CNRS, Centre de Nanosciences et de Nanotechnologies, 91120, Palaiseau, France*

² *Department of Mechanical Engineering, The University of Tokyo, Tokyo 113-856, Japan
jerome.saint-martin@universite-paris-saclay.fr*

Heat management at the nanoscale is central to the design and optimization of thermoelectric [1] and nanoelectronic [2] devices. However, common macroscopic models such as heat Fourier's formalisms assuming local equilibrium is not relevant in complex nanostructures of characteristic lengths shorter than the phonon mean free path, in which the phonon transport can be strongly out of equilibrium, especially if thermal interfaces are involved.

Even if some analytical models have been developed to extend the validity of the Fourier's formalism [3], the particle Monte Carlo (MC) technique is an efficient and accurate numerical method to capture the out of equilibrium transport regime much beyond the linear approximation, even in complex real space geometries. This approach can naturally consider all phonon transport regimes from the diffusive to the fully ballistic regime.

In this work, phonon transmission across interfaces that are perpendicular to the heat flux has been implemented in our home made Full Band Monte Carlo simulator for phonons [4] by using a Full-band version of the Diffusive Mismatch Model (DMM).

First, the Knudsen number, commonly used to characterize the different transport regimes (diffusive, ballistic and intermediate) and defined as the ratio of the effective thermal conductivity $\kappa_{effective}$ to the ballistic one $\kappa_{ballistic}$, is plotted in Fig. 1 for homogenous Ge bars. This parameter appears strongly correlated to the spectral contributions of the thermal flux plotted in Fig 2. Then, single and double Si/Ge heterostructures shown in Fig. 3 were studied from the micrometer scale down to the nanometer scale. A typical temperature profile in a 300 nm-long double heterostructure is shown in Fig. 4. The total thermal conductance obtained for different heterostructures is plotted as a function of length in Fig 5.

Finally, the spatial evolution of the different spectral contributions to the thermal flux is plotted in Fig. 6. Used as a local indicator of the phonon transport regime and associated with the information provided by Figs. 2 and 3, this modal contribution and its deviation from bulk configuration indicate the occurrence and quantify the importance of out-of-equilibrium phonon transport around the interfaces.

[1] W. Liu, Q. et al., *Acta Materialia*, **87**, 57–376 (2015)

[2] IRDS report 2017, irds.ieee.org/images/files/pdf/2017/2017IRDS_MM.pdf

[3] B. Davier et al., arXiv, 2020.

[4] B. Davier et al., *Journal of Physics: Condensed Matter*, **30**, 495902 (2018)

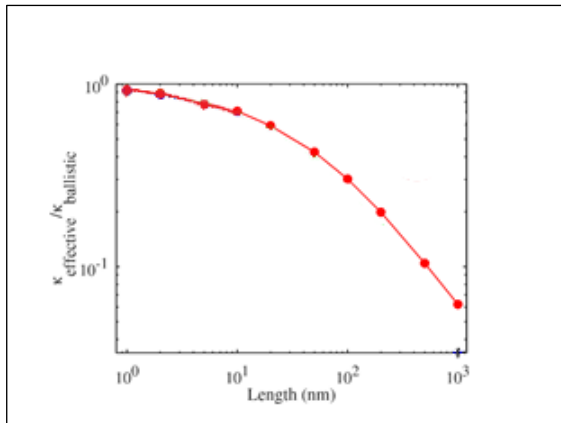


Fig.1.: The ratio $\kappa_{\text{effective}}/\kappa_{\text{ballistic}}$ as a function of the length L in Ge bars.

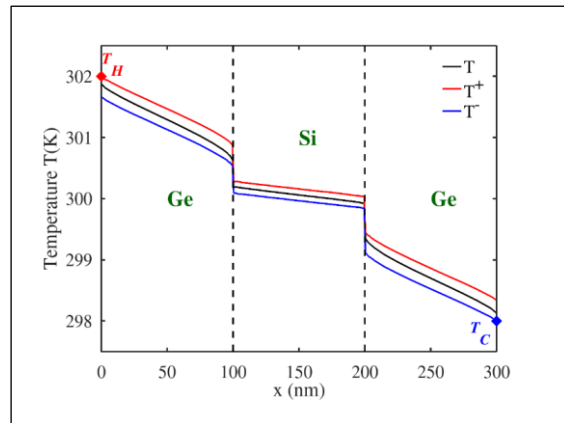


Fig.4: Temperature profiles in a Ge/Si/Ge double heterojunction. Hemispherical temperatures T^+/T^- are defined as the temperature of phonon sub-populations with a positive/negative velocity [3]

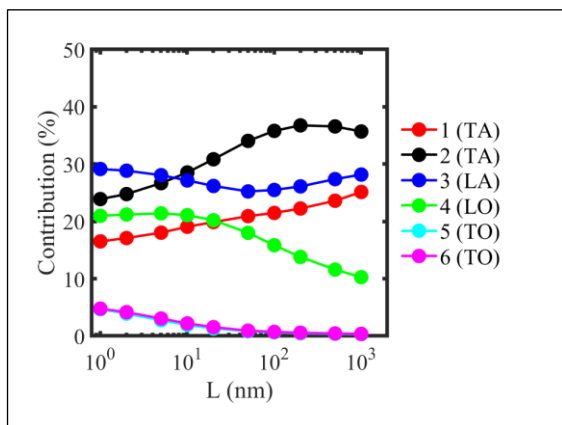


Fig.2: Modal contribution of phonons (for the 6 phonon modes) to the thermal flux as a function of the structure length in Ge bars

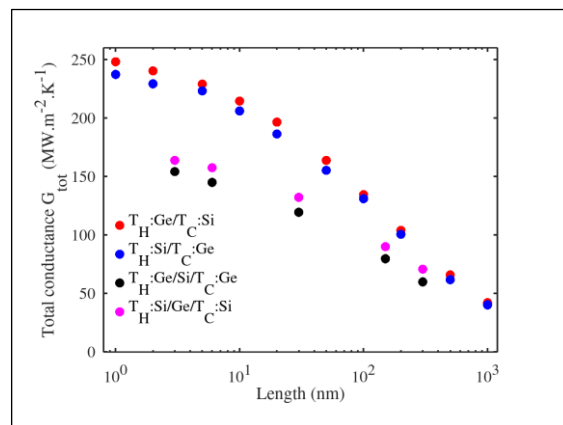


Fig.5: Total thermal conductance of simple and double heterojunctions for different device lengths

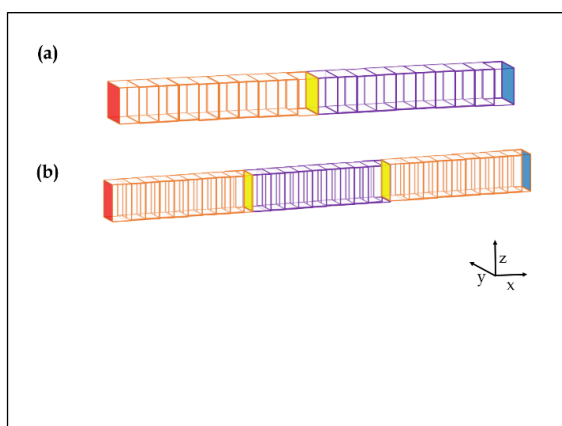


Fig.3: Heterogeneous nanostructures: (a) Simple heterojunction. (b) Double heterojunction. Red/blue faces are hot/cold thermostats. Transparent external faces: periodic boundaries. Yellow faces: DMM interfaces

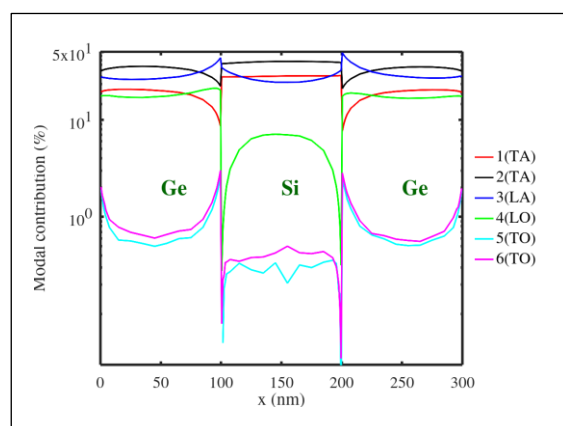


Fig.6: Variation of modal contribution to total thermal flux in 300 nm - long double heterojunction Ge/Si/Ge

Elastic-wave scattering from an object above a rough surface: A numerical time-domain technique

Laleh Avazpour, Michelle L. King, Sina Soleimanikahnoj, and Irena Knezevic

*Department of Electrical and Computer Engineering,
University of Wisconsin-Madison, Madison, WI 53706, USA
Laleh.avazpour@wisc.edu*

We developed a scattering model for layered media by introducing a π -shaped total field area over an irregular surface. This novel method utilizes the unique features of the finite-difference time-domain (FDTD) [1] and complex frequency shifted perfectly matched layer (CFS-PML) [2]. We use an auxiliary variable employed in PML formulation presented by Drossaert and Giannopoulos [2] to isolate the reflected and transmitted waves from the incident wave. Although such methods are well formulated for electromagnetic wave scattering, such formulation presented in this work is new for the elastic wave scattering. The present theory allows one to capture the scattering response for the problems containing complex scattering geometries, such as rough surfaces and interfaces in nanostructured layered media. This new formulation is suitable for precise calculation of the scattering cross-section with significantly less iteration time compared to analytical methods.

The backscattering from a random rough surface of 30 nm width and the 10 nm diameter circular inclusion above the surface are presented to show the effectiveness of the proposed formulation. The reflection/transmission behavior and the frequency response are illustrated. The scattering object under investigation is located within the FDTD volume, illuminated by a broadband pulsed plane wave centered at 2 GHz and scattered fields are simulated all around the object via FDTD directly in time domain. The mass density and Lamé parameters of silicon as the main domain material and aluminum as the scattering object are used as input for the elastic wave equation.

This work was supported by DOE-BES (award DE-SC0008712).

[1] L. N. Maurer, S. Mei, and I. Knezevic, *Phys. Rev. B* **94**, 45312 (2016).

[2] F. H. Drossaert and A. Giannopoulos, *Wave Motion* **44**, 593 (2007).

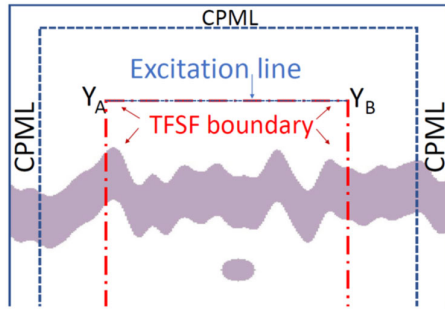


Fig.1: Schematic of a π -shaped TFSF boundary around a random rough surface and terminated by CPML absorbing boundary.

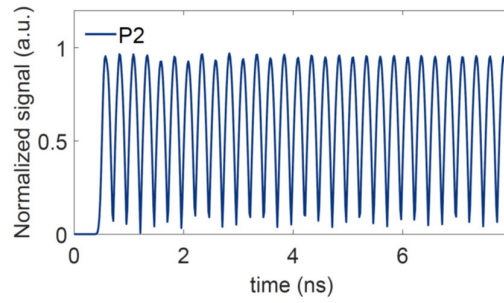


Fig. 4: The energy density captured at point P2 from Fig. 2, consist of the incident wave and reflected wave from the interface normalized to the source's maximum amplitude.

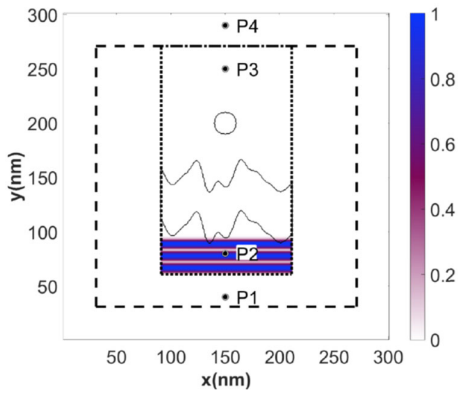


Fig.2: Snapshot of the spatial profile of the energy density captured after 0.8 ns.

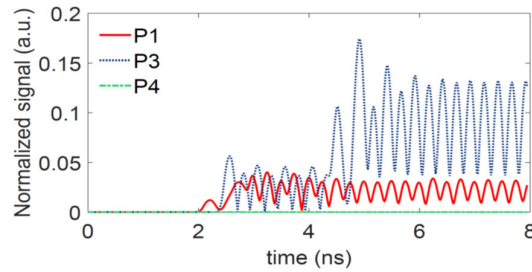


Fig.5: The energy density captured at point P1, P3 and P4; P1 is the reflected wave from the interface without source interference, P3 transmitted wave, scattered by the surface and the inclusion; and P4 wave absorbed by the CPML absorbing boundary; all normalized to the source's maximum amplitude.

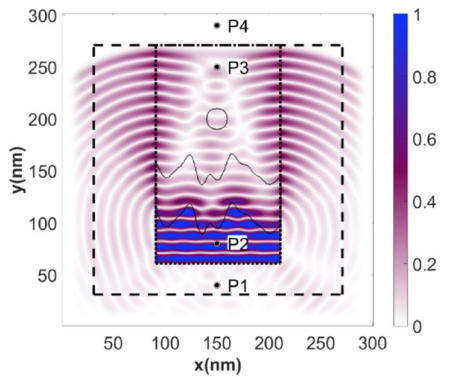


Fig.3: Snapshot of the spatial profile of the scattered and reflected energy density 4.7 ns after the launch of the source wave.

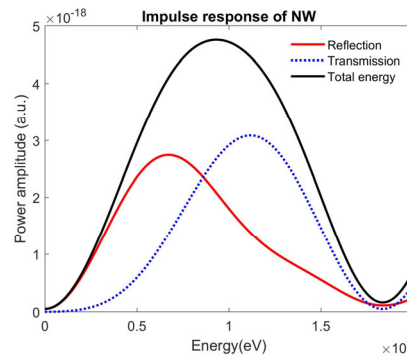


Fig.6: Impulse response of reflected and transmitted energy from and through the scattering objects

2D Plasmon-Polariton Excitation in Plasmonic THz Detector with 2D Diffraction Grating Structure

Yuma Sasaki¹, Taiichi Otsuji¹, and Akira Satou¹

¹ *Research Institute of Electrical Communication, Tohoku University, Japan*
sasaki-u@riec.tohoku.ac.jp

We have investigated plasmonic terahertz (THz) detectors with a diffraction grating structure, which utilize hydrodynamic nonlinearities of the two-dimensional (2D) plasmons in transistor channels for the photocurrent rectification, and demonstrated its high potentiality as on-chip, room-temperature operating, high-performance THz detectors for future 6G/7G wireless communication systems [1]. As depicted in Fig. 1(a), the one-dimensional (1D) metallic grating gates are arranged periodically in the channel length direction (x -direction) to enable direct coupling of 2D plasmons with incident THz waves. With the conventional 1D structure, however, only 1D oscillation of the 2D plasmons parallel to the x -direction is utilized in their operation. Recently, we have proposed the plasmonic THz detector with a novel 2D diffraction grating structure (Fig. 1(b)), consisting of 2D metallic nanoantennas and 1D grating gates, and have experimentally demonstrated that it can detect the polarization component of the incident THz wave parallel to the channel width direction (y -direction) owing to the excitation of 2D plasmons oscillating in the y -direction and its coupling with those oscillating in the x -direction [3]. This result indicates that the utilization of two-dimensionality of the 2D plasmons via the 2D diffraction structure is beneficial to improve functionalities of plasmonic THz detectors as well as their performances, although more comprehensive understanding of 2D natures of the plasmons in the 2D diffraction structure is required for it.

In this paper, we develop a simulation model for the plasmonic THz detector with the 2D diffraction grating structure for comprehensive investigation of 2D natures of the 2D plasmons, and we study the coupling of the 2D plasmon-polaritons oscillating in the x - and y -directions as one of the most fundamental properties. Our simulation model is based on 2D hydrodynamic equations self-consistently coupled with 3D Maxwell's equations (see Fig. 2 for the details). Here, we chose device parameters for an InGaAs-HEMT-based plasmonic detector (see Fig. 1), and we conducted simulations of 2D plasmon-polariton excitation in the detector by the THz wave normally incident on the detector with polarization parallel to the y -direction and with its frequency swept in the THz range. Figure 3 shows the frequency characteristics of the maximum absolute values of the electric field components in the channel. Among the several peaks corresponding to plasmon resonances, it is seen that the intensities of the peaks for x - and y -components at 1.9 THz are at the same level, meaning that the mode in the y -direction excited by the incident THz wave is strongly coupled to the mode in the x -direction via the 2D diffraction grating structure (see also the field distributions at 1.9 THz in Fig. 4). This result suggests that the 2D diffraction grating structure enables the coupling between the plasmon modes in x - and y -directions. This work was financially supported by JSPS KAKENHI #18K04277, Japan.

[1] Y. Kurita *et al.*, *Appl. Phys. Lett.* **104**, 251114 (2014).

[2] M. Suzuki *et al.*, *IRMMW-THz: the 43rd International Conference on Infrared, Millimeter and Terahertz Waves Dig.*, Tu-A2-1a-2, Nagoya, Aichi, Japan, 9-14 Sept. 2018.

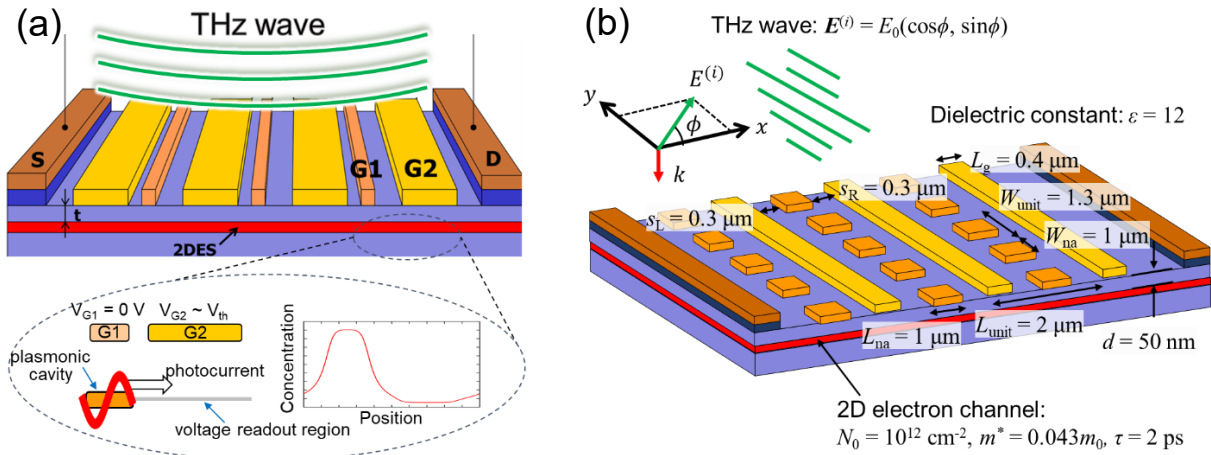


Fig.1: Schematic views of a plasmonic THz detector with the conventional 1D metallic grating gates and (b) a plasmonic THz detector with 2D metallic nano-antennas and 1D grating gates.

Maxwell's equations

$$\nabla \cdot (\epsilon \mathbf{E}) = -4\pi e \{ [N^{(ch)} - N_0] \delta(z) + [N^{(M)} - N_{M0}] \delta(z-d) \}$$

$$\nabla \cdot \mathbf{H} = 0$$

$$\nabla \times \mathbf{H} = \frac{4\pi}{c} \left[\mathbf{J}^{(ch)} \delta(z) + \sigma_{M0} \mathbf{E} \Big|_{z=d} \delta(z-d) \right] + \frac{\epsilon}{c} \frac{\partial \mathbf{E}}{\partial t}$$

$$\nabla \times \mathbf{E} = -\frac{1}{c} \frac{\partial \mathbf{H}}{\partial t}$$

Hydrodynamic equations

$$\mathbf{J}^{(ch)} = -e N^{(ch)} \mathbf{v}^{(ch)}$$

$$\frac{\partial N^{(ch)}}{\partial t} + \nabla_{xy} \cdot (N^{(ch)} \mathbf{v}^{(ch)}) = 0$$

$$\left(\frac{\partial}{\partial t} + \frac{1}{\tau} \right) \mathbf{v}^{(ch)} + (\mathbf{v}^{(ch)} \cdot \nabla_{xy}) \mathbf{v}^{(ch)} = -\frac{e}{m} \mathbf{E} \Big|_{z=0}$$

Perturbation in time & series expansion in space

System of linear equations for 1st-order in-plane fields

$$\mathbf{A} \times \begin{bmatrix} \vdots \\ E_{1,k_x,k_y}^{(ch)} \\ \vdots \\ E_{1,k_x,k_y}^{(g)} \\ \vdots \\ E_{1,k_x,k_y}^{(na)} \\ \vdots \end{bmatrix} = \mathbf{B} \times \mathbf{E}^{(in)}$$

A: $2(N^{(ch)}+N^{(g)}+N^{(na)})$ -by- $2(N^{(ch)}+N^{(g)}+N^{(na)})$ matrix

B: $2(N^{(ch)}+N^{(g)}+N^{(na)})$ -by-2 matrix

$\mathbf{E}^{(in)}$: field of incident THz wave

$N^{(l)}$: cutoff number of series expansion

$E(t, x, y, z)$ & $H(t, x, y, z)$: electric & magnetic fields

$N_{ch}(t, x, y)$: electron concentration

$J_{ch}(t, x, y)$: electron current

$v_{ch}(t, x, y)$: electron velocity

Fig.2: A simulation model developed for the plasmonic THz detector with the 2D diffraction grating structure.

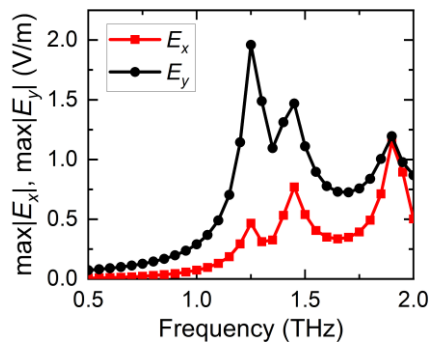


Fig.3: Frequency characteristics of the maximum absolute value of the electric field component in the channel.

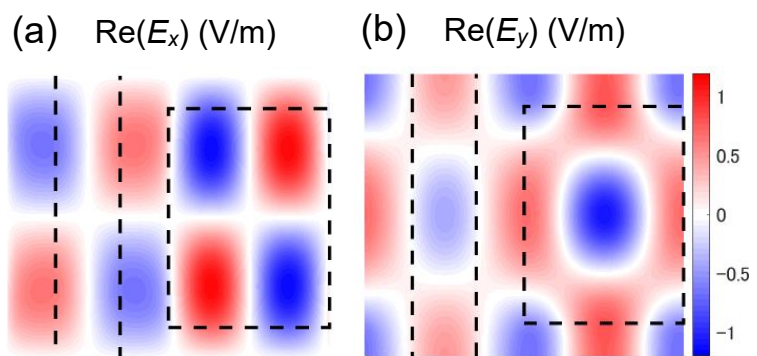


Fig.4: Electric field distribution in the channel at 1.9 THz in (a) x-direction and (b) y-direction.

A Density-Matrix Model for Photon-Assisted Electron Transport in Quantum Cascade Lasers

S. Soleimanikahnoj, M. L. King, and I. Knezevic

*Department of Electrical and Computer Engineering, University of Wisconsin-Madison,
Madison, Wisconsin 53706, USA
soleimanikah@wisc.edu*

Quantum cascade lasers (QCLs) are coherent sources of light that emit in the terahertz and infrared portions of the electromagnetic spectrum. Different theoretical models with varying levels of detail have been proposed to incorporate the effect of the optical field in the current-voltage-power characteristic of QCLs. Models based on the rate equations and density matrix (DM) often employ empirical or phenomenological parameters to incorporate radiative and nonradiative sources of scattering present in the active region of the QCL [1,2]. This limits their practicality as a modeling tool for the design and optimization of QCLs. The nonequilibrium Green's function (NEGF) technique allows for a methodical treatment of nonradiative scattering mechanisms and the optical field [3]. However, the NEGF method involves numerous matrix products and inversions, which, for a highly resolved (large matrices) calculation, can easily require modern supercomputers [4]. Therefore, there is a need for a numerically efficient quantum-transport model in QCLs that incorporates the effect of the optical field and does not require phenomenologically introduced parameters.

In this paper, we present a quantum-mechanical model for electron transport in QCLs that is computationally efficient, requires no phenomenological parameters, and incorporates the effect of the optical field nonperturbatively [5]. The model is based on a positivity-preserving Markovian master equation of motion for the DM. We use it to obtain the steady-state and frequency-dependent characteristics of a QCL. We show that the photon resonances arising with the inclusion of optical field have a pronounced effect on electron transport around and above the lasing threshold, which leads to better above-threshold agreement between the computed and experimental current densities. The model allows for the inclusion of the lasing field beyond linear response and the calculation of the output power. The calculated power is in close agreement with experiment.

This work was supported by the DOE-BES (DE-SC0008712) and AFOSR (A9550-18-1-0340).

- [1] M. Lindskog et al., *App. Phys. Lett.*, **105**, 103106 (2014).
- [2] H. Choi et al., *Phys. Rev. Lett.*, **100**, 167401 (2008).
- [3] A. Wacker et al., *IEEE. J. Sel. Top. Quantum Electron.*, **19**, 1 (2013).
- [4] C. Jirauschek and T. Kubis, *App. Phys. Rev.*, **1**, 1 (2014): 011307.

[5] S. Soleimanikahnoj, M. L. King, and I. Knezevic, Phys. Rev. Applied, in press. (2021). Preprint available on arXiv <https://arxiv.org/abs/2012.14491>

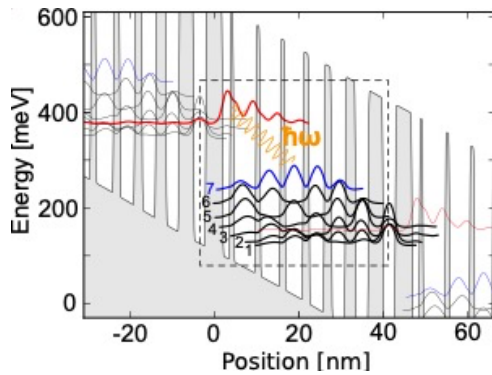


Fig.1: Conduction-band edge and probability densities for the eight eigenstates used in calculations (bold curves) at an above-threshold electric field bias of 50 kV/cm. The states that belong to neighboring periods are denoted by thin gray curves and the dashed box indicates a single stage, starting with the injection barrier. The states are numbered in the order of increasing energy, starting with the ground state; the radiative transition occurs from 8 to 7. (Reprinted from [5])

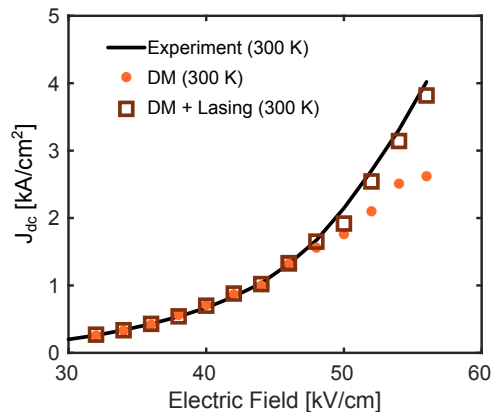


Fig.2: Calculated current density as a function of the applied bias electric field at 300 K, with (open squares) and without (solid circles) the influence of optical field. Experimental data is from Ref. [1]. (Reprinted from [5])

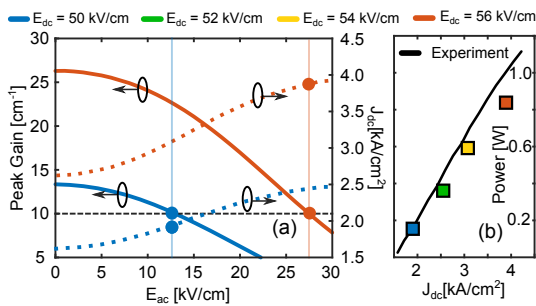


Fig.1: (a) Gain (solid lines) and current density (dotted lines) vs. optical field for $E_{dc}=50$ kV/cm (blue) and $E_{dc}=56$ kV/cm (red). The horizontal dashed line marks the threshold gain $G_{th} \approx 10\text{cm}^{-1}$. At each bias, the intercept of the gain vs. E_{ac} curve with the threshold-gain line determines the ac field where gain and losses compensate, i.e., the operational field. (b) Measured and calculated output power as a function of the current density. Data points are color-coded to indicate the corresponding bias field in the legend (top). Experimental data is from Ref. [1]. (Reprinted from [5])

FDTD Algorithm for Fields and Potentials with Convolutional Perfectly Matched Layer Absorbing Boundary Conditions

Michelle L. King, Laleh Avazpour, Samuel W. Belling, Stefan Schmidt, and Irena Knezevic

*Department of Electrical and Computer Engineering,
University of Wisconsin-Madison, Madison, WI 53706, USA
michelle.king@wisc.edu*

Accurate simulation of light–matter interaction at the nanoscale requires self-consistent coupling at every time step between quantum transport and electrodynamics solvers. We have developed an electrodynamics solver based on the finite-difference time-domain (FDTD) method, which computes the electric field \mathbf{E} and magnetic field \mathbf{H} , as well as the magnetic vector potential \mathbf{A} and scalar potential Φ . This field-potential (FiPo) FDTD method can take, as input, the current density \mathbf{J} and charge density ρ provided by the quantum transport solver, and will output \mathbf{A} and Φ , which are needed as input for the next update in the quantum-transport solver.

The FiPo FDTD algorithm employs four coupled first-order equations for \mathbf{E} , \mathbf{H} , \mathbf{A} and Φ , where the generalized Lorenz gauge is adopted [1]. The first order of the equations simplifies the creation of absorbing boundary conditions with respect to the second-order \mathbf{A}/Φ FDTD presented in [2]. We have successfully implemented a convolutional perfectly matched layer (CPML) absorbing boundary layer to absorb both fields and potentials in FiPo FDTD [3].

A FiPo FDTD simulation of electromagnetic fields arising from a differentiated Gaussian current source is illustrated for the fields just hitting the CPML (Fig. 1) and being fully in the CPML (Fig. 2); the wave appears elongated as it is absorbed, which is expected. Relative errors of the field magnitude (Fig. 3) show that the CPML is adequately absorbing all four fields. Simulations for these examples are similar to those in [2], with a differentiated Gaussian current source in z direction with a bandwidth of 6 GHz at the center of the simulation domain, relative dielectric permittivity ϵ_r of 7.73, conductivity σ of $0.273 \text{ A}^2\text{m}^{-3}\text{kg}^{-1}\text{s}^3$, α of $0.05 \text{ A}^2\text{m}^{-3}\text{kg}^{-1}\text{s}^3$, σ_{max} of $1.1*\sigma_{optimal}$, and κ_{max} of 7.

This work was supported by DOE-BES (award DE-SC0008712).

- [1] W.C. Chew, J. Appl. Phys. **75**, 4843 (1994).
- [2] C. J. Ryu, A. Y. Liu, W. E. I. Sha and W. C. Chew, IEEE J. Multiscale Multiphys. Comput. Tech. **1**, 40 (2016).
- [3] J.A. Roden and S.D. Gedney, Microw. Opt. Technol. Lett. **27**, 334 (2000).

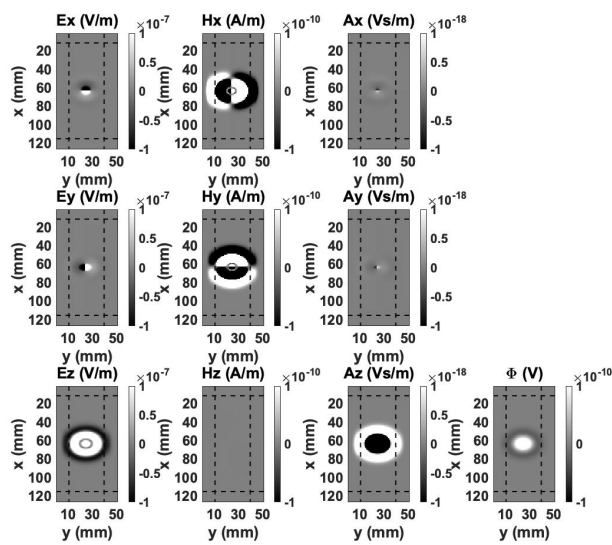


Fig.1: Snapshot of fields and potentials for FiPo FDTD at 0.32 ns.

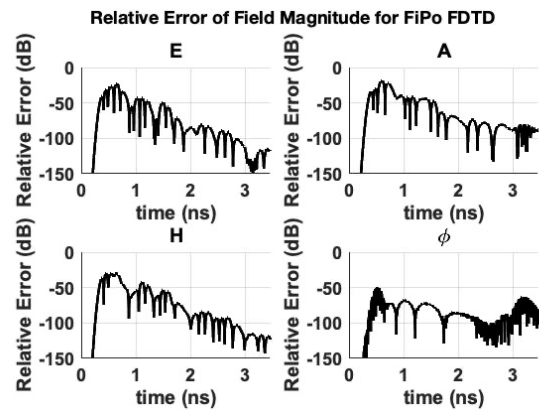


Fig.3: Relative error for magnitudes of fields with CPML implemented for E , A , H , and Φ . Reference simulation is $300 \times 300 \times 300$ where the PML is 10 cells thick. FiPo simulation was run on a $126 \times 51 \times 26$ grid with a PML of 10 cells.

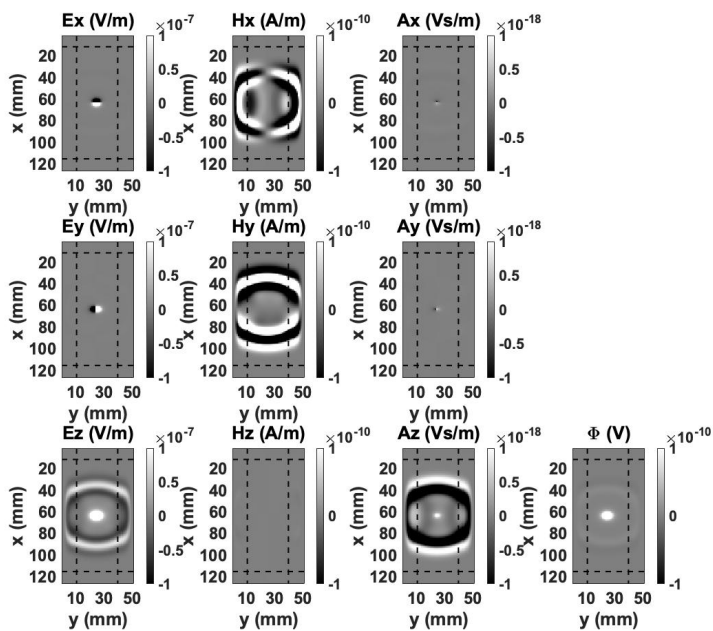


Fig.2: Snapshot of fields and potentials for FiPo FDTD at 0.49 ns.

Simulation of graphene photodetectors incorporating the photo-gating effect

Shingo Aida, Matsuto Ogawa and Satofumi Souma

Department of Electrical and Electronic Engineering, Kobe University,

1 Rokkodai, Nada, Kobe, 657-8501, Japan

E-mail: 202t201t@stu.kobe-u.ac.jp

Graphene-based photodetectors have been attracting great attention in recent years for their ability to detect weak optical signals, where the high electron mobility in graphene is beneficial for realizing the ultrafast photo detection. On the other hand, it has been proposed that high sensitivity can be realized by utilizing the photo-gating mechanism, where optical transparency of graphene and the strong electrostatic coupling between the graphene and photo-absorbing substrate play important roles. However, it has not been clarified theoretically enough how the sensitivity can be optimized by adjusting the device parameters such as the channel length and the back gate voltage. The aim of this research is to propose a scheme for the simulation of graphene photodetector (graphene/SiO₂/p-Si structure) utilizing the photo gating effect and clarify the condition to obtain the high sensitivity. By calculating the current in graphene under the light illumination based on the tight-binding formalism and the top-of-barrier model, we estimated the photo-induced current and the resulting photo responsivity. Our calculations have shown that the photo responsivity originated from the photo-gating effect is significantly larger than that obtained by conventional photo-voltaic effect in the graphene channel itself, the detailed analysis of which is useful information for the design of graphene-based photodetectors.

Figure 1 shows the schematic illustration of graphene photodetectors discussed in this study and the capacitance-based model, which is used to calculate the current density flowing through the graphene channel. Figure 2 represents a photo-induced current density (left) and a responsivity (right), which is one of the most important figures of merit for photodetectors. A photo-induced current density is the difference between a current density in case the light is irradiated and that in case not irradiated. A responsivity is the ratio of photo-induced current to the total photon energy flowing into the upper surface of the graphene channel, which indicates the conversion efficiency from the optical signal to the electric signal. As demonstrated in Fig. 2, graphene photodetectors can realize 70 A/W, when the light power is 50 W/m² and the area of the graphene channel is 20 μm². Figure 3 shows the substrate voltage dependence of photo-induced current density for various light wavelengths (left) and the responsivity as a function of the intensity of light irradiated into the graphene channel (right). In these figures, we can recognize that a larger light intensity realizes a higher responsivity. For instance, the responsivity of 348 A/W is obtained under the light intensity of 600 W/m², which can be compared to recently reported experimental 321 A/W [1], meaning that our proposed simulation scheme is useful to interpret the experimental results and to design the higher responsivity photodetectors. [1]S. Fukushima et al., Photogating for small high-responsivity graphene middle-wavelength infrared photodetectors *Optical engineering* **59**, 037101 (2020).

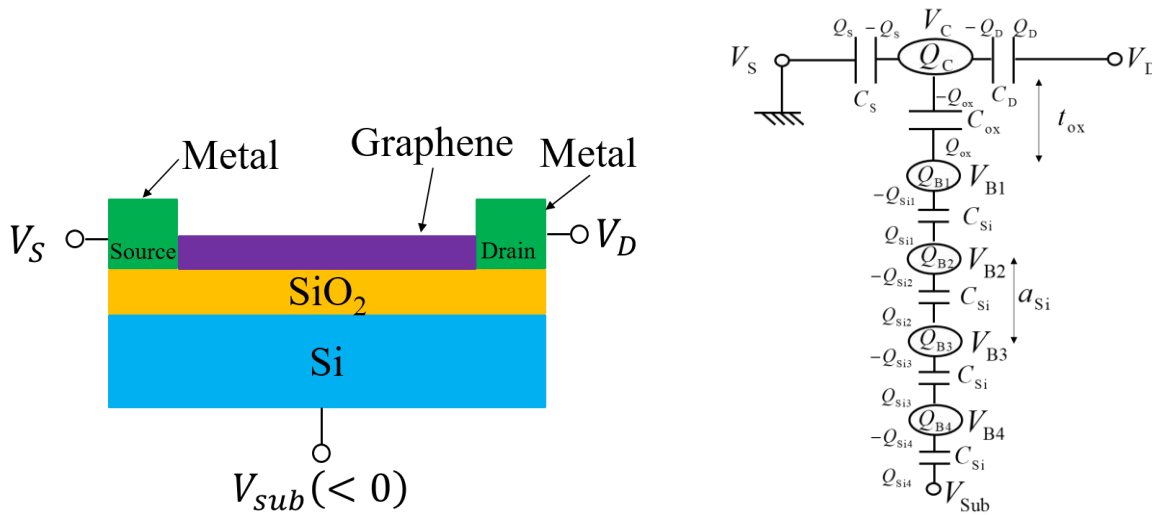


Fig.1: Schematic illustration of graphene photodetectors incorporating the photo-gating effect (left) and the capacitance-based model of the photodetectors (right).

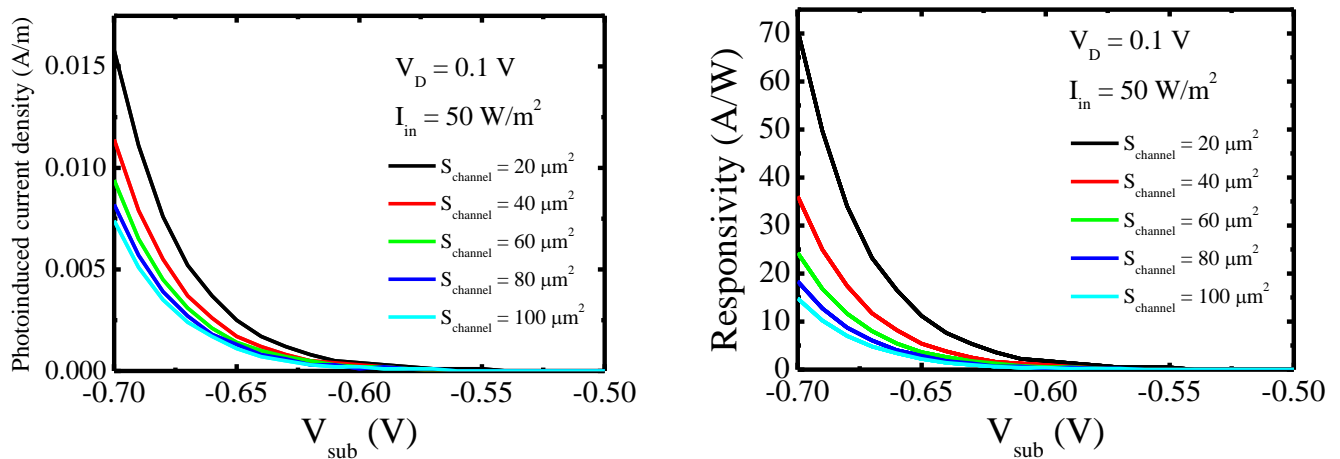


Fig.2: Photo-induced current density (left) and responsivity (right) as a function of the voltage applied at the bottom of the silicon substrate.

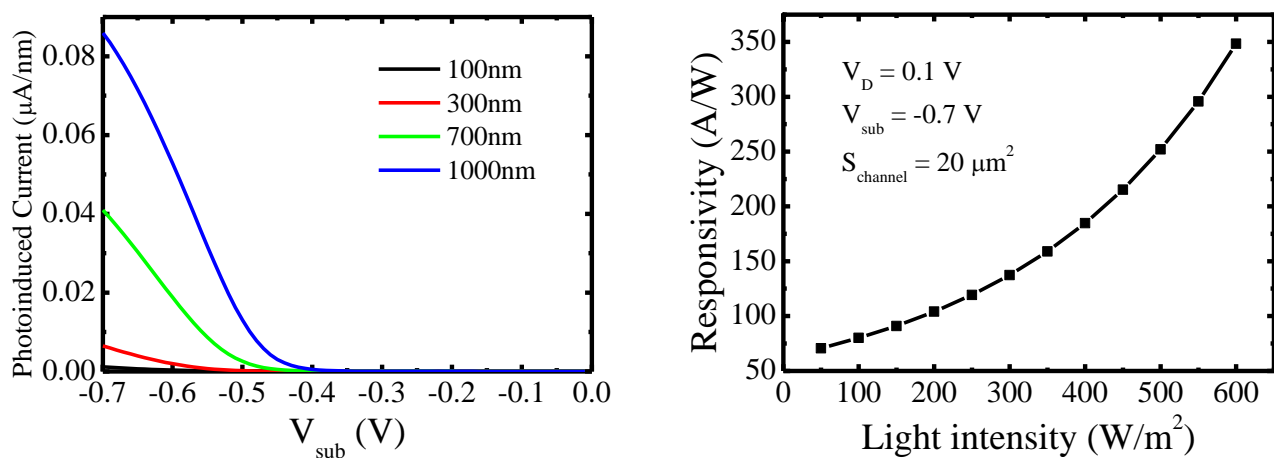


Fig.3: Photo-induced current corresponding to various wavelengths (left) and responsivity corresponding as a function of the intensity of light irradiated into the graphene channel (right).

Second-order Hall effect in insulators: the effect of interband Berry curvature dipole

Mahmut Sait Okyay, Beomseop Kim, Noejung Park

*Department of Physics, UNIST, UNIST-gil 50, Ulsan 44919, Republic of Korea
noejung@unist.ac.kr*

Noncentrosymmetric conducting materials have been shown both theoretically and practically to exhibit second-order Hall current even in the presence of time-reversal symmetry. Moreover, this nonlinear effect has been used to detect the Berry curvature of these materials via the relationship between the nonlinear response and the Berry dipole. [1,2] Here, we introduce the nonlinear Hall effect in a wide range of insulating systems. We first constructed the formalism from both the quantum perturbation theory and the semi-classical transport theory of insulators. To support our theory, we examined the oscillating second-order transverse electric current of various inversion-broken insulating materials as a response to applied linear polarized light. We performed real-time time-dependent density functional theory calculations for a CO molecule and topologically trivial (hexagonal boron nitride) and nontrivial (bismuthene) two-dimensional (2D) insulators. Irrespective of the dimension or topologic character, all samples exhibit second-order Hall current, which is found to be sensitive to the light polarization direction. Furthermore, the effect becomes visible when the light frequency exceeds one-half the bandgap energy; this effect is correlated with the interband Berry dipole of 2D systems in the sub-bandgap regime. This study suggests a new type of nonlinear Hall effect and provides methods to detect the Berry curvature, the band structure, and the symmetry properties of the insulators.

[1] I. Sodemann et al., Phys. Rev.Lett., **115**, 21 (2015)

[2] Q. Ma et al., Nature, **565**, 7739 337 (2019)

Time-dependent density functional theory calculations for spin-phonon-polarization dynamics and band topology

Mahmut Sait Okyay, Beomseop Kim, Noejung Park

Department of Physics, UNIST, UNIST-gil 50, Ulsan 44919, Republic of Korea
noejung@unist.ac.kr

Topological characterization has now been a key ingredient of present materials study, and global properties immune to local perturbations have been suggested in terms of topological invariants. Topological numbers of real materials have been evaluated through the theories of linear responses over the static ground electronic structure [Kubo formula]. Here, we present that the real-time dynamics can be alternatively used in the evaluation of topological state. By tracing the real-time evolution of the system, incurred by a time-evolving parameter of Hamiltonian, we can obtain the Berry phase accumulated over the time-evolving wave function. As an example, we deal with a trivial insulator, a spin-frozen valley-Hall system, a spin-frozen Haldane-Chern insulator, and a quantum spin-Hall insulator. [1] We also demonstrate that the TDDFT-based real-time dynamics can be an efficient tool for nonlinear dynamics of strongly coupled system. We present the spin dynamics of MoS₂ induced by a pumped phonon through strong spin-orbit coupling. [2] High harmonic responses and nonlinear Hall current under a high intensity light field will be demonstrated. [3] Specifically, we focus on the second-order nonlinear Hall current which can be thought of a new method revealing the Berry curvature distribution.

[1] D. Shin et al., *PNAS*, **116** (10), 4135-4140 (2019)

[2] D. Shin et al., *Nat. Commun.*, **9**, 638 (2018)

[3] M. S. Okyay et al., *Phys. Rev. B* **102**, 104304 (2020)

A Godunov-type Stabilization Scheme for Solving the Stationary and Transient Boltzmann Transport Equation

Paul Luckner, Hendrik Leenders, Tobias Linn, Maziar Noei, Christoph Jungemann

*Chair of Electromagnetic Theory, RWTH Aachen University, 52072 Aachen, Germany
pl@ithe.rwth-aachen.de*

We present a novel deterministic method of solving the coupled system of Poisson's equation and Boltzmann Transport Equation (BTE) using a modified version of the well-established Godunov's scheme [2]. The method is applied to a one-dimensional gallium arsenide (GaAs) Gunn-diode of 1.3 μm length [1], shown in Fig. 1.

The electron's k-space is approximated by 3 isotropic valleys of different multiplicities. Using rotational symmetry along the transport direction allows for projecting the valleys onto a 2D k-space. Triangulation of the k-space along equi-energy spheres yields triangular toroids as finite k-volumes.

Within a spatial cell the potential is approximated piecewise-constant. Therefore, the k-space can be easily discretized via a finite volume method (FVM). Another FVM along the spatial dimension leads to a Riemann problem at the interfaces which is solved by Godunov's scheme under the condition of flux conservation [3].

Numerically stable solutions are obtained under stationary, small-signal as well as transient conditions, see Figs. 1 to 4 and 6. The positivity of the electron's phase space distribution is fulfilled by construction even when considering GaAs's polar optical phonon which shows highly angle-dependent scattering behavior. Godunov's scheme introduces strong artificial damping at frequencies above 10 THz, but refining the spatial grid leads to a reduction in damping, cf. Fig. 5.

Godunov's scheme yields a straight-forward approach to implement transient simulations which is stable even for the Forward Euler scheme but implicit schemes are more efficient. First order implicit time integration methods, e.g. the Backward Euler (BE) method, introduce another source of artificial damping. By using higher-order methods, such as a trapezoidal rule (TR) or BDF2, one can reduce the damping as can be seen in Fig. 6 where a constant time step has been chosen for better comparison. Since we applied an ideal voltage source Gunn-oscillations are suppressed. Oscillations can occur when the admittance has a negative real part (see Fig. 4) and a finite load is attached. The largest negative real part of the admittance at 3V DC is found at 150 GHz near which the most powerful oscillations might occur.

We gratefully acknowledge the financial support by the DFG under contract number *JU 406/10-1*.

References

- [1] S. García et al. "Time-domain Monte Carlo simulations of resonant-circuit operation of GaN Gunn diodes". In: *2013 Spanish Conference on Electron Devices*. 2013, pp. 79–82. DOI: 10.1109/CDE.2013.6481347.
- [2] S. K. Godunov. "A difference method for numerical calculation of discontinuous solutions of the equations of hydrodynamics". In: *Matematicheskii Sbornik* 47(89) (3 1959), pp. 271–306.
- [3] Maziar Noei, Tobias Linn, and Christoph Jungemann. "A numerical approach to quasi-ballistic transport and plasma oscillations in junctionless nanowire transistors". In: *Journal of Computational Electronics* 19 (2020), pp. 975–986. DOI: 10.1007/s10825-020-01488-4.

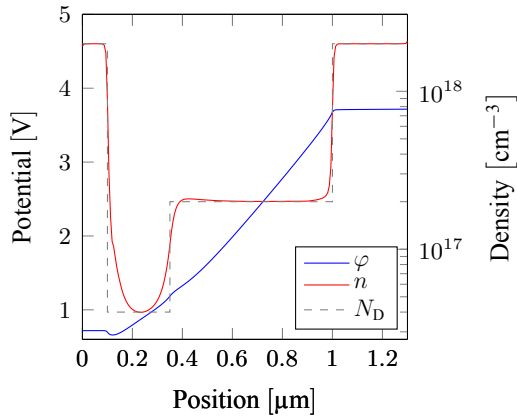


Figure 1: Potential φ , electron density n , and donor doping N_D .

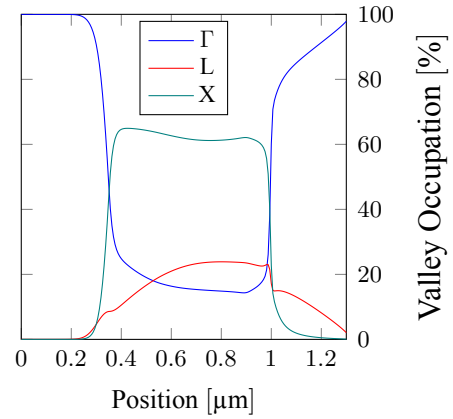


Figure 2: Valley occupation numbers o^ν for $\nu = \Gamma, L, X$ valleys.

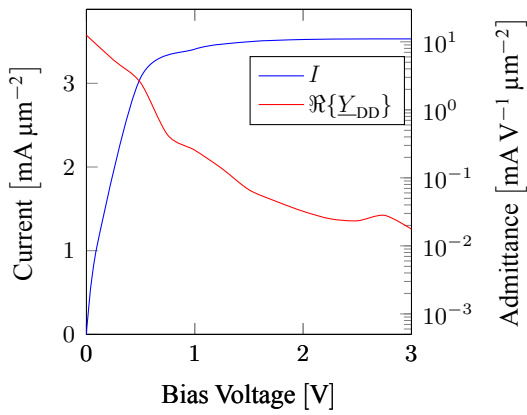


Figure 3: Current-voltage characteristic and real part of admittance $\Re\{Y_{DD}\}$ at $f = 0$ Hz.

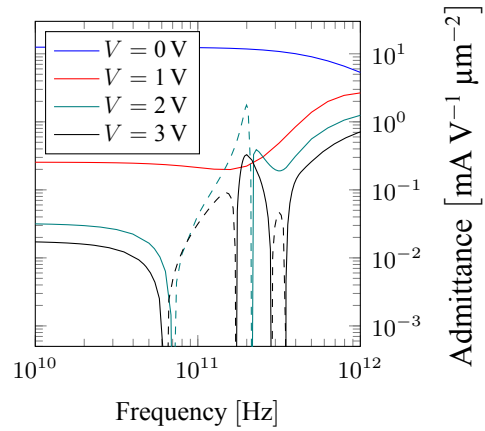


Figure 4: Real part of admittance $\Re\{Y_{DD}\}$ for multiple bias points V . Dashed lines indicate intervals of negative real part.

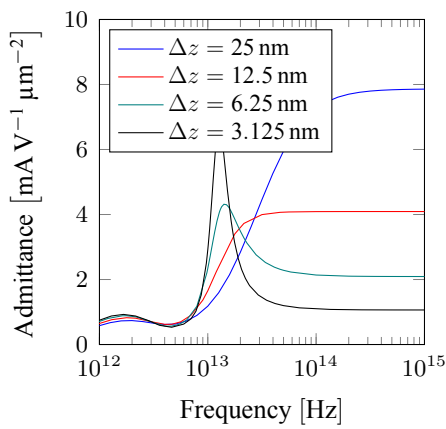


Figure 5: Real part of admittance $\Re\{Y_{DD}\}$ at high frequencies f for multiple spatial grid spacings Δz .

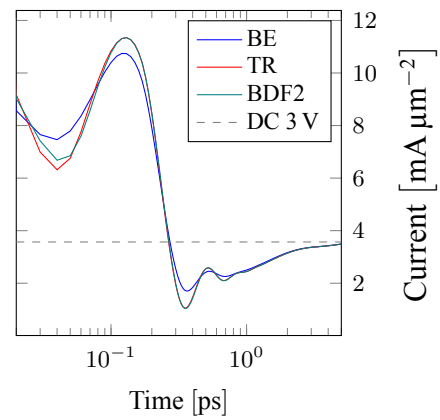


Figure 6: Current evolution for an instantaneous change in bias voltage from 0 to 3 V. All time integration schemes use a constant time step of $\Delta t = 10$ fs.

Dynamic Modelling of Quantum Transport within MGFETs

Lukas Schulz, Mathias Pech, Dirk Schulz

Chair for High Frequency Techniques, TU Dortmund, Germany

dirk2.schulz@tu-dortmund.de

The time-dependent analysis of quantum transport within MGFETs or quantum wires is of essential importance for their design. In order to analyze these components with the associated time-dependent effects, quantum kinetic models are important. The non-equilibrium Greens-function formalism (NEGF) [1] and the Wigner formalism [2] are usually available. Time-dependent simulations based on the NEGF are challenging in terms of numerical effort, especially for studies of non-ballistic transport [3]. The Wigner formalism, on the other hand, has some advantages in terms of numerical implementation and efficiency, as in the latter case, quantum transport is described in the phase space. This enables a description of coherent and incoherent phenomena, which can be taken into account by including suitable scattering operators [4].

Methodologies are needed to significantly reduce the computing time involved in the numerical analysis. For the analysis of MGFETs or especially quantum wire applications, in which the transport takes place in a preferred direction, there is the option of reducing the spatially three-dimensional problem to a spatially one-dimensional problem with regard to the transport direction. A spatial discretization takes place in the direction of transport, whereby the eigensolutions with their eigenenergies, also called modes, are determined in the lateral direction to the transport direction solving the Schrödinger equation [5, 6]. The wave function can be expanded according to these modes, so a one-dimensional problem arises, which then is solved by the von Neumann equation in center mass coordinates, which, with a spatial approximation based on a Finite Volume method and an expansion of the solution in direction of the relative coordinate on the basis of exponential functions, transforms into a Quantum Liouville von Neumann equation (QLNE) corresponding to the Wigner formalism [7].

- [1] P. Vogl et al., *J. Comput. Electron*, **9**, doi: 10.1007/s10825-010-0313-z (2010)
- [2] J. Weinbub et al., *Appl. Phys. Rev.*, **5**, doi: 10.1063/1.5046663 (2018)
- [3] E. P. et al., *Phys. Rev. B*, **82**, doi: 10.1103/PhysRevB.82.035446 (2010)
- [4] R. I. et al., *Phys. Rev. B*, **96**, doi: 10.1103/PhysRevB.96.115420 (2017)
- [5] R. V. et al., *J. Appl. Phys.*, **92**, doi: 10.1063/1.1503165 (2002)
- [6] Z. R. et al., *IEEE Trans. Electron Devices*, **50**, doi: 10.1109/TED.2003.816524 (2003)
- [7] L. Schulz et al., *IEEE Trans. Nanotechnol.*, **17**, doi: 10.1109/TNANO.2018.2868972 (2018)
- [8] B. A. Biegel et al., *Phys. Rev. B*, **54**, doi: 10.1103/PhysRevB.54.8070 (1996)

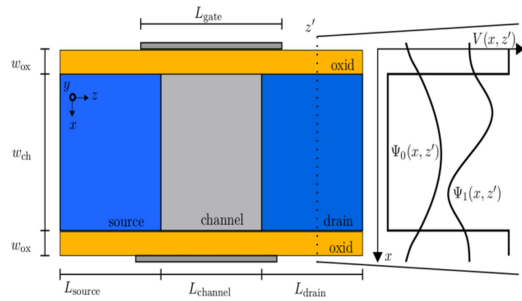


Fig.1: Schematic image of an InGaAs-DGFET with $w_{ox}=1nm$, $w_{ch}=3nm$, $L_{source}=L_{drain}=15nm$, $L_{channel}=10nm$. The potential profile V and the quantized wave functions ψ are shown. The donor concentration at source and drain is given by $N=2 \cdot 10^{19} cm^{-3}$.

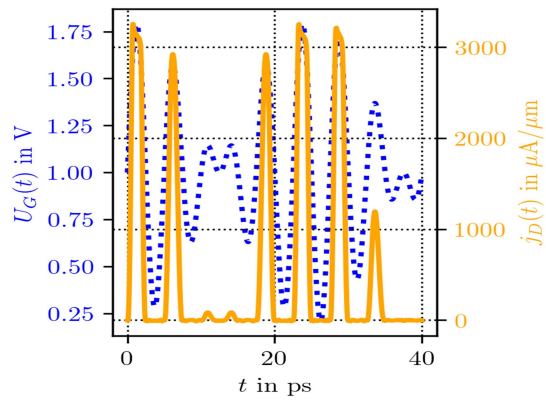


Fig.3a: Time dependent behavior of the current j_D and the applied voltage U_G in the case of a class C amplifier operation mode when considering the dynamic regime. Here, the applied voltage is defined by $U_G = 1V + 0.4V \sin(2\pi f_1 t) + 0.4V \sin(2\pi f_2 t)$ at $f_1 = 180 GHz$ and $f_2 = 220 GHz$

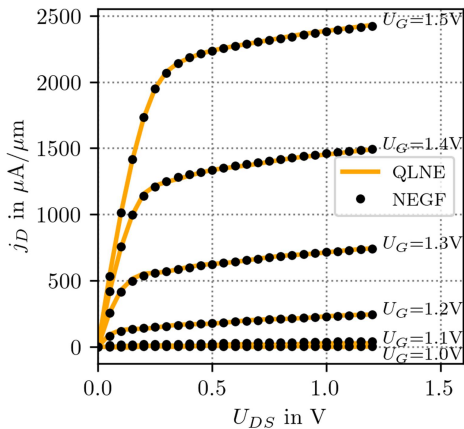


Fig.2: j_D-U_{DS} characteristic. Results of the proposed approach (QLNE) for the stationary regime compared with those from the NEGF approach (NEGF). Hereby, a self-consistent calculation [8] was carried out taking the Hartree potential into account, but the coupling between the individual modes and the scattering were neglected. The results obtained for the stationary case are compared with the NEGF formalism and show an excellent coincidence.

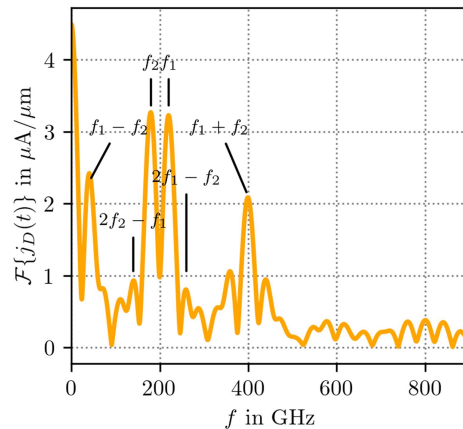


Fig.3b: The Fourier transform of the time dependent current is shown. As a consequence of intermixing (class C), the use of signals at 180 GHz and 220 GHz for example leads to an up converted larger frequency at 400 GHz and a down converted lower frequency at 40 GHz.

Parallel Solver Study for Solving the Boltzmann Transport Equation using Spherical Harmonics Expansions on Supercomputers

Felipe Senra Ribeiro¹, Karl Rupp¹, and Tibor Grasser¹

¹ *Institute for Microelectronics, TU Wien, Gußhausstraße 27-29/E360, A-1040 Wien, Austria
{ribeiro|rupp|grasser}@iue.tuwien.com*

The deterministic numerical solution of the Boltzmann Transport Equation requires Gigabytes of main memory even for spatially 2D device simulations. While detailed 3D device simulations have already been demonstrated using spherical harmonics expansions [1], it is desirable to run simulations at higher resolution - thus requiring even more memory - and to further reduce simulation time. To tackle both challenges, we have investigated how the free open-source simulator ViennaSHE [1] can be extended to compute the first scalable numerical solutions of the Boltzmann Transport Equation for semiconductors on large-scale clusters and supercomputers. In this work we focus on the linear solver stage, for which we have evaluated an algebraic multigrid solver (schematically shown in Fig. 1) [2][3][4] and a parallel sparse direct solver [5], both available through the PETSc library [6].

We have simulated the carrier distribution for a given electrostatic potential distribution in a 3D FINFET (Fig. 2) and a 2D n-channel MOSFET. Fig. 3 and Fig. 4 show our observed change of total solver time as the workload increases in proportion to the number of processes ('weak scaling'); this is typical for simulations that are re-run on a finer grid. We observe a near-optimal performance gain proportional to the number of processes used.

When keeping the problem size constant and increasing the number of processors to reduce simulation time ('strong scaling'), we see that the simulation time can be reduced by a factor of 2.25 when employing up to 16 processes for the MOSFET, and by a factor of 1.8 for the FINFET with 8 processes.

In both cases, algebraic multigrid has been identified as a promising candidate for scaling to hundreds of processes, while a parallel sparse direct solver provides the best performance at moderate problem sizes.

[1] K. Rupp et al., IEDM, 2011

[2] U. Trottenberg et al., Multigrid, Academic Press, 2000

[3] Howard Elman et al., Finite Elements and Fast Iterative Solvers, Oxford Science Publication, 2nd Ed

[4] T. Fullenbach et al., Application of an algebraic multigrid solver to process simulation problems, SISPAD, 2000

[5] X.S.Li et al., SuperLU Users' Guide, 1999

[6] S. Balay et al., PETSc Users Manual, ANL-95/11 - Revision 3.14, 2020

Acknowledgments. The financial support by the Austrian Science Fund (FWF) project FWF-P 29119-N35 is acknowledged. Some of computational results presented have been achieved using the Vienna Scientific Cluster (VSC).

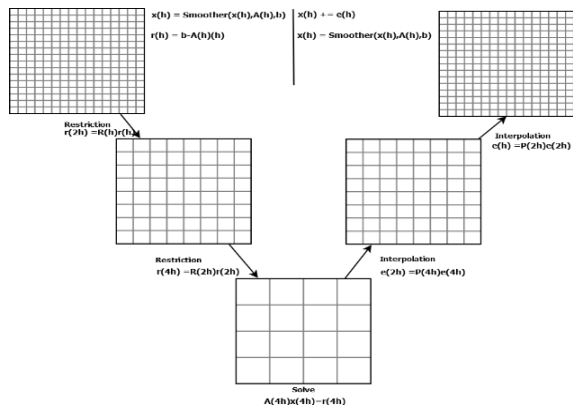


Fig. 1: A 2 level Multigrid hierarchy, where the original linear problem is Restricted two times to a coarsen problem, which is solved, and the solution is Interpolated twice to the original problem, then smoothed to remove some high frequency error.

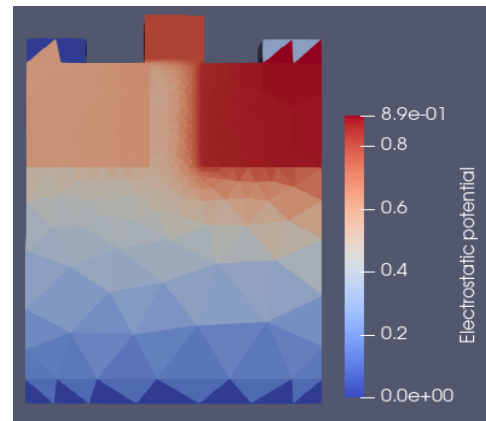


Fig. 2: Electrical Potential for the FINFET when applying 0.3 Volt between the source and the drain with 0.8 Volt at the gate.

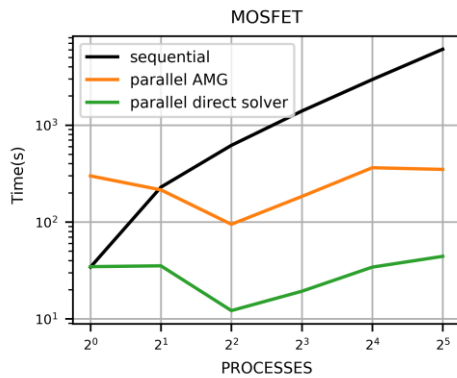


Fig. 3: Weak-scaling analysis of the MOSFET simulation. The direct solver is better for small problems, while multigrid achieves slightly better weak-scalability.

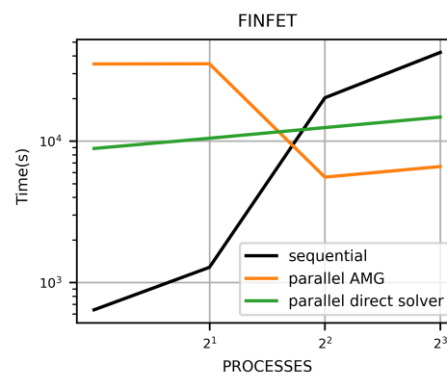


Fig. 4: Weak-scaling analysis of the FINFET simulation. The parallel solvers show large overhead when run with only one process, but are up to a factor of 2.25 faster for the larger problem sizes.

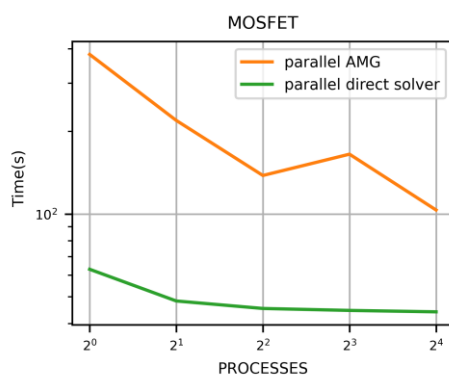


Fig. 5: Strong-scaling analysis of the MOSFET simulation. The AMG solver has higher benefit from additional processes but is still slower than the sparse direct solver overall.

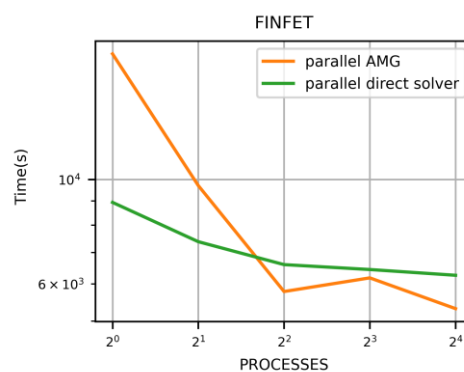


Fig. 6: Strong-scaling analysis of the FINFET simulation. Parallel AMG outperforms the parallel direct solver as soon as at least 4 processes are employed.

Ab initio quantum transport simulation of lateral heterostructures based on 2D materials: assessment of the coupling Hamiltonians

Adel M'foukh¹ and Marco Pala¹

¹ *Université Paris-Saclay, CNRS, Centre de Nanosciences et de Nanotechnologies,
F-91120 Palaiseau, France
Adel.mfoukh@c2n.upsaclay.fr*

Lateral heterostructures based on lattice-matched 2D materials are a promising option to design efficient electron devices such as MOSFETs [1], tunnel-FETs [2] and energy-filtering FETs [3]. In order to rigorously describe the transport through such heterostructures, an ab-initio approach based on density-functional theory (DFT) is almost unavoidable due to the lack of physical characterization of the interfaces. However, due to the computational cost of including the DFT Hamiltonian describing the whole interface region in transport calculations, the matrix describing the coupling between the two materials is often approximated as the one of a single material. Here, we focus on a simple lateral heterostructure based on bi-layer/mono-layer PtSe₂ and compare the use of the coupling Hamiltonian matrix of the mono-layer PtSe₂ with the one extracted from the DFT simulation of the whole bi-layer/mono-layer PtSe₂ interface. To perform our self-consistent quantum transport calculations, we used the NEGF method and a reduced basis composed of unit-cell restricted Bloch functions [4]. To compute the coupling Hamiltonian between the bi- and the mono-layer PtSe₂, we first performed a DFT simulation of the heterostructure sketched in Fig.1, where the dangling bonds at the interfaces are passivated by H atoms and all atomic positions have been relaxed. Hence, the plane-wave DFT Hamiltonian was transformed in the hybrid space having real-space along the x-axis and plane waves in the orthogonal directions, then, the block-matrix Hamiltonians representing the coupling between the two materials were extracted by selecting specific elements of the whole Hamiltonian and further reduced in the Bloch function basis.

Fig. 3 shows the transfer characteristics of the bi-layer/mono-layer PtSe₂ MOSFET in Fig.2 computed with either the coupling Hamiltonian of the mono-layer or the one extracted from the supercell in Fig 1. An appreciable difference is found at high V_{GS} values. Fig. 4 shows the comparison between the lowest conduction band (LCB) profile and the transmission probability of such a device computed with the two types of coupling matrix. The second method provides a more efficient coupling between the two materials and consequently a larger transmission. A similar analysis can be extracted from Figs. 5-6 showing the local density of states at high V_{GS} .

[1] G. Iannaccone et al. *Nat. Nanotechnol.* **13**, 183–191 (2018).

[2] J. Choukroun et al., *Nanotechnology* **30**, 025201 (2018).

[3] E. Marin et al., *ACS Nano*, **14**, 2, 1982-1989 (2020).

[4] M. G. Pala et al., *Phys. Rev. B.*, **102**, 045410 (2020).

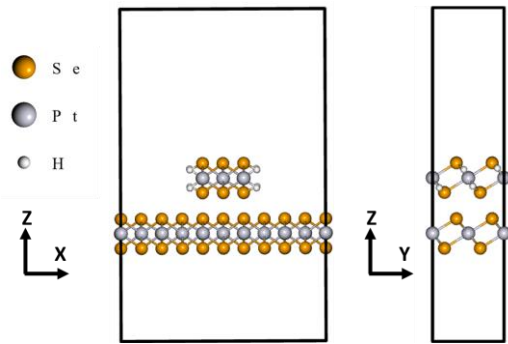


Fig.1: Sketch of the orthorhombic supercell used to simulate the monolayer/bilayer $PtSe_2$ lateral heterostructure. The dangling bonds at the interfaces were passivated with H atoms. Unit-cell vectors: $a_x=11.136 \text{ \AA}$, $a_y=6.429 \text{ \AA}$, $a_z=30.0 \text{ \AA}$.

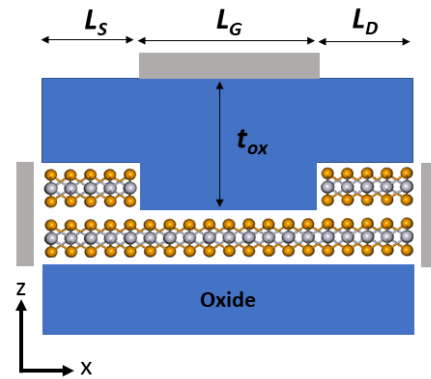


Fig.2: Sketch of the bi-layer/monolayer $PtSe_2$ single-gate MOSFET. Geometrical parameters: $L_S=L_D=11 \text{ nm}$, $L_G=15 \text{ nm}$, $t_{ox}=2 \text{ nm}$. The bi-layer is n-doped with a concentration of $N_D=5 \times 10^{13} \text{ cm}^{-2}$.

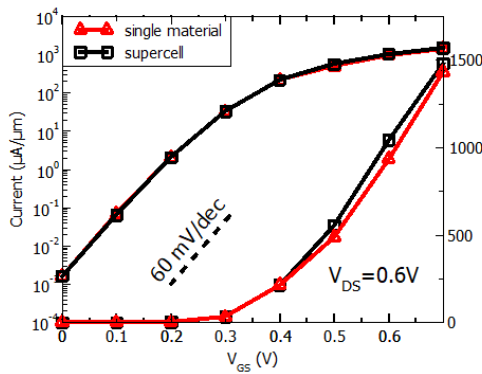


Fig.3: Transfer characteristics of the device in Fig. 2 computed by using the coupling matrix of the single material (mono-layer $PtSe_2$) and the one extracted from the supercell in Fig. 1.

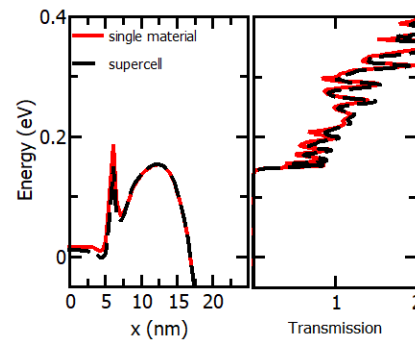


Fig.4: Conduction band profile and transmission probability computed at $V_{GS}=0.5 \text{ V}$ by using the coupling matrix of the single material and the one extracted from the supercell in Fig. 1.

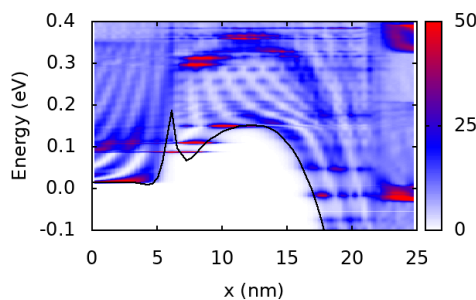


Fig.5: Lowest CB profile along the transport direction (black line) and LDOS of the device in Fig. 2 simulated with the coupling matrix of the monolayer. $V_{GS}=0.5 \text{ V}$.

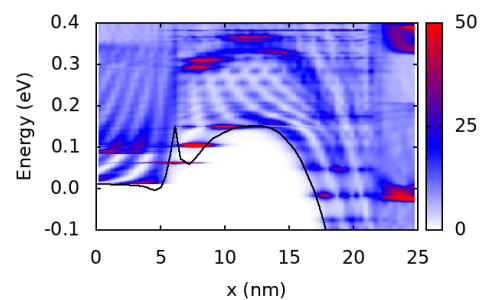


Fig.6: Same as in Fig. 5, but simulated with the coupling matrix extracted from the supercell in Fig. 1. A small difference can be detected at the interface between bi- and mono-layer ($x=7 \text{ nm}$).

Feature Scale Modeling of Fluorocarbon Plasma Etching for Via Structures including Faceting Phenomena

Frâncio Rodrigues¹, Luiz Felipe Aginsky¹, Alexander Toifl¹,
Andreas Hössinger² and Josef Weinbub¹

¹ *Christian Doppler Laboratory for High Performance TCAD,
Institute for Microelectronics, TU Wien, Gußhausstraße 27-29/E360, 1040 Wien, Austria.*

² *Silvaco Europe Ltd., Compass Point, St Ives, Cambridge PE27 5JL, United Kingdom.
rodrigues@iue.tuwien.ac.at*

With the continuous miniaturization of electronic device structures which is necessary to improve performance, plasma etching challenges continue to evolve in the semiconductor industry [1]. Higher aspect ratios and higher density features are required for new device technologies and the precise modeling of etching processes can greatly aid manufacturing [1]. To that end, we have implemented a modeling methodology for feature scale fluorocarbon reactive-ion-etching (RIE) and integrated it into Silvaco's Victory Process [2] simulator for evaluation purposes. The methodology (Fig. 1) integrates a bottom-up ray-tracing scheme [3] for the simulation of the fluxes associated with impinging plasma species. The fluxes feed a Langmuir set of surface coverage equations [4] (Figs. 2-4), which outputs either a substrate etching rate or a polymer deposition rate. The rates are provided to a level-set [5] topography engine which updates the geometry accordingly. We also implemented different angular yield functions for RIE and physical sputtering mechanisms (Fig. 5) to enable the reproduction of faceting phenomena [6]. We applied the developed methodology to a typical via etching of SiO₂ with an Ar/C₄F₈ plasma chemistry, adapting parameters from [4]. The simulated via (Fig. 6) was etched for 25s and exhibits a polymer sidewall; the shape and maximum thickness (17nm) agree with experimental data [4]. The faceting is observed at the mask material as expected (Fig. 6) and the tapering angle agrees with the experimentally observed angle of 45° [6]. The developed methodology can be extended to different materials and can be fully incorporated into TCAD workflows.

Acknowledgements. The financial support by the Austrian Federal Ministry for Digital and Economic Affairs and the National Foundation for Research, Technology and Development is gratefully acknowledged.

[1] T. Iwase et al., *Jpn. J. Appl. Phys.*, **58**, SE0802 (2019)

[2] Silvaco Victory Process, www.silvaco.com/tcad/victory-process-3d/ (2021)

[3] P. Manstetten et al., *Proc. Comput. Sci.*, **108**, 245-254 (2017)

[4] A. Magna et al., *J. Electroch. Soc.*, **150**, F178-F185 (2003)

[5] J. A. Sethian, Cambridge University Press, ISBN 0521645573 (1999)

[6] A. G. Nagy, *Microsc. Spectrosc. Electro.*, **132**, 689-693 (1977)

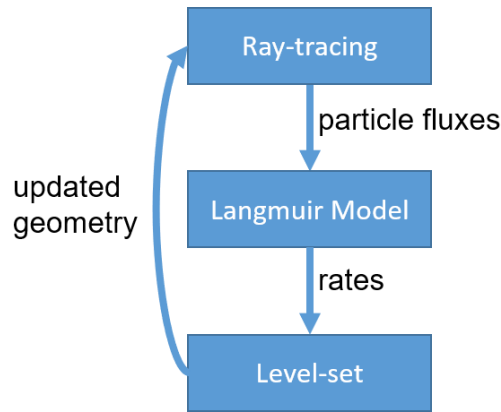


Fig. 1: Flow diagram of the developed methodology. Bottom-up ray-tracing is used to evaluate the flux of neutral, polymer, and ion particles for different geometries and source distributions. The set of equations (Fig. 3) is solved and outputs an etching or deposition rate to the level-set engine which evolves the surface accordingly.

Symbol	Description
Θ_x	Coverage
J_x	Flux
S_x	Sticking coefficient
Y_x	Yield of ion related mechanisms
k_x	Stoichiometric coefficient
R	Rate of deposition or etching
ρ	Density of substrate material

Fig. 2: Variables used to describe the coverage equations (Fig. 3). The coverages represent the fraction of the surface that is covered by a given species. The subscript x identifies either an evaporation mechanism (ev) or the involved chemical species: neutrals (n), polymers (p), ions (i), and neutrals over polymers (n/p).

$$\frac{d\Theta_n}{dt} = J_n S_n (1 - \Theta_n - \Theta_p) - J_i Y_n k_n \Theta_n - J_{ev} k_{ev} \Theta_n \approx 0 \quad (1)$$

$$\frac{d\Theta_p}{dt} = J_p S_p - J_i Y_{n/p} \Theta_p \Theta_{n/p} \approx 0 \quad (2)$$

$$\frac{d\Theta_{n/p}}{dt} = J_n S_{n/p} (1 - \Theta_{n/p}) - J_i Y_{n/p} \Theta_{n/p} \approx 0 \quad (3)$$

$$\Theta_p = \frac{J_p S_p}{J_i Y_{n/p} \Theta_{n/p}} \quad (4)$$

$\Theta_p > 1$ results in a deposition rate given by:

$$R_{dep} = \frac{J_i Y_{n/p} - J_p S_p}{\rho_p} \quad (5)$$

$\Theta_p < 1$ results in an etching rate given by:

$$R_{etch} = \frac{1}{\rho_{sub}} (J_i Y_n \Theta_n + J_i Y_s (1 - \Theta_n - \Theta_p) + J_{ev} k_{ev} \Theta_n) \quad (6)$$

RIE
sputtering
evaporation

Fig. 3: For each surface element and time step the system of equations for neutrals and polymer coverage (1)-(3) is solved under a steady-state condition. Each term represents a mechanism of addition or removal of species into the surface. The steady-state condition is applicable because the coverage mechanisms reach equilibrium much faster than the etching rate time scales [4].

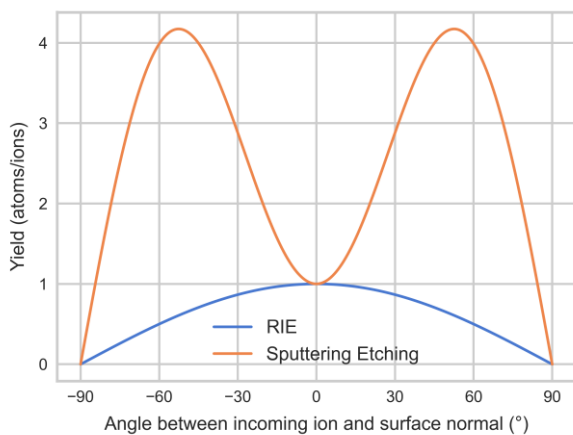


Fig. 5: Angular yield dependencies of RIE and sputtering etching mechanisms. The difference in angular dependencies between mechanisms influences the shape of the via and gives rise to faceting observed at the mask material (Fig. 6) [6].

Fig. 4: The value of the polymer coverage given by (4) determines whether a deposition or etching rate is applied to the local surface element. When Θ_p is larger than 1, the surface is covered in polymers, the set of equations simplifies to equation (3) and polymer deposition occurs (5). Otherwise, an etching rate (6) is applied.

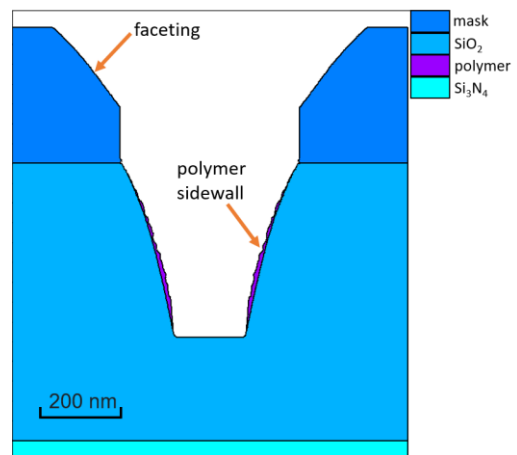


Fig. 6: The resulting SiO_2 via after 25s of etching by an $\text{Ar}/\text{C}_4\text{F}_8$ plasma. The maximum polymer sidewall thickness of 17nm agrees with experiments [4]. The faceting of 45° at the mask is expected for materials for which the main etching mechanism is sputtering [6].

Modeling GaN Nanowire and Nanofin FETs Electrostatics using Fast 2D/3D Schrödinger-Poisson Solver.

Viswanathan Naveen Kumar¹, Pranay Kumar Reddy Baikadi¹, Dragica Vasileska¹ and Michael Povolotskyi^{1,2}

¹ *School of ECEE, Arizona State University, Tempe, AZ, 85287-5706, USA*

² *Vantage Point Consulting Inc. USA*

Vkumar21@asu.edu (e-mail address of the corresponding author)

Gallium Nitride is a material of extreme interest for high-frequency and high-power applications. This has led to the development of GaN HEMTs and GaN nanowires. Computing carrier densities in such devices requires generic, accurate and fast solution of the coupled Schrödinger-Poisson problem to describe formation of the Q2DEG and Q1DEG, respectively. In this work, PETSc linear solver and SLEPc eigenvalue solver packages are used to achieve this goal.

GaN HEMTs retain the same topology as their GaAs counterparts. Split-gate nanostructures (Fig. 1a) and 3D Nanofin (NF) FETs [1] (Fig. 1b), realized by etching parallel mesa channels under the gate of AlGaN/GaN HEMTs [2], offer an alternative technology. A variant of the 3D NF FETs is the AlGaN/GaN MISFET (Fig. 1c), wherein a layer of Al₂O₃ surrounds the AlGaN/GaN fin [3]. Vertical confinement for the split-gate structure and the corresponding wavefunctions are shown in Fig. 2a. In Fig. 2b, we show the lateral confinement in the Schottky NF FET and the MISFET. Variation of the subband energies with fin width for the MISFET is shown in Fig. 2c. Carrier density in the center of the fin, as a function of gate bias, is shown in Fig. 3a, from where we can extract the threshold voltage of the MISFET. We find that under positive bias, AlGaN/GaN MISFET has two conduction channels: (1) due to the confined 2DEG at the hetero-interface, and (2) due to the formation of side-wall channels under the vertical gates (Fig. 3b). These two conduction pathways exhibit different transport characteristics, and, consequently, differently affect the I-V characteristics. As an example, we will show confined systems that exhibit enhanced electron mobilities [4], which will be computed from the self-consistent solution of the Schrödinger-Poisson-Boltzmann problem.

- [1] M. F. Fatahilah, K. Stempel, F. Yu, S. Vodapally, A. Waag, and H. S. Wasisto, *Micro Nano Eng.*, vol. 3, no. December 2018, pp. 59–81, 2019.
- [2] K. Ohi, J. T. Asubar, K. Nishiguchi, and T. Hashizume, *IEEE Trans. Electron Devices*, vol. 60, no. 10, pp. 2997–3004, 2013.
- [3] J. H. Lee *et al.*, *Solid. State. Electron.*, vol. 97, pp. 66–75, 2014.
- [4] V. N. Kumar and D. Vasileska, *J. Appl. Phys.*, vol. 125, no. 11, 2019.

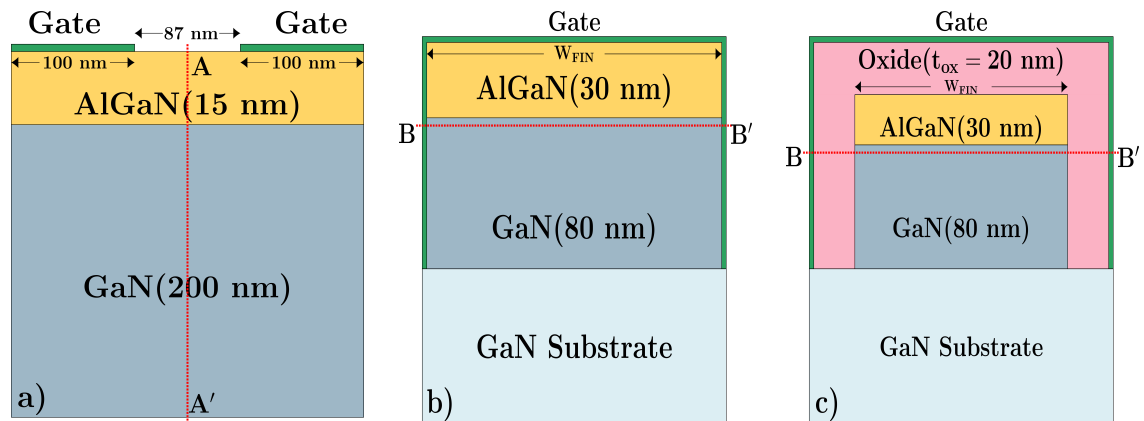


Figure 1: Cross section of different AlGaIn/GaN FET variants. **a)** Split-Gate AlGaIn/GaN nanowire. **b)** AlGaIn/GaN FinFET with Schottky gate. **c)** AlGaIn/GaN MISFET with Al₂O₃.

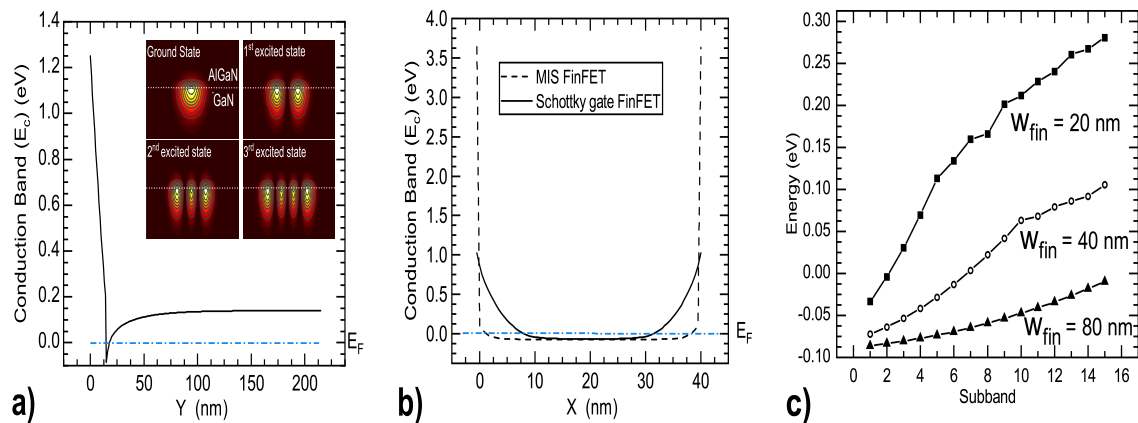


Figure 2: **a)** Conduction band (CB) profile along cutline A-A' of the split-gate nanowire (figure 1a). Inset shows the probability density functions of the first four eigenvalues. **b)** The CB profile along the cutline B-B' of the FinFETs shown in figure 1b) and 1c). **c)** The lowest 15 subband energies for FinFET structure from figure 1c) and for three different values of the fin widths.

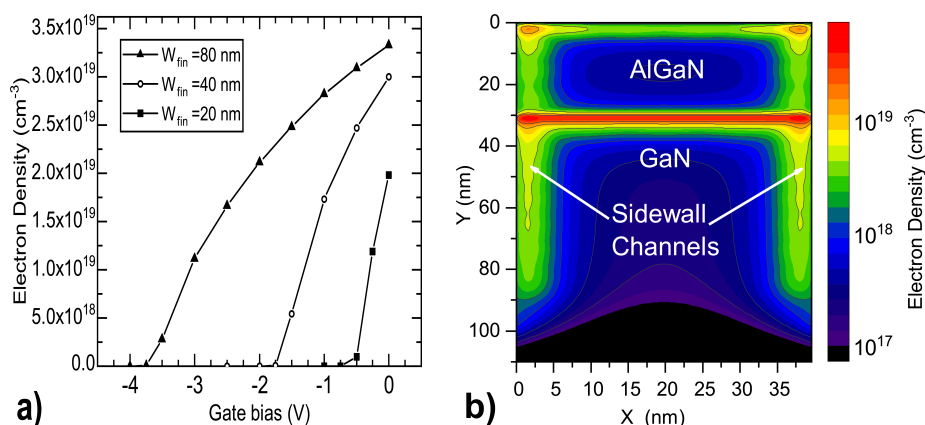


Figure 3: **a)** The electron density at the center of the fin in the MISFET from figure 1c) as a function of gate bias, for three different fin widths. The threshold voltage is less negative as the fin width reduces. **b)** Electron density in the MISFET at a positive gate bias of 2.0 V. Sidewall MOS like channels form along the vertical gates.

A practical Peierls phase recipe for periodic atomistic systems under magnetic fields

Alessandro Cresti¹

¹ *Univ. Grenoble Alpes, Univ. Savoie Mont Blanc, CNRS, Grenoble INP, IMEP-LAHC, 38000 Grenoble, France*
alessandro.cresti@grenoble-inp.fr

The Peierls phase conveniently describes the orbital effect of a relatively weak magnetic field \mathbf{B} on atomistic systems represented by a tight-binding-like Hamiltonian [1]. The phase multiplies the Hamiltonian elements between couples of atomic orbitals and is proportional to the line integral of the vector potential \mathbf{A} (with $\mathbf{B} = \nabla \times \mathbf{A}$) along the straight path between them. The Peierls phase changes under gauge transformations $\mathbf{A} \rightarrow \mathbf{A} + \nabla\chi$, but its circulation as well as the physical observables are gauge independent.

For periodic systems, or systems with periodic components (as contacts and probes in a Hall bar), a generic gauge will not guarantee the Hamiltonian to be invariant under spatial translations. However, this invariance is desirable to allow the use of convenient techniques for electronic structure and transport simulations, as the Bloch theorem for the Hamiltonian diagonalization, or the Sancho-Rubio algorithm [2] for determining the contact self-energies.

In this contribution, by a proper gauge choice, I will provide general ready-to-use formulas to determine Peierls phase factors that preserve the translation symmetry of any periodic quasi-one-dimensional or two-dimensional system under a homogeneous magnetic field [3]. Some examples of applications will be briefly illustrated, see figures. First, I will present the case of a metallic carbon nanotube in high magnetic fields. Depending on the angle between field and nanotube axis, the electronic structure exhibits a rich physics ranging from Landau states to Aharonov-Bohm effect. Then, based on Green's function transport simulations, we will discuss the importance of disorder for the observation of extended Hall resistance plateaus in 2DEG Hall bars. Finally, I will present the case of periodic 2D graphene with Gaussian bumps, where the induced strain makes Landau levels dispersive and lifts the valley degeneracy.

The provided formulas represent a practical and useful tool for the simulation of electronic and transport properties of mesoscopic systems in the presence of magnetic fields.

[1] R. Peierls, *Z. Phys.*, **80**, 763 (1933).

[2] M. P. Lopez Sancho et al., *J. Phys. F*, **15**, 851 (1985).

[3] A. Cresti, *Phys. Rev. B.*, **103**, 045402 (2021).

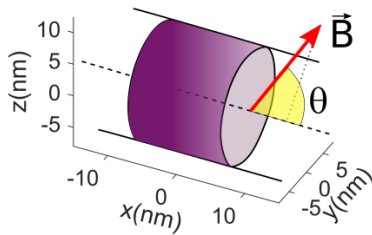


Fig.1: Sketch of a metallic carbon nanotube with chirality (204,0), corresponding to a circumference of 50 nm. The homogeneous magnetic field \mathbf{B} forms an angle θ with the nanotube axis.

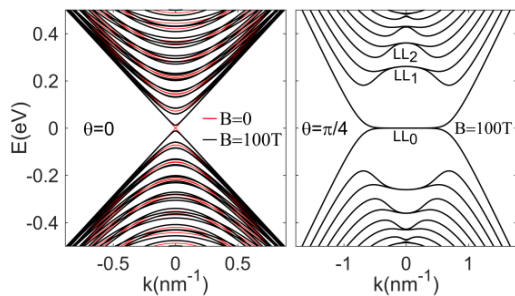


Fig.2: Band structure of the metallic carbon nanotube of Fig. 1 in the absence and in the presence of a 100 T magnetic field with $\theta=0$ and 45° . The magnetic field along the nanotube axis opens a small gap due to Aharonov-Bohm effect. When the magnetic field is not along the nanotube axis, dispersive Landau levels appear.

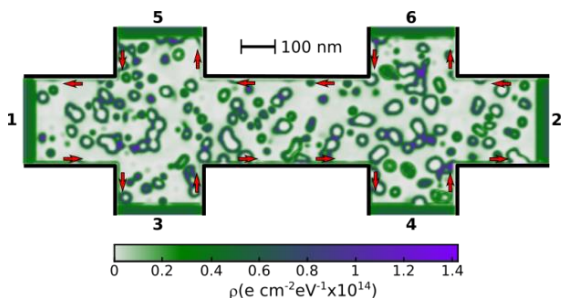


Fig.3: Six-terminal Hall bar obtained in a GaAs/AlGaAs 2DEG with effective mass $0.068 m_e$. Terminals 1 and 2 are source and drain contacts, while terminals 3-6 are voltage probes. In the presence of impurities (here with density $7 \times 10^{10} \text{ cm}^{-2}$ and Gaussian potential profile with maximum height 150 meV) and under high magnetic fields, the current flows along the edges, while localized states form around the impurities, thus pinning the Fermi energy and leading to extended Hall resistance plateaus, see Fig. 4. The color map represents the density of states in such a situation. The red arrows indicate the current flow.

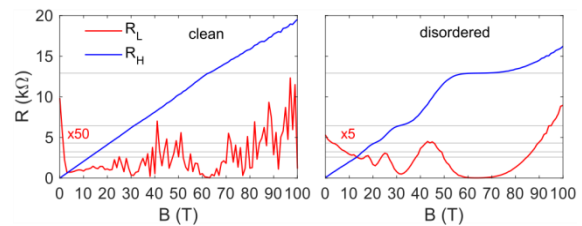


Fig.4: Longitudinal R_L and Hall R_H resistances as a function of the magnetic field B in clean and disordered Hall bars with the geometry illustrated in Fig. 3, for average charge density $3 \times 10^{13} \text{ e/cm}^2$, temperature 77.36 K and drain current $0.1 \mu\text{A}$. Hall plateaus are observed in the disordered case, in correspondence of the R_L dips. The horizontal lines indicate the resistance quantum $h/(2e^2) \approx 12.9 \text{ k}\Omega$ and its submultiples.

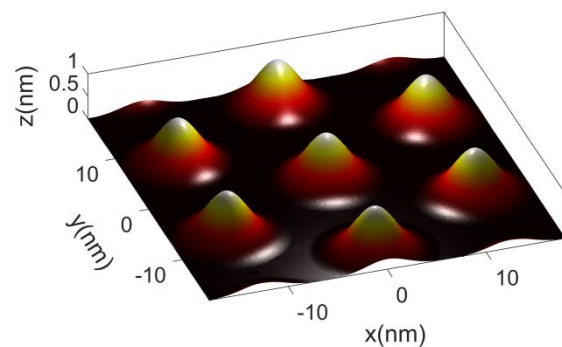


Fig.5: Superlattice of bumps in two-dimensional graphene. The bumps have a Gaussian profile with a height of 1 nm. This results in a tensile strain on the sides of the bumps. The superlattice is triangular and thus has a hexagonal Brillouin zone.

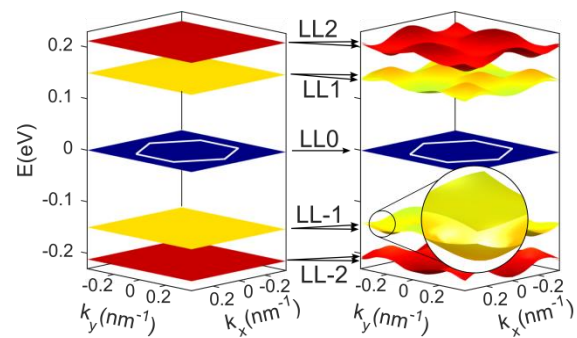


Fig.6: Low-energy band structure for 2D graphene in the absence (left) and in the presence (right) of the superlattice of periodic bumps described in Fig. 1, under a 22.74 T orthogonal magnetic field. The first Brillouin zone is indicated by a white hexagon. In flat graphene, the usual sequence of Landau levels appears. Strain makes Landau levels dispersive and removes the valley degeneracy. Only the Landau level with zero energy is unchanged, since its value is independent of the Fermi velocity of low energy electron, which is affected by strain.

Recursive open boundary and interfaces method for material property predictions

James Charles¹, Sabre Kais^{2,3}, Tillmann Kubis^{1,4,5,6}

¹ *School of Electrical and Computer Engineering, Purdue University, West Lafayette, IN, USA*

² *Department of Physics and Astronomy, Purdue University, West Lafayette, IN, USA*

³ *Department of Chemistry, Purdue University, West Lafayette, IN, USA*

⁴ *Network for Computational Nanotechnology, Purdue University, West Lafayette, IN, USA*

⁵ *Purdue Center for Predictive Materials and Devices, West Lafayette, IN, USA*

⁶ *Purdue Institute of Inflammation, Immunology and Infectious Disease, West Lafayette, IN, USA*

tkubis@purdue.edu

Simulations are essential to accelerate the discovery of new materials and to gain full understanding of known ones. Although hard to realize experimentally, periodic boundary conditions are omnipresent in material simulations. We introduce ROBIN (recursive open boundary and interfaces) [1], the first method allowing open boundary conditions in material and interface modeling. The computational costs are limited to solving quantum properties in a focus area which allows explicitly discretizing millions of atoms in real space and to consider virtually any type of environment (be it periodic, regular, or random). Figure 1 verifies the local density of states resulting of an all-real space ROBIN calculation of pristine graphene against analytical results. The impact of the periodicity assumption is assessed in detail with silicon dopants in graphene. Graphene was confirmed to produce a band gap with periodic substitution of 3% carbon with silicon in agreement with published periodic boundary condition calculations [2]. Instead, 3% randomly distributed silicon in graphene only shifts the energy spectrum. The predicted shift agrees quantitatively with published experimental data [2]. The shift is a linear function of the Si concentration (see Fig. 3) in agreement with the small linear response a few-percent Si perturbation should yield.

The ROBIN method allows to consider the interface between graphene alloyed with 3% randomly and 3% periodically distributed Si. Figure 4 shows the significant density of states difference these only stoichiometrically identical systems show.

In summary, we show that assuming periodicity elevates a small perturbation of a periodic cell into a strong impact on the material property prediction. Periodic boundary conditions can be applied on truly periodic systems only. More general systems should apply an open boundary method for reliable predictions.

[1] Charles J. et al., *ACS Materials Lett.* **2**, 247 (2020)

[2] Zhang, S. J. et al., *Nanoscale* **8**, 226 (2015)

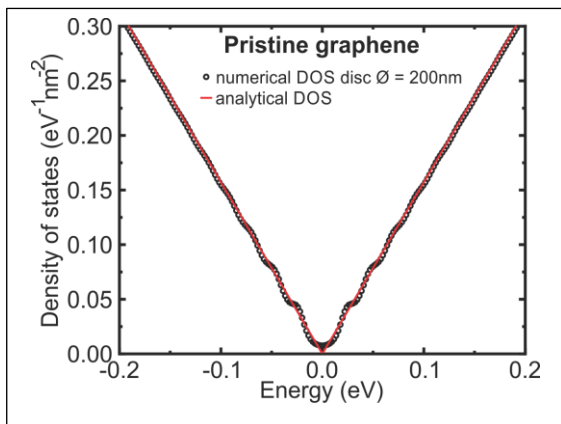


Fig.1: Verification of the ROBIN method against analytical results: The numerical density of states resulting of the ROBIN method (symbols) of graphene discs agree better with the analytical density of states (line) with larger discretized disc diameter.

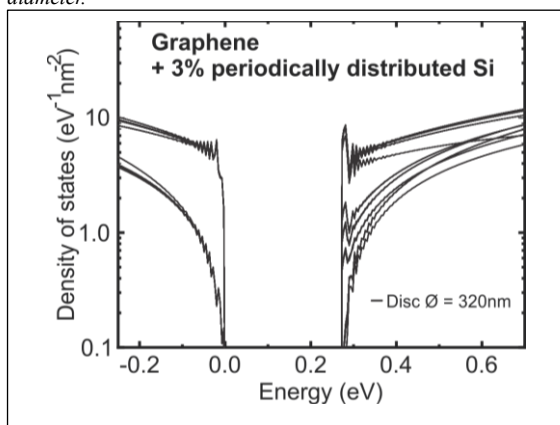


Fig.2: The density of states of graphene with 3% periodically distributed silicon solved with the ROBIN method reproduces the 0.28eV band gap of Ref.19 when the on-site energy of Si is chosen as 4.75eV. The 282 individual atoms considered in the DOS-solution area fall into 9 distinct groups of DOS lines – corresponding to the 9 different chemical atom environments in the graphene + 3% Si unitcell.

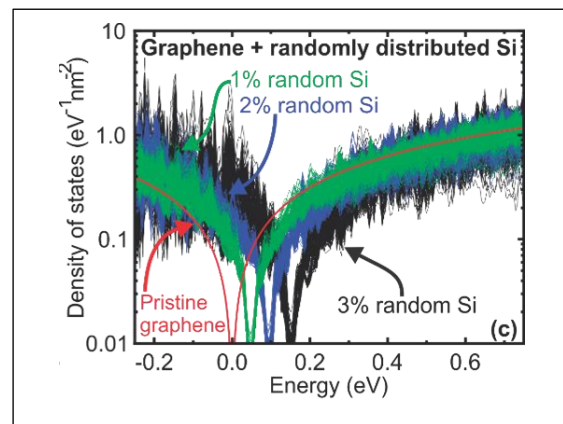


Fig.3: The DOS solved in the ROBIN method of randomly distributed Si atoms in graphene does not show a bandgap. Instead, increasing Si content shifts the DOS to higher energies by about 47meV per Si-percentage (i.e. about 1% of the assumed onsite energy difference of carbon and silicon atoms). This value is in quantitative agreement with the experimental observations in Ref.2

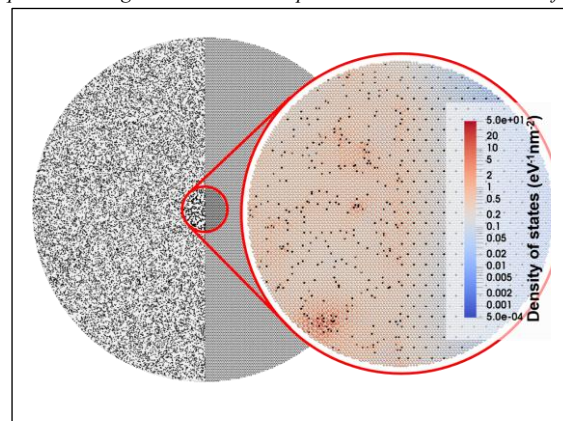


Fig.4: (left) 200nm disc of graphene (carbon atoms are white) with 3% Si atoms (black) distributed randomly on the left, and periodically on the right half of the disc. (right) Electronic density of states of the center 25 nm of the 200nm graphene disc solved with open boundary conditions at 10meV above the Dirac point of pristine graphene. Carbon atoms are colored according to the electronic DOS, silicon atoms are black. The electronic DOS shows domain formation in the left half and electronic tunneling into the right half of the disc.

Exciton Diffusion Properties in Carbon Nanotube Films

Y. C. Li, S. W. Belling, and I. Knezevic

Department of Electrical and Computer Engineering, University of Wisconsin–Madison, Madison, Wisconsin 53706; li779@wisc.edu

Carbon nanotube (CNT) films have been introduced into organic photovoltaic devices as optical absorbers [1]. Illumination generates excitons inside CNT films, so it is important to understand exciton diffusion properties for the purpose of improving device efficiency. We studied exciton transfer in binary CNT systems in our previous papers [2,3] and now introduce our new numerical tool DECaNT (Diffusion of Excitons in Carbon NanoTubes) [4] that simulates exciton diffusion in complex CNT films with various morphologies.

The simulation tool can be divided into two parts: a virtual CNT-film generator and a Monte Carlo simulator. The CNT generator uses the Bullet Physics C++ library to generate a realistic three-dimensional model of the CNT mesh with desired parameters (the chirality and length of each individual tube, intertube spacing, whether tubes are aligned in parallel, whether tubes are bundled or not, and the presence and density of trapping sites that can dissociate excitons). The Monte Carlo simulator captures exciton diffusion through the virtual CNT film. The simulator records the displacement of every exciton inside the CNT film at each simulation step, and calculates the diffusion tensor from the long-time limit of the position–position correlation function. It can also record exciton lifetime and calculate the diffusion length in the presence of disorder.

In Fig. 1, we present the cross-plane correlation functions versus time for films of CNTs with two different chiralities [(4,2) and (6,1)] and three different morphologies for each chirality (parallel, single tubes randomly oriented, and bundled tubes with bundles randomly oriented). Aligning tubes helps with exciton diffusion, but the magnitude of this effect depends on tube chirality. In Fig. 2, we show how intertube spacing affects the diffusion rate. The diffusion rate decreases with increasing intertube distance for all morphologies, with the decay being fastest in the parallel and slowest in the bundled random morphology. At the conference, we will also discuss the role of disorder in exciton diffusion length and lifetime, as well as the effects of possible polydispersity (mixture of chiralities) in CNT films.

This work was supported by DOE-BES (DE-SC0008712).

- [1] D. J. Bindi, M. Wu, F. C. Prehn, and M. S. Arnold, *Nano Lett.* 11, 455–460 (2011).
- [2] A. H. Davoody, F. Karimi, M. S. Arnold, and I. Knezevic, *J. Phys. Chem. C* 120, 16354–16366 (2016).
- [3] A. H. Davoody, F. Karimi, M. S. Arnold, and I. Knezevic, *J. Phys. Chem. C* 121, 13084–13091 (2017).
- [4] S. W. Belling, Y. C. Li, A. H. Davoody, A. J. Gabourie, and I. Knezevic, “DECaNT: Simulation Tool for Diffusion of Excitons in Carbon Nanotube Films,” submitted (2020). <https://arxiv.org/abs/2010.11992>

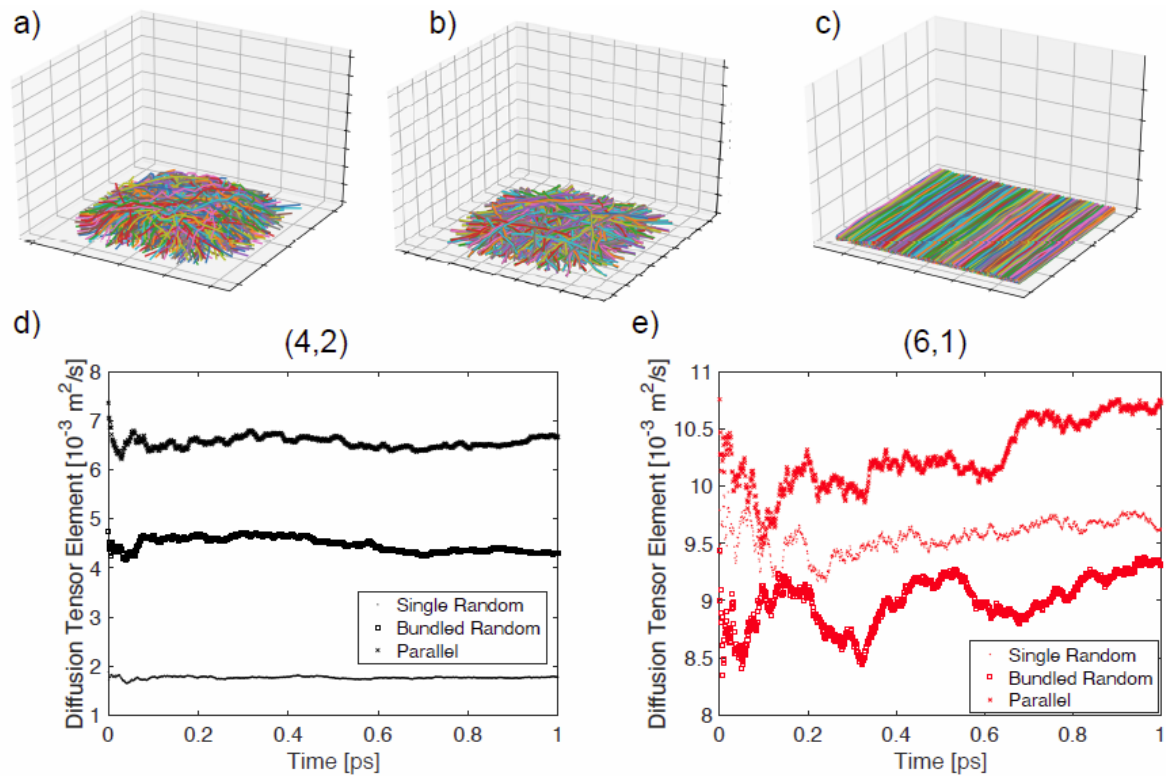


Fig. 1. Cross-plane position-position correlation function as a function of time (its long-time limit is the diffusion-tensor element) for two chiralities, (4,2) and (6,1) (panels (d) and (e), respectively) in the three film morphologies shown on top: (a) single random, (b) bundled random, and (c) parallel and each of the.

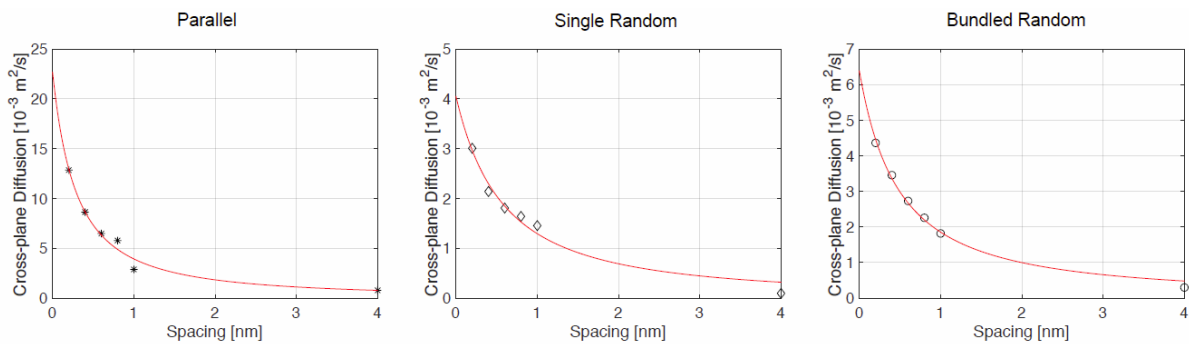


Fig. 2. Cross-plane diffusion-tensor element as a function of intertube wall-to-wall spacing. Diffusion decreases with increased spacing for all morphologies, but the rate of this decrease depends on morphology. The parallel morphology exhibits the quickest decrease, while the bundled random film exhibits the slowest. This is because CNTs with random orientation could be partially oriented in the cross-plane direction and CNTs within a bundle don't have added spacing, allowing for motion in the cross-plane direction within a given bundle. The red lines are fits according to $D(d)=D(0)/(d+d_0)^n$, where d is the intertube spacing (horizontal axis in the graphs above), d_0 plays the role of an effective tube diameter and is dependent on morphology, and $n \approx 2$ [4].

Constructing machine-learning potentials derived from disordered structures for crystal structure prediction

Changho Hong¹, Jeong Min Choi¹, Wonseok Jeong¹, Sungwoo Kang¹, Suyeon Ju¹,
Kyeongpung Lee¹, Jisu Jung¹, Yong Youn², and Seungwu Han^{1,*}

¹ *Department of Materials Science and Engineering and Research Institute of Advanced Materials, Seoul National University, Korea*

² *Center for Green Research on Energy and Environmental Materials and International Center for Materials Nanoarchitectonics, National Institute for Materials Science, Japan*

* hansw@snu.ac.kr

Crystal structure prediction (CSP) is a problem of finding a structure with the lowest free energy in given chemical compositions. First-principles calculation based on density functional theory (DFT) is known to be very accurate in evaluating free energies because of its non-empirical nature. The DFT-based CSP has been successful in identifying inorganic crystals under extreme conditions and organic crystals. However, cost of *ab initio* calculations is prohibitive in exploring huge configuration space of multinary (ternary or higher) phase. Neural network potentials (NNP) have much lower cost with comparable accuracy to DFT, but scarcity of information on crystal structures impedes selecting training sets. Herein we suggest developing a training set from dynamical trajectories of disordered phases: liquid and amorphous phases. Molecular dynamics of them are simulated by DFT without any precedent information of structures except for chemical composition. To validate accuracy of NNP for crystal structure prediction, we compare DFT and NNP energies of experimental phases as well as theoretical crystal structures with low energy for Ba₂AgSi₃, Mg₂SiO₄, LiAlCl₄, and InTe₂O₅F. We find very good correlation between DFT and NNP energies, which ensures NNP is able to rank energies of low-energy structures. We also find that NNP can accelerate the speed of crystal structure prediction compared DFT-based one. This work proposes very efficient method in crystal structure prediction with reliable neural network potentials.

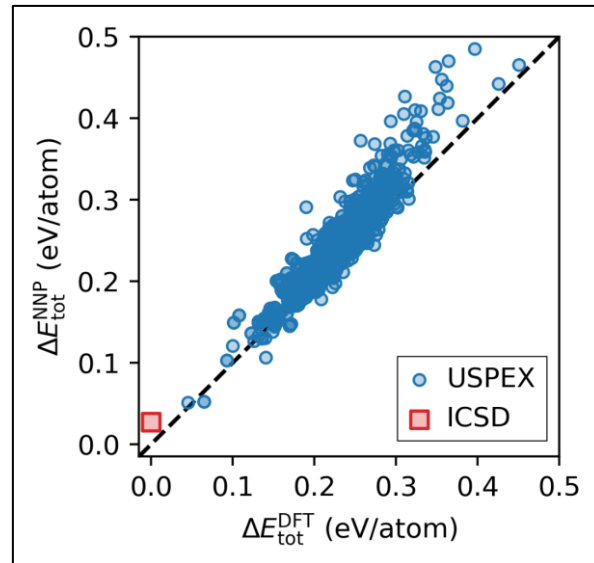


Fig.1: Energy correlation between DFT and NNP energy in Ba_2AgSi_3 for experimental phases as well as theoretical low-energy phases. The DFT and NNP energy reference is based on experimental phase which is optimized in DFT.

Numerical Solution of Poisson and Landau-Khalatnikov Equations for Negative Capacitance Devices with PZT and HZO Ferroelectric Films

Yu-Chin Tsai^{1-2,5-6} and Yiming Li^{1-8,*}

¹ Parallel and Scientific Computing Laboratory; ² Institute of Biomedical Engineering; ³ Institute of Communications Engineering; ⁴ Department of Electrical and Computer Engineering, National Yang Ming Chiao Tung University, 1001 Ta-Hsueh Rd., Hsinchu 300, Taiwan.

⁵ Parallel and Scientific Computing Laboratory; ⁶ Institute of Biomedical Engineering; ⁷ Institute of Communications Engineering; ⁸ Department of Electrical and Computer Engineering, National Chiao Tung University, 1001 Ta-Hsueh Rd., Hsinchu 300, Taiwan.

*ymli@faculty.nctu.edu.tw

In order to promise the high performance of devices, many researches have been proposed various methods in recent years [1-2]. Negative capacitance (NC) field-effect transistor (FET) is one of solutions which can boost the devices performance effectively based on the concept of the ferroelectric (FE) polarization [3-5]. Many groups have proposed the NC effect can improve the devices characteristic adequately [6-7], where the detail of numerical method used to solve NC devices plays a key role to explore their physics. To explore the physical insight of NC devices, such as the polarization phenomenon, we investigate and compare the NC device with different FE films by solving one-dimensional (1D) Poisson equation coupled with Landau-Khalatnikov (LK) equation.

Fig. 1 (a) shows the program flow chart of the numerical solution. In this flow, we discretize the Poisson equation by using the finite difference method (FDM) and solve it by using the monotone iterative (MI) method. The MI method replaces the Newton's method for the numerical solutions of the nonlinear algebraic equations due to its effective execution and global convergence [8]. The devices structure and parameters are listed in Fig. 1 (b). Fig 1(c) reveals the discretized equations of the Poisson equation by using FDM over the uniform rectangular mesh in the different region. The schematic of 1D MFIS discretization also demonstrate the boundary condition between the interface of different regions. Figs. 2 show the electrostatic potential of (a) metal-SiO₂-Si and (b) metal-HfO₂-SiO₂-Si under V_G is 1V. Because of the different dielectric constant, the larger voltage across the SiO₂ layer than that of the HfO₂ layer. The band diagram of HfO₂ and HZO are demonstrated in Figs. 2 (c) and (d). Notably, the dipoles in the FE layer will be rearranged due to occurring the polarization by applying the gate voltage, the potential in the FE and the insulator layer will drop in the opposite direction and increase the surface potential simultaneously. Therefore, the potential will be raised in the FE region. Figs. 3 illustrate the (a) PZT and (b) HZO's potential profile, respectively. We can observe that the slope is steeper in the HZO than that in PZT, which indicate the polarization in the HZO is strong. Fig. 3(c) shows the polarization of HZO and PZT along the FE layer. The FE layer will obtain the polarization term due to solving the LK equation. The result indicates that the HZO has higher polarization than the PZT. However, the variation of polarization at each grid points along the FE layer is much small. It means the FE polarization distribution is uniform in the 1D NC MOS simulation. Fig. 3 (d) shows the total capacitance which correspond to PZT and HZO. As the applied voltage increase, the charges which in the bulk region will reduce so that the effect of the FE series capacitance will not prominent. The NC MOS capacitance can be denoted by a series connection of FE, insulator and bulk capacitance. When the stronger polarized occur in the FE layer, the FE capacitance will influence the total capacitance of NC MOS. Thus, the higher capacitance can be observed in HZO due to the stronger NC effect which lead the HZO capacitance larger than that of PZT. Not shown here, we do also check the absolute error variation versus the number of iterations. The MI method converges globally for different voltage conditions. Thus, it provides a robust way to solve the Poisson equation coupled with LK equation.

In summary, we have explored the numerical method to solve Poisson equation coupled with LK equation and compare with different FE materials of NC devices. The results indicate that the voltage across the FE layer will increase the electrical potential due to the polarization occur in the FE layer. Compared with PZT, the material of HZO has strong NC effect which has the larger electrical potential. Based on the developed numerical method, we are now studying the 2D numerical solution of NCFET.

This work was supported in part by Ministry of Science and Technology (MOST) of Taiwan under Grant MOST-109-2221-E-009-033 and Grant MOST-109-2634-F-009-030, and in part by the "Center for mm Wave Smart Radar Technologies" under the Featured Areas Research Center Program within the framework of the Higher Education Sprout Project by Ministry of Education in Taiwan.

- [1] L. Zhang et al., IEEE Electron Device Letters, 32(9), pp. 1188-1190, 2011.
- [2] J. Hur et al., IEEE Electron Device Letters, 37(5), pp. 541-544, 2016.
- [3] W. Cao et al., Nat. Commun., 11(1), pp. 196, 2020.
- [4] G. Pahwa et al., IEEE Trans. Electron Devices, 63(12), pp. 4981-4985, 2016.
- [5] K. Li et al., IEEE IEDM, pp. 22.6.1-22.6.4, 2015.
- [6] J. Li et al., IEEE Electron Device Letters, 38(10), pp. 1500-1503, 2017.
- [7] M. H. Lee et al., IEDM, pp. 22.5.1-22.5.4, 2015.
- [8] Y. Li, Comput. Phys. Commun., 153(3), pp. 359-372, 2003.

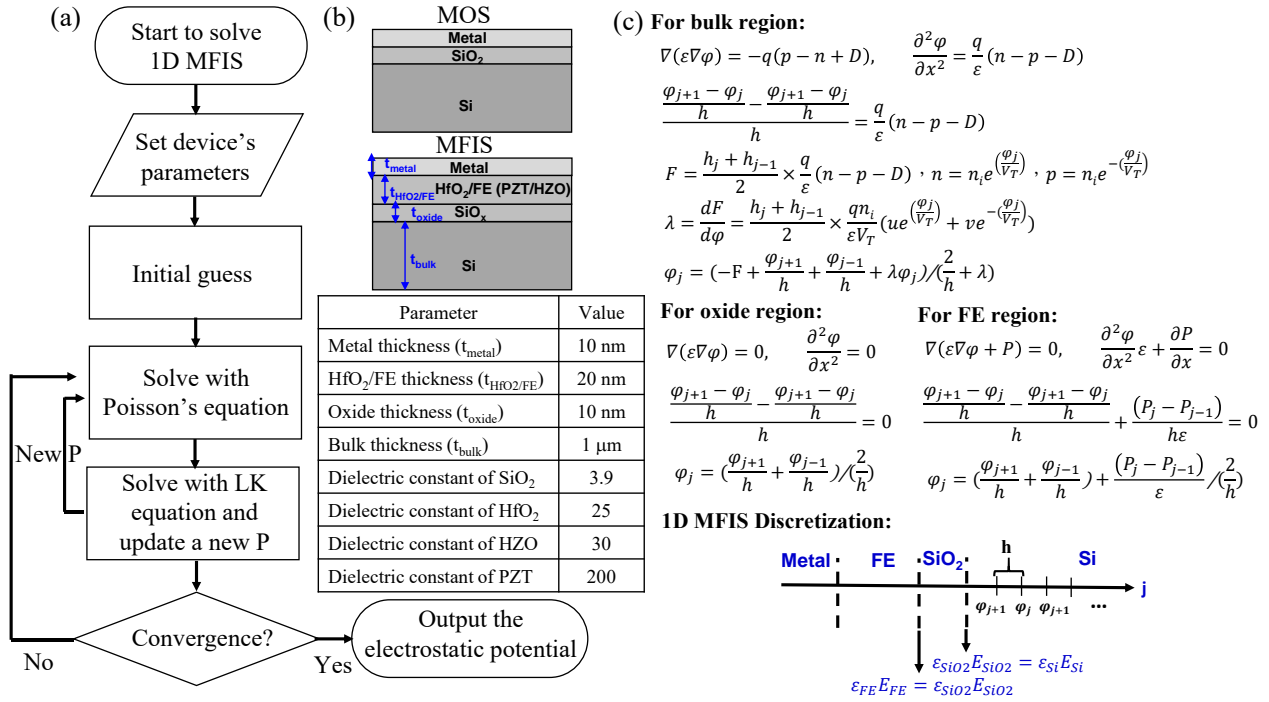


Fig. 1 (a) The program flow chart for solving the 1D Poisson equation coupled with the LK equation. (b) The devices of metal-SiO₂-Si and metal-HfO₂/FE-SiO₂-Si. The devices' parameters are listed in the table. Notably, the FE material parameters are different in the PZT and HZO. In this study, we adopt the PZT layer for α is -1.35×10^8 m/F and the HZO layer α is -7.91×10^8 m/F which have been calibrated with the experimental data. (c) The discretized equations of the Poisson equation by using FBM over the uniform rectangular mesh in the bulk, insulator and FE region, respectively.

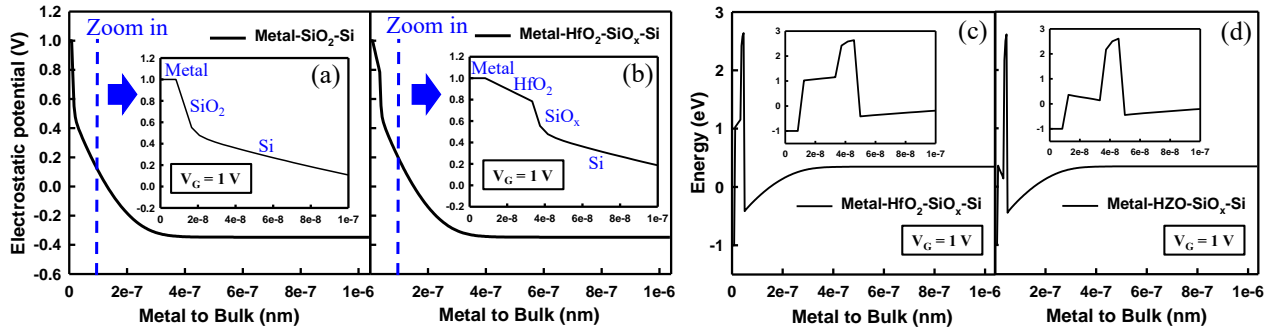


Fig. 2 (a) The electrostatic potential profile of metal-SiO₂-Si and (b) metal-HfO₂-SiO₂-Si under V_G is 1V. The larger voltage across the SiO₂ layer than that of the HfO₂ layer due to the different dielectric constant. (c) The band diagram of metal-HfO₂-SiO₂-Si and (d) metal-HZO-SiO₂-Si. The dipoles which in the FE layer will be rearranged due to occurring the polarization by applying the external voltage, the potential in the FE region and the insulator will drop in the opposite direction. Therefore, the surface potential of FE layer will be raised.

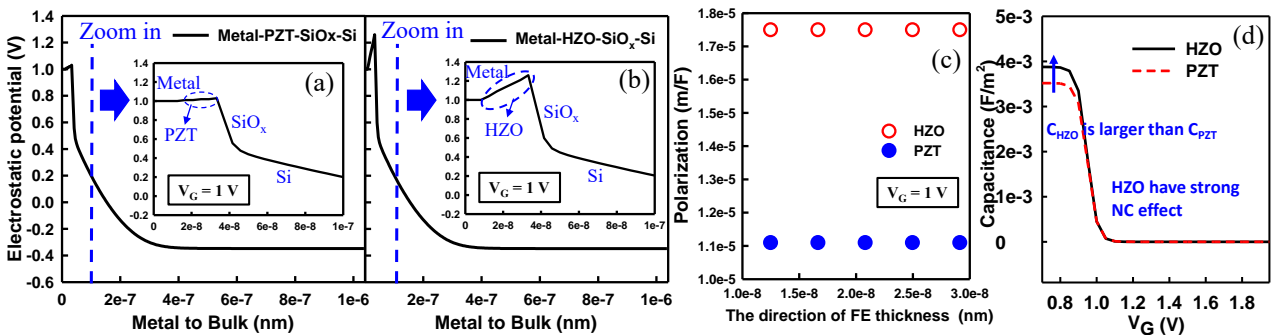


Fig. 3 The electrostatic potential profiles of (a) PZT and (b) HZO for FE layer, respectively. Compared with the PZT, the strong polarized occurs in the HZO; and, thus the surface potential will be increased in the HZO obviously. (c) The polarization of HZO and PZT along the FE layer. The FE layer will obtain the polarization term due to solving the LK equation. The result indicates that the HZO has higher polarization than the PZT. However, the variation of polarization at each grid points along the FE layer is much small. It means the FE polarization distribution is uniform in the 1D NC MOS simulation. (d) The capacitance comparison of PZT and HZO. The capacitance of NC MOS can be denoted by a series connection of FE, insulator and bulk capacitance. Notably, the FE capacitance can be simply described as $C_{FE} = 1/2\alpha t_{FE}$. When the stronger polarized occurs in the FE layer, the FE capacitance will be large and it will influence the total capacitance of NC MOS. We can obtain the higher capacitance due to HZO has the stronger NC effect.

Analysis and Simulation of Basic Memristor Properties

Bernardo Tellini¹, Mauro Bologna², and Kristopher J. Chandia², Massimo Macucci³

¹ *Dipartimento di Ingegneria dell'Energia, dei Sistemi, del Territorio e delle Costruzioni,
University of Pisa, Pisa, Italy*

² *Departamento de Ingeniería Eléctrica – Electrónica, Universidad de Tarapacá, Arica, Chile
Dipartimento di Ingegneria dell'Informazione, University of Pisa, Pisa, Italy
macucci@mercurio.iet.unipi.it*

We present an analysis of the memristor concept first defined by Chua in 1971 [1], pointing out that the flux linkage appearing in its definition cannot be considered to be equivalent to the actual magnetic flux (as claimed in [1]). The flux linkage is just the time integral of the voltage and coincides with the magnetic flux only in the case of an inductor. Once this fact is recognized, it is straightforward to show that the memristor is a dissipative element and that it is just an extension of the resistor concept: a resistor whose value evolves in time according to a set of state variables. In the original formulation, one of the defining properties of a memristor was that it established a single-valued relationship between the flux linkage ϕ and the charge q : we show that this is guaranteed only for the most basic memristors, i.e. those in which the resistance depends only on the charge. As an example, we perform a numerical simulation of a particular memristor: a thermistor, whose resistance is a decreasing function of temperature. In Fig. 1 we report the behavior in the V - I plane of such a thermistor for a very low frequency cyclic excitation. In Fig. 2, we present the corresponding curve in the ϕ - q plane: it is single-valued because of the very low frequency (leading to a “steady-state” thermal condition), but as the frequency is raised (and becomes comparable with the reciprocal of the thermal time constant), a hysteretic behavior appears both in the V - I (Fig. 3) and in the ϕ - q (Fig. 4) plane. In this specific case, the ϕ - q curve is not single-valued, but it is at least closed (as a result of a particular symmetry in the V - I curve). In order to further support our conclusion that the memristor is just an extension of the resistor concept, we present a simple memristor model, consisting of resistors and charge-controlled switches. The schematic diagram is reported in the top panel of Fig. 5, while in the bottom panel we show its behavior in the V - I plane. As for all memristors, the curve in the V - I plane is pinched in the origin. In Fig. 6 we report the corresponding curve in the ϕ - q plane, which, consistently with the original definition, is a single-valued curve. After discussing some other examples, we remark that the requirement that the V - I curve be pinched in the origin is an expression of the fact that no energy can be stored and that the memristor is a purely dissipative element. Furthermore, a direct consequence of our analysis is that the memristor is not a fourth basic circuit element.

[1] L. O. Chua, IEEE Trans. Circuit Theory, **CT-18**, n. 5, 507 (1971)

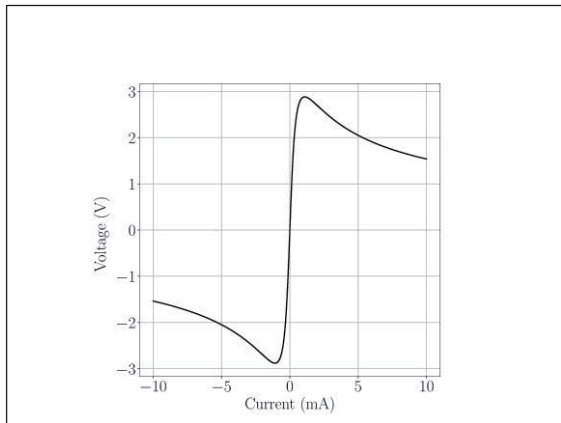


Fig.1: Curve in the V - I plane for a thermistor operated at a very low frequency with a cyclic current excitation.

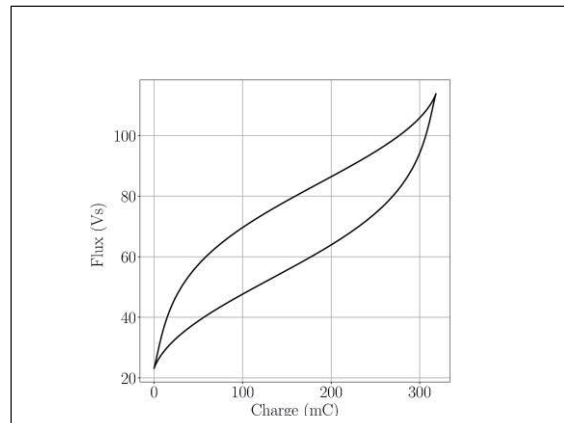


Fig.4: Curve in the ϕ - q plane for a thermistor operated at a frequency comparable to the reciprocal of the time constants characteristic of the device.

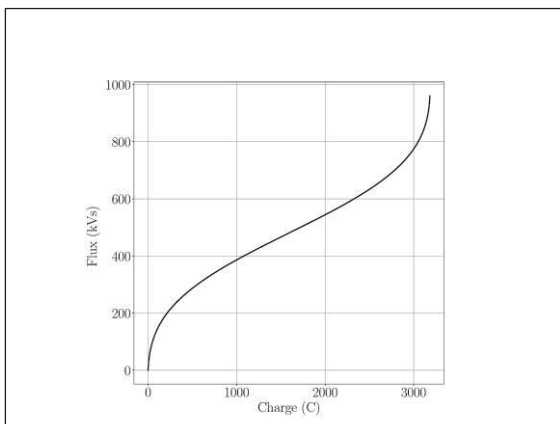


Fig.2: Curve in the ϕ - q plane for a thermistor operated at very low frequency.

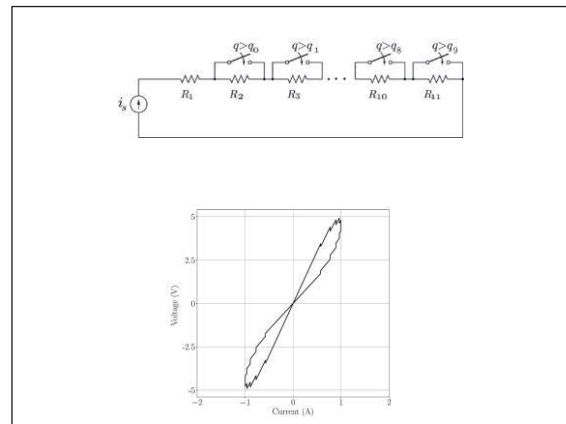


Fig.5: Top panel: memristor model based on resistors and charge-controlled switches; Bottom panel: Curve in the V - I plane for the memristor based on resistors and charge-controlled switches.

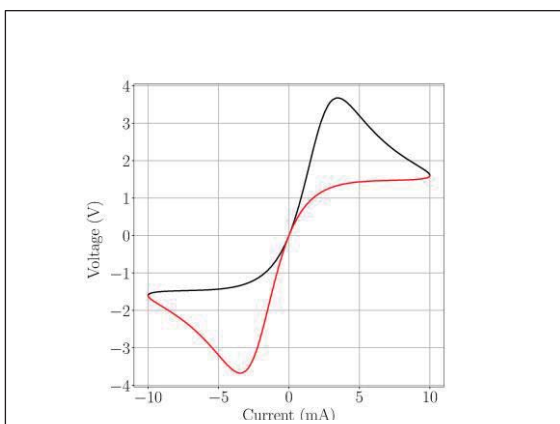


Fig.3: Curve in the ϕ - q plane for a thermistor operated at a frequency comparable to the reciprocal of the main time constants characteristic of the device.

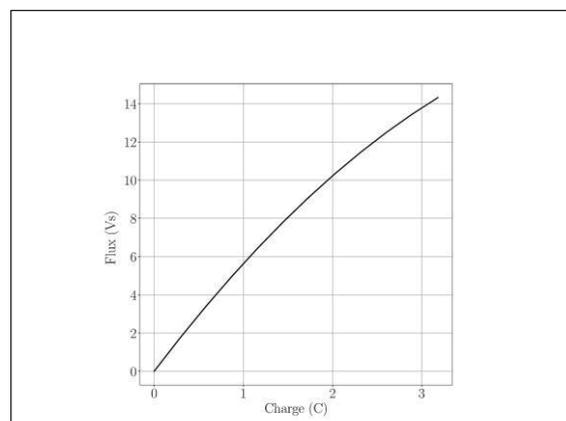


Fig.6: Single-valued curve in the ϕ - q plane for our memristor model based on resistors and charge-controlled switches.

Hybrid Modeling of TCAD and AI for Semiconductor Design

Changwook Jeong¹, Sanghoon Myung¹, Jinwoo Kim¹, Hyunjae Jang¹,
Byungseon Choi¹, Hyowon Moon¹, Jisu Ryu¹, Jae Myung Choe¹, and Dae Sin Kim¹

¹*Data & Information Technology Center, Samsung Electronics*
chris.jeong@samsung.com

Data-driven and physics-based models are complementary to each other in solving scientific or engineering problems, as shown in Table I. As such, merging machine learning (ML) or artificial intelligence (AI) and simulation has received growing interest to completely exploit their combined potential [1]–[4]. Here we concentrate on application of hybrid modeling of ML/AI and TCAD simulation to develop and optimize semiconductor process technologies and devices. Fig. 1(a) shows a schematic of AI-based emulator to mimic the TCAD process and device simulation for real-time prediction. First, to generate doping profiles as shown in Fig. 1(c), AI-learned process emulator uses a tailored convolutional neural network. Secondly, for a device emulator we adopted a recurrent neural network structure which is specially designed to learn sequential data, because current vs. voltage (I-V) curves can be regarded as sequential data and current values of neighboring voltage points are highly correlated. To improve a prediction accuracy for I-V, trans-conductance characteristics is considered simultaneously while training the AI model. Fig. 1(b) shows that the emulator reproduces the relationship between drain current and gate voltage and drain voltage, and cross-section of device with current density contours at different drain bias is as shown in Fig. 1(d). Fig. 2 illustrate a hybrid approach of ML and physical model to accurately describe the etch processes for deep trench isolation with considering features such as type of process scheme, equipment information that physical simulator cannot take into account. Sequence-to-sequence ML model is used as a baseline model since both inputs and outputs are sequential data in time as in Fig. 2(a). Fig. 2(b) shows how the baseline model works and that the predicted profile at a final time step (denoted as t_{final}) well match actual process results (red dashed line). It turns out, however, that the baseline AI model cannot properly predict profile evolution as the time progresses ($t_1 \sim t_5$). A physical compact model is used to impose a physics-based topology constraint on the baseline model to learn causality between each steps. Fig. 2(c) demonstrates that incorporating such physical insights help AI model predict correctly profile evolution at intermediate steps.

[1] A. Karpatne et al., IEEE Trans. Knowl. Data Eng., **29**, 2318 (2017)

[2] I. Huh et al., NeurIPS 2020, **33**,19016 (2020)

[3] S. Myung et al., NeurIPS Workshop 2020

[4] K. Lee et al., Comput. Phys. Commun., **242**, 95 (2019)

Table 1: Comparison of Pros (⊙) and Cons (○) between Physics-based Model and Data-driven Model

Symbol	Physics-based Model	Data-driven Model
Data Cost	⊙	○
Accuracy	Extrapolation	○
	Interpolation	⊙
Inverse Optimization	○	⊙
Interpretability	⊙	○
Prediction Time	○	⊙

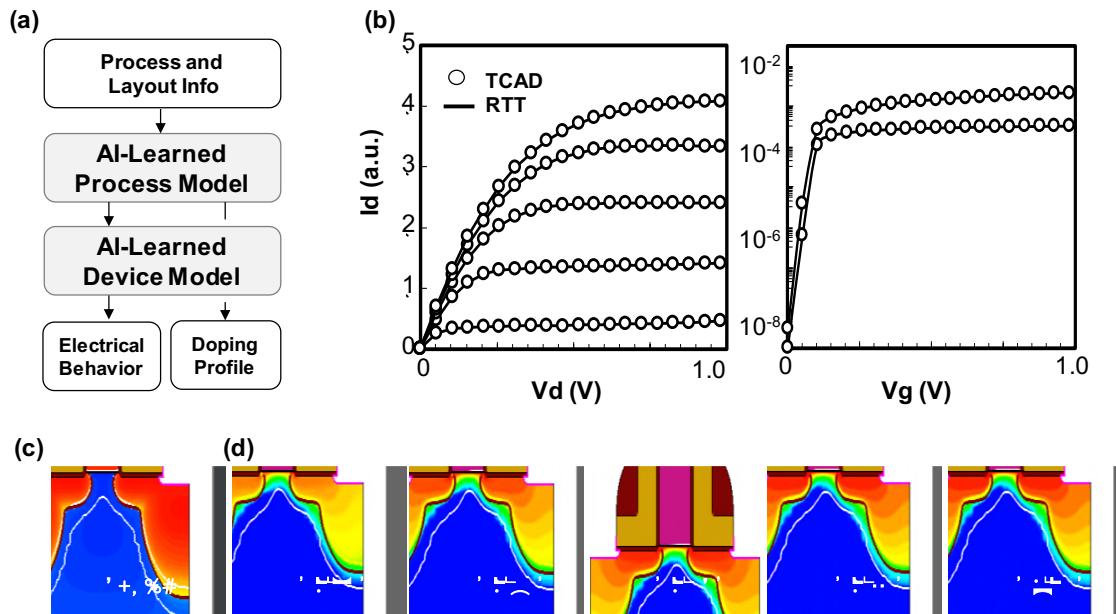


Figure 1: (a) a schematic of AI-based emulator for real-time prediction. (b) current-voltage characteristics between TCAD and AI-emulator shows good agreement with each other. (c) AI-emulator generated doping profiles and (d) cross-section of device with current density contours at different drain bias

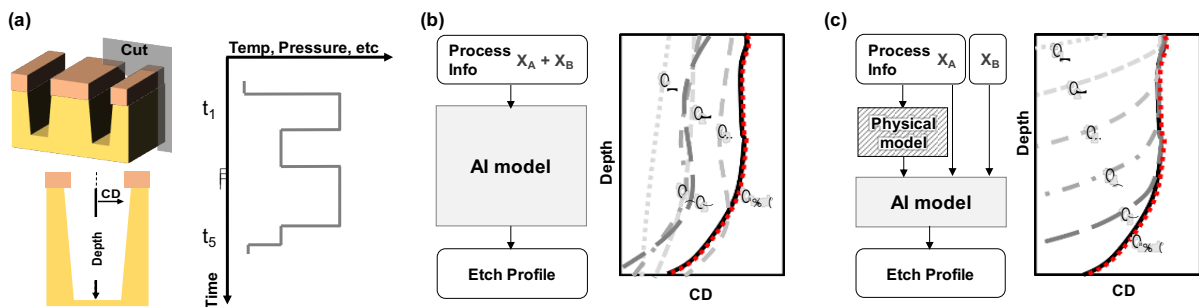


Figure 2: (a) a schematic of deep trench isolation (DTI), and input example for DIT etching process such as type of gas, temperature, pressure, etc. (b) predicted profile with the baseline model : the DTI is vertically etched down to bottom layer in the beginning of processes. (c) The unphysical behavior is fixed with hybrid modeling of physical and AI model.

Quantum information and quantum foundations with spins in silicon

Andrea Morello

Centre for Quantum Computation and Communication Technology, School of Electrical Engineering and Telecommunications, UNSW Sydney, Australia

Dopant atoms in silicon are a versatile platform for experiments in quantum information processing, as well as quantum foundations. The electron [1] and nuclear [2] spin of a ^{31}P donor were the first qubit demonstrated in silicon, and went on to become among of the most coherent qubits in the solid state, with coherence times exceeding 30 seconds [3], and quantum gate fidelities approaching 99.99% [4].

In this talk I will present the state of the art and future directions for donor spins in silicon. For quantum information, the current focus is on two-qubit operations. An embryonic demonstration of an exchange-based two-qubit CROT gate was recently achieved [5], using a device in which we implanted a high dose of ^{31}P donors. Future experiments will focus on using deterministic, counted single-ion implantation, for which we have recently demonstrated the capability to detect an individual ion with 99.87% confidence [6].

Heavier donors possess a high nuclear spin quantum number, which could be an important resource to encode error-protected logical qubits in its large Hilbert space. Our group began the study of ^{123}Sb donors for the goal of observing quantum chaotic dynamics in a single quantum system [7]. Understanding the interplay between chaos and quantum dynamics is a key aspect for the foundational question of how the classical world emerges from the quantum world. Moreover, chaotic dynamics must be understood and controlled for the correct operation of quantum computers and quantum simulators [8]. In the process of operating a single ^{123}Sb nucleus, we (re)discovered the phenomenon of nuclear electric resonance, and applied it for the first time to a single nuclear spin [9].

- [1] J. Pla et al., Nature **489**, 541 (2012)
- [2] J. Pla et al., Nature **496**, 334 (2013)
- [3] J. Muhonen et al., Nature Nanotechnology **9**, 986 (2014)
- [4] J. Muhonen et al., J. Phys: Condens. Matter **27**, 154205 (2015)
- [5] M. Madzik et al., Nature Communications **12**:181 (2021)
- [6] A. Jakob et al., arXiv:2009.02892 (2020)
- [7] V. Mourik et al., Physical Review E **98**, 042206 (2018)
- [8] L. Sieberer et al., NPJ Quantum Information **5**:78 (2019)
- [9] S. Asaad et al., Nature **579**, 205 (2020)

Analogue computing with resistive memory devices

Daniele Ielmini

Politecnico di Milano, Italy

Abstract: In the era of artificial intelligence, unconventional computing attracts an increasing interest to accelerate sensing and computation by taking advantage of novel devices and novel architectures. Among these unconventional concepts, in-memory computing (IMC) shows the ability to accelerate computation by minimizing data movement and improving the parallelism. A key enabling technology for IMC is the matrix vector multiplication (MVM) in a crosspoint memory array of memory devices, such as resistive switching memory (RRAM) or phase change memory (PCM). MVM is currently being explored for novel accelerators of deep neural network (DNN). Recently, it has been shown that MVM can be extended to a wider class of linear algebra operations, including solution of linear set of equations ($Ax = b$), matrix inversion, eigenvector calculation and various types of regression, all executed in one step in the analogue domain. Given the ubiquitous nature of linear algebra in modern data processing, the new wave of analogue IMC operations is extremely promising for accelerating computation in many applications. This work presents the status of analogue IMC with resistive memory devices, discussing the underlying concept and the technology, addressing the time response, accuracy, stability and complexity. The underlying opportunities, potential applications and challenges from the viewpoints of device, circuit and architectural will also be discussed.

Keywords:

In-memory computing, resistive switching device, analogue computing

Bio:

Daniele Ielmini is a Professor at the Dipartimento di Elettronica, Informazione e Bioingegneria, Politecnico di Milano, Italy. He received the Ph.D. from Politecnico di Milano in 2000. He held visiting positions at Intel Corporation and Stanford University in 2006. His research interests include the modeling and characterization of non-volatile memories, such as phase change memory (PCM), resistive switching memory (RRAM), and spin-transfer torque magnetic memory (STT-MRAM). He authored/coauthored more than 300 papers in international journals and conferences. He is Associate Editor of IEEE Trans. Nanotechnology and Semiconductor Science and Technology (IOP). He received the Intel Outstanding Researcher Award in 2013, the ERC Consolidator Grant in 2014, and the IEEE-EDS Paul Rappaport Award in 2015. He is a Fellow of the IEEE.



Mechanism of Resistance Switching in Hexagonal Boron Nitride

Fabian Ducry¹, Jan Aeschlimann¹, and Mathieu Luisier¹

¹*Integrated Systems Laboratory, ETH Zurich, Gloriastrasse 35, CH-8092, Zurich, Switzerland*
e-mail: ducryf@iis.ee.ethz.ch

Resistance switching (RS) is a phenomenon where a material changes its resistance upon application of an external voltage. Hexagonal boron nitride (h-BN) exhibits RS in few or monolayer configurations as well as in bulk-like conditions [1]. The mechanism responsible for the RS effect in h-BN is however still debated. Here, we present a vacancy-driven mechanism that could explain the nonvolatile switching behavior both in bulk as well as in thin h-BN films encapsulated by Au contact. It is supported by *ab initio* device simulations.

The hypothesis that we will demonstrate is that defects can form reversible bonds between adjacent 2-D layers of h-BN [2] and change the conductivity of this material. This is the case of triangular defects, as visualized in Fig. 1. The dependence of the bonding properties of such defects on the charge state is investigated with density-functional theory (DFT) using CP2K [3]. A DZVP basis and the PBE functional is employed for that purpose. First, the forces acting on the neutral configuration of the defect in bulk h-BN are minimized. Then, the charge is decremented in steps of the elementary charge q and the forces minimized at each step. This concept is illustrated in Fig. 2. As the defect charge decreases more interlayer bonds form, up to a maximum of four at $-6q$. Next, the charging is reversed (from $-6q$ to 0), again with force minimizations at each step. During the discharge the bonds remain stable up to the $-3q$ charge state, leading to a hysteresis. Evidently, the charging and discharging of the defect corresponds to the SET and RESET processes of the proposed RS mechanism. The preferred charge state of the defect is shown in Fig. 3 as a function of the Fermi energy. When h-BN is in contact with Au the $2e^-$ and $4e^-$ charge states are preferred at equilibrium, depending on the presence or absence of interlayer bonds. This fact leads to a nonvolatile RS characteristic.

The impact of the defect-induced bonds on the conductance of the h-BN is investigated using a DFT-based quantum transport solver [4]. An Au/h-BN/Au device made of 4 layers of h-BN with a defect is constructed, as drawn in Fig. 4. The electronic conductance is then extracted with the quantum transmitting boundary method (QTBM). The conductance can be seen in Fig. 5, highlighting the presence of a hysteresis as a function of the charge state.

Similarly, bonds can also form between h-BN defects and an Au or graphene contact (Fig. 6). A hysteretic behavior analogous to the one presented here is expected in these cases too. It can therefore be concluded that defect charging is probably at the origin of RS in h-BN.

[1] X. Wu et al., *Adv. Mater.* 2019;31(15):1-7 [2] J. Strand et al., *J. Phys. Condens. Matter.* 2020;32(5)

[3] T Kühne et al., *J. Chem. Phys.* 2020;152(19) [4] S. Brück et al., *J. Chem. Phys.* 2017;147(7)

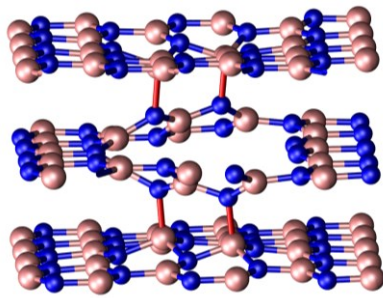


Fig.1: Representation of the atomic configuration of a triangular defect in h-BN where two bonds are formed between the defect and each adjacent layers. The blue and brown spheres represent N and B, respectively, and the interlayer bonds are marked in red.

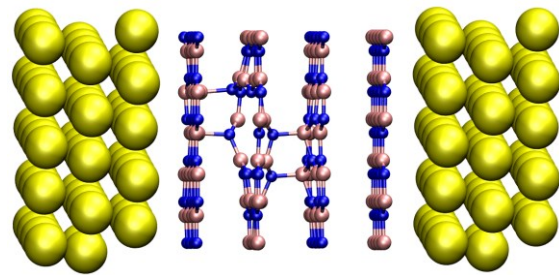


Fig.4: Schematic view of the Au/h-BN/Au structure used to evaluate defect-induced conductance changes. The yellow spheres represent the Au contact atoms. The entire structure is optimized with DFT.

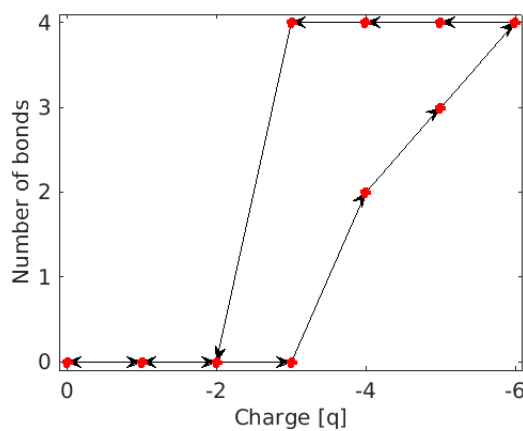


Fig.2: Number of interlayer bonds formed between a defective h-BN layer and its neighbors as a function of its charge. Increasing or decreasing the charge and minimizing the forces may result in a configuration change. Each arrow represents a different step, including a minimization of the force acting on the h-BN structure.

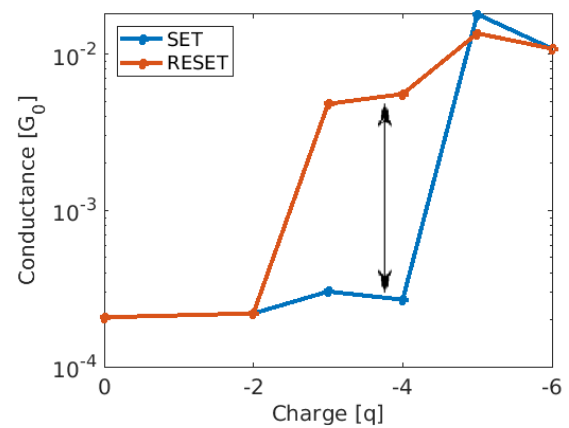


Fig.5: Conductance of the Au/h-BN/Au structure in Fig. 4 as a function of the charge during the SET and RESET processes. States with three or four interlayer bonds are conductive. Hence a hysteresis forms with an ON-OFF conductance ratio of more than one order of magnitude, as indicated by the black double arrow.

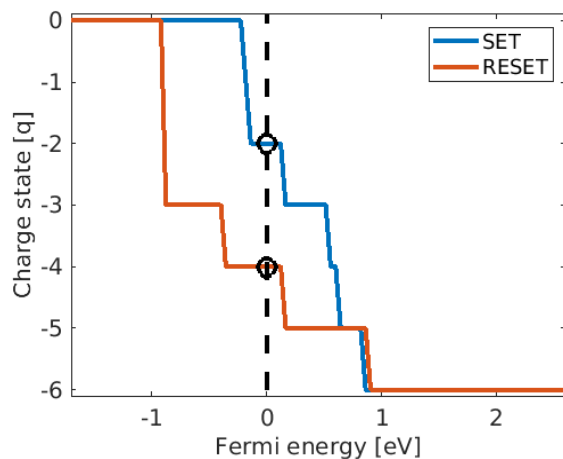


Fig.3: The preferred charge state of the triangular defect as a function of the Fermi energy. The SET and RESET potentials are around 1 eV and -1 eV. These are probably underestimated due to the nature of the PBE functional employed in DFT. The dashed black line indicates the equilibrium potential when the h-BN is in contact with Au. The upper (lower) black circle mark the equilibrium OFF- (ON-) state.

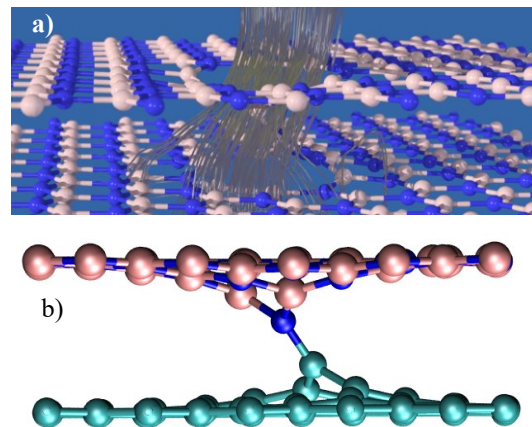


Fig.6: a) The gray lines are an illustration of the current flowing through a defect in h-BN with a single interlayer bond. The pink and blue spheres are the B and N atoms, respectively. b) Example of a defect forming a bond between an h-BN layer and a graphene electrode, where the cyan spheres represent C atoms. The resulting bonding could induce a similar resistance switching characteristic as the one presented here for bulk h-BN.

Extraction of contact resistance from Green's function simulations of 2D material nanoribbon devices

Mirko Poljak and Mislav Matić

Computational Nanoelectronics Group

Faculty of Electrical Engineering and Computing, University of Zagreb, Zagreb, Croatia

mirko.poljak@fer.hr

Promising electronic and transport properties of 2D material nanostructures are usually shrouded by contact resistance that limits their feasibility for high performance devices. In this work we extract contact resistance (R_C) from MOSFET simulations with silicene nanoribbons (SiNR) as channel material. We employ atomistic tight-binding Hamiltonians and top-of-barrier (ToB) MOSFET model combined with transmission and density of states (DOS) obtained from the device Green's function [1], [2]. Simulations are done for two cases: ideal contacts (ICs), where semi-infinite nanoribbons are assumed (Sancho-Rubio method), and metal contacts (MCs) defined within the wide-band limit (WBL) approximation with moderate interacting parameters and imaginary-only contact self-energy ($-\text{Im}\Sigma_{S/D}^R = 1 \text{ eV}$) [3]. We assume that this model metal results in purely Ohmic contacts with SiNRs. The MCs are attached in the edge-contact geometry that enables encapsulation and preservation of 2D material properties (Fig. 1) [4]. The R_C is extracted from the difference in the ON-state current (I_{ON}) between the IC and MC case (Fig. 2). WBL metal contacts introduce Lorentzian peaks and oscillations into transmission (Fig. 3) and DOS (Fig. 4). The transmission is generally lower, which leads to decreased current driving capabilities of MC SiNR MOSFETs, whereas DOS exhibits similar averaged values and the appearance of metal-induced gap states (MIGS). The MIGS are localized on the atoms connected to MCs (not shown) so that states within the bandgap in Fig. 4 do not contribute to transport. When downscaling nanoribbon width (W) from 5.2 nm to 0.6 nm, I_{ON} decreases significantly for both types of contacts (Fig. 5). This behavior results in an increase of R_C from 196 $\Omega\mu\text{m}$ to 574 $\Omega\mu\text{m}$ when W is decreased from 5.2 nm to 0.6 nm (Fig. 6). The R_C value for silicene (limit of wide SiNRs) of $\approx 200 \Omega\mu\text{m}$ agrees with experimental data for edge-contacted graphene ($\approx 150 \Omega\mu\text{m}$ [5]), which validates our approach despite the simplifications of the TB Hamiltonian and ToB device model.

Acknowledgment: This work was supported by Croatian Science Foundation (HRZZ) through Project CONAN2D (Grant No. UIP-2019-04-3493).

References: [1] A. Rahman et al., IEEE Trans. Electron Devices 50, 9, 1853–1864 (2003) [2] S. Kaneko et al., Appl. Phys. Express 7, 3, 035102 (2014) [3] M. Pourfath, The Non-Equilibrium Green's Function Method for Nanoscale Device Simulation, Springer-Verlag, 2014. [4] A. Jain et al., Nano Lett. 19, 10, 6914–6923 (2019) [5] L. Wang et al., Science 342, 6158, 614–617 (2013)

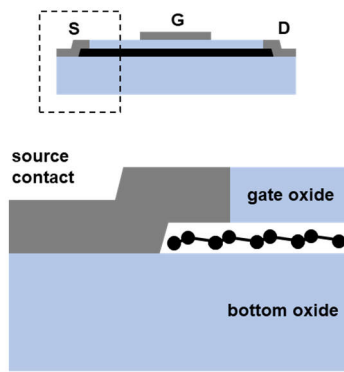


Fig.1: Illustration of a silicene nanoribbon MOSFET with S/D electrodes in edge-contact configuration.

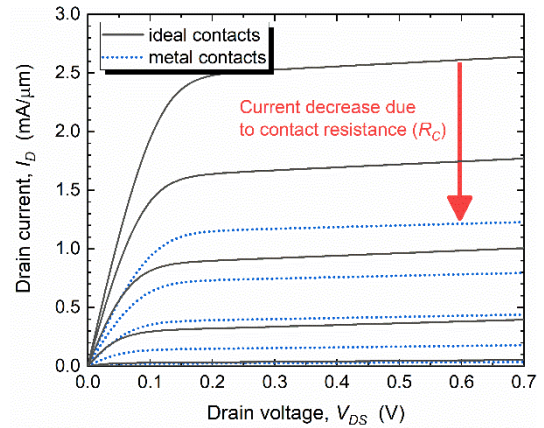


Fig.2: Output characteristics of SiNR MOSFETs with ideal and metal contacts. The SiNR channel is 4 nm wide and 15 nm long.

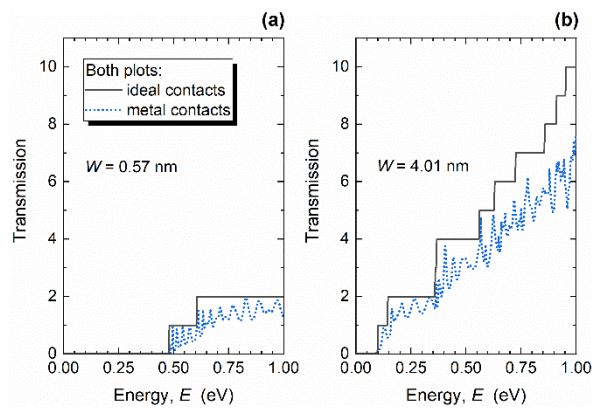


Fig.3: Transmission in (a) 0.57 nm and (b) 4.01 nm wide SiNRs with ideal and metal contacts.

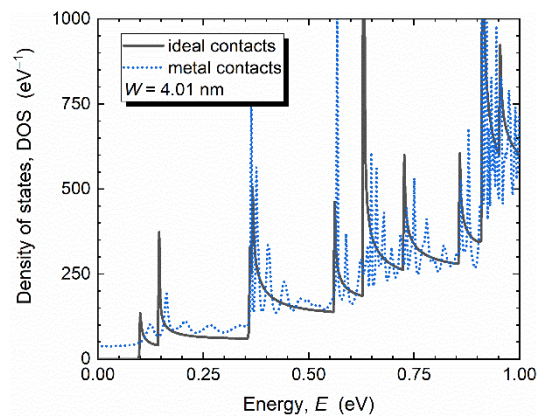


Fig.4: Density of states of 4.01 nm wide SiNRs with ideal and metal contacts.

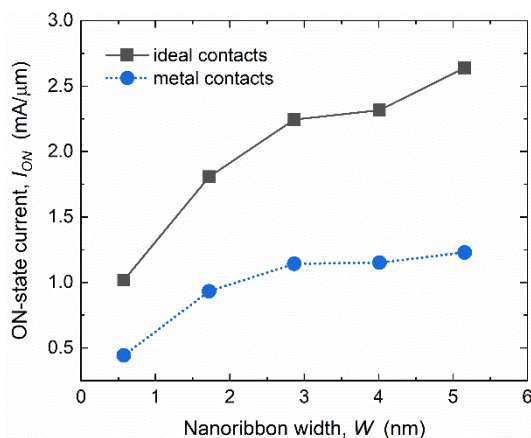


Fig.5: ON-state drain current vs. SiNR width in 15 nm long SiNR MOSFETs with ideal and metal contacts.

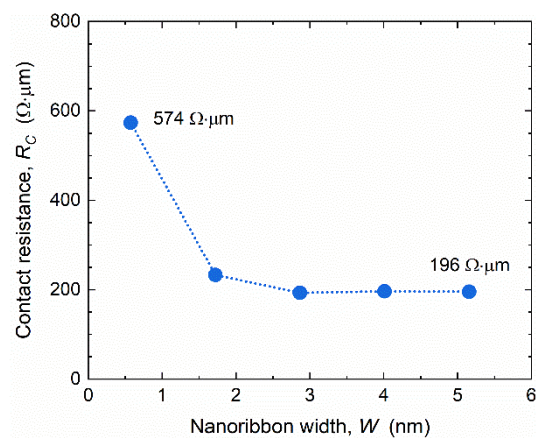


Fig.6: Impact of downscaling nanoribbon width on contact resistance in SiNR MOSFETs.

Machine Learning Models for Diffused Copper Doping Profiles in CdTe Solar Cells

Ghaith Salman¹, Stephen Goodnick², Abdul R. Shaik², and Dragica Vasileska²

¹ *Computing, Informatics, and Decision Systems Engineering, Arizona State University, Tempe, AZ, USA*

² *School of Electrical, Computer and Energy Engineering, Arizona State University, Tempe, AZ, USA*

gsalman@asu.edu (corresponding author)

It is well known that Cu plays an important role in CdTe solar cells for back contact formation and providing p-type doping. Therefore, an important outcome of the simulation effort of the DOE PREDICTS project was to gain insight into the formation and evolution of doping during the annealing process and the cool-down. In the work presented here, we use machine learning to shed light on the Cu profiles that result from the diffusion and cool-down process in the fabrication sequence of CdTe solar cells. The calculation of the profile of the majority holes in the absorber of the CdTe solar cells will be described in a subsequent study. In this paper, we establish the methodology of neural networks machine learning (ML) as applied to the diffusion and cool-down process steps. The big dataset was generated using the PVRD-FASP Solver [1].

Artificial Neural Network models (ANN) have been widely used to model complex problems. In material science, neural network algorithms have been used to search for a total energy minimization and material parametrization. In this work we interpolate from one multi-dimensional space (slow variables, $n_{\text{slow}} \sim 100$) to another multidimensional space (fast variables, $n_{\text{fast}} \sim 10$). For such problems, it is difficult to determine an adequate number of hidden layers and number of neurons. An alternative way is to implement an ANN using keras with backend TensorFlow that uses Radial Basis Function (RBF) network and has only three layers. Hence, its training is much simpler. This approach is able to approximate any multivariate continuous function on a compact domain to a desirable accuracy by using a sufficient number of units. In this work, the ANN and RBF approaches are used. In other words, we have developed and implemented a machine learning model based on neural networks designed to predict the Cu diffusion profile given input parameters (temperature and duration of the diffusion process with subsequent cool-down). Excellent agreement is found between the test and predicted datasets, the difference between the two being smaller than 0.009 μm .

- [1] Abdul R Shaik, Daniel Brinkman, Igor Sankin, Christian Ringhofer, Dmitry Krasikov, Hao Kang, Bedrich Benes, Dragica Vasileska, "PVRD-FASP: A Unified Solver for Modeling Carrier and Defect Transport in Photovoltaic Devices", IEEE J. Photovoltaics, Vol. 9(6), pp. 1602-1613, November 2019.

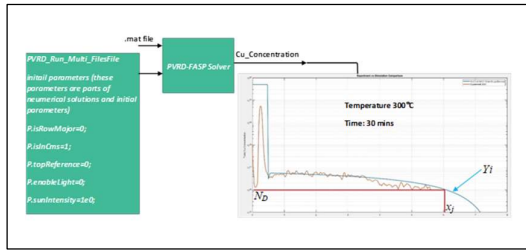


Fig.1: Generation of the dataset to be used in machine learning. In the graph that depicts the copper concentration vs. depth, the blue line is the doping profile generated with the PVRD-FASP solver and the red line are the experimental data provided to us by First Solar. Parameters in these curves are the temperature 300C and the duration of the diffusion process 30mins.

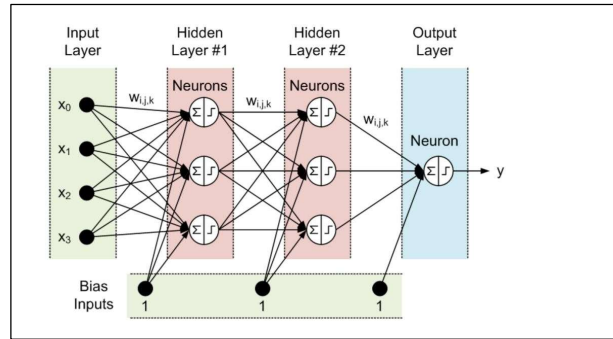


Fig.3: Artificial Neural Network ANN diagram of the machine learning used in this work.

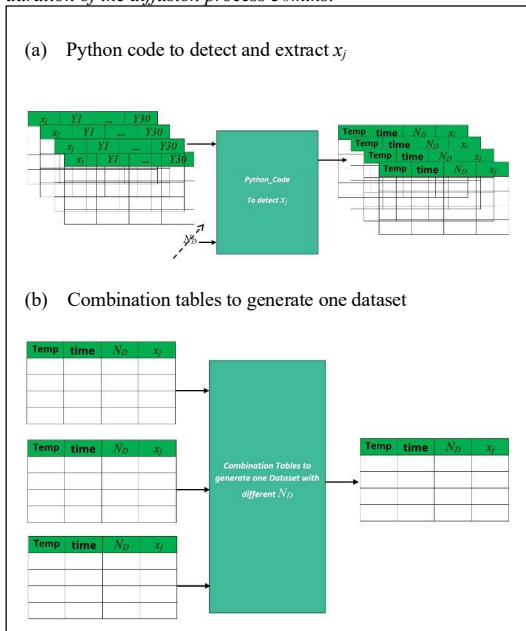


Fig.2: (a) Python code used to detect x_j for different input parameters. (b) Generation of one dataset.

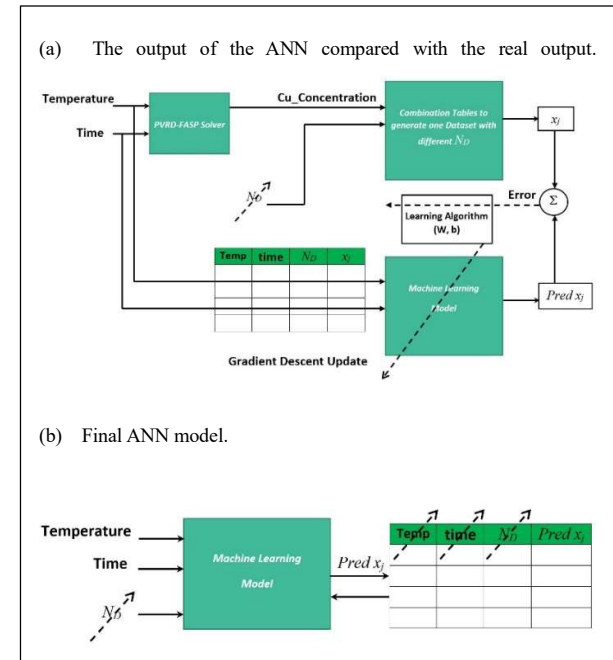


Fig.4: (a) The output of the ANN compared with the real output. (b) Final ANN model.

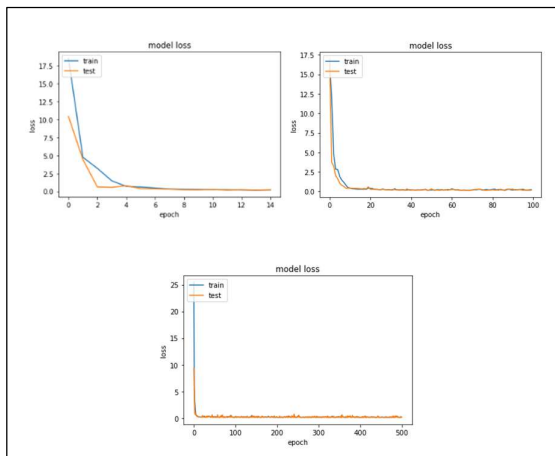


Fig.5: Loss function (error) vs. epoch (number of iterations after which we update the weights and the bias).

Table 1: test vs. predicted data	
Test (x_j) (μm)	Predicted x_j (μm)
8.69000	8.502874
5.66750	5.5411371
10.15250	9.890299
8.93375	8.9742605
6.44750	6.910209
3.96125	3.82681
5.32625	5.2161648
10.00625	9.954606
7.03250	6.982865
8.20250	8.460101
4.74125	4.9217137
6.30125	6.536751

Understanding Sensitivity of Entangled Qubit Logic Operations in Electrode-driven Semiconductor Quantum Dot Platforms

Hoon Ryu^{1*}

¹ Division of National Supercomputing,

Korea Institute of Science and Technology Information, Daejeon 34141, Republic of Korea

* Electronic mail: elec1020@kisti.re.kr

Electron spin in isotopically enriched Silicon (Si) has been known as a promising mechanism for encoding quantum bits (qubits) as the coherence time can be extremely long (> 30 seconds) even though electrons are subjected to strong quantum confinement [1]. Here, we examine the behaviors of quantum bits (qubits) encoded to electron spins in gate-driven Si double quantum dot (DQD) systems with a multi-scale modeling approach that combines Thomas-Fermi calculations and electronic structure simulations based on the effective mass approach [2]. Covering the full functionality of DQD structures from charge controls to time responses of spin-qubits, we study the sensitivity of exchange interaction between initialized spin-qubits and investigate how it affects the fidelity of 2-qubit entangled logic operations (represented with controlled-NOT (CNOT) logic operations in this work) to understand the reported features of experimental devices [3]. This preliminary study not only presents theoretical clues for figuring out the major control factors that directly affects the robustness of entangled qubits encoded to electron spins, but also opens the possibility for further exploration of the engineering details for designs of higher-degree quantum logic gate blocks (e.g., 3-qubit Toffoli (CCNOT) gate) that are not easy to be procured solely with experiments due to time and expense.

Acknowledgements

This work has been supported by the Korea Institute of Science and Technology Information (KISTI) Institutional R&D program (K-21-L02-C09) and by a grant from the National Research Foundation of Korea (NRF-2020-M3E4A1079792). The NURION high performance computing resource [4] has been extensively utilized for all the simulations.

References

- [1] J. Muhonen *et al.*, *Nature Nanotechnology* **9**, 986-991 (2014).
- [2] J.-H. Kang *et al.*, *Nanoscale* **13**, 332-339 (2021).
- [3] D. M. Zajac *et al.*, *Science* **26**, 439-442 (2018).
- [4] The NURION high performance computer in Top500 site, <https://www.top500.org/system/179421/>

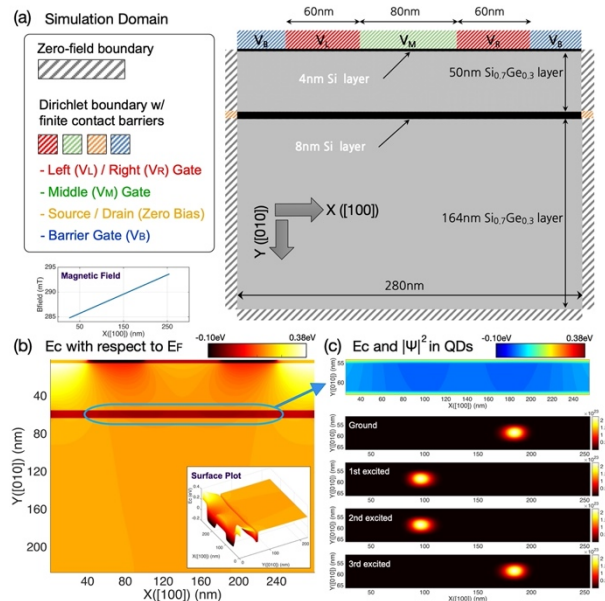


Fig. 1: Si DQD systems and electronic structures. (a) A 2D representation of Si double quantum dot (DQD) structure that is assumed to be very long along the [001] direction as the reported experimental device is (~200nm along the [001] direction). Quantum confinement along the [100] direction is formed by controlling top-gate biases (V_L, V_M, V_R). (b) Local bandstructure (E_c , spatial distribution of conduction band minimum) of the DQD system that is simulated at $V_L = 400\text{mV}$ & $V_L = V_R = 542\text{mV}$, and (c) corresponding electron density profiles at the four lowest conduction band states. Due to the magnetic field gradient along the [100] direction, Zeeman-splitting in the right QD is slightly larger than the one in the left QD.

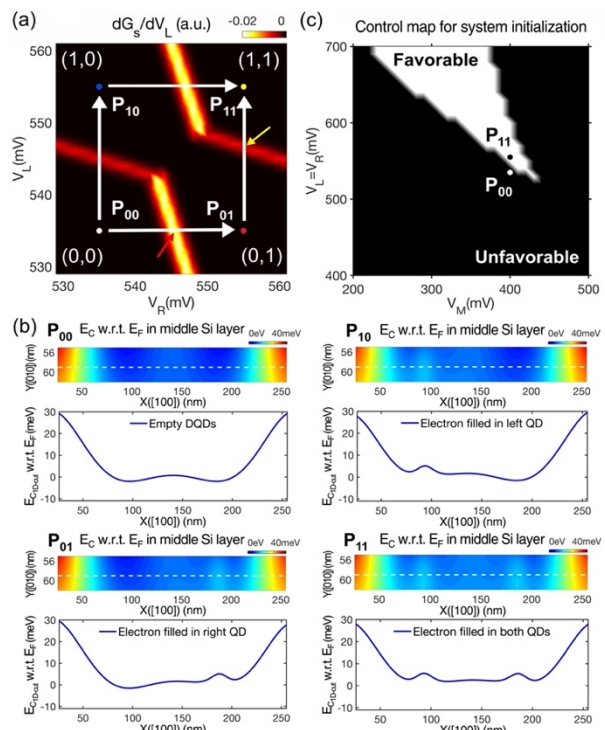


Fig. 2: Electrostatic charge control and qubit initialization in Si DQD system. (a) Charge stability diagram modelled at $V_M = 400\text{mV}$. (b) 1D potential profiles that are plotted along the [100] direction in the middle Si layer at each charge state. (c) Range of top gate biases that can initialize the DQD system, which is marked with a white color.

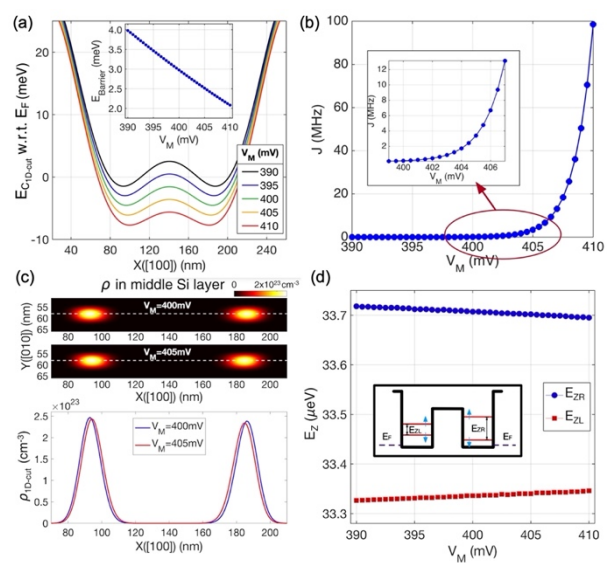


Fig. 3: Effects of the middle gate (V_M) control. (a) The 1D potential profile cut along the [100] direction in the middle Si layer, which is given as a function of V_M varying from 390mV to 410mV . The barrier height between two QDs reduces as V_M increases, and the lever-arm of the middle electrode on the top turns out to be about 10%. (b) Even though variation in the barrier height is a few mVs in the V_M range of our interest, corresponding change of the exchange interaction (J) is extremely huge, and (c) this huge change is mainly due to the change of charge distribution. (d) The Zeeman-splitting energy of the ground state in each QD turns out to be almost independent of V_M , which is good because the result indicates that the control of J and electron spin resonance frequency can be independent.

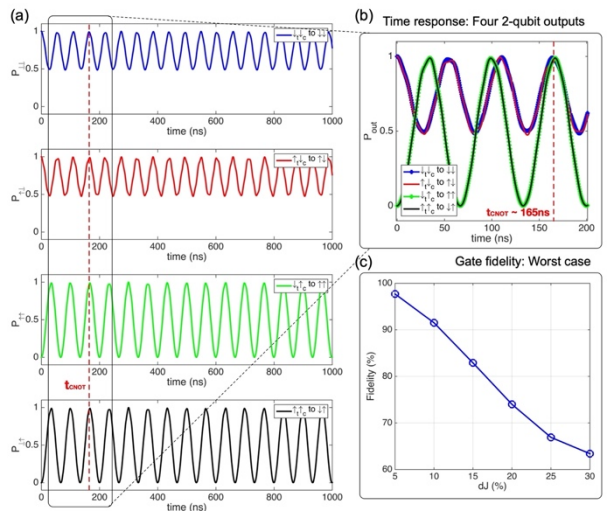


Fig. 4: Entangled 2-qubit logic operation and its sensitivity to the top gate controls. (a) 2-qubit time responses that are simulated for the four input qubits ($|\downarrow\downarrow\rangle, |\downarrow\uparrow\rangle, |\uparrow\downarrow\rangle, |\uparrow\uparrow\rangle$). Top gate biases are set to initialize the DQD system to the (1,1) charge state, where J (exchange coupling) between two QDs becomes about 10MHz . (b) Controlled-NOT (CNOT) operation is achieved at $t = \text{multiples of } 165\text{ns}$. (c) The state fidelity of CNOT operations at $t = 165\text{ns}$ is plotted as a function of ΔJ , which indicates the percentile deviation of J with respect to the reference value. Note that just 15% deviation of J already lowers the state-fidelity under 80% (the best state-fidelity reported for single-pulse CNOT operation so far is around 78%). So, the precise control of J is the key to improve the fidelity of entangled qubit logic operations that are represented by the CNOT gate in this work.

Inverse-designed spin dynamics for neuromorphic computation

Adam Papp¹, Gyorgy Csaba¹, and Wolfgang Porod²

¹ *Faculty for Information Technology, Pázmány Péter Catholic University, Budapest, Hungary*

² *Department of Electrical Engineering, University of Notre Dame, Notre Dame, IN 46556*

porod@nd.edu

It is well known that interference of linear waves can be used for special-purpose computing, such as calculating convolutions, Fourier transforms and vector-matrix products. This fact has long been used in optical computing. It has also been hypothesized that nonlinear waves have potential for neuromorphic and general-purpose computing [1]. So far, however, no concrete physical system has been engineered to perform such computational tasks, which is likely due to the complexities of non-linear wave propagation.

In this work, we integrate the Pytorch machine learning engine with a custom-built GPU-based micromagnetic simulator for the inverse-design of a magnetic medium where spin-wave dynamics performs computational tasks [2]. Specifically, the computational learning algorithm designs a magnetic field distribution that focuses scattered spin waves with high wave intensity at a certain output point that represents the result of the neuromorphic computation. Figure 1 shows snapshots of the designed spin-wave scatterer. The input waveforms (this case vowels) are recognized by focusing them to the desired output. We demonstrate that such a spin-wave substrate operating in the high-intensity non-linear regime is capable of functions that are not computable by a linear system.

The Pytorch engine relies on gradient-based learning. The algorithm requires a micromagnetic simulator to be fully integrated with the learning engine and the intermediate steps of the computation to be saved and passed on to the learning engine. A block diagram of the algorithm is shown in Fig 2 and details will be shown in our presentation. The system can, in principle, optimize for any computing function, without any manual intervention – albeit the numerical algorithm is demanding and this limits the size of the system that can be designed.

We believe that this work demonstrates a new methodology for the design of functional nanoelectronic/magnetic devices, and presents a specific physical system towards the longtime dream of doing computation by a material substrate.

[1] Hughes, et. al: "Wave physics as an analog recurrent neural network." *Science advances* 5, no. 12 (2019):

[2] Papp et. al: "Nanoscale neural network using non-linear spin-wave interference." arXiv preprint arXiv:2012.04594 (2020).

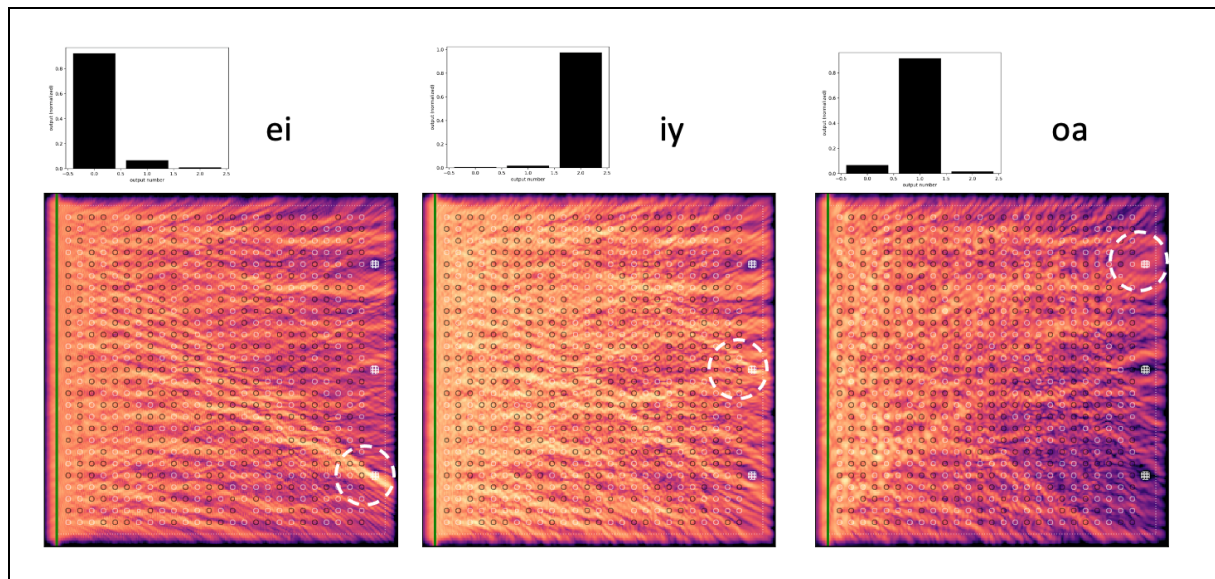


Fig 1. Spin-wave interference patterns formed as a response to various input vowel waveforms. Different vowels result in energy focused to different output points. These images resemble field-intensity distributions from linear nanophotonic designs, but they show nonlinear (rather than linear) interference patterns.

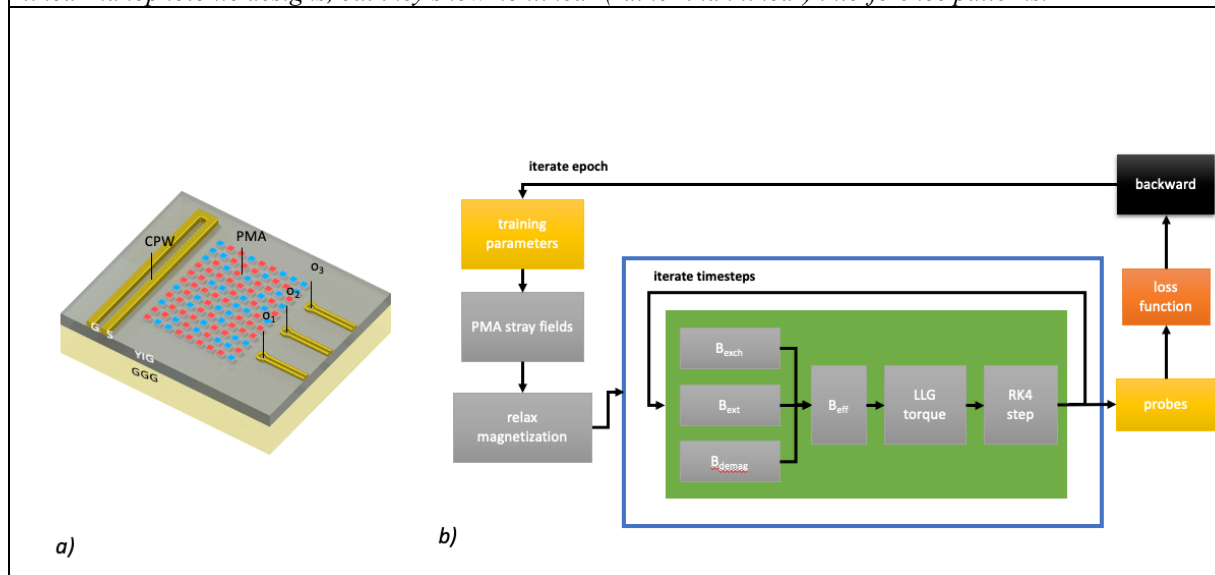


Fig. 2. a) Schematic layout of the spin-wave scatterer with waveguide inputs and field-sensor outputs. The learning algorithms adjust the orientations of the PMA magnets on top, which function as the scattering centers. b) flowchart of the numerical engine, with the micromagnetic simulation code depicted in the framed area, and around it the controlling numerical engine.

Analytical Models of Ferroelectric Field Effect Transistor with Two-Dimensional Channel Material

Jeonghyeon Kim, and Jiwon Chang

*Department of Electrical Engineering, Ulsan National Institute of Science and Technology,
Ulsan 44919, Republic of Korea*

jiwon.chang@unist.ac.kr

Ferroelectric non-volatile memory has been extensively investigated due to the promising properties such as low-voltage and low-power consumption. In order to analytically understand the electrical characteristics of Si-based ferroelectric field-effect transistor (FeFET), mathematical models have been suggested by Miller et al. [1]. Meanwhile, two-dimensional (2D) transition metal dichalcogenides (TMDCs) have emerged as a promising channel material in ultra-scaled FET due to the atomically thin nature. Accordingly, there have been several experimental demonstrations of FeFET with 2D channel material (2D FeFET), but little development of analytical models to describe the behavior of 2D FeFET.

Here, we present analytical models of 2D FeFET which are developed by modifying Miller's FeFET model using the Poisson equation [2,3] rather than using the Brews charge sheet model [1]. In order to obtain the channel charge in 2D TMDCs, Ward-Dutton charge partitioning method adopted by Jiang et al [2] is used. To explain FeFET behavior more precisely, the mathematical model to describe the non-saturated hysteresis loop of ferroelectrics is adopted [4]. We consider Metal-Ferroelectric-Insulator-Semiconductor (MFIS) structure for 2D FeFET which could be constructed using CuInP_2S_6 (CIPS), h-BN and WSe_2 as 2D ferroelectric, 2D insulator and 2D channel materials, respectively. Models for 2D FET without ferroelectrics are also presented to be compared with 2D FeFET and clarify how 2D FeFET works.

We study the dependency of memory window in 2D FeFET on the ferroelectric properties (remnant polarization P_r and coercive field E_c), thickness and dielectric constant of ferroelectric and insulator. Consequently, our work aims to present the optimized 2D FeFET structure that can maximize the memory window.

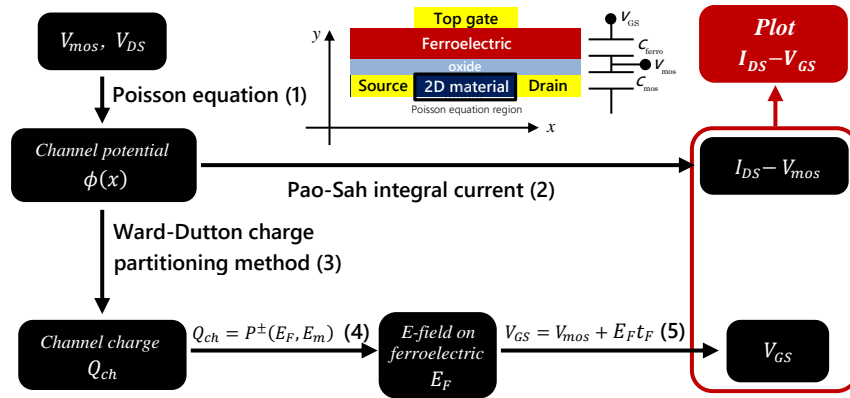
Acknowledgement: This research was supported by the Basic Science Research Program through the National Research Foundation of Korea (NRF) funded by the Ministry of Science, ICT & Future Planning (2020R1F1A1069417).

[1] S. L. Miller and P. J. McWhorter, *J. Appl. Phys.* **72**, 5999 (1993)

[2] C. Jiang et al., *IEEE J. Electron Devices Soc.* **6**, 189 (2018)

[3] W. Cao et al., *IEEE Trans. Electron Devices*, **61**, 4282 (2014)

[4] Hang-Ting Lue et al., *IEEE Trans. Electron Devices*, **49**, 1790 (2002)



Poisson's equation:

$$\frac{d^2\phi}{dx^2} - \frac{d^2\phi}{dy^2} = \frac{q(n_{2D} - N_d)}{\epsilon_{2D}t_{2D}} \quad \phi(x): \text{Electrostatic potential of the channel along } x \text{ direction}$$

$$\frac{d^2\phi}{dx^2} - \frac{\phi}{\lambda^2} + \xi = \frac{q(n_{2D} - N_d)}{\epsilon_{2D}t_{2D}} \quad V_{ch}: \text{Applied voltage on the channel along } x \text{ direction}$$

$$\phi(x) = V_{ch} + \frac{k_B T}{q} \ln \left\{ \frac{\epsilon_{2D} t_{2D}}{q n_{2D}} \left[\xi - \frac{\phi(x)}{\lambda^2} \right] + \frac{N_d}{n_{2D}} \right\} \quad \text{where } \xi \equiv \frac{V_{mos} - V_{FB}}{\lambda^2}, \quad \lambda \equiv \sqrt{\frac{\epsilon_{2D} t_{ox} t_{2D}}{\epsilon_{ox}}} \quad (1)$$

Pao-Sah integral current:

$$I_{DS} = \mu_n \frac{qW}{L} \int_0^{V_{DS}} n_{2D} dV_{ch} = \mu_n \frac{qW}{L} \int_0^{V_{DS}} \left[N_d + \frac{\epsilon_{2D} t_{2D}}{q} \right] d\phi \frac{dV_{ch}}{d\phi} \quad (2)$$

Ward-Dutton charge partitioning method:

$$Q_{ch} = qW \int_0^L (n_{2D} - N_d) dx = qW \int_0^L (n_{2D} - N_d) d\phi(x) \frac{dx}{d\phi(x)} \quad (3)$$

P-E hysteresis loop analytical model for a MFM structure:

$$P^\pm(E, E_m) = P_S \tanh\left(\frac{E \mp E_c}{2\delta}\right) + \epsilon_F \epsilon_0 E \pm \frac{P_S}{2} \left(\tanh\left(\frac{E_m + E_c}{2\delta}\right) - \tanh\left(\frac{E_m - E_c}{2\delta}\right) \right) \quad (4)$$

Modified Gate Bias:

$$V_{GS} = V_{mos} + V_F = V_{mos} + E_F t_F, \quad \text{where } Q_{ch} = P^\pm(E_F, E_m) \quad (5)$$

Fig1. Schematic device structure and a modeling flow of 2D FeFET with modeling equations.

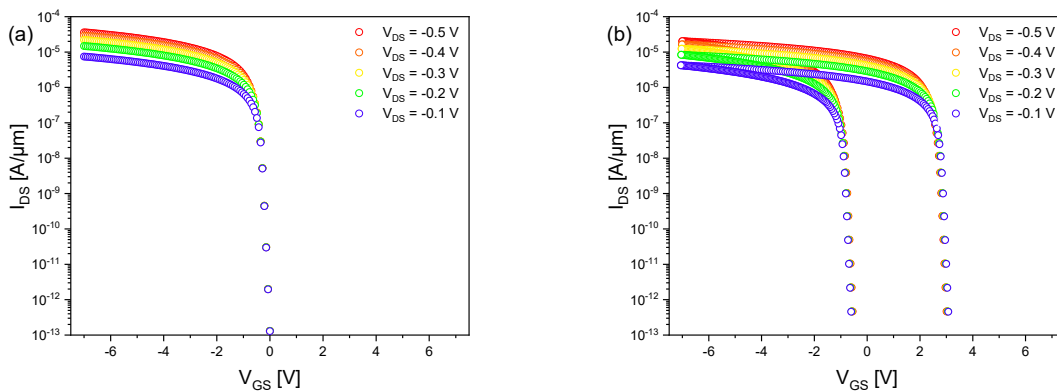


Fig2. Simulated transfer characteristics for 2D FET with gate stack of WSe₂/h-BN (a), FeFET with gate stack of WSe₂/h-BN/CIPS (b).

Metadynamics Sampling in Atomic Environment Space for Collecting Training Data for Machine Learning Potentials

Dongsun Yoo^{1,2}, Jisu Jung¹, Wonseok Jeong¹ and Seungwu Han¹

¹ *Department of Materials Science and Engineering and Research Institute of Advanced Materials, Seoul National University, Seoul 08826, Korea.*

² *Present address: Samsung Display Co., Ltd., 1, Samsung-ro, Giheung-gu, Yongin-si, Gyeonggi-do 17133, Korea.*

wjdwlt928@snu.ac.kr

Machine learning potentials (MLPs) are garnering attention in atomistic simulation by providing the accuracy of quantum mechanical calculations at much lower costs. Due to its flexible functional form, MLPs shift the heart of interatomic potential development from building mathematical formula to collecting a proper training set. As an interpolation algorithm, MLPs can guarantee their reliability only within the training set. Therefore, the training set should cover all local atomic environments that may appear in the target simulation ideally. Usually, the training set is constructed from the crystal structure or molecular dynamics (MD) simulations. However, these conventional approaches govern by Boltzmann statistics have difficulty in sampling various configurations, so that practitioners handpick the essential configuration with expertise iteratively to improve MLPs. Recently, some researchers try to sample the diverse configuration with methods such as random structure search and entropy-maximization[1, 2], but their applications are still limited.

In this presentation, we suggest a novel sampling method based on metadynamics. The thermal barrier is overcome through the metadynamics accumulating bias potential along with the collective variables (CVs). The metadynamics using the coordinate in local atomic environment space, encoded atom-centered symmetry function vector, as collective variable drives the system into the unvisited configuration semi-automatically. We apply proposed metadynamics sampling to H:Pt (111), GeTe, and Si systems. According to the examples, a small number of metadynamics trajectories can collect enough diverse configurations to develop the reliable MLPs.

[1] V. L. Deringer, C. J. Pickard, & G. Csányi, *Phys. Rev. Lett.*, **120**, 156001 (2020).

[2] M. Karabin & D. Perez, *J. Chem. Phys.*, **153**, 094110 (2020).

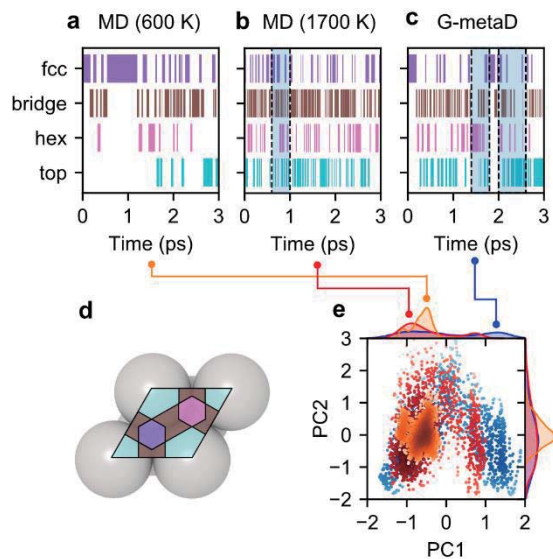


Fig. 1: Sampled configurations during MD and Metadynamics. **a-c** The classification of H sites along the time for MD at 600 K, 1700 K, and proposed metadynamics (G-metaD) at 600 K, respectively. The shaded area means that the H atom is on the sublayer. The color of sites is corresponded to **d**. **d** Characteristic area on Pt(111) surface. **e** Distribution of sampled points of H atom on principal components axes.

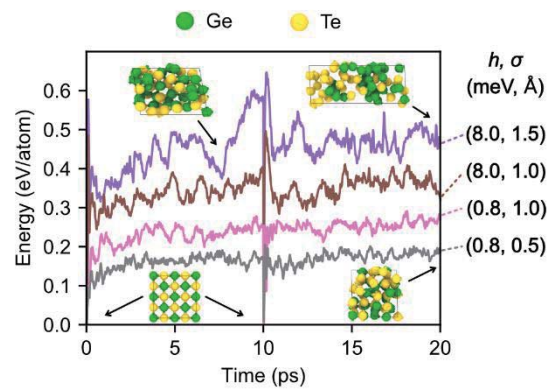


Fig. 3: Time evolution of potential energy of four G-metaD along the time. The energy is referenced to that of the rock-salt structure. Structures during G-metaD are shown as inset figures.

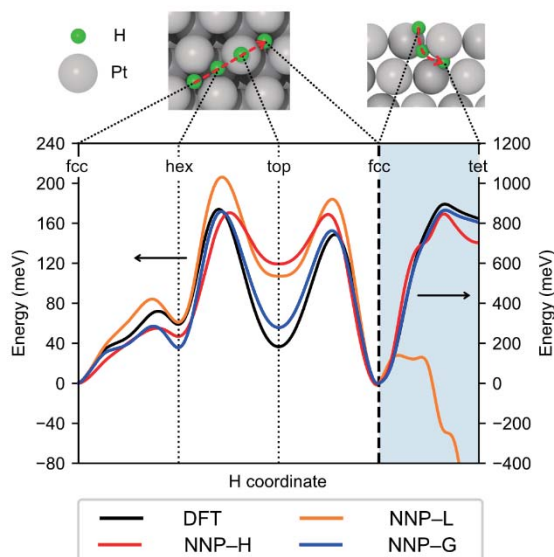


Fig. 2: The minimum energy paths along $fcc \rightarrow hex \rightarrow top \rightarrow fcc \rightarrow tet$ (subsurface tetrahedral site). NNP-L, NNP-H, and NNP-G stand for the NNP constructed from the MD 600K, MD 1700 K, and G-metaD, respectively.

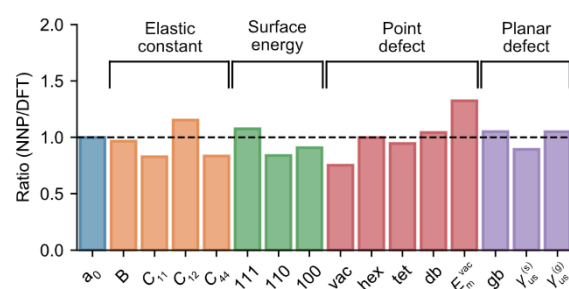


Fig. 4: Ratios of NNP to DFT for static properties of Si in the diamond structure. Surface energies are calculated for $(100)-(2 \times 2)$, 47 $(110)-(1 \times 1)$, 48 and $(111)-(3 \times 3)$ reconstructions. 49 Defect formation energies for the vacancy (vac) and interstitials (hexagonal (hex), tetrahedral (tetra), and dumbbell (db)). E_m^{vac} is the migration energy of the vacancy. For extended defects, gb means the $(112)\Sigma 3$ grain boundary. γ_{sh} (s) and γ_{gl} (g) are unstable stacking-fault energies on shuffle and glide planes of the diamond (111) plane.

Edited by

Mincheol Shin
Sung-Min Hong
Jiwon Chang
Hoon Ryu
Yong-Hoon Kim

ISBN 978-89-89453-30-7

© 2021 School of Electrical Engineering, Korea
Advanced Institute of Science and Technology, Daejeon
34141, Rep. of Korea